Numerical Simulation and Experimental Investigation of the Fracture Behaviour of an Electron Beam Welded Steel Joint

Von der Fakultät für Energie-, Verfahrens- und Biotechnik der
Universität Stuttgart zur Erlangung der Würde eines
Doktors der Ingenieurwissenschaften (Dr.-Ing.) genehmigte Abhandlung

Vorgelegt von

M. Eng. Haoyun Tu

aus Xi'an, V.R. China

Hauptberichter: Prof. Dr. rer. nat. Siegfried Schmauder, Stuttgart
Mitberichter: Associate Prof. Thilo Frank Morgeneyer, Chargé de recherches, HDR, PhD, Mines ParisTech, Paris

Tag der mündlichen Prüfung: 06. November 2015

Institut für Materialprüfung, Werkstoffkunde und Festigkeitslehre
der Universität Stuttgart

2016

Legal statement

I declare that all works in the thesis are produced by me. Ideas taken directly or indirectly from other sources are cited accordingly. This work has not been shown to any other board of examiners so far and some of the work has not been published yet. I am fully aware of moral and legal consequences of making a false declaration.

12th May, 2015, Stuttgart
Haoyun Tu

Table of Contents

Notations and Symbols

Symbols

	Unit	
a	mm	Half of the crack length
a_0	mm	Initial crack length (of the specimen)
σ	MPa	Stress
σ_c	MPa	Critical cleavage stress
σ_{ij}	MPa	Stress tensor
σ_{eq}	MPa	Von Mises equivalent stress
σ_k	MPa	Material constant of the Rousselier model
σ_m	MPa	Mean (hydrostatic) stress
σ_0	MPa	Yield stress
Δa	mm	Crack extension
ΔD	mm	Cross section reduction
K_I	$MPa\sqrt{m}$	Stress intensity factor
f	-	Void volume fraction
f_0	-	Initial void volume fraction
f_c	-	Critical void volume fraction in the Rousselier model
	-	Void volume fraction of void coalescence in the GTN model
f_f	-	Final void volume fraction (in the GTN model)
f_u^*	-	f^* in the GTN model ($f = f_f$)
l_c	mm	main distance between two neighbouring voids
T_0	MPa	Cohesive strength
r	mm	Void radius
G	J/m^2	Energy release rate
π	-	Pi
q_1, q_2, q_3	-	Model parameters affecting the GTN yield surface
W	Pa	Strain energy density
ε_n	-	Mean strain when void nucleation happens
s_n	-	Standard deviation

ε_{ij}	-	Strain tensor
η	-	Stress triaxiality ($\eta = \sigma_m/\sigma_{eq}$)
k	-	Damage acceleration factor in the GTN-model
θ	Degree	Laminographic angle
ν	-	Poisson's ratio
δ	mm	Separation of the cohesive element
δ_0	mm	Critical displacement at failure in the cohesive model
δ_{init}	mm	Displacement when void initiation happens in the cohesive zone model

Capital symbols

A	-	Strain at rupture
A_g	-	Uniform strain
K_{nn}	N/mm^3	Cohesive stiffness ($\delta = \delta_{init}$)
W	mm	Width of fracture mechanics specimen
Γ_0	N/mm	Cohesive energy
E	MPa	Young's modulus
F	N	Force
F*	-	Revised factor for initial void volume fraction
J	N/mm	J-integral
$J_{0.1}$	N/mm	J-value when Δa=0.1 mm
J_i	N/mm	J-value when the first finite element is damaged
J_R		Fracture resistance

Abbreviations

2D	Two Dimensional
3D	Three Dimensional
ASTM	American Society for Testing and Materials
B	Thickness of the specimen
Bcc	Body-centered cubic
BM	Base material
B_n	Net thickness of the specimen

C	Compliance of the C(T)-specimen
CCD	Charge coupled device
CMOD	Crack mouth opening displacement
COD	Crack opening displacement
CTOD	Crack tip opening displacement
C(T)	Compact tension
D	Damage variable in cohesive zone model
EBW	Electron beam welding
EDM	Electrical discharge machining
EDX	Energy-dispersive X-ray spectroscopy
FEM	Finite Element Method
FZ	Fusion zone
GTN	Gurson-Tvergaard-Needleman (model)
HEDB	High energy density beam
HAZ	Heat affected zone
HV	Vickers hardness
M(T)	Middle cracked tension (specimen)
SEM	Scanning electron microscope
SENB	Single Edge Notched Bend
SRCL	Synchrotron radiation-computed laminography
SRCT	Synchrotron radiation-computed tomography
TSL	Traction separation law

Abstract

Welding techniques are widely applied in many industry fields. As the damage behavior of the weldment influences the service life of the component, strong attention is drawn to the weldment. This thesis focuses on the fracture behavior of an S355 electron beam welded joint. Three different models are adopted to describe the damage behavior of the welded joints, namely the Rousselier model, the Gurson-Tvergaard-Needleman (GTN) model and the Cohesive zone model (CZM). Although differences exist between these models, they successfully describe the damage behavior of the weldment and are able to predict the crack propagation of C(T)-specimens obtained from S355 electron beam welded joints. Simulation results are shown in the form of force vs. crack opening displacement (COD) and fracture resistance J_R-curves. The cohesive zone model is considered to be the best model for the investigation of the fracture behavior of S355 electron beam welded joints as it can simulate both ductile and brittle fracture. Compared to the GTN model, the Rousselier model for ductile fracture simulations shows its superiority because of simplicity and reduced model parameters.

In order to visualize the crack propagation at the surface of the material, C(T)-specimens extracted from the S355 base material are tensile tested together with the ARAMIS system monitoring the material deformation and crack growth behavior in the notched area. Images in the notched region and the equivalent strain distribution calculated from the ARAMIS system are shown. 2D and 3D GTN models are used to investigate the fracture behavior of a C(T)-specimen under tensile test process monitored with the ARAMIS system. To understand the damage mechanisms of the S355 base material and to show the real crack propagation within the material during the deformation process, Synchrotron radiation-computed laminography (SRCL) is performed on a thin sheet specimen from S355 base material for the first time. Reconstructed 2D laminography images from the middle section and from the section where the main crack is observed in the sheet specimen are shown in this work. Additionally, 2D cross-sections at the through thickness plane at two positions located ahead of the initial notch are shown. A shear band is observed between two neighbouring cracks before crack advancement at CMOD=1.25 mm. 3D reconstruction of the laminography scanning data confirms the damage evolution through void initiation, growth and coalescence originating from non-metallic inclusions being the main reason for

a flat fracture happening before the slant fracture. Shear fracture connecting two neighbouring flat cracks to form the main crack is observed in 3D laminography images. The 3D Rousselier model is adopted to predict the flat fracture of the thin sheet specimen. The material in front of the initial notch is divided into many partitions of which the true f_0-values are obtained. According to the positions of the partitions, the Rousselier elements in front of the initial notch are divided into many sets where the corresponding true f_0-values are used in the simulations. With the true f_0-values, the longest 2D cracks (T-L) in an analyzed specimen are located at a cross section which is around 200 µm apart from the middle section of the sheet specimen which coincides with the laminographic image. The Rousselier model is able to predict the fracture surface of the sheet specimen before the occurrence of the shear fracture.

Zusammenfassung

Schweißtechniken werden in der Industrie in vielen Anwedungen eingesetzt. Da die Schweißverbindung die Lebensdauer eines Bauteils wesentlich beeinflusst, ist das Schädingungsverhalten der Schweißverbindung von besonderem Interesse. Diese Arbeit befasst sich mit dem Bruchverhalten einer S355- Elektronenstrahlschweißverbindung. Das Schädigungsverhalten der Schweißverbindungen wird mit drei verschiedenen Modellen, dem Rousselier-Modell, dem Gurson-Tvergaard-Needleman (GTN)-Modell und dem Kohäsivzonenmodell (CZM) beschrieben. Obwohl Unterschiede in diesen Modellen bestehen, können sie das Schädigungsverhalten der Schweißverbindung sehr gut beschreiben und können die Rissausbreitung in C(T)-Proben von S355-Elektronenstrahlschweißverbindungen vor-aussagen. Die Simulationsergebnisse werden in Form von Diagrammen dargestellt, die die Kraft über der Rissöffnung (COD) sowie die Bruchwiderstandskurven J_R-zeigen. Das Kohäsivzonenmodell zeigte sich als das am besten geeignete Modell zur Untersuchung des Bruchverhaltens von S355 Elektronenstrahl Schweißverbindungen, da es die Modellierung von duktilem und sprödem Bruchverhalten ermöglicht. Im Vergleich zum GTN-Modell zeigt das Rousselier-Modell bei Simulationen des duktilen Bruchverhaltens seine Stärken, da es vereinfachte und reduzierte Modellparameter besitzt.

Um die Rissausbreitung an der Oberfläche des Materials zu untersuchen, wird ein Zugversuch mit C(T)-Proben aus dem S355-Basismaterial mit dem ARAMIS-System durchgeführt, wobei die Materialdeformation und das Rissausbreitungsverhalten im Bereich der Kerbe betrachtet wird. Bilder der Kerbregion, sowie die äquivalente Dehnungsverteilung (berechnet mit dem ARAMIS-System), werden gezeigt. 2D und 3D GTN-Modelle werden verwendet, um das Bruchverhalten einer C(T) Probe in einem durch ARAMIS beobachteten Zugversuch zu beschreiben. Mit dem Ziel, die Schädigungsmechanismen des S355-Basismaterials zu verstehen und die Rissausbreitung innerhalb des Materials während der Materialverformung zu zeigen, wird erstmalig Synchrotron Radiation-Computed Laminography (SRCL) an einer Probe aus einer dünnen Folie des S355-Basismaterials durchgeführt. Rekonstruierte 2D Laminographiebilder der Folienprobe des Mittelteils sowie aus dem Bereich vor dem Hauptriss werden in dieser Arbeit vorgestellt. Zudem wurden 2D-

Schnitte durch die Probe senkrecht zur Folienebene an zwei verschiedenen Stellen in Rissausbreitungsrichtung erstellt. Um CMOD=1.25 mm wird vor weiterem Rissfortschritt die Bildung eines Scherbandes zwischen zwei benachbarten Rissen beobachtet. Die 3D-Rekonstruktion des S355-Basismaterials aus Laminographie-Scandaten bestätigt die Schädigungsentwicklung im Werkstoff durch Hohlraumbildung, Hohlraumwachstum und Hohlraumkoaleszenz bedingt durch nichtmetallische Einschlüsse. Diese sind die Hauptursache für das Auftreten von Längsrissen vor Scherbruch. Der Scherbruch, welcher zwischen zwei benachbarten Längsrissen auftritt, und damit den Hauptriss bildet wird in 2D Laminographiebildern beobachtet. Das 3D Rousselier-Modell wird verwendet, um den Längsriss einer Probe vorherzusagen. Vor der Anfangskerbe wird der Werkstoff in verschiedene Partitionen unterteilt, in denen die wahren f_0-Werte ermittelt werden. Die Rousselier Elemente vor der Anfangskerbe sind ebenso wie die Positionen der Partitionen unterteilt in viele Sets, in denen die korrespondierenden wahren f_0-Werte für die Simulationen ermittelt werden. Mit den wahren f_0-Werten zeigt sich der längste 2D Riss (T-L) in einer Schnittebene, die etwa 200 µm vom mittleren Bereich der flachen Probe entfernt ist. Dies stimmt mit den Laminographie-Aufnahmen überein. Das Rousselier-Modell kann die Bruchfläche der dünnen Probe vor Eintritt des Scherbruchs vorhersagen.

1. Introduction

1.1 Motivation

Steel, an ancient metal, is assumed to be produced and used since around 4000 years. Since the industrial revolution in the 18th century, with the high requirement of machines, modern steels have found many applications in different industry fields, e.g., railway construction, house and ship building. Since then, material scientists have been investigating the material behavior of different steels and the corresponding fracture behavior of components. The riveting technique was adopted widely to connect different components of structures. With the requirement of lighter structures, welding techniques have been used instead of riveting. As the fracture behavior of a structural component influences the service life of machines, in order to increase the lifetime of a machine, scientists have been trying to answer why structural components fail. Nowadays, electron beam welded joints are used widely in automotive and aircraft industries. These applications require appropriate crack growth resistance since crack growth and fracture are unavoidable in service of engineering materials which affect the service life and safety of components in certain key applications. Since the development of damage models, numerical simulations of crack propagation in homogenous and inhomogeneous structures are possible. One motivation of the thesis is that a lot of money and research time from experiments can be saved and the numerical simulation can predict the crack propagation of the welded joints. Another motivation is to visualize the damage evolution during material deformation and to show how the cracks propagate on the surface of the tested specimen and within the material during the material deformation process.

1.2 Outline

The present work is structured into 11 chapters and summarized as follows:

Chapter 2 provides the introduction of the electron beam welding process. The fundamental concepts of fracture mechanics are also shown. The development of the constitutive damage models and typical damage models, e.g., the GTN model and the Rousselier model are introduced in this chapter as well. The concept of the cohesive zone model and

its application is presented. Finally, applications of the ARAMIS system and of the synchrotron radiation-computed laminography (SRCL) are presented.

Chapter 3 shows some experimental investigations performed on the S355 welded joints. They are hardness measurement, tensile tests of flat specimens, smooth round and notched round specimens. Optical microscopy measurements on the different welded regions are also discussed in this chapter. Fracture toughness tests were performed on the C(T)-specimens extracted from different weld regions and the SEM results on the fracture surfaces of these C(T)-specimens are presented. These experimental data provide usefully information for the following finite element models.

Chapter 4 summarizes the simulation results obtained from the Rousselier model. Firstly, the parameter studies are performed in order to show the influence of the Rousselier parameters on the tensile test results of notched round specimens and C(T)-specimens. The Rousselier parameters are calibrated on the notched round specimens. Then the same Rousselier parameter set is used to investigate the crack propagation of C(T)-BM and C(T)-HAZ specimens extracted from different weld regions.

Chapter 5 shows the applications of the GTN model investigating the fracture behavior of the S355 welded joints. As the GTN model has more parameters in comparison to that of the Rousselier model, a more detailed parameter study is presented which shows the influences of the GTN parameter on the tensile test results of the notched round specimens and the C(T)-specimens. Using the parameter set obtained from the notched round specimen, the GTN model is adopted to predict the crack propagation of C(T)-BM and C(T)-HAZ specimens.

Chapter 6 discusses the influence of the cohesive parameters and other factors (cohesive element, shape of TSL, etc.) on the F-COD-curve. Exponential and tabular TSLs are adopted to investigate the fracture behavior of C(T)-BM and C(T)-HAZ. A linear softening TSL is used to predict the fracture of the C(T)-FZ.

Chapter 7 presents the images from the camera and the strain distribution results calculated from the ARAMIS system for the notched region of a C(T)-BM under monotonic

loading process. 2D and 3D GTN models are adopted to describe the damage evolution of a C(T)-BM specimen under monotonic loading condition monitored by the ARAMIS system.

Chapter 8 discusses the experimental results obtained from the SRCL scanning. 2D (T-L) laminography images from the middle section and from the section where the longest crack observed are shown. 2D images through the thickness plane (T-S) at two positions ahead of the initial notch are shown. Reconstructed 3D images of the bulk material at different loading steps are presented. A 3D Rousselier model is adopted to predict the fracture surface of the C(T)-specimen before the slant fracture happens.

Chapter 9 summarizes the main achievements of the dissertation. The outlook for possible future works is discussed.

Chapter 10 summarizes the publications achieved during the PhD period and chapter 11 shows the literature cited in this thesis.

2. Scientific background

Fracture is a problem which troubles structural engineers for centuries. People have been trying to answer when, where, and why the structures fail. Scientists have been trying to investigate the fracture mechanisms of complex components, e.g., the weldment, as the fracture behaviour of weldments influences the crack growth in structures which affects the lifetime and safety of the components. With the rapid development of the finite element method, it is possible to investigate the fracture mechanisms and to predict numerically crack propagation in the materials under investigation. Recently, some scientific activities were performed to investigate the fracture behavior of advanced weldments, for instance, the electron beam welded joints. In the following subchapters, the experimental investigations and numerical simulation activities are presented for the electron beam welded joints. Before explaining the scientific activities, background information is introduced in this chapter to help the reader to acquire the necessary knowledge.

2.1 Electron beam welding

Electron beam welding (EBW) is the welding process in which the material is melted and jointed by a high-velocity electron beam, as depicted in Fig. 2.1(a). During the welding process, a keyhole can be formed because high density electron beam melting the metal, as described in Fig. 2.1(b). The welding speed and the beam current used during the welding process are the major parameters which influence the quality of the welded joints. The EBW is one of the components in High Energy Density Beam (HEDB) welding techniques. Compared to traditional welding processes, like arc welding process, the EBW possesses many benefits. For example, thick joints can be electron beam welded with a single pass whereas multiple passes for the welding process are needed for the arc welding technique. Narrow heat affected zones, little distortion and less residual stresses can be obtained after the welding process due to the high power density during the EBW. Of course, the electron beam welding also provides some drawbacks: the equipment cost for EBW is very high and the requirement of X-ray shielding is inconvenient and time consuming [Kou, 2002].

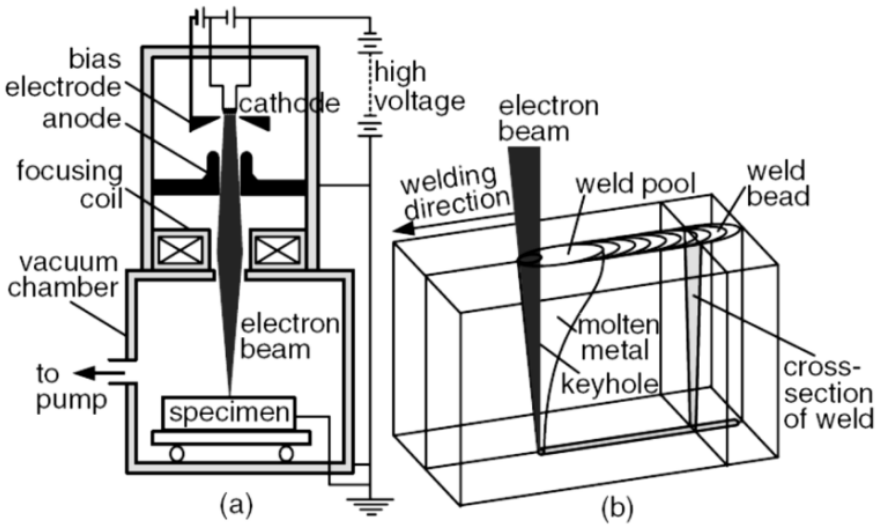

Fig. 2.1: Electron beam welding: (a) process and (b) a keyhole formed during the welding process [Kou, 2002].

2.2 Fracture mechanics

2.2.1 The fracture mechanics approach

There are two different judgment ways for the facture analysis: the energy criterion and the stress intensity approach. The energy approach assumes that crack propagation happens when the energy available for the crack is high enough to overcome the fracture resistance of the material. Griffith [Griffith, 1920] was the first who proposed an energy criterion for fracture, while Irwin [Irwin, 1957] is responsible for developing the approach in the current state. For a crack of length 2a in an infinite plate subject to a remote tensile stress (see Fig. 2.2) [Anderson, 2005], the energy release rate which is the driving force for the fracture can be expressed as follows:

$$\mathrm{G} = \frac{\pi\sigma^2 \mathrm{a}}{\mathrm{E}} \tag{2.1}$$

where E is Young's modulus, G is the energy release rate, σ is the remotely applied stress and a is half of the crack length.

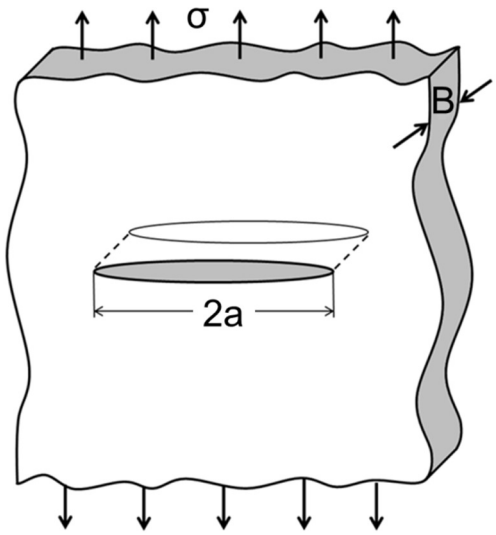

Fig. 2.2: Crack in an infinite plate subject to a remote tensile stress [Anderson, 2005].

The other approach for the fracture analysis is the stress intensity method. Fig. 2.3 shows one element near the tip of a crack in an elastic material and the in-plane stresses on this element is shown [Anderson, 2005]. Fracture happens at the critical value of K_I, where the entire stress distribution at the crack tip can be calculated with the equations in Fig. 2.3.

For the infinite plate subject to a remote stress shown in Fig. 2.2, the stress intensity factor can be written as follows:

$$K_I = \sigma\sqrt{\pi a} \tag{2.2}$$

Combining equation (2.1) and equation (2.2), the relationship between K_I and G is derived as follows:

$$G = \frac{K_I^2}{E} \tag{2.3}$$

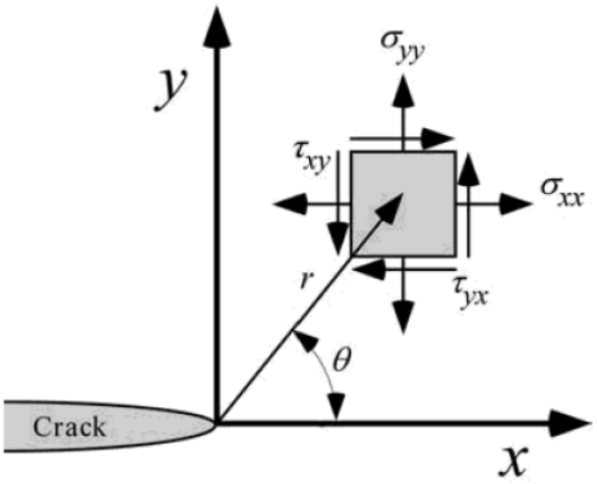

$$\sigma_{xx} = \frac{K_I}{\sqrt{2\pi r}} \cos\left(\frac{\theta}{2}\right)\left[1 - \sin\left(\frac{\theta}{2}\right)\sin\left(\frac{3\theta}{2}\right)\right]$$

$$\sigma_{yy} = \frac{K_I}{\sqrt{2\pi r}} \cos\left(\frac{\theta}{2}\right)\left[1 + \sin\left(\frac{\theta}{2}\right)\sin\left(\frac{3\theta}{2}\right)\right]$$

$$\tau_{xy} = \frac{K_I}{\sqrt{2\pi r}} \cos\left(\frac{\theta}{2}\right)\sin\left(\frac{\theta}{2}\right)\cos\left(\frac{3\theta}{2}\right)$$

Fig. 2.3: Stresses near the tip of a crack in an elastic material [Anderson, 2005].

2.2.2 The Brittle fracture

There are two types of fracture mechanism: ductile and brittle. Ductile fracture applies when the material sustains large plastic strain or deformation before the final fracture. Brittle fracture occurs when a relative small or negligible amount of plastic strain is observed before fracture. Brittle failure results usually from cleavage where separation along specific crystallographic planes is found. At low temperatures, body-centered cubic (Bcc) metals fail by cleavage when the plastic flow is restricted by a limited number of active slip systems [Anderson, 2005]. When the maximum principal stress reaches the critical one (so called critical cleavage stress σ_c), cleavage fracture will occur [Beremin, 1983]. Bcc metals, e.g., mild steels will become brittle at low temperatures. For Bcc metals, the force needed to move dislocations is strongly dependent on the temperature and the movement of the dislocations becomes difficult at low temperature. If the maximum principal stress is high enough brittle fracture will happen, otherwise fracture will only happen when a sufficient level of the principle stress is reached [Beremin, 1983]. According to the discussion of Griffiths [Griffiths et al., 1971], the critical cleavage stress is independent of temperature and can be obtained from notched bend specimens.

The mechanics of fracture progressed from being a scientific curiosity to an engineering discipline, primarily due to what happened to the liberty ships during World War II [Irwin, 1957]. Many liberty ships built in the early days of World War II ruptured suddenly in 1940s. One of the main reasons is due to the weld, which was produced by a semi-skilled work

force and which contained crack-like flaws [Anderson, 2005]. The weld with initial defects always ruptures suddenly, showing brittle fracture. With the development of weld quality control standards, high quality weldments without initial defects are obtained nowadays.

2.2.3 The J-integral

The J-integral is a contour integral which was introduced by Rice [Rice, 1969] as a fracture parameter in a nonlinear elastic material. The mathematical expression of the J-integral is given as follows:

$$J = \int_{\Gamma} \left(W dy - T_i \frac{\partial u_i}{\partial x} ds \right) \tag{2.4}$$

where the strain energy density reads as $W = \int_0^{\varepsilon_{ij}} \sigma_{ij} \varepsilon_{ij}$, $T_i = \sigma_{ij} n_j$ is the traction vector, u_i are the displacement vector component, and ds is a length increment along the contour Γ, n is the unit vector normal to Γ, while σ_{ij} and ε_{ij} are stress and strain tensors, respectively (Fig. 2.4).

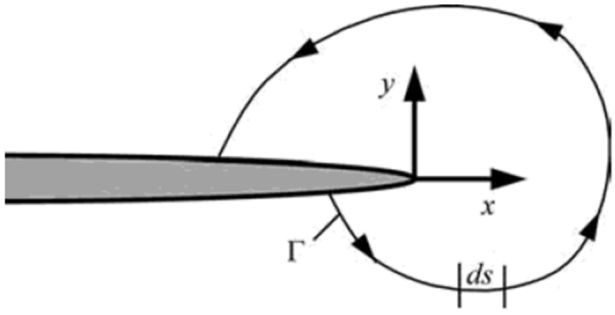

Fig. 2.4: Arbitrary J-integral contour around the tip of a crack [Anderson, 2005].

As what has been demonstrated by Rice [Rice, 1969], for a nonlinear material which contains a crack, J is a path independent integral and equal to the energy release rate G. The J-value was measured firstly experimentally by Landes and Begley [Begley et al., 1972; Landes et al., 1972]. According to their method, the same specimens with different initial crack lengths were tensile tested. The force vs. displacement curves are shown in Fig. 2.5(a). The area under a given curve is equal to U, which is the energy absorbed by the specimen. The U vs. crack length curves at different displacements are shown in Fig. 2.5(b) and the J-values vs. displacement at various crack lengths are presented in Fig. 2.5(c)

[Anderson, 2005]. The J-integral can be calculated as a function of the area under the force vs. displacement curve when an edge cracked specimen is adopted:

$$J = -\frac{1}{B}\left(\frac{\partial U}{\partial a}\right) \tag{2.5}$$

where B is the thickness of the specimen and U is the energy absorbed by the specimen.

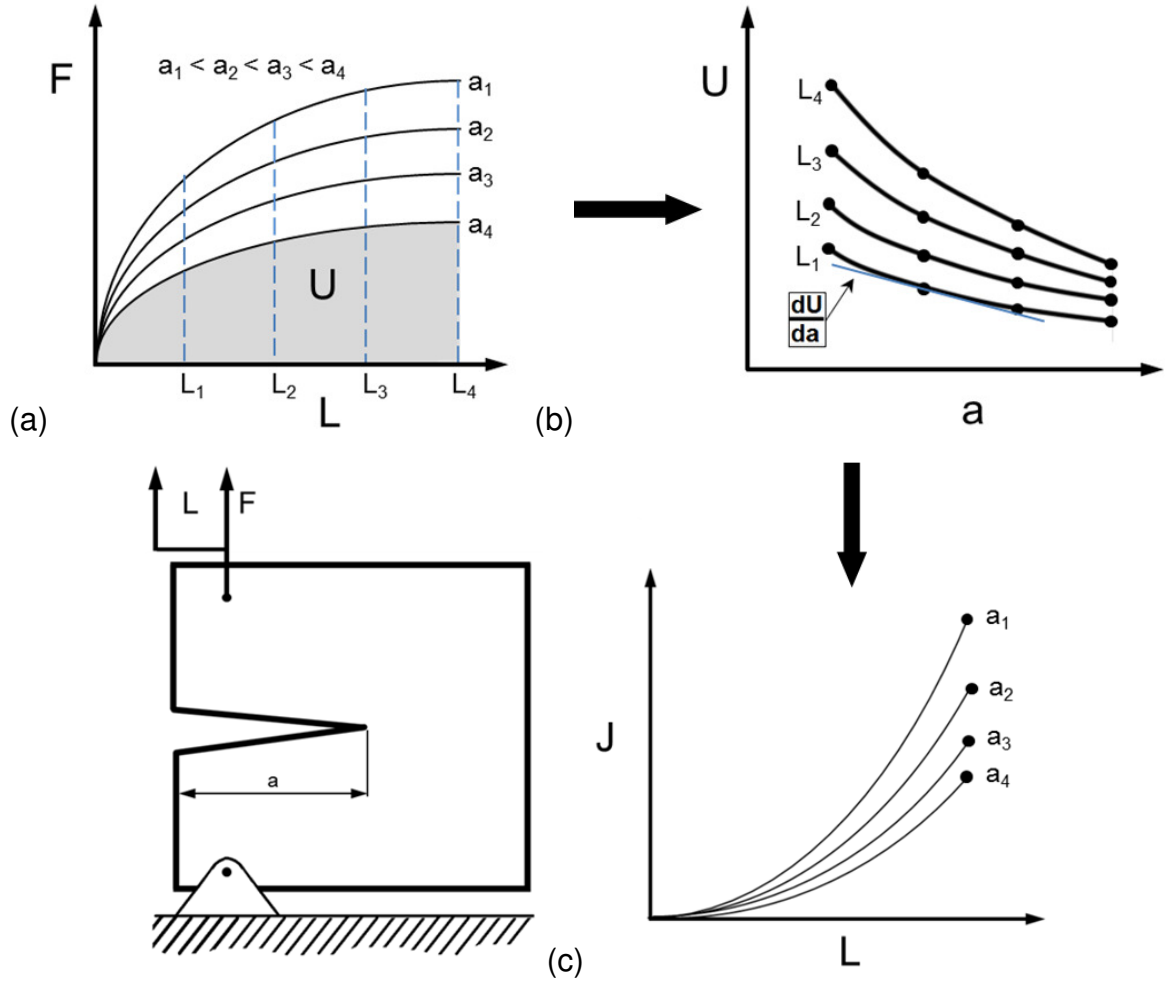

Fig. 2.5: Schematic of experimental measurements of J [Begley et al., 1972; Landers et al., 1972].

For linear elastic material behavior, the relation between the crack tip opening displacement (CTOD) δ and J is given as follows:

$$J = m\sigma_0\delta \tag{2.6}$$

where m is a material dependent constant which is influenced by the stress state and σ_0 is the yield stress.

2.3 Constitutive damage models

Ductile damage in crystalline solids originates from the nucleation, growth, and coalescence of microvoids [Tvergaard, 1989]. The voids nucleate mainly at second phase particles [Tvergaard, 1989]. In the early study of void growth in ductile materials, various models exist focusing on the description of void growth alone. The surrounding material is taken to be rigid perfectly plastic and a state of plane strain is assumed with a prescribed strain rate.

2.3.1 The Rice and Tracey model

Rice and Tracey [Rice et al., 1969] performed micromechanical studies which focused on the growth of a single void in an infinite elastic-plastic solid. The rate of variation of void radius can be expressed as follows:

$$\frac{\mathrm{dr}}{\mathrm{r}} = 0.283\exp\left(\frac{3\sigma_{\mathrm{m}}}{2\sigma_0}\right)\mathrm{d}\varepsilon_{\mathrm{eq}}^{\mathrm{pl}} \tag{2.7}$$

where r is the radius of the void, σ_{m} is the mean stress, σ_0 is the yield stress and $\varepsilon_{\mathrm{eq}}^{\mathrm{pl}}$ is the equivalent plastic strain of a perfectly plastic matrix material. This model does not consider the interaction between neighbouring cavities.

For a strain hardening material, the σ_0 value in equation (2.7) can be replaced by the von Mises equivalent stress σ_{eq}, and the revised equation (2.8) is as follows:

$$\frac{\mathrm{dr}}{\mathrm{r}} = 0.283\exp\left(\frac{3\sigma_{\mathrm{m}}}{2\sigma_{\mathrm{eq}}}\right)\mathrm{d}\varepsilon_{\mathrm{eq}}^{\mathrm{pl}} \tag{2.8}$$

Huang [Huang et al., 1991] assumes that the growth rate of a spherical void in an infinite perfectly plastic matrix is underestimated by equation (2.8) and they introduced a new equation to explain the variation of the void radius:

$$\frac{\mathrm{dr}}{\mathrm{r}} = \begin{cases} 0.427(\eta)^{\frac{1}{4}}\exp\left(\frac{3}{2}\eta\right)\mathrm{d}\varepsilon_{\mathrm{eq}}^{\mathrm{pl}}, & \frac{1}{3} \le \eta \le 1 \\ 0.427\exp\left(\frac{3}{2}\eta\right)\mathrm{d}\varepsilon_{\mathrm{eq}}^{\mathrm{pl}}, & \eta > 1 \end{cases} \tag{2.9}$$

where $\eta = \frac{\sigma_m}{\sigma_{eq}}$ represents the stress triaxiality. The equation does not consider the influence of void coalescence. Moreover, material softening due to damage has not been considered in the Rice and Tracey model.

2.3.2 The Rousselier model

Within a thermodynamic framework, Rousselier [Rousselier, 1987; Rousselier, 2001] developed a damage model. In the Rousselier model, damage is defined by a variation of the void volume fraction originating from second phase particles under tensile loading conditions. The general yield condition of the Rousselier model is as follows:

$$\Phi = \frac{\sigma_{eq}}{1-f} + Df\sigma_k \exp\left(\frac{\sigma_m}{\sigma_k(1-f)}\right) - R(p) = 0 \qquad (2.10)$$

where σ_{eq} is the von Mises equivalent stress, σ_m is the hydrostatic stress, f is the void volume fraction (initial value f_0), σ_k and D are material constants, p is the cumulated plastic strain and R(p) is true stress-true plastic strain curve of the material. The von Mises yield surface and the yield surface modified by the Rousselier equation (2.10) can be found in Fig. 2.6 [Seebich, 2007].

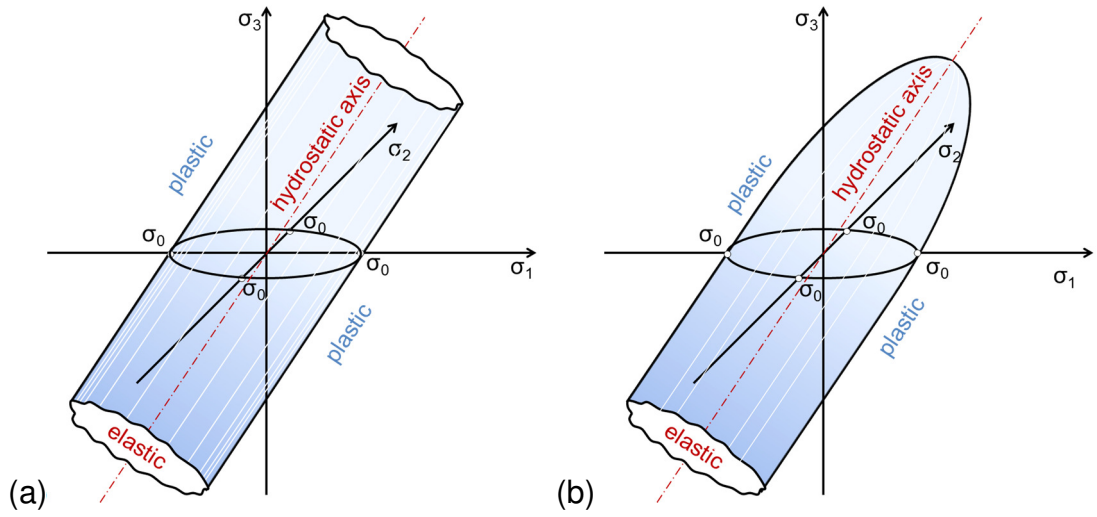

Fig. 2.6: (a) Von Mises yield surface and (b) Rousselier yield surface [Rousselier, 1987; Seebich, 2007].

From cavity growth measurements [Rousselier, 1987; Rousselier, 2001] and theoretical considerations, the parameter D is considered as a material independent parameter. For

most materials this value can be set to D = 2. The initial void volume fraction, f_0, depends on the volume fraction of all inclusions in the material (voids plus non-metallic particles). The f_0 is suggested to be determined from metallographic investigations on the polished material surface. For steel, if the metallographic experiment is not available, f_0 can be estimated from the chemical composition thanks to Franklin's equation [Franklin, 1969] in which the manganese (Mn), sulphide (S), and oxide (O) inclusions are considered as inclusions:

$$f_0 = 0.054\left[\%S(wt) - \frac{10^{-3}}{\%Mn(wt)}\right] + 0.055\%O(wt) \tag{2.11}$$

According to the discussion of Rousselier [Rousselier, 2001], the first try for σ_k is set equal to the value of two thirds of the equivalent stress (σ_{eq}) for the smooth round specimen under tensile test when the final fracture happens. Based on the previous experiences at MPA [Seidenfuss, 1992], σ_k is assumed to be 445 MPa for the current investigated steels (10MnMoNi55, S355NL, et al.). When the critical void volume fraction f_c is reached, the stress carrying ability of the material will be loosed completely. Damage mechanical studies of tensile tests have shown that f_c=0.05 is a reasonable value [Seidenfuss, 1992; Mohanta, 2003; Weber et al., 2007]. The Rousselier model was used successfully to study the ductile fracture behaviour of homogenous materials [Kussmaul et al., 1995; Uhlmann et al., 1999; Schmauder et al., 2002, 2009] and inhomogeneous electron beam welded steel joints [Tu et al., 2011, 2013] at IMWF/MPA Stuttgart.

The ductile crack propagation in precracked specimens (compact tension (C(T)) depends on the element size l_c, element type, symmetries, mesh geometry, etc. [Rousselier, 2001]. Before the numerical application, the l_c-value should be calibrated first. The parameter l_c is calibrated on notched round specimens, then the same l_c-value is adopted to study the crack propagation of C(T)-specimens. This is the so called mesh dependence of the Rousselier model, where the numerical simulation result is affected by the element size l_c. The classical Rousselier model is called the local Rousselier model where the material damage process at a certain point has a close relationship with the stress and strain field at the same point. Samal developed a nonlocal damage law trying to overcome the drawbacks of the local Roussellier model [Samal et al., 2008, 2009] where the damage growth law is defined in terms of the local void volume fraction but keeping a local definition for strain. This is the new trend for the Rousselier model as well as for the GTN model. However, a

large amount of debugging time is needed to develop the user defined code and to derive results calculated from the non-local Rousselier model which is limiting the application of the non-local damage model.

2.3.3 The Gurson-Tvergaard-Needleman (GTN) model

Like Bishop and Hill [Bishop and Hill, 1951], the widely well-known porous ductile material model is that developed by Gurson [Gurson，1977]. The material simulated by the Gurson model behaves as a continuum since the voids appear through their influence on the global flow behaviour. The yield condition of the Gurson model is written as:

$$\Phi = \left(\frac{\sigma_{eq}}{\sigma}\right)^2 + 2f\cosh\left(\frac{\sigma_m}{2\sigma}\right) - 1 - f^2 = 0 \tag{2.12}$$

where σ_{eq} is the von Mises equivalent stress, σ is the flow stress for the matrix material of the cell, f is the void volume fraction and σ_m is the mean stress. The implication of this analysis is that the voids are assumed to be randomly distributed, so that the macroscopic response is isotropic.

The original yield condition of the Gurson model was modified by Tvergaard [Tvergaard, 1982a] and Needleman [Tvergaard and Needleman, 1984] and the equation of the so called Gurson-Tvergaard-Needleman (GTN) model is as follows:

$$\Phi = \left(\frac{\sigma_{eq}}{\sigma}\right)^2 + 2q_1 f^* \cosh\left(\frac{q_2\sigma_m}{2\sigma}\right) - 1 - q_3 f^{*2} = 0 \tag{2.13}$$

where q_1, q_2 and q_3 are parameters introduced by Tvergaard which can improve the accuracy of the predictions of the Gurson model [Tvergaard, 1982b]. The function f^* is a function of f as shown in Fig. 2.7 which represents the accelerated damage originated from the void coalescence when a critical volume fraction f_c [Tvergaard et al., 1984] is reached:

$$f^* = \begin{cases} f & f < f_c \\ f_c + k(f - f_c) & f_c < f < f_f, \quad k = \frac{f_u^* - f_c}{f_f - f_c} \\ f_u^* & f \geq f_f \end{cases} \tag{2.14}$$

According to this model, a crack appears when the current f value reaches the final void volume fraction, f_f. That means the material loses its stress carrying ability completely when the ultimate void volume fraction f_u^* is reached, where $f_u^* = 1/q_1$. Zhang thought the value f_c can be determined from unit cell modeling results (Zhang et al., 2000).

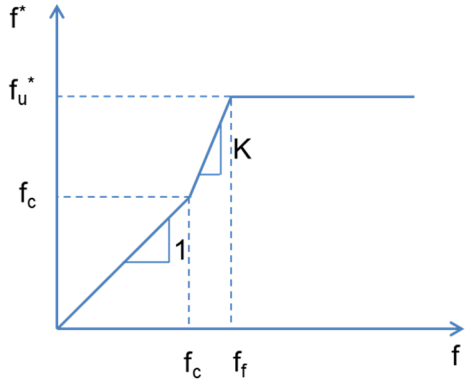

Fig. 2.7: The function of the modified void volume fraction $f^*(f)$.

It is assumed that the rate of the void volume fraction consists of the growth of existing voids and the nucleation of new voids, as explained by Needleman [Needleman et al., 1978] and Chu [Chu et al., 1980]:

$$\dot{f} = \dot{f}_{growth} + \dot{f}_{nucleation} \tag{2.15}$$

The void growth is given according to the following equation:

$$\dot{f}_{growth} = (1 - f)\dot{\varepsilon}_{kk}^{pl} \tag{2.16}$$

where $\dot{\varepsilon}_{kk}^{pl}$ is the plastic volume dilatation rate and the matrix is assumed behaving plastically incompressible.
The nucleation of new voids is given as follows:

$$\dot{f}_{nucleation} = A\dot{\varepsilon}_{kk}^{pl} + B(\dot{\sigma}_m + \frac{1}{3}\dot{\sigma}_{kk}) \tag{2.17}$$

The influence of the void nucleation is either strain controlled (B=0) or stress controlled (A=0). The void nucleation rate for the strain controlled nucleation situation, as suggested by Chu [Chu et al., 1980] is as follows:

$$\dot{f}_{\text{nucleation}} = A\dot{\varepsilon}_{kk}^{pl}, \quad A = \frac{f_n}{s_n\sqrt{2\pi}} \exp\left[-\frac{1}{2}\left(\frac{\varepsilon_{eq}^{pl}-\varepsilon_n}{s_n}\right)^2\right] \tag{2.18}$$

where f_n is the void volume fraction of the void-nucleating particles, ε_n is the mean strain when void nucleation occurs and s_n is the corresponding standard deviation of the nucleation strain, which follows a Gaussian distribution.

For stress controlled void nucleation, the void nucleation rate is shown in the equation as follows:

$$\dot{f}_{\text{nucleation}} = B(\dot{\sigma}_m + \frac{1}{3}\dot{\sigma}_{kk}), \quad B = \frac{f_n}{s_n\sqrt{2\pi}} \exp\left[-\frac{1}{2}\left(\frac{\sigma_m+\frac{1}{3}\sigma_{kk}-\sigma_n}{s_n}\right)^2\right] \tag{2.19}$$

where $\sigma_m + \frac{1}{3}\sigma_{kk}$ is an approximate value of the maximum normal stress acting on the particle/matrix interface [Needleman, 1987; Xia, 1996], σ_m is the mean stress for nucleation.

With the development of computer power, the GTN model is used to investigate the fracture behavior of homogeneous materials, e.g., steel StE690 [Springmann et al., 2005a, 2005b], X100 pipeline steel [Tanguy et al., 2008], X70 ferritic–pearlitic steel [Rivalin et al., 2001a, 2001b] and Al2024 sheets [Chabanet et al., 2003]. The GTN model was also used to study the fracture bahaviour of inhomogeneous structures [Østby et al., 2007a, 2007b]. In recent years, the GTN model has found wide application in the fracture analysis of welded joints. The GTN model was used by Needleman [Needleman et al., 1999] and Tvergaard [Tvergaard et al., 2000, 2004] in studies of conventional fusion welded joints. After the initial study of the fracture behaviour of a laser welded joint [Çam et al., 1999; Santos et al., 2000], the GTN model was adopted to study the ductile fracture behaviour of a laser welded joint at the Helmholtz-Zentrum Geesthacht Centre for Materials and Coastal Research [Nègre et al., 2003, 2004; Cambrésy, 2006]. The GTN model was used to predict crack propagation when different initial crack positions were considered. It has been proved that the GTN model can be successfully used to study the fracture mechanisms of an inhomogeneous laser welded joint [Nonn et al., 2008]. Meanwhile, the GTN model was used to study the ductile fracture behaviour of friction stir welded AA2024 joints by Nielsen [Nielsen et al., 2008]. Nielsen focuses on studying the ductile damage development in an FS-welded aluminium joint under tensile loading normal to the weld line. A study of the effect of varying

the distribution of the volume fraction of second phase particles, from which voids are assumed to nucleate, was carried out as well.

2.4 Cohesive zone model (CZM)

The concept of a cohesive zone model was introduced by Dugdale [Dugdale, 1960] and Barenblatt [Barenblatt, 1962]. Dugdale and Barenblatt assume that the crack consists of two parts: the stress-free part and the parts loaded by cohesive stresses. In 1960, Dugdale introduced a strip-yield model where he assumed that the cohesive stress is equal to the yield stress and the material is supposed to perform as elastic-ideally plastic [Schwalbe et al., 2009], as shown in Fig. 2.8. The model presented by Barenblatt adopted a cohesive law to describe the decohesion of atomic lattices [Schwalbe et al., 2009] where the stresses in the ligament of the crack follows a prescribed distribution σ(x) which is related to the material, as shown in Fig. 2.9. The special zone where damage occurs is called the cohesive zone. As shown in Fig. 2.10, under loading conditions, the void initiation, growth and coalescence process of a ductile material is described by the damage of the cohesive element. The damage of the cohesive element is described by a traction-separation law (TSL) which consists of three cohesive parameters: the cohesive strength T_0, the critical separation length δ_0 and the cohesive energy Γ_0. The cohesive strength T_0 is the maximum stress obtained when the crack initiates and the cohesive energy Γ_0 is the energy for the total separation of a unit area of the material. When the cohesive strength T_0 and the cohesive energy are known, the third parameter δ_0 can be calculated with the following equation:

$$\Gamma_0 = \int_{\delta}^{\delta_0} T(\delta)\, d\delta \tag{2.20}$$

Therefore, there are only two independent cohesive parameters: the cohesive strength T_0 and the cohesive energy Γ_0. For mode I loading, when the normal component of the separation reaches δ_0, the cohesive element fails completely where the stresses become zero. The cohesive energy can be calculated by equation 2.20 and is assumed equal to the J-integral value at initiation of ductile crack extension (J_i) as discussed by Brocks [Brocks et al., 2004].

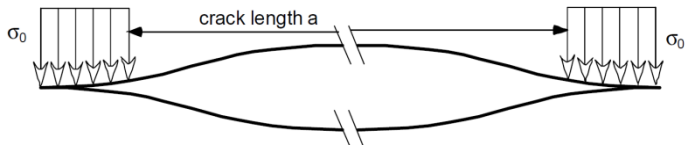

Fig. 2.8: The Dugdale model [Dugdale, 1960].

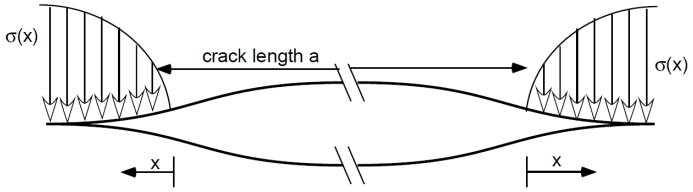

Fig. 2.9: The Barenblatt model [Barenblatt,1962].

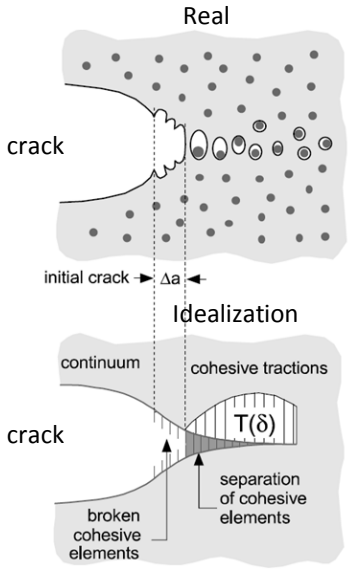

Fig. 2.10: Depiction of the ductile failure process by a cohesive zone model [Cornec et al., 2003].

Following this idea of the cohesive zone model, different TSLs were proposed in the past to investigate the ductile and the brittle fracture behaviour of a number of materials. The first application of the cohesive model in the FE simulation was performed by Hillerborg [Hillerborg, 1976] to describe the brittle fracture behavior of a concrete beam. The linear decreasing TSL introduced by Hillerborg is shown in Fig. 2.11(a). The equation of the linear decreasing TSL is as follows:

$$\mathrm{T}(\delta) = \mathrm{T}_0 \left(1 - \frac{\delta}{\delta_0}\right) \tag{2.21}$$

This kind of TSL is normally adopted to study the behavior of brittle material.

Needleman introduced two TSLs to describe the decohesion behavior of a ductile material. The polynomial and the exponential TSLs are shown in Fig. 2.11(b-c). A polynomial shaped TSL [Needleman, 1987] can be found in Fig. 2.11(b), where the equation of T(δ) is given as:

$$\mathrm{T}(\delta) = \frac{27}{4}\mathrm{T}_0 \frac{\delta}{\delta_0}\left(1 - \frac{\delta}{\delta_0}\right)^2 \tag{2.22}$$

The function T(δ) with an exponentially shaped TSL [Needleman, 1990] can be depicted as follows:

$$\mathrm{T}(\delta) = \mathrm{T}_0 \mathrm{ez} \frac{\delta}{\delta_0} \exp\left(-\mathrm{z}\frac{\delta}{\delta_0}\right) \tag{2.23}$$

where $\mathrm{e} = \exp(1)$ and $\mathrm{z} = 16\mathrm{e}/9$.

For materials which show a more ductile behavior, Tvergaard and Hutchinson [Tvergaard, 1992] proposed a trapezoidal shaped TSL to describe the fracture behavior which is shown in Fig. 2.11(d). They introduced two additional parameters, δ_1 and δ_2 in the equation, the initial cohesive stiffness $K_{nn}=T_0/\delta_1$ is constant before T(δ) reaches T_0 and the formulation of T(δ) is explained in the equation as follows:

$$\mathrm{T}(\delta) = \mathrm{T}_0 \begin{cases} \left(\frac{\delta}{\delta_1}\right) & \delta < \delta_1 \\ 1 & \delta_1 < \delta < \delta_2 \\ \left(\frac{\delta_0 - \delta}{\delta_0 - \delta_2}\right) & \delta_2 < \delta < \delta_0 \end{cases} \tag{2.24}$$

This TSL was later modified by Scheider [Scheider, 2001] where the initial cohesive stiffness varies. This TSL proposed by Scheider was used to study the fracture behavior of laser weldments of which the TSL function is as follows:

$$\mathrm{T}(\delta) = \mathrm{T}_0 \begin{cases} 2\left(\frac{\delta}{\delta_1}\right) - \left(\frac{\delta}{\delta_1}\right)^3 & \delta < \delta_1 \\ 1 & \delta_1 < \delta < \delta_2 \\ 2\left(\frac{\delta - \delta_2}{\delta_0 - \delta_2}\right)^3 - 3\left(\frac{\delta - \delta_2}{\delta_0 - \delta_2}\right)^2 + 1 & \delta_2 < \delta < \delta_0 \end{cases} \tag{2.25}$$

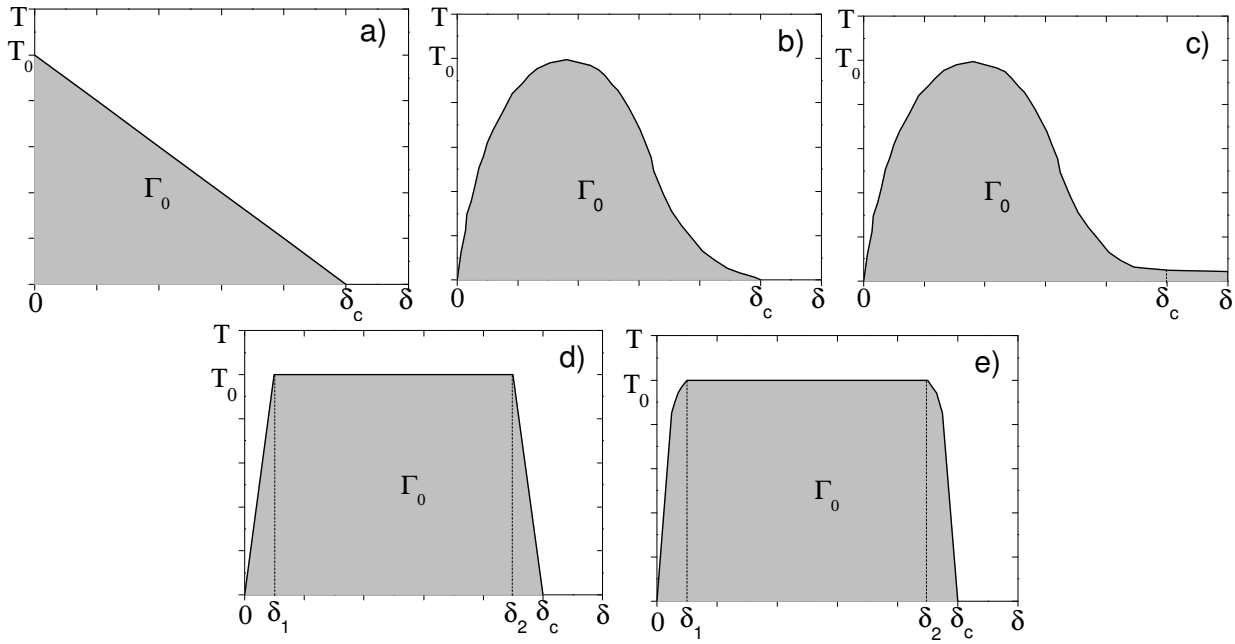

Fig. 2.11: Shape of traction separation laws according to: (a) Hillerborg [Hillerborg, 1976], (b) Needleman [Needleman, 1987], (c) Needleman [Needleman, 1990], (d) Tvergaard and Hutchinson [Tvergaard et al., 1992], and (e) Scheider [Scheider, 2001].

The shape influence of the TSL on the damage behavior of a material has not been reported uniformly so far. Some authors concluded the shape of the TSL has only tiny influence [Yuan et al., 1991; Tvergaard et al., 1992] on the fracture behavior of the material. However, in recent publications [Scheider et al., 2003b], the shape of the TSL has been found having a severe influence on the damage behaviour.

After the successful application of the cohesive zone model in different homogeneous structures [Siegmund et al., 2000; Chen et al., 2003, Lin, 1998a; Li, 2002], the cohesive zone model has been applied to investigate the fracture behavior of complex structures, e.g., welded joints [Anvari et al., 2006; Lin et al., 1998b, 1999; Scheider, 2001, Tu et al., 2013]. This proves that the cohesive model is able to describe the damage behaviour of homogeneous structures and inhomogeneous welded joints.

2.5 ARAMIS system

ARAMIS is an optical 3D deformation analysis system which is based on an image evaluation technique to capture the surface deformation of a sample under load. The ARAMIS system can be used to analyze, calculate and document the surface

displacements and surface strains at each deformation step [ARAMIS, 2008]. Some applications of the ARAMIS system monitoring the deformation of tested samples are shown as follows. For example, the ARAMIS system was used to record the true stress-strain behavior of flat specimens of PA6/elastomer composites [Huang et al., 2011]. During the tensile test process, the effective length and diameter change (Δl and Δd) is recorded by the ARAMIS system; see Fig. 2.12(a). The sample is viewed by two CCD cameras which record the surface deformation (see Fig. 2.12(b)). The ARAMIS system recorded the deformation process of flat specimens and middle cracked tension (M(T)) specimens extracted from Al6013-T6 laser beam welded and friction stir welded joints at the Helmholtz-Zentrum Geesthacht Centre for Materials and Coastal Research [Seib, 2006]. The strain distribution of steel adhesive joints is shown, e.g., by Sadowski [Sadowski et al., 2011]. As shown on the website of GOM company [GOM, 2014], the ARAMIS system is also able to monitor the crack propagation of Single Edge Notched Bend (SENB) specimens. The crack propagation during three point bending tests on the clay brick panel was shown by Graziani [Graziani et al., 2014]. These works have confirmed that the ARAMIS facility is qualified for 3D deformation measurements and the applications in the fracture mechanics field.

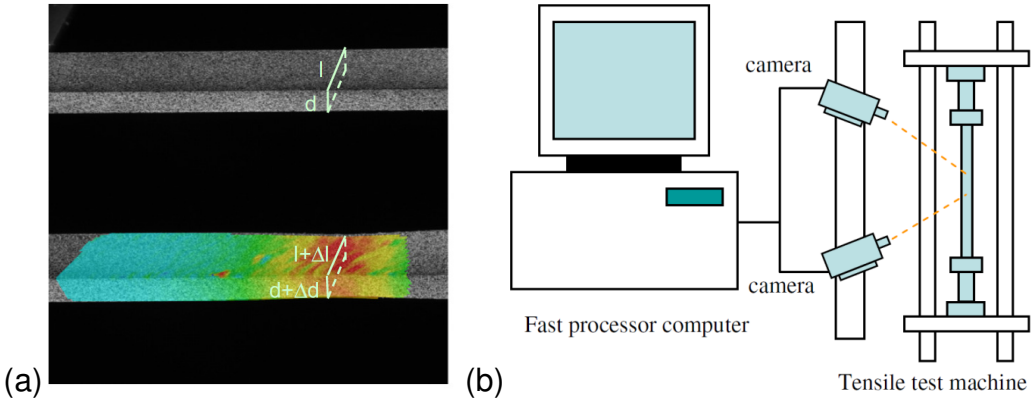

Fig. 2.12: (a) Measurement of the effective length (Δl) and diameter changes (Δd); (b) sketch of the tensile test combined with the ARAMIS system [Huang et al., 2011].

2.6 Synchrotron Radiation-Computed Laminography (SRCL)

With the development of phase contrast methods [Nugent et al., 1996; Cloeten et al., 1999, 2002; Paganin et al., 2002], 3D imaging with Synchrotron radiation-computed tomography (SRCT) became possible. The SRCT technique can help to understand the structure within

the material in a non-destructive way. However, SRCT is particularly suitable for the investigation of the damage evolution of bulk materials with the thickness of 1 mm, it is difficult to image the local microstructure when the sample size significantly exceeds the field of view (1.5 mm) of the detector, such as in the case of a flat specimen [Shen et al., 2013]. Synchrotron radiation-computed laminography (SRCL) has been developed as a non-destructive three dimensional (3D) imaging method for flat specimens [Helfen et al., 2005]. In comparison to the SRCT, SRCL provides better scanning results [Helfen et al. 2011] resulting from the change of the laminographic angle ($\theta = 90^0$ for SRCT, $\theta<90^0$ for SRCL), which is the angle between the rotation axis and the incident of the X-ray beam. Fig. 2.13 shows the comparison of the schematic views of a typical SRCT setup (Fig. 2.13(a)) and SRCL setup (Fig. 2.13(b)). The SRCT is particularly used to scan and image the stick-like samples (Fig. 2.13(a)) where the SRCL is developed to image the laterally extended specimen, like the flat specimen, as shown in Fig. 2.13(b).

With the development of the SRCL technique at ANKA (Synchrotron Radiation Facility at the Karlsruhe Institute of Technology (KIT)), an increasing number of scientific publications are found in literature. The SRCL technique was adopted to investigate the crack initiation of Al2139 [Morgeneyer et al., 2009, 2013], the crack initiation and propagation in Al6061 aluminum alloy sheets [Shen et al., 2013] and the damage evolution in a polymer composite [Xu et al., 2010; Laiarinandrasana et al., 2012; Cheng et al., 2013b]. These scientific investigations confirm that the SRCL technique is qualified for 3D imaging of the damage evolution of different materials.

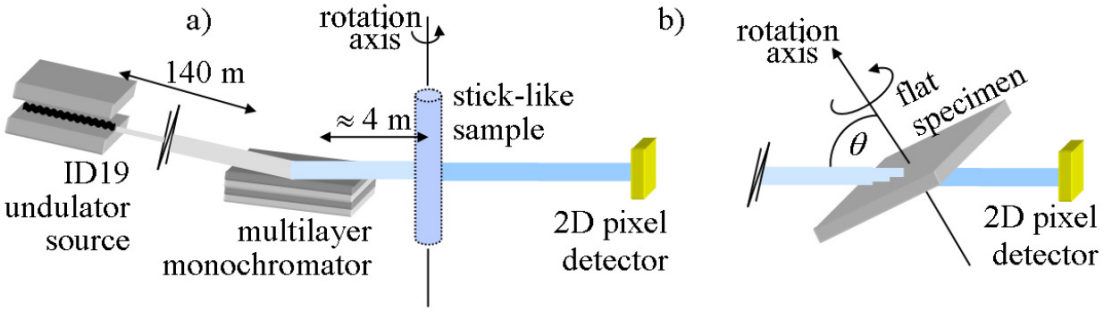

Fig. 2.13: Schematic views of a typical (a) SRCT setup in comparison to the (b) SRCL setup [Morgeneyer et al., 2013].

3. Characterization of steel S355 electron beam welded (EBW) joints

A low-alloyed structural steel S355 is chosen as the base material (BM) to produce electron beam welded butt joints. During the electron beam welding process, the welding parameters were adjusted in order to get sound welded joints without surface pores or microcrack defects. The welding parameters chosen are: welding speed 2 mm/s and beam current 230 mA. After the electron beam welding process, a butt joint is obtained from two S355 plates with the thickness of 60 mm. In order to investigate the mechanical properties, the fracture mechanism and crack propagation for S355 electron beam welded butt joints, and some related experimental works are presented below.

First, a spectrometric analysis was carried out on the base material in order to obtain the chemical composition. After the laser welding process, one block including the weld seam was extracted from the welded joint. In order to define the initial void volume fractions (f_0) and the mean void distances (l_c) for the BM, FZ and HAZ, optical microscopy investigations were made on these regions. After surface etching, microstructures of different weld joints were obtained. The welded joints were hardness tested in order to define the dimensions of different weld regions. Due to the narrowness of the fusion zone and the heat affected zone, it is impossible to extract round specimens from these regions. As a consequence, flat specimens extracted from different weld regions were tested to achieve the local mechanical properties, such as stress-strain curves. Unnotched round tensile specimens and flat specimens obtained from the BM were compared in order to check whether flat specimens can provide the same stress-strain curves as round tensile specimens. Notched round specimens from the base material and notched round specimens with the HAZ located in the middle of the specimens were tested experimentally in order to provide standards for the calibration of parameters of the Rousselier model, the GTN model and the cohesive zone model later. Further details of the methodology are summarized as follows.

3.1 Chemical composition

The chemical composition of S355 was measured by spectrometric analysis at five random points on the BM. The chemical components of S355 are shown in table 3.1. According to the suggestion of Rousselier [Rousselier 2001], for steel, the initial void volume fraction f_0 can be estimated from the chemical component thanks to Franklin's formula if manganese, sulphide and oxide are the reasons of non-metallic inclusions:

$$f_0 = 0.054\left[\%S(wt) - \frac{10^{-3}}{\%Mn(wt)}\right] + 0.055\%O(wt) \quad (3.1)$$

The f_0-value for the steel S355 obtained according to Franklin's formula is 0.7×10^{-3}.

Table 3.1: Chemical composition of the steel S355, mass contents (wt) in %

Steel	C	Si	Mn	P	S	Cr	Mo	Ni	Al	Co	O
S355	0.198	0.260	1.386	0.026	0.013	0.020	<0.005	<0.005	0.013	0.006	0

3.2 Microstructures of steel S355 EBW joints

The microstructures of steel S355 EBW joints were investigated by optical microscopy and scanning electron microscopy separately. In order to identify the volume fraction of non-metallic inclusions and the average distance between two neighbouring inclusions, optical microscopy investigations on polished surfaces of the specimens were performed, for the BM, the FZ and the HAZ. Typical microscopy pictures of different weld regions can be found in Fig. 3.1(a)-(c). It can be seen that the inclusions are not equally distributed in the material but localized or clustered in some regions. The volume fraction of non-metallic inclusions was measured with the software Image J by applying the binary method. The optical separation of the particles and matrix was obtained by processing the normal optical microscope picture to the binary picture where the black regions are particles and the matrix are white regions. By calculating the ratio of the black regions to the whole measurement region, the initial volume fraction of the particles (f_0) is obtained. Quantitative analyses of microscope pictures from different weld regions were made in order to quantify these experimental values. From these analyses, the volume fraction of all inclusions for the BM, the FZ and the HAZ are 0.0009, 0.0018 and 0.0016, respectively. The f_0-values

measured from microscope pictures is slightly higher than the value calculated from Franklin's equation because the particles are not randomly distributed but localized at some regions. During the measurement of optical micrographs, only the regions with visible particles are considered, this overestimates the f_0-value slightly. Five particles are randomly chosen and the distances between these particles are measured. The mean distance between neighboring inclusions for the BM, the FZ and the HAZ is found to be 100 µm, 80 µm and 120 µm, respectively.

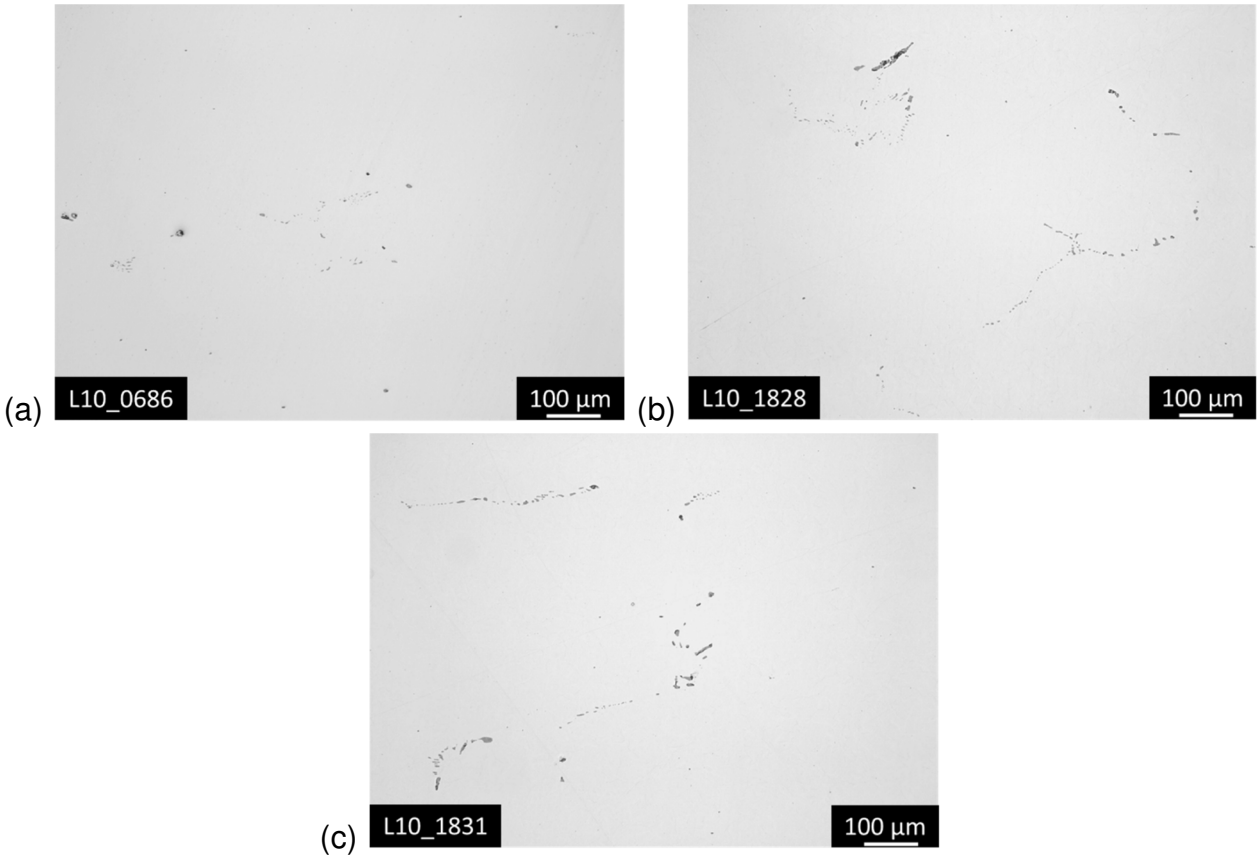

Fig. 3.1: Typical microscope pictures of different weld regions of an S355 EBW joint: (a) base material (BM), (b) fusion zone (FZ) and (c) heat affected zone (HAZ).

In order to get the microstructures of different weld regions, one block of material was cut across the welded joint. After surface etching with 3% HNO_3, the microstructures of different weld regions are obtained and presented in Fig. 3.2. The microstructure of the BM of the top face and the right surface of the block are shown in Fig. 3.2(a)-(b). As shown in Fig. 3.2(c), the BM shows the typical microstructure of steel, which is comprised of Ferrite and Perlite. The typical Ferrite and Pearlite is marked in Fig. 3.2(c), in which the white region is Ferrite and the black region is Pearlite. The microstructure of the HAZ consisting of Ferrite,

Pearlite and Martensite as shown in Fig. 3.2(d), which is a transitional region between the BM and the FZ. In Fig. 3.2(e), acicular Martensite structures can be found in the FZ.

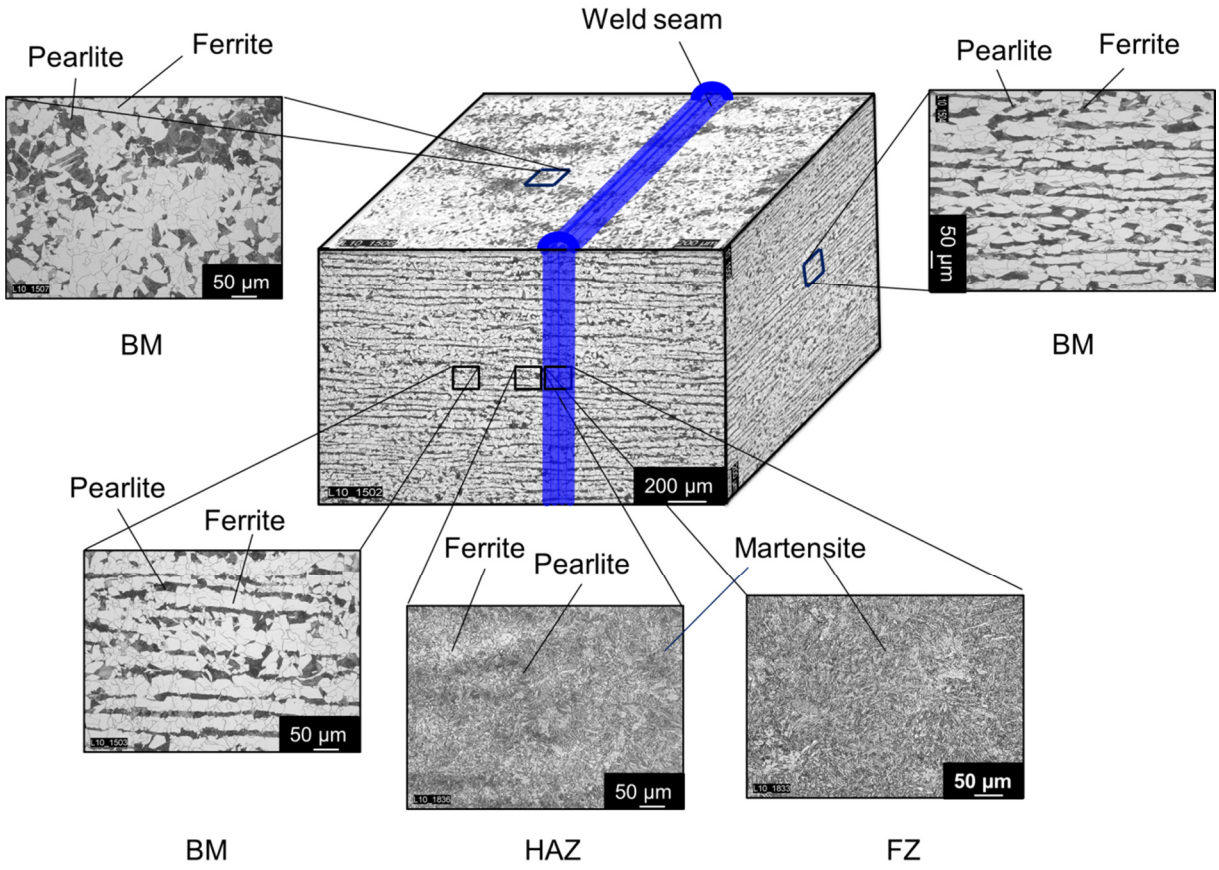

Fig. 3.2: Microstructures of different weld regions of an S355 EBW joint: (a) base material (BM) from marked region on the top face, (b) base material (BM) from marked region on the side face (c) base material (BM) from marked region on the front face (d) heat affected zone (HAZ) and (e) fusion zone (FZ).

3.3 Mechanical properties of S355 EBW

3.3.1 Hardness measurement

For the purpose of identifying different weld regions, especially the FZ and the HAZ, the hardness was measured across the welded joint. The hardness measurements were performed across the weld regions at three different test locations, namely at the weld root, the middle-section and the top part of the joints, as shown in Fig. 3.3. For the hardness measurement, Vickers hardness tests were adopted. During the hardness measurement, 5 kp (ca. 50 N) test load was performed with an indenter. Every 1 mm a measurement was

performed in order to define the Vickers hardness values of different weld regions. The hardness profile across the welded joint is shown in Fig. 3.4. From Fig. 3.4, the fusion zone possesses the highest hardness value (HV=258-283), whereas the base material attains the lowest hardness value around HV170 (HV=162-176). The hardness values of the HAZ increase near the FZ. This can be explained from microstructures of respective weld regions, which are shown in Fig. 3.2. The FZ is comprised of pin-structural martensite which is harder than perlite and ferrite which are the main components for the BM. From the macrograph picture as shown in Fig. 3.3 and the hardness test profile cross the welded joint (Fig. 3.4), the dimensions of FZ and HAZ are found to be 2.8 mm and 3.1 mm, respectively.

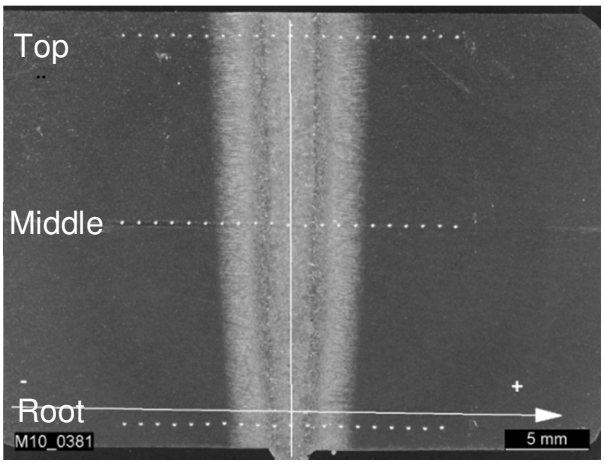

Fig. 3.3: Hardness test positions across the weld joint.

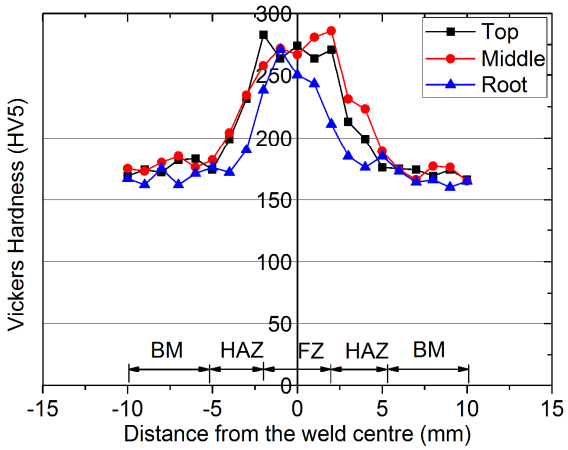

Fig. 3.4: Hardness profile across the electron beam welded joint.

3.3.2 Tensile behaviour of different tensile specimens

1. Smooth round specimens

Standard smooth round specimens were extracted from the BM with a computer controlled turning machine (TRAUB TNB160). Tensile tests were performed at room temperature with

the MTS Sintech 65/G universal testing machine. Four round specimens named RB1-RB4 with the diameter of 10 mm and a gauge length of 50 mm were extracted from the BM in which the loading direction is the same as the rolling direction, as shown in Fig. 3.5. The engineering stress vs. strain curves of round specimens (RB1-RB4) are shown in Fig. 3.6. Yield plateaus are found at the stress vs. strain curves. After averaging the tensile test results, the mechanical properties can be obtained. Table 3.2 shows the mechanical properties of the base material containing Young's modulus E, yield stress σ_0, tensile strength σ_m, uniform strain A_g and strain at rupture A.

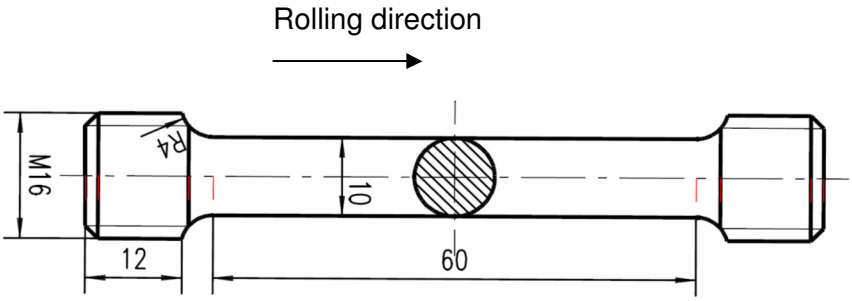

Fig. 3.5: Sketch of standard tensile round bar in which the loading direction is the same as the rolling direction.

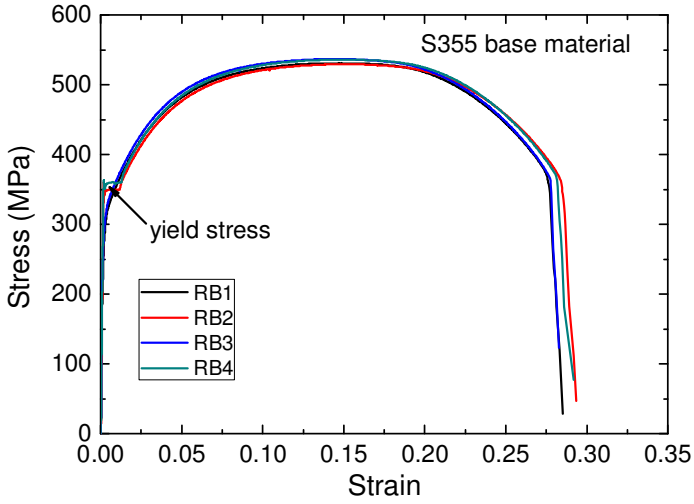

Fig. 3.6: Engineering stress-strain curves of round specimens extracted from the base material (BM) (RB1-RB4).

Table 3.2: Mechanical properties of the S355 BM

E-Modulus (MPa)	σ_0^{BM} (MPa)	σ_m^{BM} (MPa)	A_g^{BM}	A^{BM}
207750	353	533	0.151	0.246

Three round specimens named A1-A3 with the diameter of 8 mm and a gauge length of 30 mm were extracted from the BM in which the loading direction is perpendicular to the rolling direction, as shown in Fig. 3.7. The engineering stress vs. strain curves of round specimens (A1-A3) are shown in Fig. 3.8. After averaging the tensile test results, the mechanical properties are derived in table. 3.3. Table 3.3 shows the mechanical properties of the base material containing E-modulus, yield stress σ_0, tensile strength σ_m, uniform strain A_g and strain at rupture A. A comparison of the engineering stress versus strain curves obtained from these two types of round specimens extracted from the different positions of the base material (BM) can be found in Fig. 3.9. The curves confirm that for S355 BM the rolling direction has almost no influence on the mechanical properties of the base material.

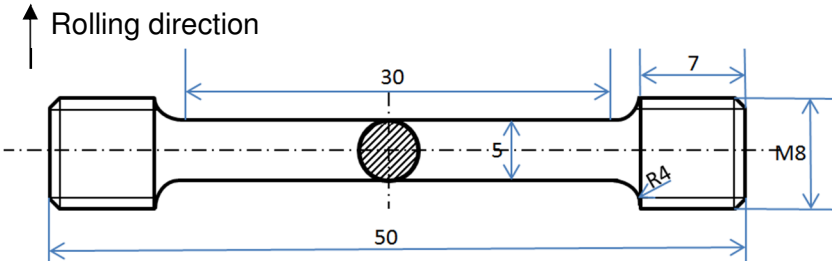

Fig. 3.7: Sketch of standard tensile round bar in which the loading direction is perpendicular to the rolling direction.

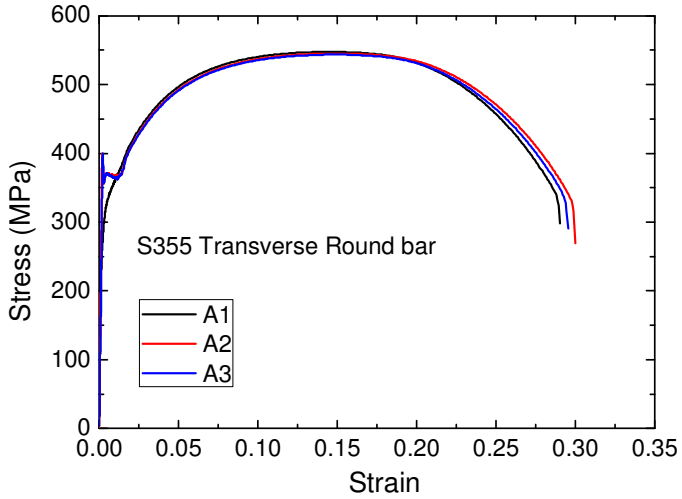

Fig. 3.8: Engineering stress-strain curves of round specimens extracted from base material (A1-A3).

Table 3.3: Mechanical properties of different weld regions of S355 EBW joint

E-Modulus (MPa)	σ_0^{BM} (MPa)	σ_m^{BM} (MPa)	A_g^{BM}	A^{BM}
202000	348	545	0.147	0.292

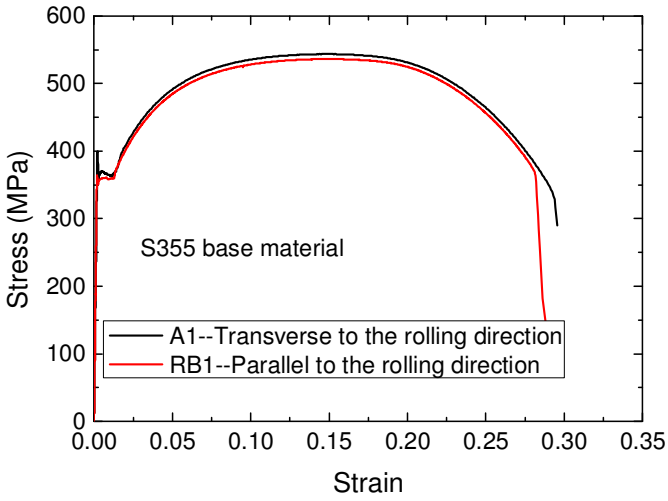

Fig. 3.9: Comparison of engineering stress-strain curves obtained from two different types of round specimens extracted from the S355 BM.

2. Flat specimens

As explained in the previous section, after the electron beam welding process, narrow FZ (FZ=2.8 mm) and HAZ (HAZ=3.1 mm) regions were obtained. Thus, it is impossible to extract smooth round specimens from the respective areas. Flat specimens were manufactured and tested from these areas in order to get the mechanical properties of different weld areas. Local mechanical properties of different weld areas of S355 EBW joints are obtained from flat specimens where the length direction is the same as the welding direction, as shown in Fig. 3.10. In this work, flat specimens were manufactured by an electrical discharge machining (EDM) technique to avoid residual stresses results from the saw cutting for the tensile specimens. The first thin manufactured sheet (0.5 mm thickness) was extracted from a position which has 0.5 mm distance from the center of the FZ, as shown in Fig. 3.11. The second manufactured sheet was extracted from the position 2.5 as shown in Fig. 3.11. The third manufactured sheet was extracted from a position at a 1 mm distance from the second block (position 3.5 in Fig. 3.11). Every new manufactured sheet was obtained from the new position at a 1 mm distance from the old manufacture position, as shown in Fig. 3.11. Manufactured sheets were extracted from different positions in order to get stress-strain curves of different weld regions. Two 0.5 mm thick flat specimens were cut off from a manufacture sheet, as shown in Fig. 3.11. The specimens were surface grinded before tensile testing in order to avoid stress concentrations around the imperfections which are introduced by production. Microcracks on the surface of the flat specimen as shown in Fig. 3.12 should be avoided after polishing which affect the accuracy of tensile test results.

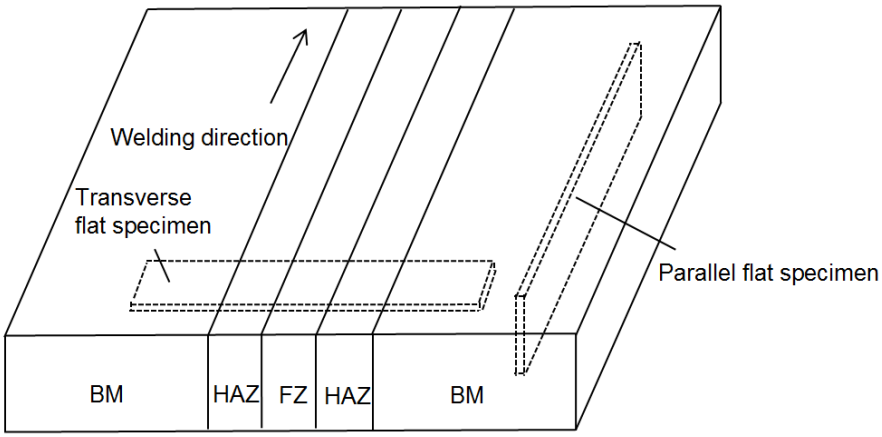

Fig. 3.10: Sketch of laser weld joint and extraction of flat specimens at different regions.

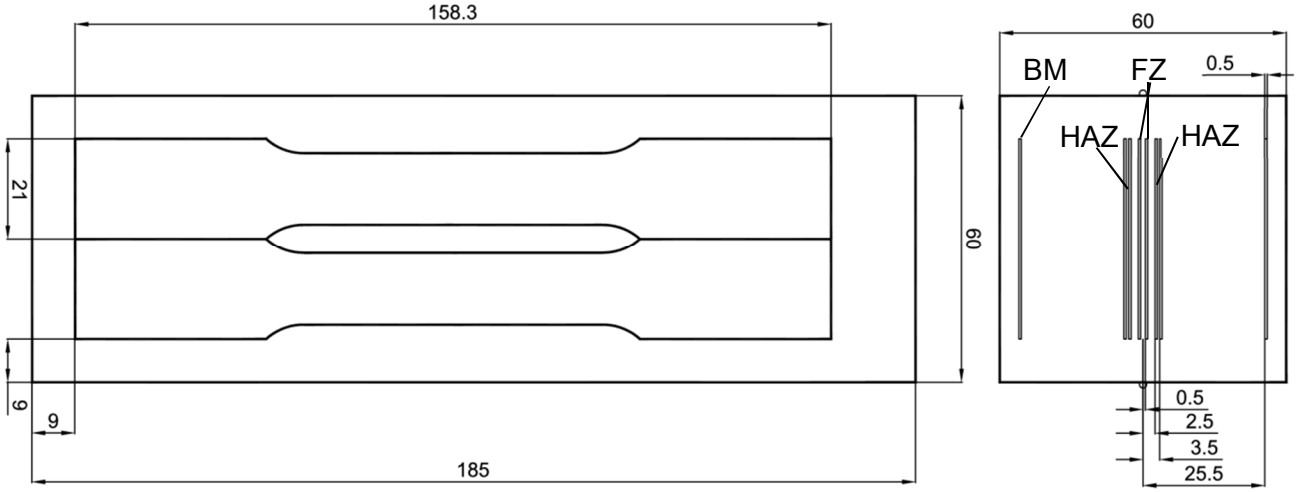

Fig. 3.11: Sketch of extraction positions of manufacture blocks and the dimension of the flat specimens.

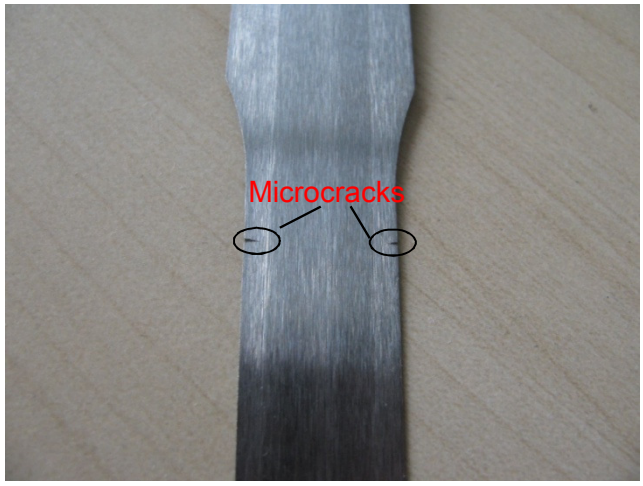

Fig. 3.12: Microcracks appear on the surface of flat specimen after polishing.

Flat specimens obtained from the BM, from the FZ and from the HAZ were tensile tested at room temperature. After the tensile process, engineering stress-strain curves of different weld regions of S355 EBW joints are obtained from flat specimens with a gauge length of 50 mm, as shown in Fig. 3.13. Table 3.4 shows the mechanical properties of the welded joints. The stress-strain curve of the BM derived from unnotched round bars were compared with that of flat specimens in order to verify whether flat specimens produce the same stress-strain curves as smooth round bars. Good comparison is obtained between the stress-strain curves obtained from flat and round specimen, showing that the flat specimens can provide a similar stress-strain curve as smooth round specimens, as shown in Fig. 3.14. These stress-strain curves will be used as model input data.

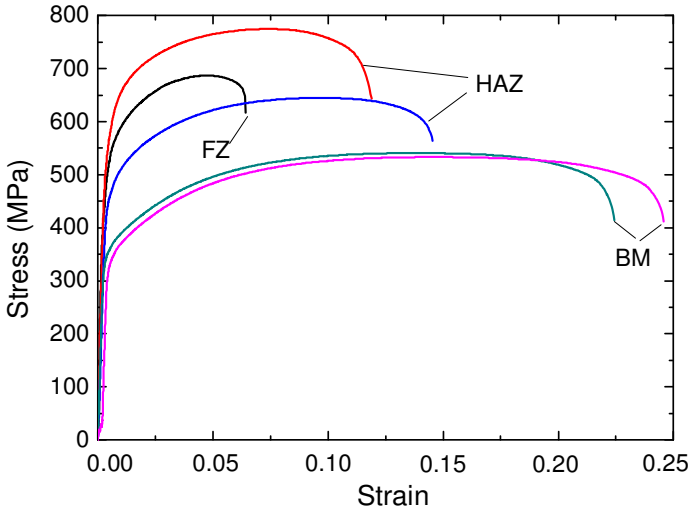

Fig. 3.13: Engineering stress-strain curves obtained from tensile test results of flat specimens extracted from different weld regions of S355 electron beam welded joints.

Table 3.4: Mechanical properties of different weld regions of S355 EBW joint

σ_0^{BM} (MPa)	σ_0^{FZ} (MPa)	σ_m^{BM} (MPa)	σ_m^{FZ} (MPa)	A_g^{BM}	A_g^{FZ}	A^{BM}	A^{FZ}
348	513	533	687	0.151	0.037	0.246	0.052

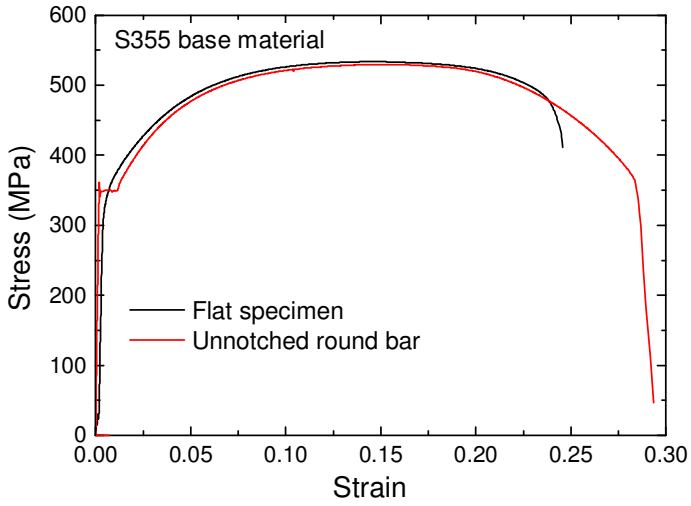

Fig. 3.14: Comparison between the stress-strain curves obtained from flat and round specimens extracted from S355 base material.

3. Notched cylindrical tensile specimens

Notched cylindrical specimens were extracted from the BM and from the HAZ, of which the length direction is perpendicular to the weld line. For the HAZ, notched specimens in which the HAZ is located in the middle of the notched area were manufactured. The sketch of a notched specimen with 4 mm notch radius is shown in Fig. 3.15. Tensile tests were performed at room temperature, in which the gauge length is 20 mm. During the tensile test process, force vs. cross section reduction curves and force vs. elongation curves were recorded. For the notched round specimens (NB1-NB3) extracted from the BM, the experimental force vs. elongation curves match well each other as shown in Fig. 3.16, although there exists some scatter between the force vs. cross section reduction curves as shown in Fig. 3.17. For the notched round specimens (TN1-TN4) where the HAZ is located in the center of the notched area, force vs. cross section reduction curves were obtained and are shown in Fig. 3.18. Some scatter of the fracture moment of the notched round specimens obtained from the HAZ is found which is due to the influence of the HAZ. The experimental findings will be used for the calibration of the Rousselier and the GTN model and also the cohesive parameters for the BM and HAZ as shown later.

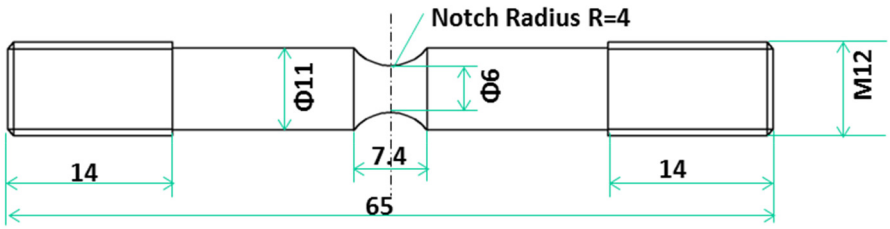

Fig. 3.15: Sketch of 4 mm notched round bar.

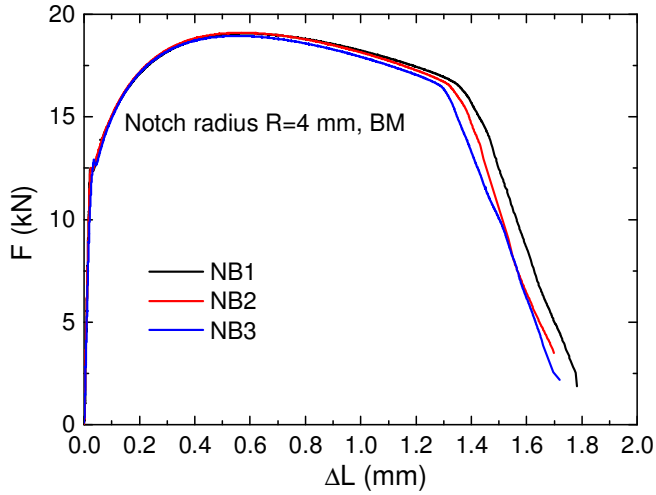

Fig. 3.16: Experimental force vs. elongation curves of the notched round specimens extracted from BM.

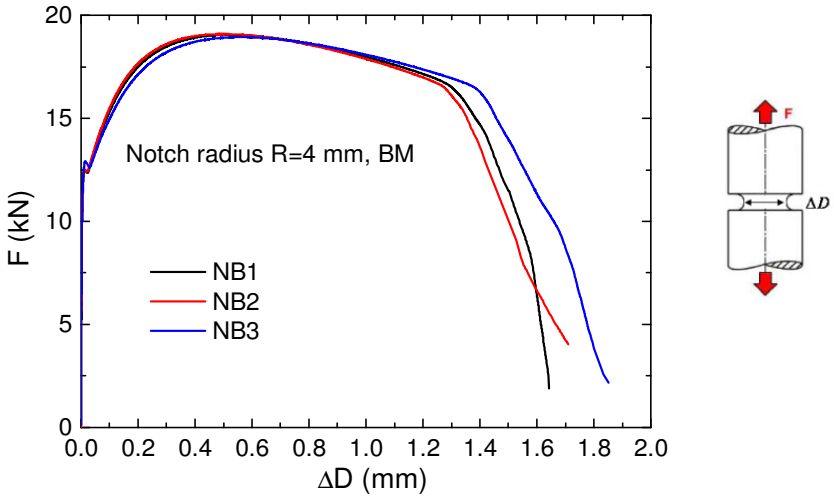

Fig. 3.17: Experimental force vs. cross section reduction curves of the notched round specimens where the HAZ is located in the center of the notched area.

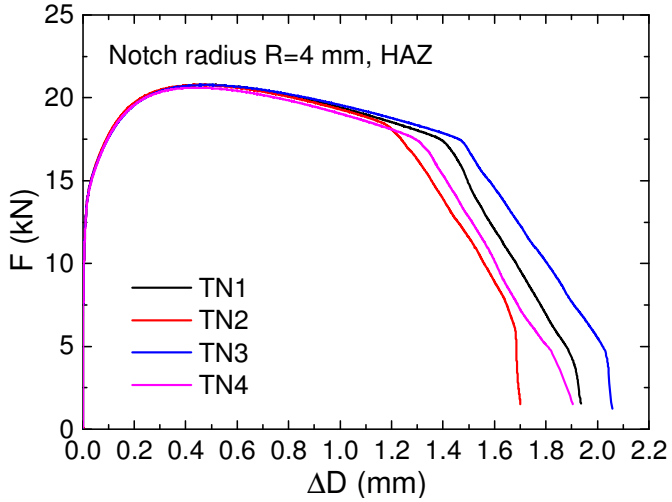

Fig. 3.18: Experimental force vs. cross section reduction curves of the notched round specimens extracted from HAZ.

4. Transverse flat tensile specimens

Transverse flat tensile specimens (T3-T6) where the weld seam is located exactly in the middle of the specimen were extracted across the joined plates. A sketch of the transverse flat specimen where the gauge length is 20 mm is shown in Fig. 3.19. After surface grinding, transverse flat specimens were tensile tested and the engineering stress vs. strain curves were recorded. A view of the specimens before and after tensile testing can be found in Figs. 3.20(a)-(b). The final fracture position locates in the BM, as shown in Fig. 3.20(b), showing the FZ is stronger than the BM which coincides with the information in Fig. 3.13. During the tensile process, the engineering stress vs. strain curves of the flat specimens where the FZ located in the center can be found in Fig. 3.21. After comparison of stress-strain curves from the BM and from the welded joint (Fig. 3.14 vs. Fig. 3.21), higher tensile strength and a complete different hardening obtained from the welded joint shows the superiority of the welded joint, as shown in Fig. 3.22.

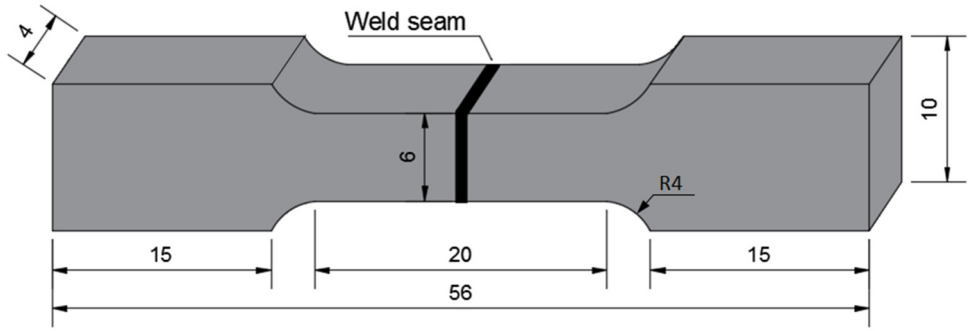

Fig. 3.19: Sketch of transverse flat specimen where the weld seam is located in the center of the specimen.

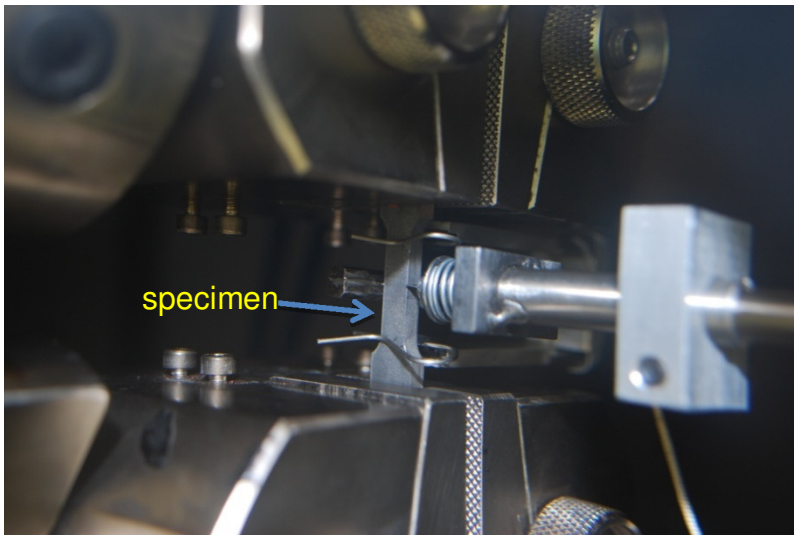

(a)

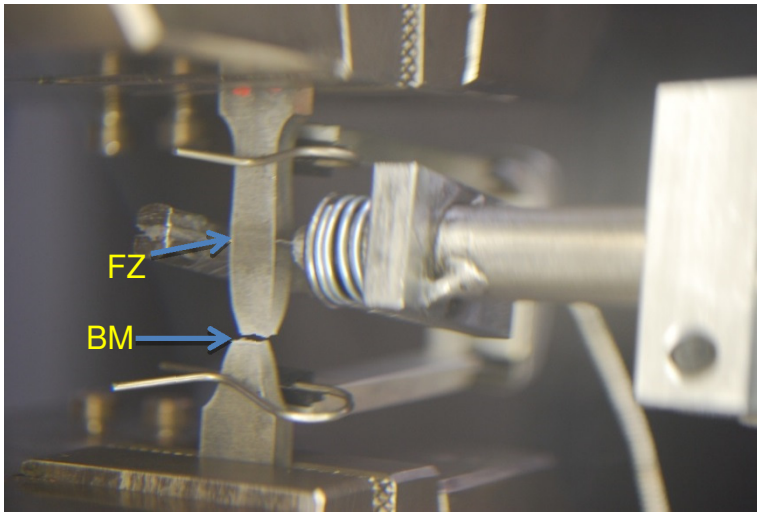

(b)

Fig. 3.20: Tensile test of transverse flat specimen (a) before tensile test, (b) after tensile test.

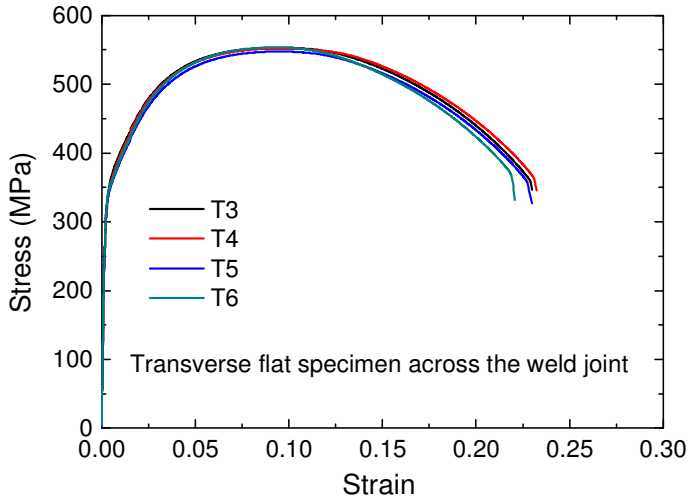

Fig. 3.21: Engineering stress vs. strain curves obtained from transverse flat specimens (T3-T6) where the weld seam is located in the center of the specimens.

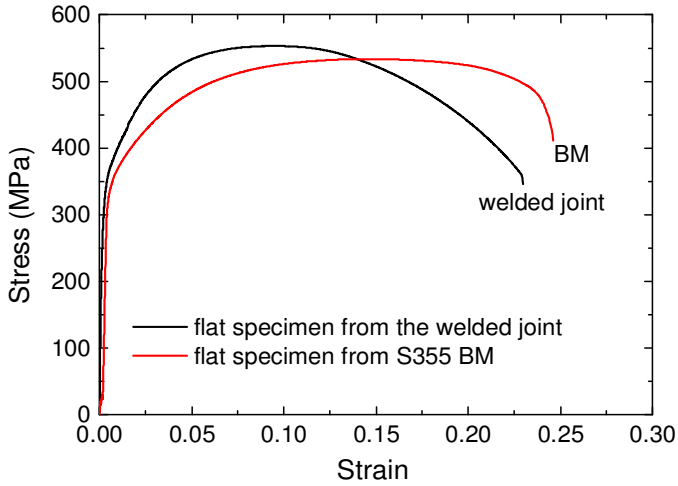

Fig. 3.22: Comparison between stress vs. strain curves obtained from the S355 BM and welded joint where the weld seam is located in the center of the specimen.

3.3.3 Fracture surface of notched specimens

After the tensile test of notched round specimens which were extracted from the BM, scanning electron microscope investigations were performed for the fracture surfaces. Figs. 3.23(a)-(g) show the fracture surfaces of notched specimens under different magnifications. Fig. 3.23(a) is the overview picture of the fracture surface. In order to derive detailed information of fracture surfaces, two marked regions shown in Fig. 3.23(a) were investigated. Figs. 3.23(b)-(d) are enlarged pictures with different magnifications obtained from the marked region I in Fig. 3.23(a). Figs. 3.23(e)-(g) are enlarged pictures with different magnifications obtained from the marked region II in Fig. 3.23(a). For S355 BM, the large voids are connected with neighboring smaller voids, showing typical ductile fracture behaviour, confirming that void initiation, growth and coalescence is the main reason for fracture.

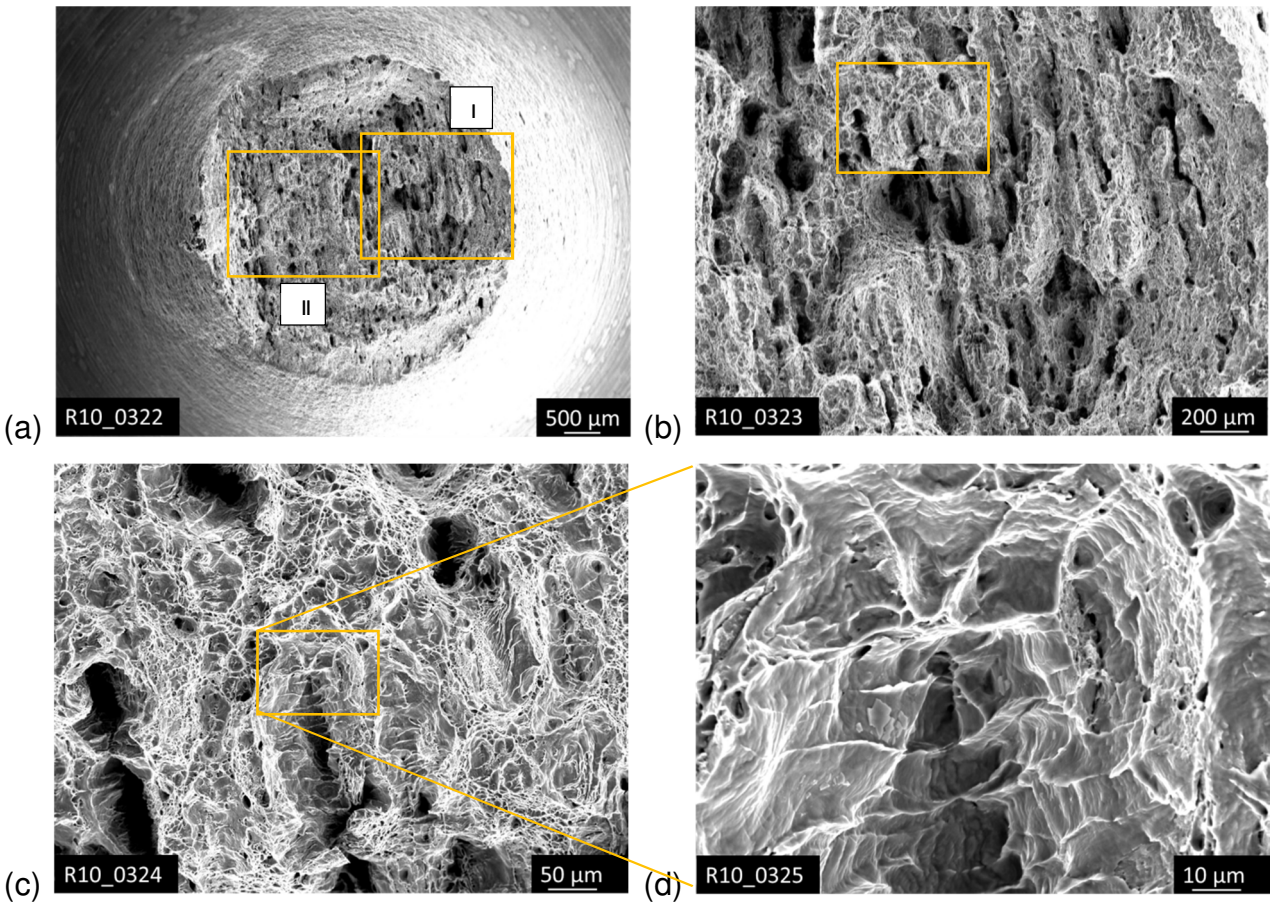

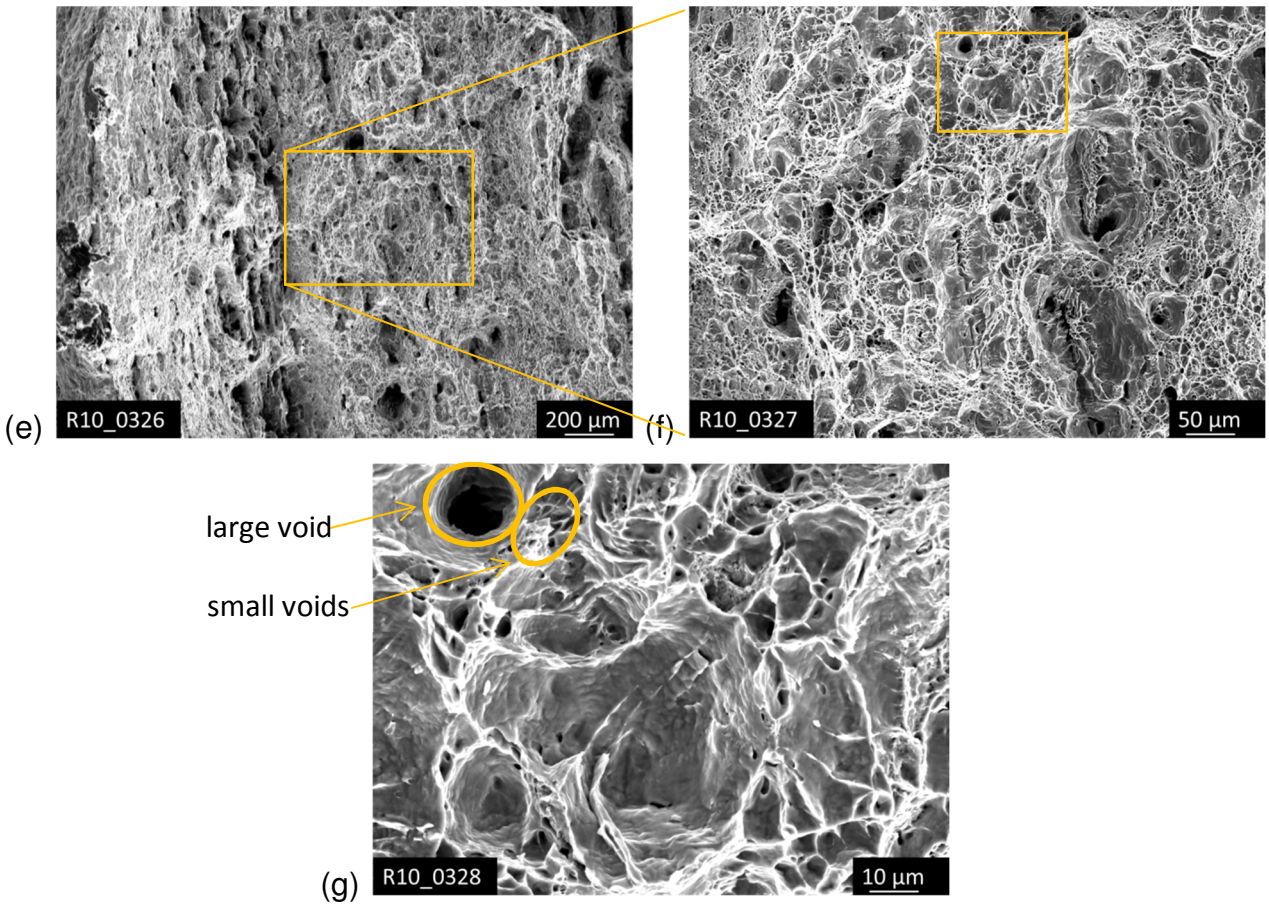

Fig. 3.23: SEM pictures of the fracture surface of a notched round specimen extracted from S355 BM shown at different magnifications: (a) overview of fracture surface, (b) enlarged image of marked region I of picture (a), (c) enlarged image of marked regions of picture (b), (d) enlarged image of marked region of picture (c), (e) enlarged image of marked region II of picture (a), (f) enlarged image of marked regions of picture (e), and (g) enlarged image of marked region of picture (f).

3.4 Fracture behaviour of S355 EBW joints

3.4.1 Fracture toughness tests

Fracture toughness tests of S355 electron beam welded joints were performed with compact tension (C(T)25) specimens. Specimens were manufactured and tensile tested according to ASTM standard [ASTM E1820, 2003] which have a thickness of B=25 mm, a net thickness of B_n=20 mm due to 20% side grooves, and a width of the specimens of W=50 mm. A sketch of the C(T)-specimens can be found in Fig. 3.24. In order to investigate

crack propagation at different weld regions, C(T)-specimens were manufactured with different configurations, i. e., the initial crack was located in the BM (C(T)-BM), in the middle of the FZ (C(T)-FZ) and in the HAZ where the crack is situated at the interface between the FZ and the HAZ (C(T)-HAZ), separately, as shown in Figs. 3.25(a)-(c). In order to create the desired crack length a_0, a notch was first machined with the Electron Discharge Machining (EDM) up to a length of 0.44W, then the specimen was fatigue loaded until the initial crack length a_0 (for C(T)-BM: a_0=0.535W, C(T)-FZ: a_0=0.48W, C(T)-HAZ: a_0=0.569W was recorded).

During the test process, loading was controlled by quasi-static displacements perpendicular to the initial crack and the force vs. Crack Opening Displacement (COD) curve was recorded. As explained by Anderson [Anderson, 2005], the unloading compliance method, as shown in Fig. 3.26, was adopted in order to get the compliance (C) of the specimen. The unloading compliance method which can save experimental costs is used instead of the multiple specimen technique where a series of identical specimens are loaded to different crack lengths. The crack propagation Δa is computed at regular intervals according to ASTM standard [ASTM, 2003] which has a relation to the compliance of the specimen.
After the C(T) test, the experimental results are shown in terms of force vs. Crack Opening Displacement (COD) as well as fracture resistance J_R-curves. The F-COD-curves of compact tension (C(T)) specimens with the initial crack located in different weld regions of S355 electron beam welded joints can be found in Fig. 3.27. As the FZ shows a higher tensile strength compared to that of the BM (see Fig. 3.13) and the initial crack length a_0 for the C(T)-FZ is less than that of the C(T)-BM, a C(T)-FZ specimen shows higher forces in the F-COD-curve compared to the BM as shown in Fig. 3.27. For a C(T)-FZ, the specimen suddenly ruptures, showing a more brittle fracture behaviour. The C(T)-FZ specimen breaks suddenly before stable crack propagation happens, therefore, no fracture resistance J_R-curve was obtained during the test process. J_R-curves for C(T)-BM and C(T)-HAZ specimens are shown in Fig. 3.28. The J-value from the C(T)-HAZ is slightly higher than that of the C(T)-BM at the early stage of the J_R-curve, see Fig. 3.28. This is because at the early stage of the tensile test, a slightly higher force in the F-COD-curve is obtained in the C(T)-HAZ due to higher stresses at certain strain obtained from the FZ and the HAZ in comparison to the BM, as shown in Fig. 3.13. After some crack propagation (round Δa=0.4 mm), a lower J_R-curve is obtained for the C(T)-HAZ because a lower force in the F-COD-

curve arises from less ductility of the HAZ, as indicated in Fig. 3.28 and Fig. 3.13 respectively.

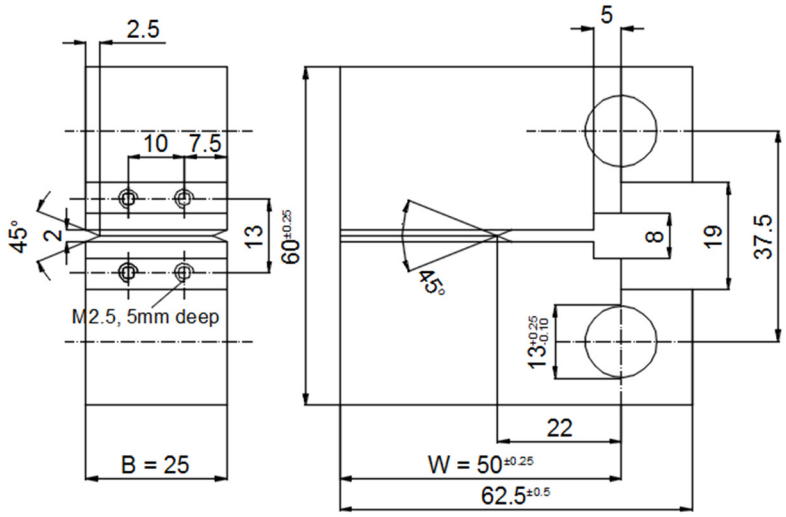

Fig. 3.24: Sketch of the compact tension specimen ((C(T)25) with 20% side groove.

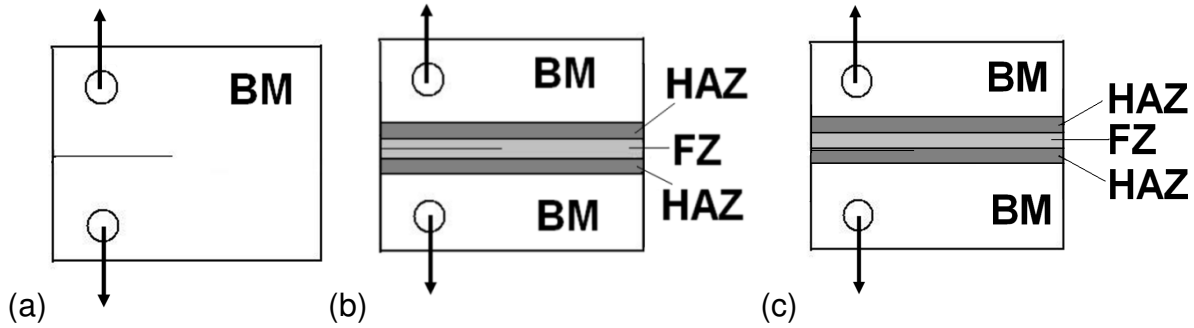

Fig. 3.25: Standard compact tension (C(T)25) specimens with the initial crack located at different positions: (a) in the BM (C(T)-BM), (b) in the center of the FZ (C(T)-FZ) and (c) in the HAZ where the crack is situated at the interface between the FZ and the HAZ (C(T)-HAZ).

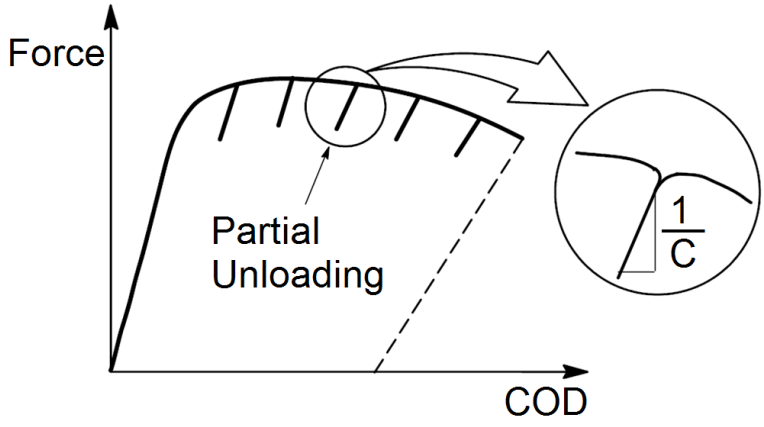

Fig. 3.26: The unloading compliance method for monitoring crack growth [Anderson, 2005].

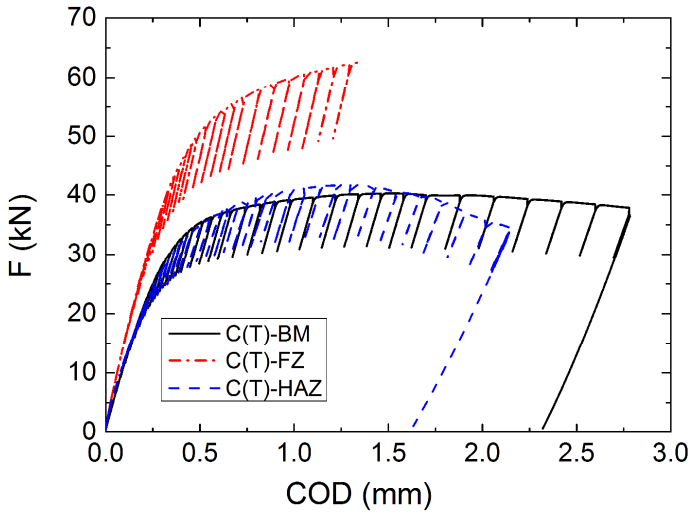

Fig. 3.27: Force vs. Crack Opening Displacement (COD) curves of compact tension (C(T)) specimens with the initial crack located in the BM, in the center of the FZ and in the HAZ where the crack is situated at the interface between the FZ and the HAZ, respectively.

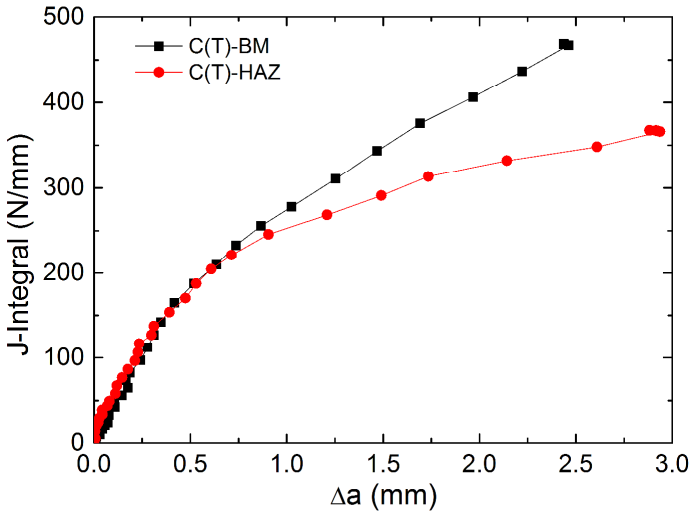

Fig. 3.28: Fracture resistance J_R-curves obtained from C(T)-specimens when the initial crack is located in the BM and in the HAZ where the crack is located at the interface between the BM and the HAZ.

3.4.2 Fracture surface analysis of C(T)-specimens

After the designed stable crack propagation was achieved during the fracture toughness test, C(T) specimens were firstly heated up to 280 ℃, then maintained for around 30 minutes, later on cooled naturally (heat tinting process), both for the C(T)-BM and the C(T)-HAZ specimens. After the heat tinting, the specimens were cooled with liquid nitrogen, then broken finally with the test machine. For the case of the C(T)-FZ, as the specimen ruptures

suddenly before the stable crack starts, no heat tinting was performed on the C(T)-FZ specimen. The metallographic analyses were performed for the fracture surface using SEM investigations under different magnifications. The overview of the fracture surface of a C(T)-specimen extracted from the BM can be found in Fig. 3.29. It can be seen that the whole fracture surface can be divided into the fatigue crack region, the stretched zone region, the stable crack growth region and the brittle fracture region. The SEM picture of the marked position 1 in the fatigue region is depicted in Fig. 3.30(a). Fig. 3.30(b) is the enlarged image of the marked region in Fig. 3.30(a). The marked region in the stretched zone region is shown in Fig. 3.30(c). The marked region in the stable crack region shows typical dimple structures as observed in Fig. 3.30(d)-(e). Fig. 3.30(e) is the enlarged image of the marked region in Fig. 3.30(d). The fracture surfaces show typical ductile fracture characteristics, large dimples with sizes of 20-30 µm are surrounded by smaller dimples with the sizes of 3-4 µm. In Fig. 3.30(e), large dimples are connected with smaller dimples; broken particles are visible at the bottom of large dimples. These dimples are a consequence of void coalescences. Due to the influence of cooling with liquid nitrogen, the C(T) specimen shows a brittle fracture behavior. The marked region 4 in the brittle fracture region is presented in Fig. 3.30(f) and the enlarged image of the marked region in Fig. 3.30(f) is shown in Fig. 3.30(g).

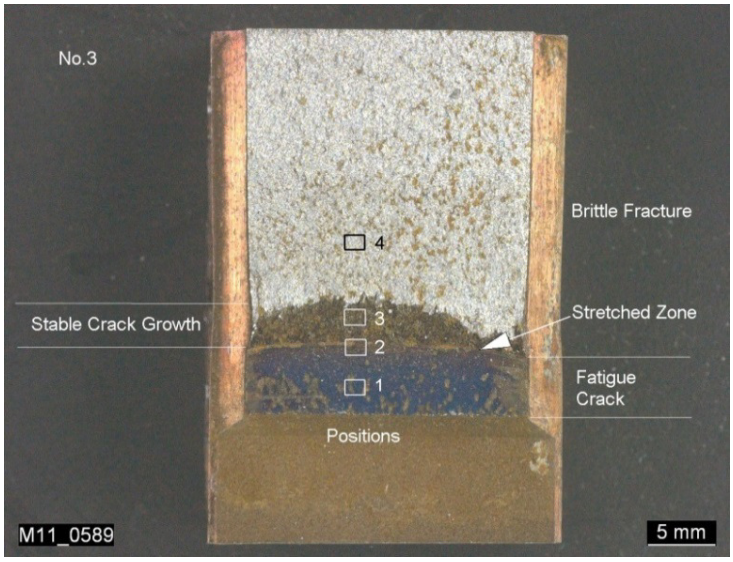

Fig. 3.29: Overview of the fracture surface of a C(T)-BM.

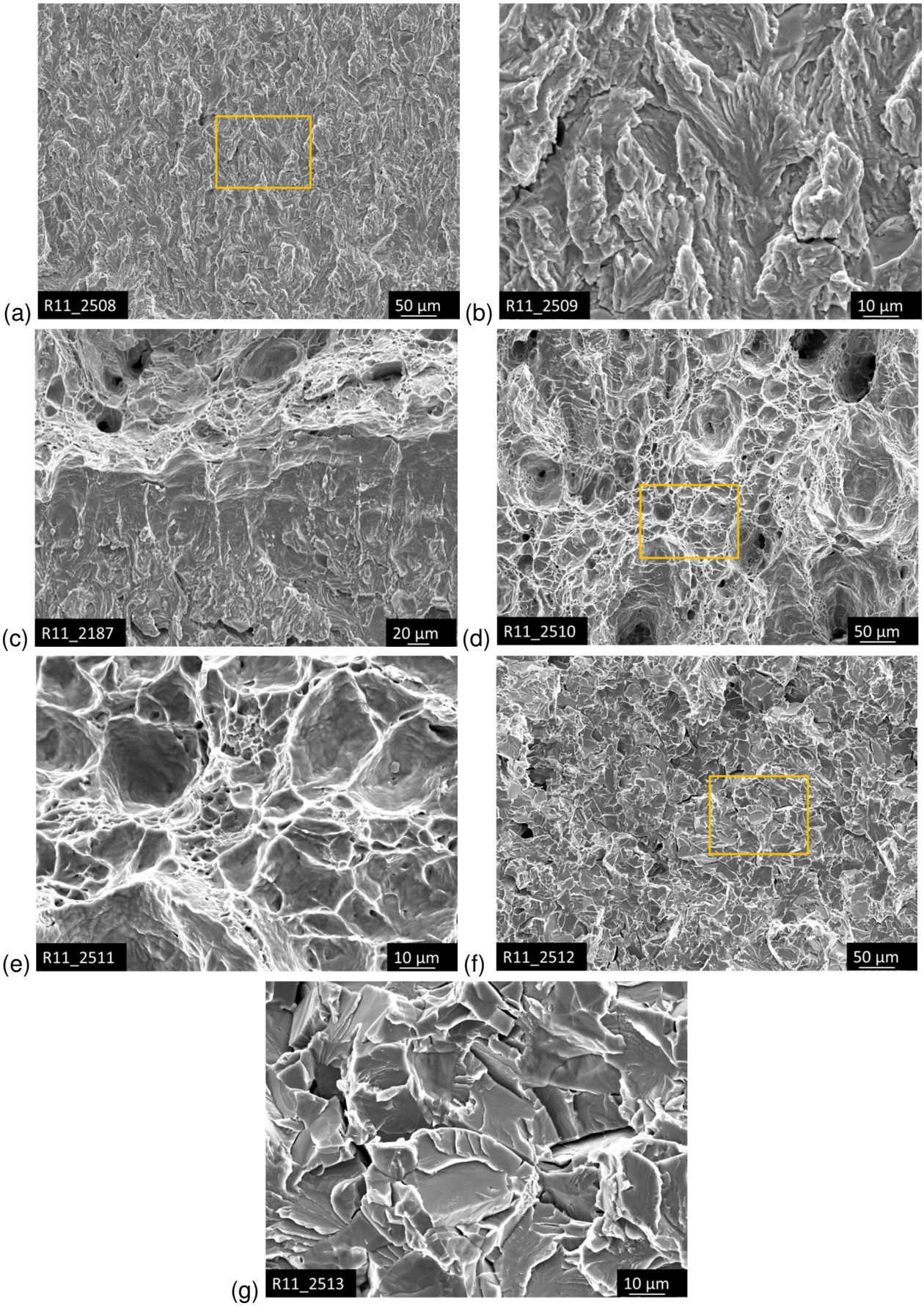

Fig. 3.30: Fracture surface of S355 BM (a) marked region 1 in the fatigue region, (b) enlarged image of marked region 1 in (a), (c) marked region 2 in the stretched zone region,

(d) marked region 3 in the stable crack growth region, (e) enlarged image of the marked region in figure (d), (f) marked region 4 in the brittle fracture region and (g) enlarged image of marked region 4 in picture (f).

The overview of the fracture surface of a C(T)-specimen for which the initial crack is located in the center of the FZ is presented in Fig. 3.31. The whole fracture surface is observed to be divided into the fatigue crack region, the stretched zone region, the stable crack growth region and the brittle fracture region. The SEM picture of the marked position 1 in the fatigue region is shown in Fig. 3.32(a). Fig. 3.32(b) is the enlarged image of the marked region in Fig. 3.32(a). The marked region in the stretched zone region is presented in Fig. 3.32(c). Fig. 3.32(e) is the enlarged image of the marked region in Fig. 3.32(d). Similar dimple fracture structures are also observed in the stable crack growth region as shown in Fig. 3.32(d)-(e), with big dimples of sizes of 8-10 µm being surrounded by smaller dimples with sizes of 1-2 µm. However, compare that for the BM (Fig. 3.29), smaller ductile crack growth regions (Fig. 3.31) and smaller dimple sizes at the same magnification (see Fig. 3.32(e)) are found on the fracture surface. Furthermore, besides the dimple areas, some flat regions (marked regions in Fig. 3.32(e)) can be observed on the fracture surface, which are due to the unstable fracture of the FZ. This leads to less ductile or even some brittle behaviour of the C(T)-FZ specimen as the C(T)-FZ specimen were broken suddenly during the test (see Fig. 3.27). The marked region in the region 4 of brittle fracture region is shown in Fig. 3.32(f) and the enlarged image of the marked region in Fig. 3.32(f) is presenting in Fig. 3.32(g).

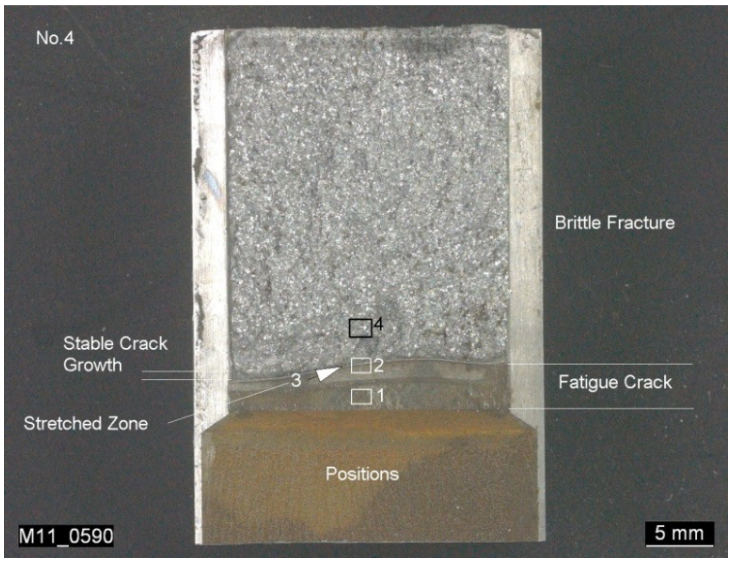

Fig. 3.31: Overview of fracture surface of a C(T)-FZ.

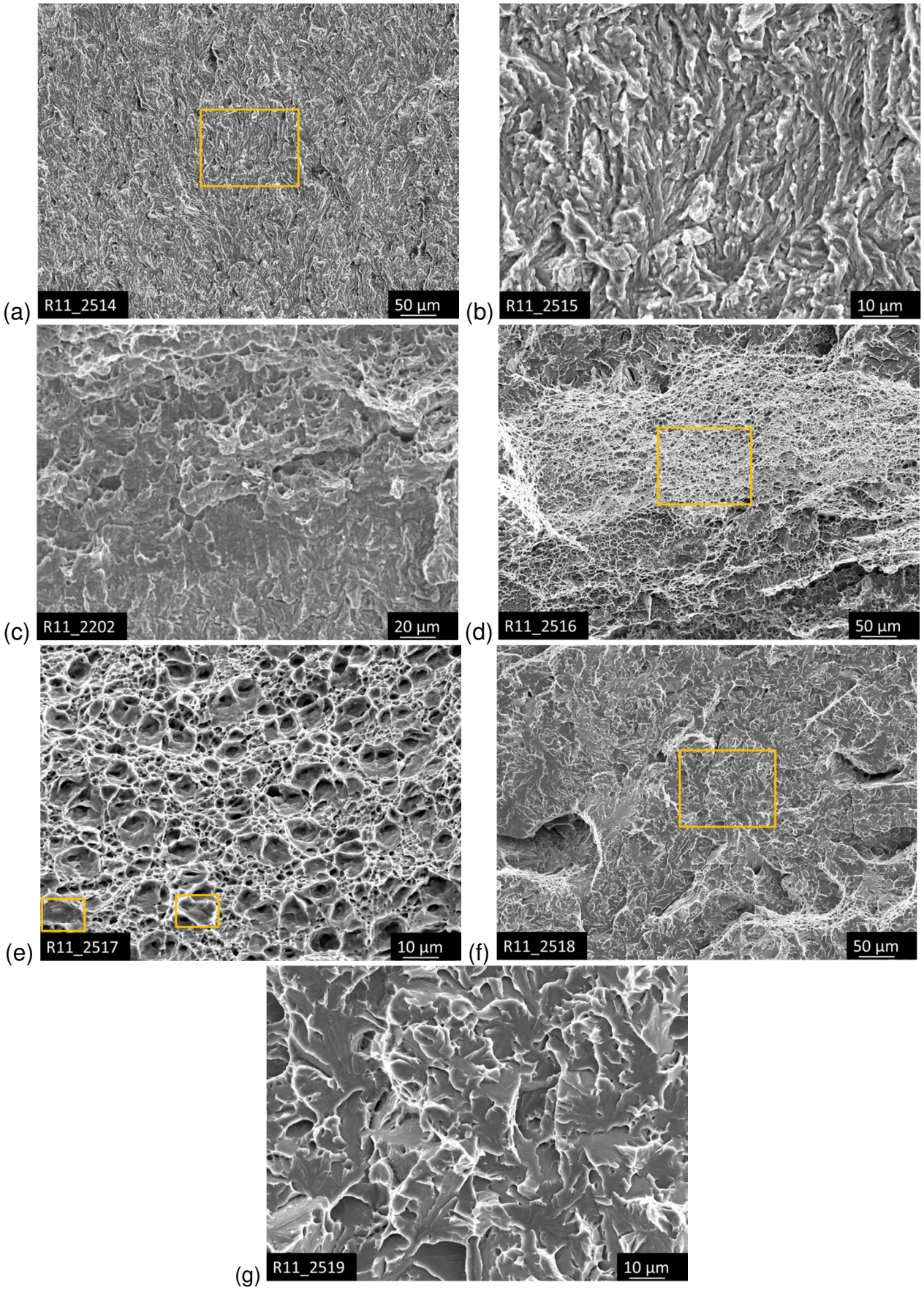

Fig. 3.32: Fracture surface of S355 FZ (a) marked region 1 in the fatigue region, (b) enlarged image of marked region 1 in figure (a), (c) marked region 2 in the stretched zone

region, (d) marked region 3 in the stable crack growth region, (e) enlarged image of the marked regions in figure (d), (f) marked region 4 in the brittle fracture regions and (g) enlarged image of marked region in figure (f).

The overview of the fracture surface of a C(T)-specimen with the initial crack located at the interface between the BM and the HAZ is shown in Fig. 3.33. It can be again seen (as for the BM) that the fracture surface can be divided into the fatigue crack region, the stretched zone region, the stable crack growth region and the brittle fracture region. The SEM picture of the marked position 1 in the fatigue region is presented in Fig. 3.34(a). Fig. 3.34(b) is the enlarged image of the marked region in Fig. 3.34(a). The marked region 2 in the stretched zone region is depicted in Fig. 3.34(c). Fig. 3.34(e) is the enlarged image of the marked region in Fig. 3.34(d). For the HAZ, similar stable crack regions as for the BM can be found in Fig. 3.34(e). Large voids are connected with smaller voids; this indicates that the fracture of the HAZ is also controlled by void nucleation, growth and void coalescence during deformation. The marked region in the brittle region can be found in Fig. 3.34(f) and the enlarge image of the marked region in Fig. 3.34(f) can be found in Fig. 3.34(g).

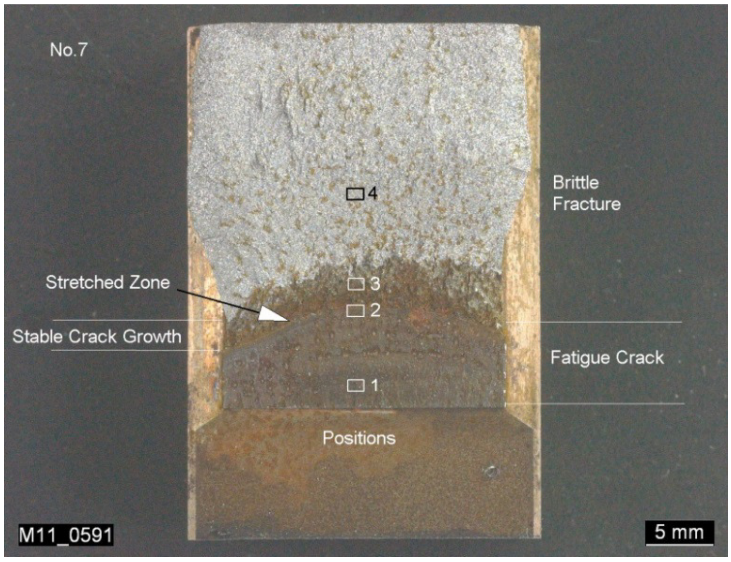

Fig. 3.33: Overview of fracture surface of a C(T)-HAZ.

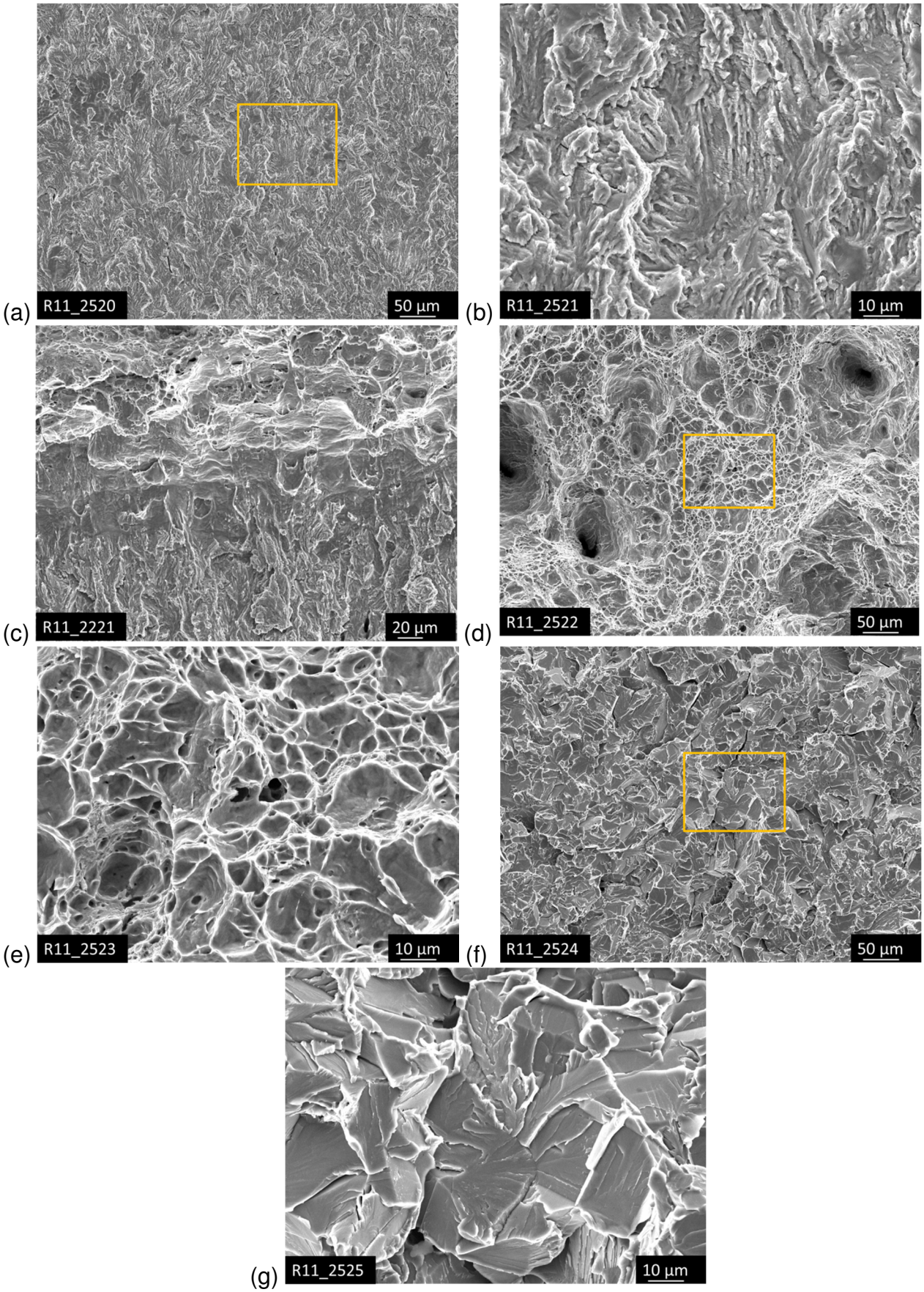

Fig. 3.34: Fracture surface of S355 HAZ (a) marked region 1 in the fatigue region, (b) enlarged image of marked region 1 in figure (a), (c) marked region 2 in stretched zone

region, (d) marked region 3 in stable crack growth region, (e) enlarged image of marked region in figure (d), (f) image of marked region 4 in brittle fracture region and (g) enlarged image of marked region 4 in picture (f).

3.5 Summary and conclusions

Experimental investigations were performed on the S355 EBW joints. Based on chemical composition of the S355 base material, the volume fraction of non-metallic inclusions is obtained from Franklin's formula (0.7×10^{-3}) firstly. The dimensions of different weld regions are defined by the hardness test across the welded joint. This hardness profile provides the dimensions of different weld regions in the finite element model. Optical microscopy investigations were performed on different weld regions. The volume fraction of non-metallic inclusions and the mean distance between neighboring inclusions for the BM, the FZ and the HAZ are defined. After surface etching, the microstructures of different weld regions are obtained in which the BM is comprised of Ferrite and Pearlite, while the FZ is comprised of acicular martensite structures and the HAZ is the transitional area between the FZ and the BM. Smooth round specimens extracted from the BM and flat specimens from the BM, the FZ and the HAZ are tensile tested and the respective stress-strain curves are used as model input in the following chapters. Notched round specimens from the BM and from the HAZ are tensile tested. The tensile results are shown in the form of F-ΔL- and F-ΔD-curves. The experimental F-ΔD-curves are used for later numerical calibration of the Rousselier parameters and the GTN parameters. Fracture toughness tests of S355 electron beam welded joints were performed with compact tension (C(T) with 20% side groove) specimens. C(T)-BM, C(T)-FZ and C(T)-HAZ specimens were tensile tested and the results are shown in the form of F-COD- and fracture resistance J_R-curves. Fracture surface analyses of C(T)-specimens were made on the mentioned C(T)-specimens. Both C(T)-BM and C(T)-HAZ show typical ductile fracture behavior with large stable crack growth regions are obtained. C(T)-FZ specimen ruptures suddenly before stable crack propagation and shows a more brittle fracture behavior. The damage models (Rousselier model and GTN model) which describe the evolution of void initiation, growth and coalescence are adopted to investigate the crack propagation of C(T)-BM and C(T)-HAZ in chapter 4 and chapter 5. The cohesive zone model will be used to describe the ductile fracture behavior of C(T)-BM and C(T)-HAZ together with quasi-brittle fracture behavior of C(T)-FZ in chapter 6.

4. The Rousselier model

In the following chapter, the Rousselier model is applied to study numerically the crack propagation in S355 electron beam welded joints. As explained in chapter 3, crack propagation in C(T)-specimens (C(T)25 with 20% side groove) with different initial crack positions, i.e., the initial crack located in the BM, in the center of the FZ or at the interface between the FZ and the HAZ were tested. As the FZ shows less ductile or some brittle behaviour, the Rousselier model is used to investigate the homogenous BM and the inhomogeneous welded joint only. In order to identify the influence of the Rousselier parameters on the fracture behavior of S355 additionally, parametric studies are performed for the notched round specimen and for the C(T)-specimens. After the calibration of the Rousselier parameters on the notched round specimen, the same parameter set is used to fit the crack propagation in C(T)-specimens. The numerical simulation results are compared with the experimental ones in terms of the F-COD- and J_R-curves.

4.1 Parameter study using the Rousselier model

The general equation of the yield surface for the Rousselier model is as follows:

$$\Phi = \frac{\sigma_{eq}}{1-f} + Df\sigma_k \exp\left(\frac{\sigma_m}{\sigma_k(1-f)}\right) - R(p) = 0 \tag{4.1}$$

where σ_{eq} is the von Mises equivalent stress, σ_m is the mean (hydrostatic) stress, f is the void volume fraction (initial value f_0), D is material constant (D=2, see [Rousselier, 1987]), σ_k is a material dependent parameter, p is the cumulated plastic strain and R(p) is the true stress-true plastic strain curve of the material. From the previous explanations in chapter 2, f_0 and σ_k are Rousselier parameters to be adjusted. The numerical parameter (l_c) which stands for the average distance between neighboring particles should be calibrated before the application.

For ductile fracture, within the framework of damage models, it is assumed that a crack propagates from void to void. This can be simulated by the finite element model that a crack

propagates from integration point to integration point. As square finite elements with 4 integration points are used for the calculation, the main distance between voids (l_c) is equal to half of the element size (2* l_c). Based on the experimental investigation summarized in chapter 3.2 and the information from literature [Schmauder et al., 2002], some typical material parameters are used for the parameter study, which is shown in table 4.1. The method is to change one parameter at one time while keeping the rest of the parameters fixed during the simulation. In this section, the parameter study will show how the Rousselier parameters influence the simulation results. The influences of parameters on the force vs. cross section reduction curves of notched round specimens, on the F-COD- and J_R-curves of C(T)-specimens are shown in the following.

Table 4.1: Basic parameters used in the parameter study of the Rousselier model

f_0	f_c	σ_k	l_c
0.001	0.05	445 MPa	0.05 mm

4.1.1 Influence of f_0

The initial void volume fraction f_0 is taken as the volume fraction of all possible inclusions. For steel, f_0 depends on the volume fraction of non-metallic inclusions, like sulphides and oxides, as explained by Seidenfuss [Seidenfuss, 1992] and Schmauder [Schmauder et al., 2002]. For the notched round specimen, as the geometry and loading are axisymmetric and symmetric with respect to the cross section, only one quarter of the structure was used for the modeling and isoparametric 8 node quadratic elements (suitable for modeling the complicated geometry, e.g., notched round specimen and C(T)-specimen) with reduced integration points are chosen. The finite element mesh of the notched round specimen and the detailed mesh can be found in Fig. 4.1. As can be seen in Fig. 4.2, the f_0-values influence the sudden drop positions of the F-ΔD-curves of notched round specimens. When the material is under external deformation, higher f_0-values let the material deform more easily and results in an earlier void coalescence stage when micro cracks emerge on the surface of the material. Higher f_0 let the final fracture happen earlier while the slope of the curves after the final fracture point is not affected by the f_0-values. In Fig. 4.3, higher f_0-values mean the material contains more voids which can more easily coalesce microcracks during material deformation, results in lower forces for the F-COD-curve of the C(T)-specimens. Although the J-value at the initial crack stage is not affected much by the f_0-

values, f_0-values result in a significant influence on the slope of the fracture resistance J_R-curve. A higher f_0-value stands for that less energy is needed for fracture, resulting in a more flat J_R-curve, as shown in Fig. 4.4.

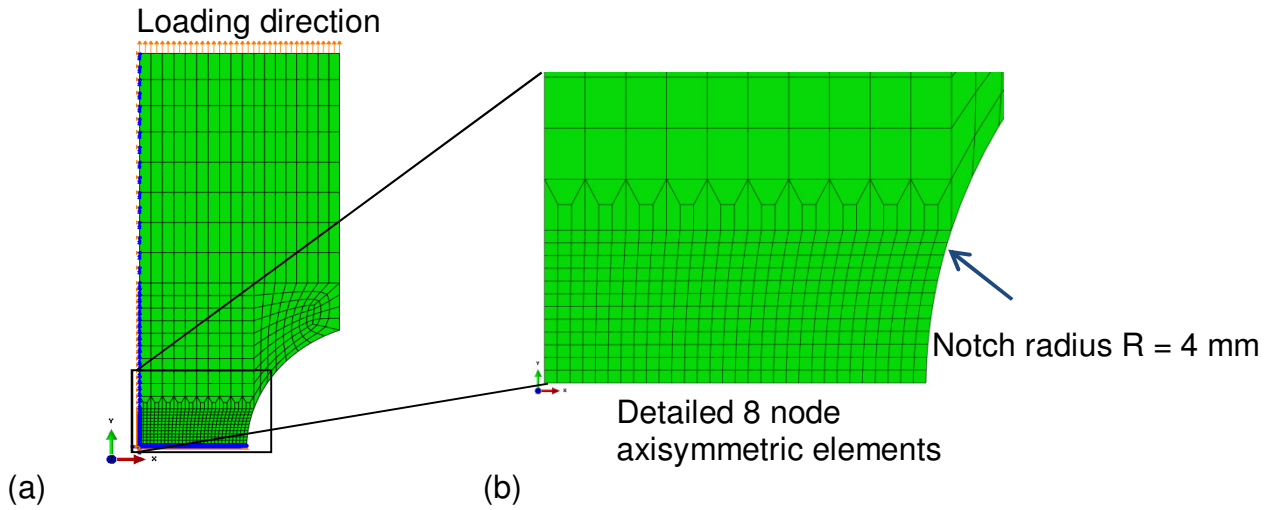

Fig. 4.1: (a) Axisymmetric finite element mesh and boundary conditions of the notched round specimen and (b) detailed mesh.

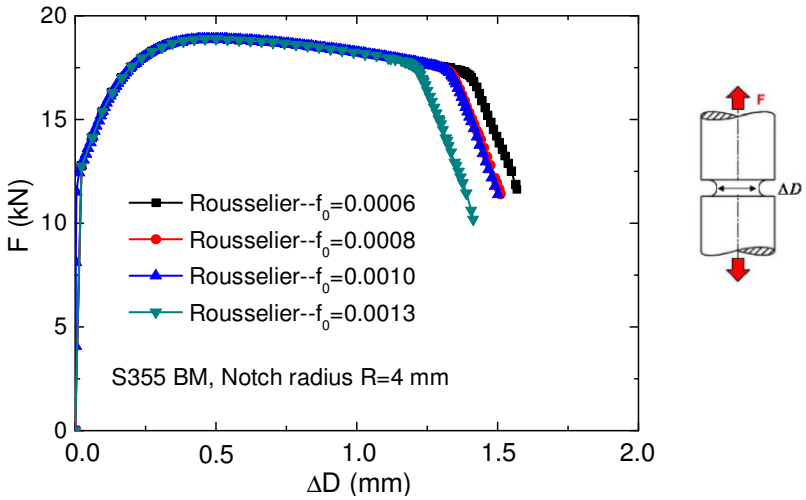

Fig. 4.2: Influence of f_0 on the F-ΔD-curve of notched round specimens extracted from S355 base material when f_c=0.05, σ_k =445 MPa and l_c=0.05 mm.

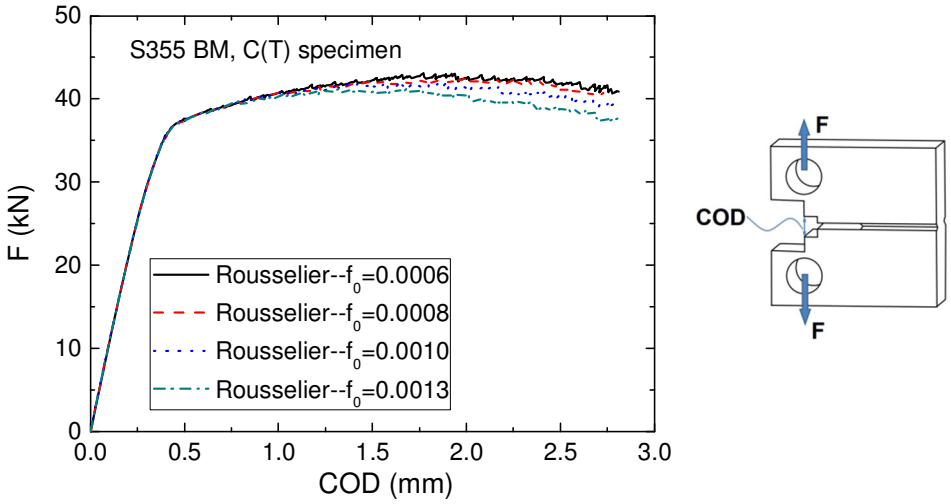

Fig. 4.3: Influence of f_0 on the F-COD-curve of a compact tension (C(T)) specimen extracted from S355 base material when f_c=0.05, σ_k =445 MPa and l_c=0.05 mm.

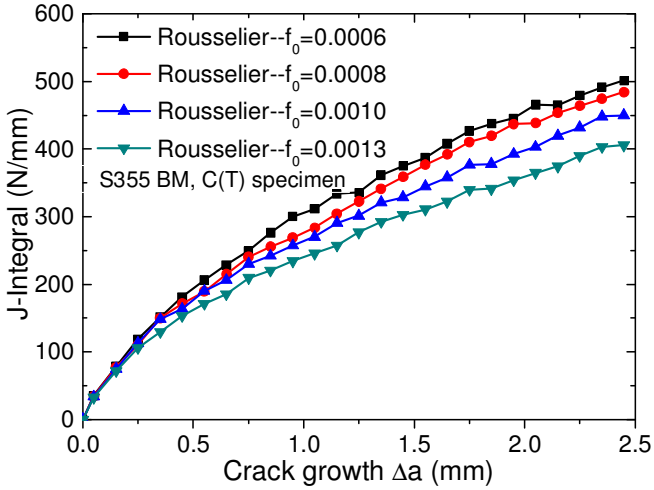

Fig. 4.4: Influence of f_0 on the J_R-curve of a compact tension (C(T)) specimen extracted from S355 base material when f_c=0.05, σ_k =445 MPa and l_c=0.05 mm.

4.1.2 Influence of f_c

The critical void volume fraction is the volume fraction when the material loses its stress carrying ability completely. It is not a parameter of the Rousselier model but a numerical parameter which helps to accelerate the void growth and overall damage of the material. A lower f_c-value means the damage of the material happens earlier, resulting in a steeper slope after the drop point, as shown in Fig. 4.5.

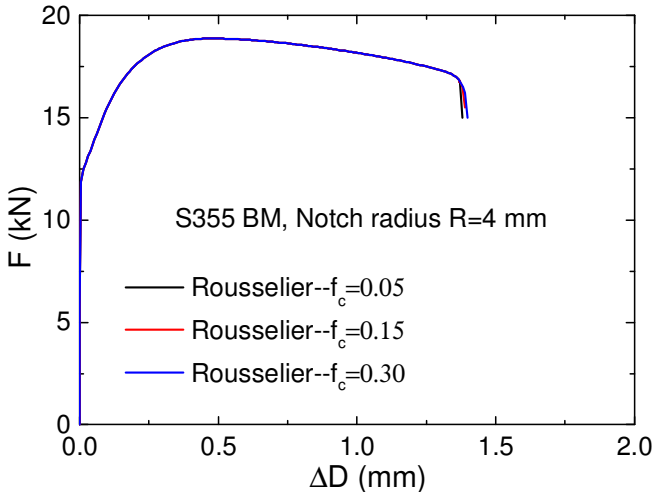

Fig. 4.5: Influence of f_c on the F-ΔD-curve of notched round specimens extracted from S355 base material when f_0=0.001, σ_k =445 MPa and l_c=0.05 mm.

4.1.3 Influence of σ_k

Here, σ_k is the material constant parameter as explained by Rousselier [Roussselier, 1987; Rousselier, 2001]. The first approach for σ_k is the value of $\frac{2}{3}\sigma_m$ when the final fracture happens for the smooth round specimen. For S355, the first estimation for σ_k is 355 MPa which is estimated according to σ_m shown in table 3.2. However, this is an underestimated value which is lower than the real one. In this chapter, according to the investigations on Rousselier model performed at MPA [Seidenfuss, 1992; Schmauder, 2002] and the suggestions of Rousselier [Rousselier, 2001], for most of the so far investigated steels, σ_k=445 MPa is found to be a reasonable value. Parameter studies are performed with different values (around ±10%) around σ_k=445 MPa. As shown in Fig. 4.6, σ_k has a strong influence on F-ΔD-curve of notched round specimen; however the slope after the fracture point of the F-ΔD-curve is not affected. A higher σ_k-value results in later fracture stage. For C(T)-specimen, higher σ_k results in a higher force of the F-COD-curve, as shown in Fig. 4.7. Although the J-value at the initial crack stage is not much affected by the σ_k-value, a higher σ_k-value results in a more significant influence on the slope of the fracture resistance J_R-curve. Higher σ_k-values result in a steeper J_R-curve, as shown in Fig. 4.8. According to the discussion of Rousselier [Rousselier, 1987], σ_k is a parameter translating the resistance of material to the growth and coalescence of voids. Besides that, σ_k has a close relation with the flow stress of the material. Higher σ_k mean the material reaches the void coalescence moment at a later stage, resulting in a later fracture position on the F-ΔD-curve for notched

specimens and a higher F-COD-curve together with steeper J_R-curves for the C(T)-specimen.

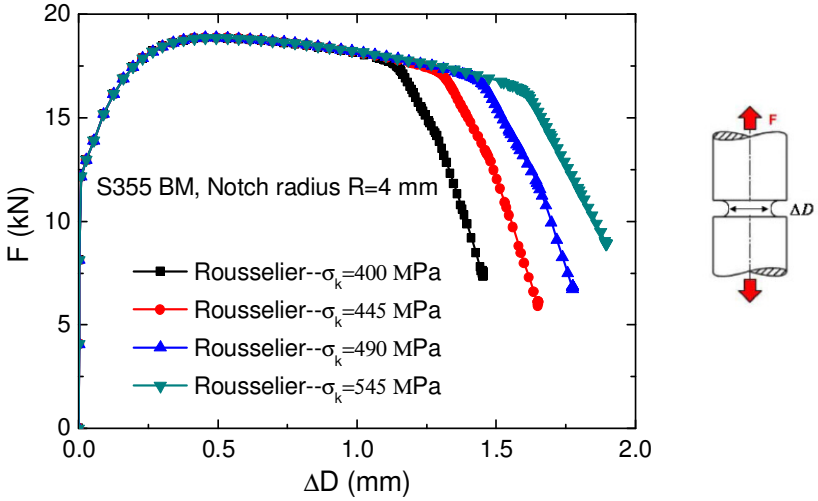

Fig. 4.6: Influence of σ_k on the F-ΔD-curve of notched round specimens extracted from S355 base material when f_0=0.001 and f_c=0.05 and l_c=0.05 mm.

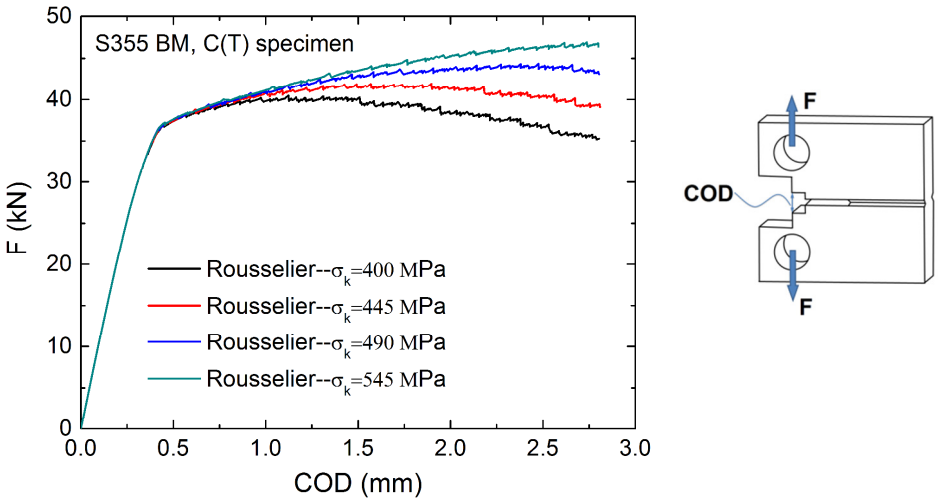

Fig. 4.7: Influence of σ_k on F-COD-curves of compact tension (C(T)) specimen extracted from S355 base material when f_0=0.001 and f_c=0.05 and l_c=0.05 mm.

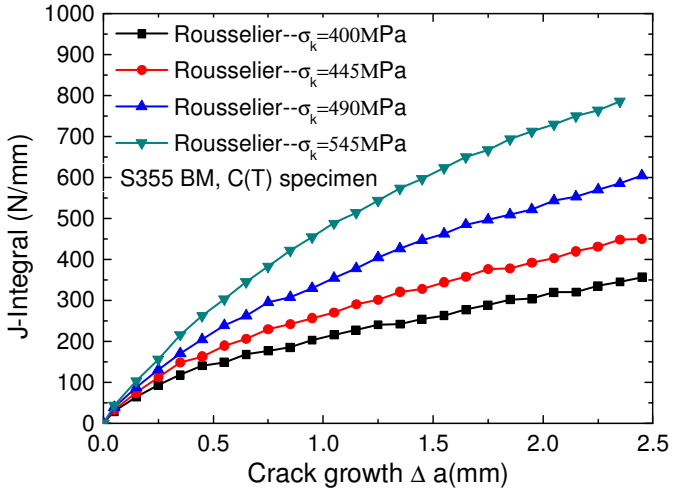

Fig. 4.8: Influence of σ_k on fracture resistance curves of compact tension (C(T)) specimen extracted from S355 base material when f_0=0.001 and f_c=0.05, l_c=0.05 mm.

4.1.4 Influence of l_c

The l_c-value is the average distance between voids (neighboring non-metallic inclusions). In the 2D finite element model, square finite elements with 4 integration points are used for the calculation; the l_c-value is equal to half of the element size. Based on the optical microscope pictures (l_c=0.1 mm for S355 BM), typical l_c-values are used for the parameter study. As can be found in Fig. 4.9, the l_c-value does not influence the fracture position on the F-ΔD-curve for notched round specimens but influences the slope of the curve after the drop point. Higher l_c-values lead to flatter curves after fracture of the notched round specimen because it is more difficult to damage larger elements which stand for longer distance between the neighboring particles in the microstructure. A longer particle distance stands for a higher l_c-value, means more energy is needed to drive the crack propagation from one particle to the other. Higher l_c-values lead to a higher force when the crack initiation happens and higher forces of the F-COD-curve and steeper J_R-curves, as shown in Fig. 4.10 and Fig. 4.11, respectively. This is because more force and energy is required to damage larger elements which stand for more material.

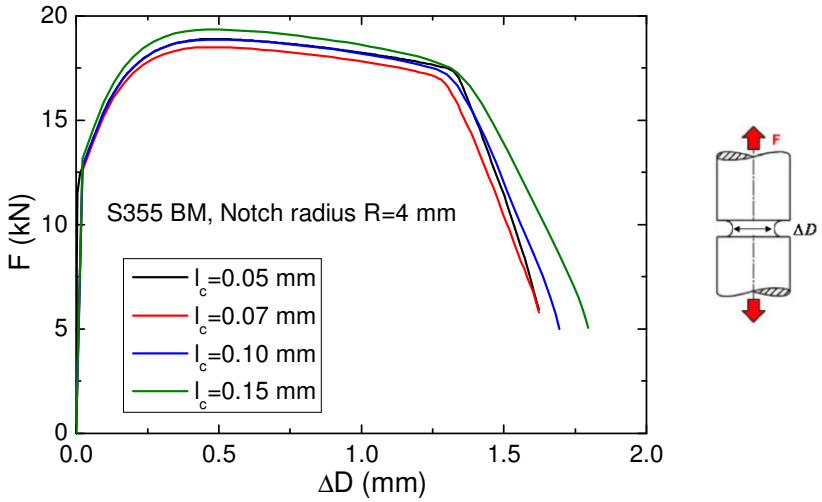

Fig. 4.9: Influence of l_c on the F-ΔD-curve of notched round specimens extracted from S355 base material when f_0=0.001, f_c=0.05 and σ_k=445 MPa.

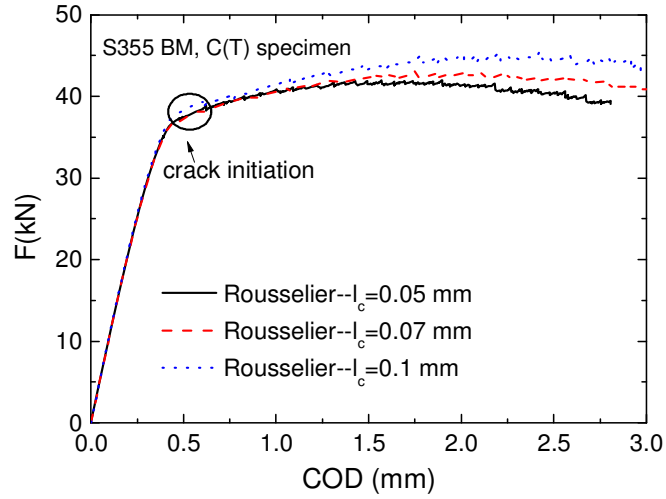

Fig. 4.10: Influence of l_c on F-COD-curve of compact tension (C(T)) specimens extracted from S355 base material when f_0=0.001, f_c=0.05 and σ_k=445 MPa.

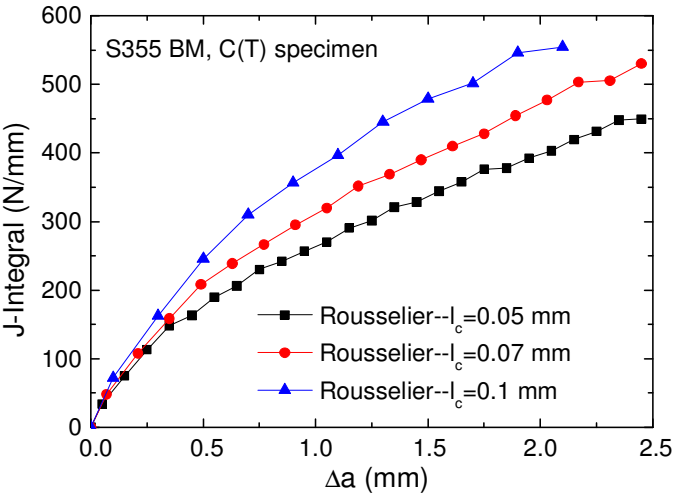

Fig. 4.11: Influence of l_c on fracture resistance curves of compact tension (C(T)) specimens extracted from S355 base material when f_0=0.001, f_c=0.05 and σ_k=445 MPa.

The influences of f_0, f_c, σ_k and l_c on the tensile test results of notched round specimens and the compact tension (C(T)) specimens are summarized in Fig. 4.12. For notched round specimens, higher f_0-values or lower σ_k-values lead to earlier breakpoint of a rapid decrease of force of F-ΔD-curves. After the breakpoint of rapid decrease of force, a steeper slop of the F-ΔD-curve is obtained when lower f_c and smaller l_c are used in the Rousselier model. For C(T)-specimens, the f_0- and σ_k-values does not influence the force of the F-COD and the corresponding numerical J-value when the crack initiation happens, as shown in Fig. 4.12(c) and Fig. 4.12(e). However, higher forces for the F-COD-curve and higher J_i-values are obtained when lower f_0-values or larger l_c-values are used, as displayed in Fig. 4.12(d) and Fig. 4.12(f). After the crack initiation, higher force of the F-COD-curve and steeper J_R-curves are obtained when lower f_0-values or larger l_c and σ_k-values are used. In the next subchapter, the experiences obtained in the parameter study will be used for the numerical calibration of the Rousselier parameters.

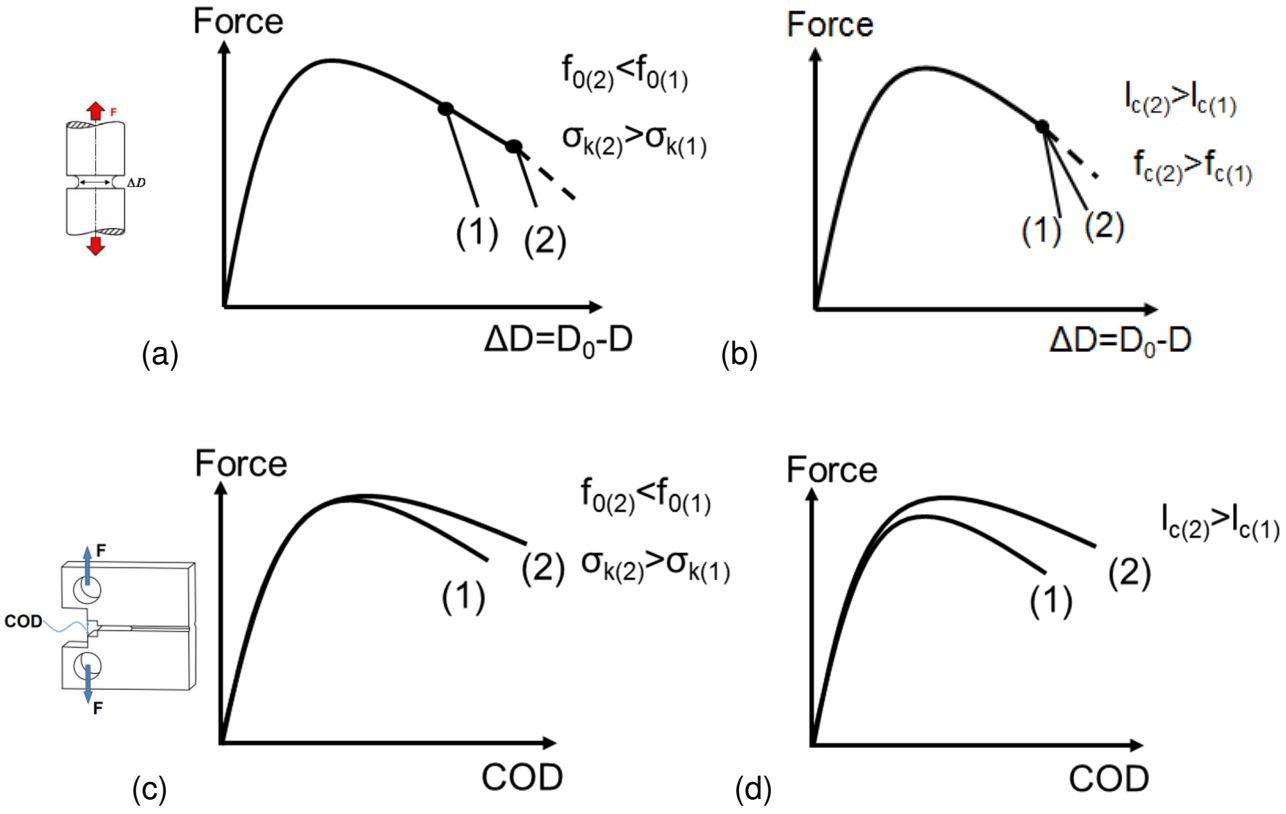

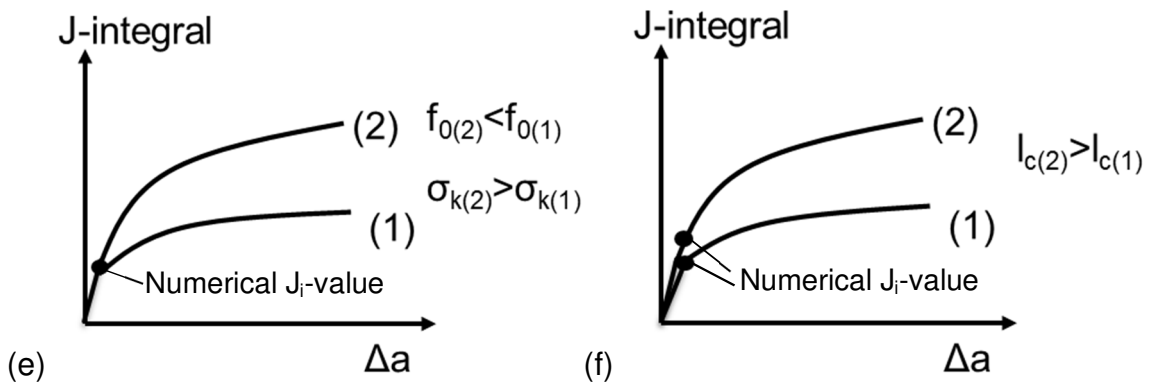

Fig. 4.12: Schematic influence of Rousselier parameters f_0, σ_k, and l_c on the F-ΔD-curves of the notched specimens and on the F-COD- and J_R-curves of C(T)-specimens extracted from S355 base material.

4.2 Crack propagation in the homogeneous base material

From previous explanations, σ_k=445 MPa is adopted for S355 BM and f_c=0.05 is adopted for all the simulations. The initial void volume fraction f_0 and the average distance between voids l_c are the Rousselier model parameters to be fixed. These Rousselier parameters can be obtained from the optical microscope pictures. From the optical microscope pictures of the BM and the HAZ, see Fig. 3.1, the voids are not equally distributed but localized at some regions. Before adopted in the Rousselier model directly, these experimental values should be calibrated numerically. For the BM, numerical calibrations are performed based on force vs. diametral reduction curves of notched round specimens. Based on the metallographic investigations (l_c=0.1 mm), two additional l_c-values (l_c=0.07 mm and l_c=0.05 mm) were used for the calibration of f_0. For notched round specimens with 4 mm notch radius, good agreement can be obtained when f_0 is between 0.001-0.0012 for l_c=0.1 mm, see Fig. 4.13(a). Good agreement can also be achieved when f_0 is between 0.0008-0.001 for l_c=0.07 mm and when f_0 is between 0.0008-0.001 for l_c=0.05 mm, separately, see Figs. 4.13(b)-(c). The comparisons between the experimental and numerical force vs. elongation curves of the notched round specimens extracted from the BM are shown in Fig. 4.14(a)-(c). It is confirmed that the best agreement can be obtained when f is around 0.001 with l_c=0.1 mm, l_c=0.07 mm and l_c=0.05 mm, separately. These comparisons show that f_0=0.001 is a good numerical value for all the calibrations. This numerical f_0-value is very close to the experimental value (f_0=0.0009), showing that if the numerical calibration of the Rousselier

parameter is not available the correct f_0 -value can be inversely obtained from the experimental investigations.

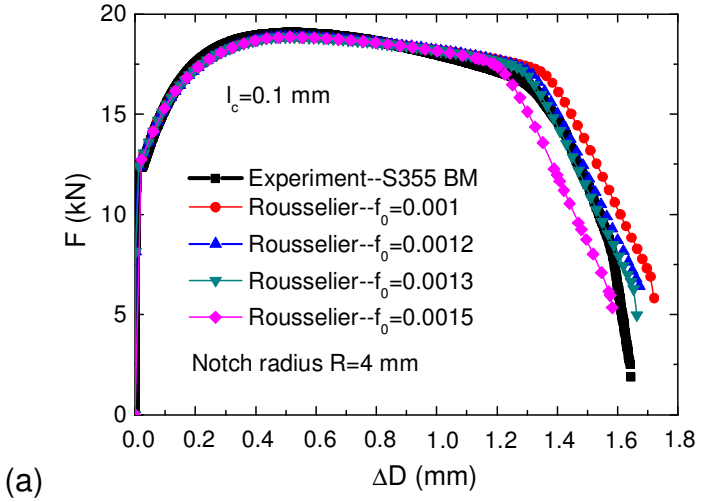

(a)

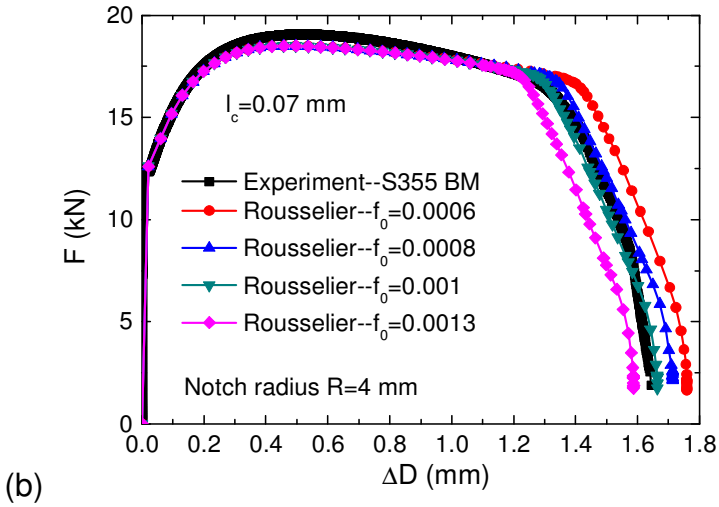

(b)

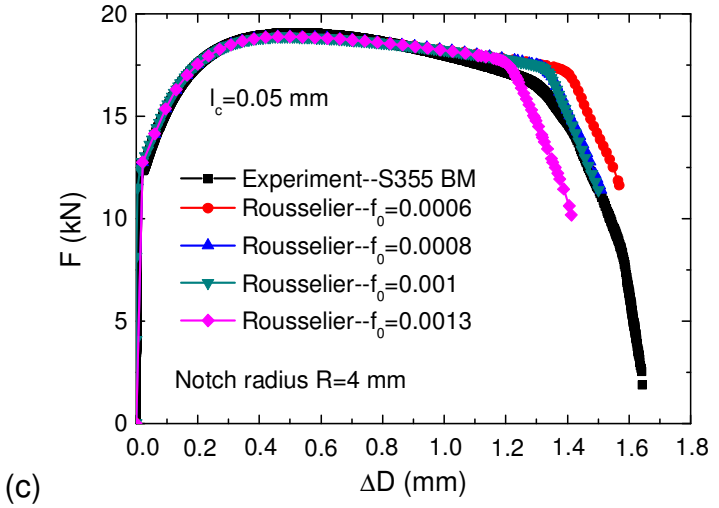

(c)

Fig. 4.13: Comparison of experimental and numerical force vs. cross section reduction curves when (a) l_c=0.1 mm, (b) l_c=0.07 mm, and (c) l_c=0.05 mm for notched round specimens extracted from the BM.

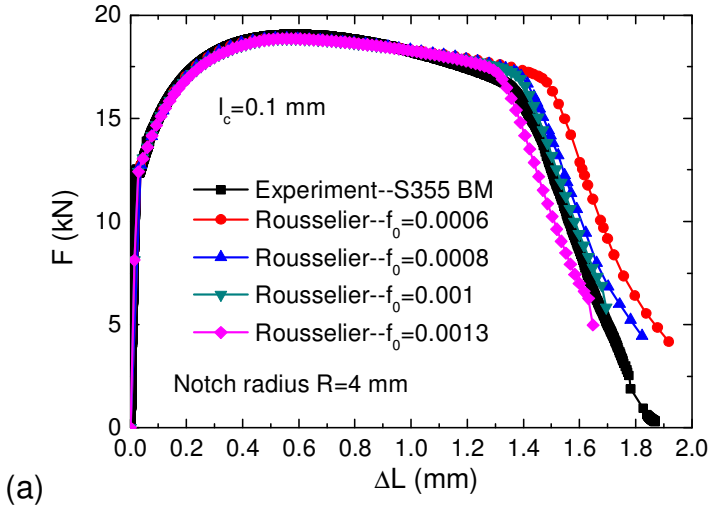

(a)

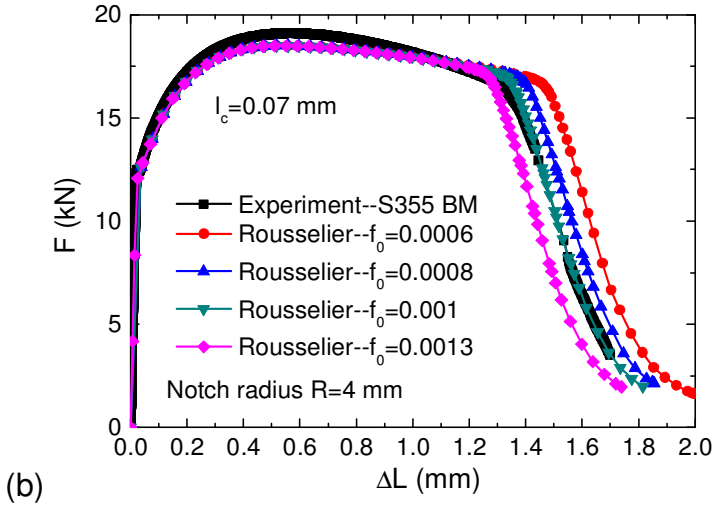

(b)

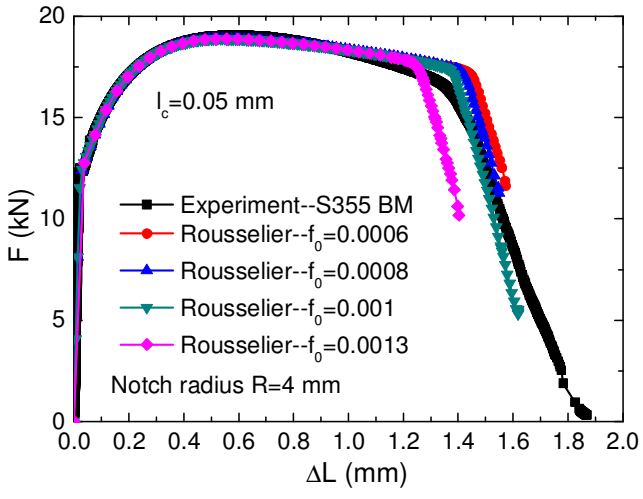

(c)

Fig. 4.14: Comparison of experimental and numerical force vs. elongation curves when (a) l_c=0.1 mm, (b) l_c=0.07 mm, and (c) l_c=0.05 mm for notched round specimens extracted from the BM.

Different l_c-values with the variation of the f_0-values around f_0=0.001 are used to predict the crack propagation in C(T)-specimens with the initial crack located in the BM. For the C(T)-

specimens extracted from the BM, because the structure shows symmetry with respect to the crack plane, only half of the C(T)-specimen is modeled, loading is defined on the loading point by external displacements, the finite element mesh and boundary conditions are shown in Fig. 4.15. Fig. 4.16 shows the detailed mesh around the initial crack tip. The element size around the initial crack tip is defined by the l_c-value. Fig. 4.17 shows how the predicted F-COD-curves of C(T)-specimens varied with different f_0-values when choosing l_c=0.1 mm, l_c=0.07 mm and l_c=0.05 mm, separately. For all the simulation results in Fig. 4.17(a), the Rousselier model predicts too high forces at the crack initiation stage, showing that the l_c-value obtained from experiments is too high for the numerical simulation. When l_c=0.07 mm is chosen for the calculation, the predicted forces of the F-COD-curves at crack initiation and the F-COD-curves after crack initiation are still higher than the experimental one, showing that l_c=0.07 mm is still not appropriate. When l_c=0.05 mm was chosen for the calculation, the Rousselier model can provide good predictions when f_0 is varied, as shown in Fig. 4.17(c). The comparison between the experimental and numerical fracture resistance curves when changing the f_0-values for l_c=0.1 mm, l_c=0.07 mm and l_c=0.05 mm can be found in Fig. 4.18(a)-(c). It seems that when l_c=0.1 mm and l_c=0.07 mm, the Rousselier model predicts a too high J_i-value at crack initiation and a higher J_R-curve after the first crack compared to the experimental value which is due to higher predicted F-COD-curves as shown in Figs. 4.18(a)-(b). A good match of the numerical J-value when the first element is damaged can be obtained when l_c=0.05 mm is chosen for the calculation as shown in Fig. 4.18(c).

The best fitted F-COD- and J_R-curves for C(T)-specimens obtained from the BM compared to the experiment can be found in Fig. 4.19. In Fig. 4.19(a), the calculated elastic plastic material behaviour provides good agreement to the experiment until the crack initiates. However, as no damage is considered during the deformation, the elastic plastic behaviour overestimates the force after the crack appears. The Rousselier model can reliably predict F-COD-curves of C(T)-specimens with the initial crack located in the BM when l_c=0.05 mm and f_0=0.001. It seems that the experimental l_c-value (l_c=0.1 mm) is not a good one for the Rousselier model to predict the crack propagation of C(T)-BM. Thus, a smaller finite element mesh (l_c=0.05 mm) is chosen for the Rousselier model. The reason is because in reality, the crack prefers to propagate from one particle to the nearest neighboring particle in particle-localized regions where the distance between these particles is smaller than the average particle distance.

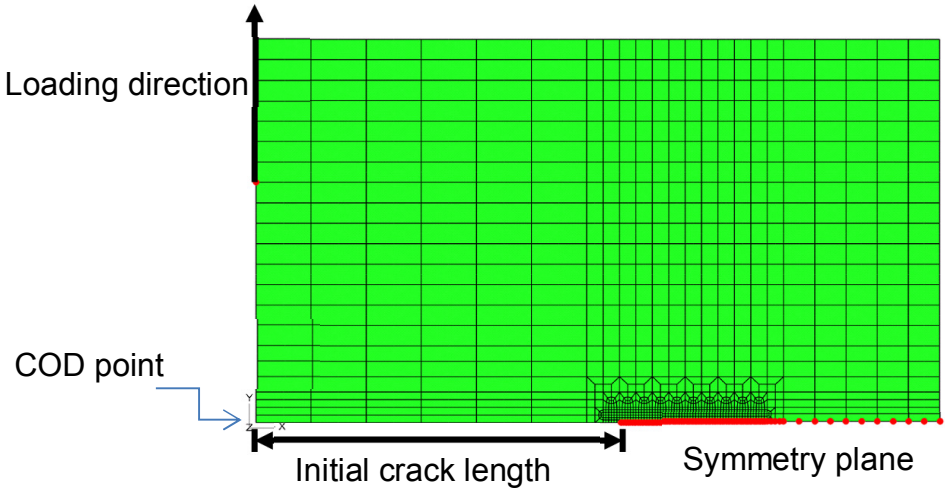

Fig. 4.15: Finite element mesh and boundary conditions of the C(T)-specimen.

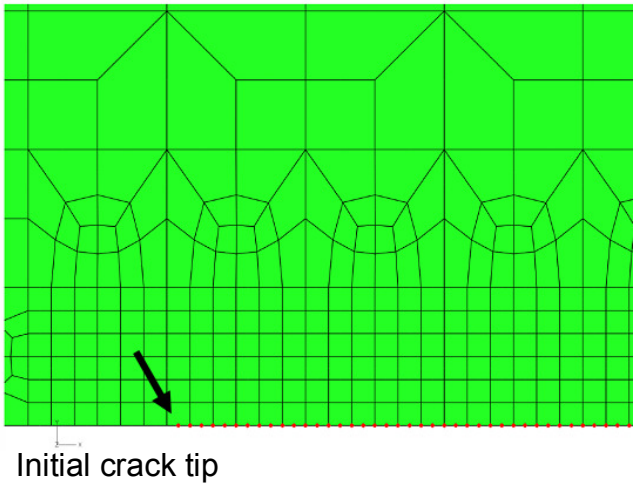

Fig. 4.16: Detailed 2D finite element mesh around the initial crack tip position.

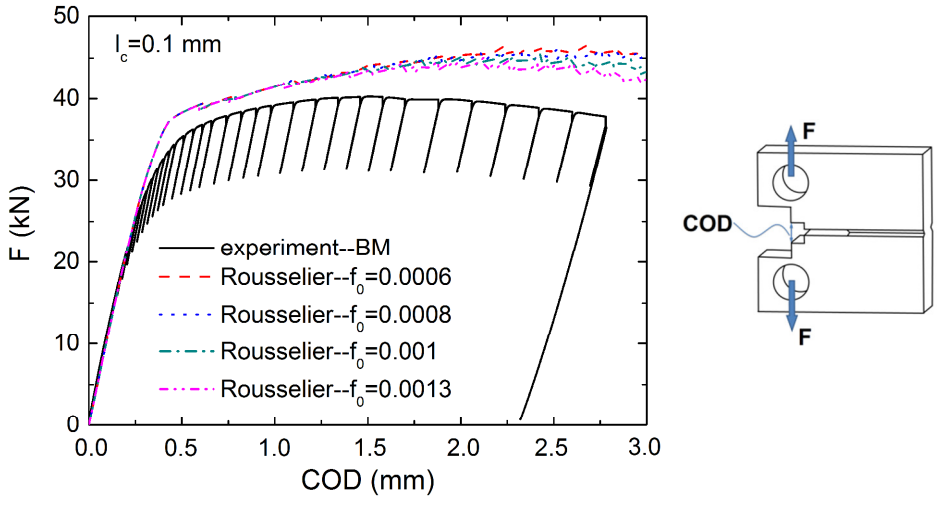

(a)

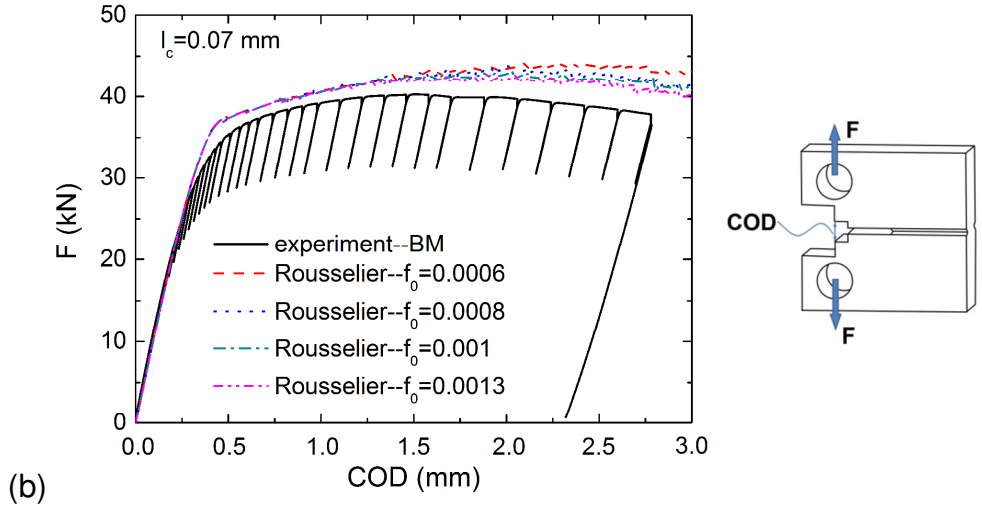

(b)

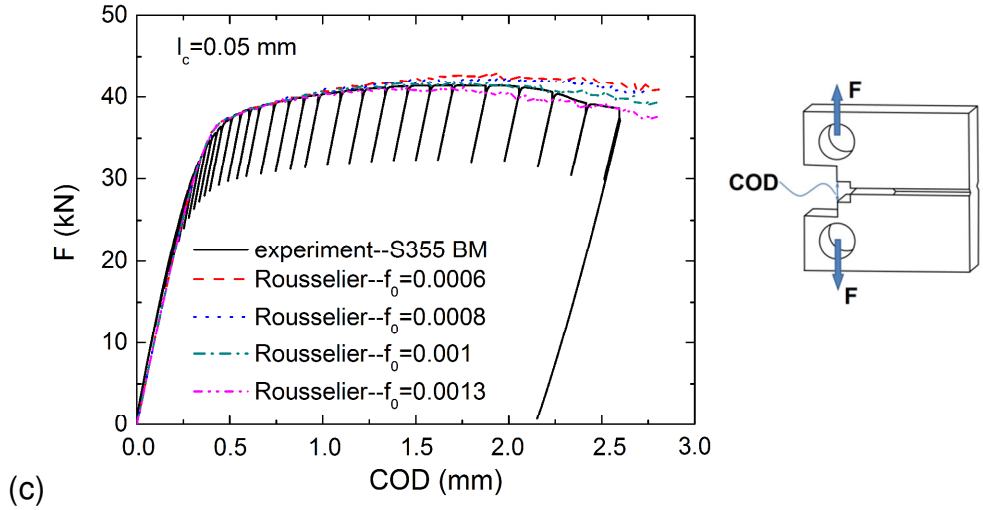

(c)

Fig. 4.17: Comparison of experimental and numerical force vs. Crack Opening Displacement (COD) curves when (a) l_c=0.1 mm, (b) l_c=0.07 mm, and (c) l_c=0.05 mm.

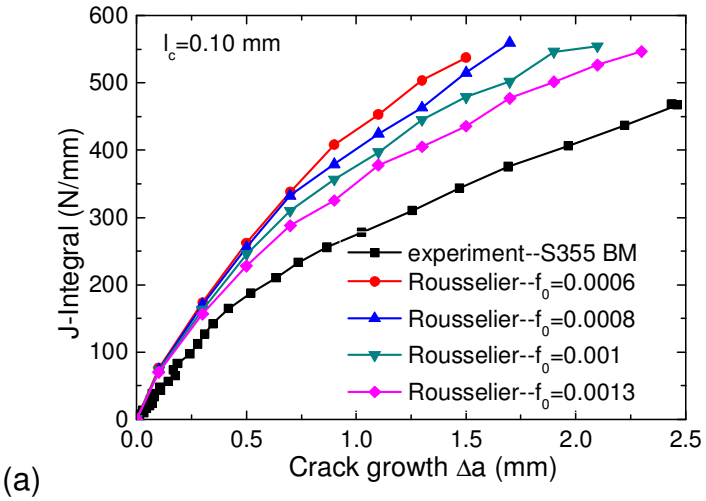

(a)

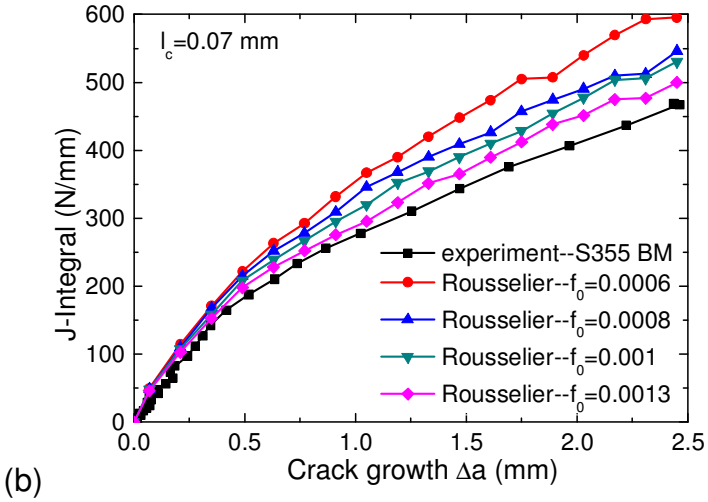

(b)

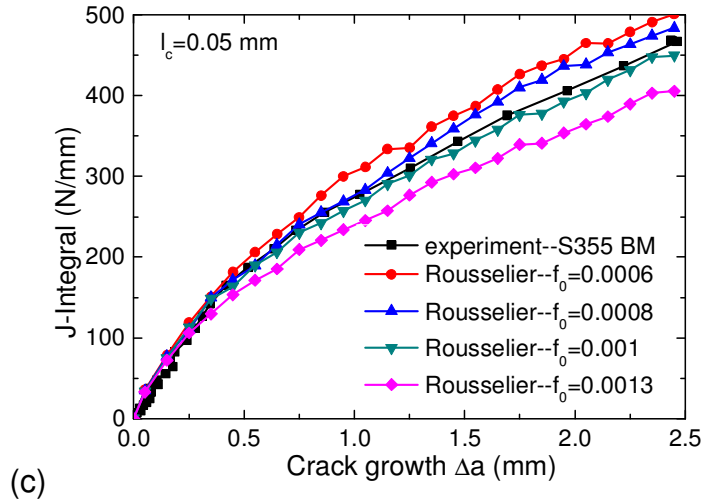

(c)

Fig. 4.18: Comparison of experimental and numerical crack resistance J_R-curves when (a) l_c=0.1 mm, (b) l_c=0.07 mm, and (c) l_c=0.05 mm.

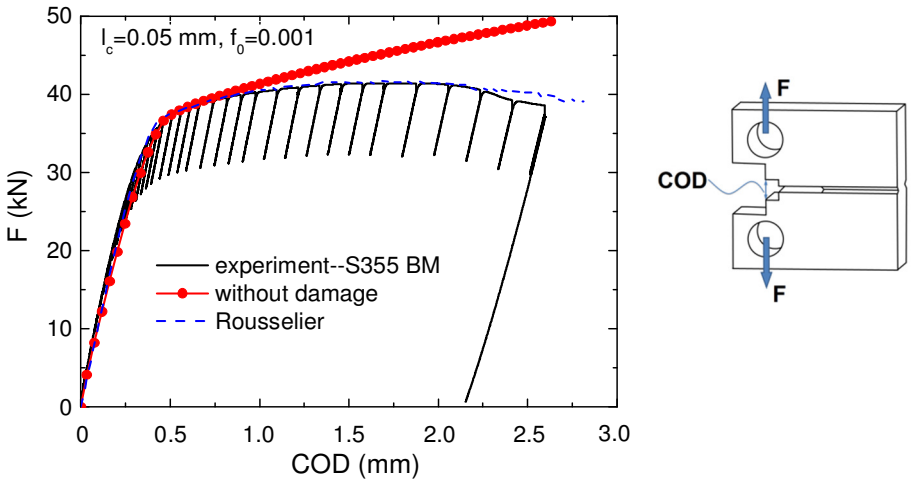

(a)

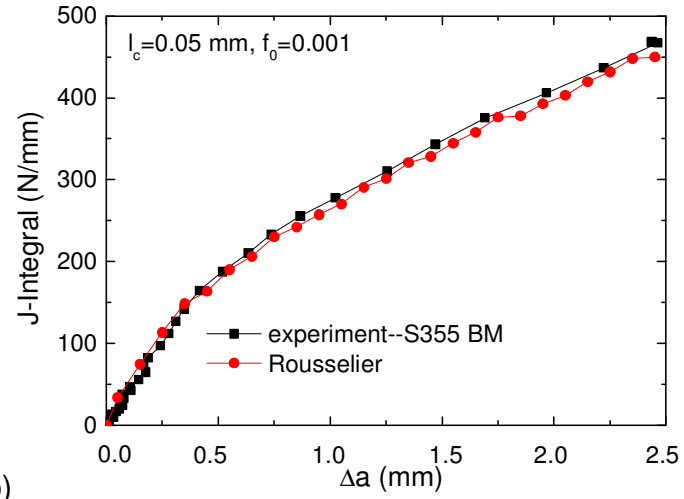

(b)

Fig. 4.19: Comparison of experimental and numerical (a) force vs. Crack Opening Displacement (COD) curves and (b) fracture resistance curves for C(T)-specimen with the initial crack located in the BM (l_c=0.05 mm).

During the calculation of the Rousselier model, when one Rousselier element is considered as damaged, the symmetry boundary condition of this element is released for later calculation steps, as shown in Fig. 4.20. The von Mises equivalent stress distribution of the C(T)-specimen at the end of the calculation is given in Fig. 4.20. The stress concentration area is mostly observed in the layer of Rousselier elements which is ahead of the current crack tip. The virtual crack propagation at the end of the calculation is depicted in Fig. 4.21. The failure indicator of the Rousselier model UMAT in ABAQUS (SDV3) indicates the failure of the element when the current volume fraction $f \geq f_c$=0.05. When the failure indicator SDV3=1, this means the element is damaged. For 8-noded quadratic elements with reduced integration points (CPE8R), when the current f-value in two Gauss points of the Rousselier element reaches the f_c-value, the elements are assumed losing their stress carrying ability completely.

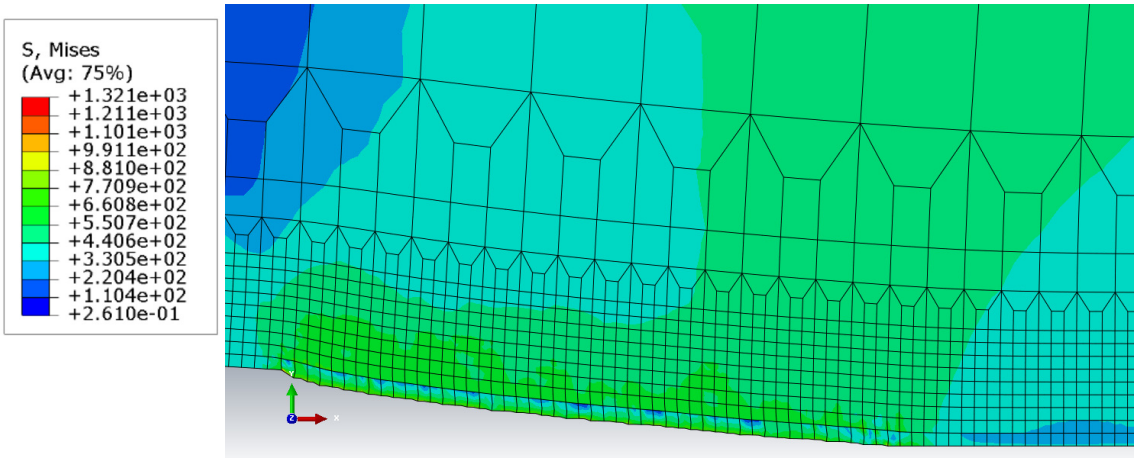

Fig. 4.20: The Von Mises equivalent stress distribution at the end of calculation time (COD=2.81 mm in F-COD-curve, Δa =2.45 mm in J_R-curve).

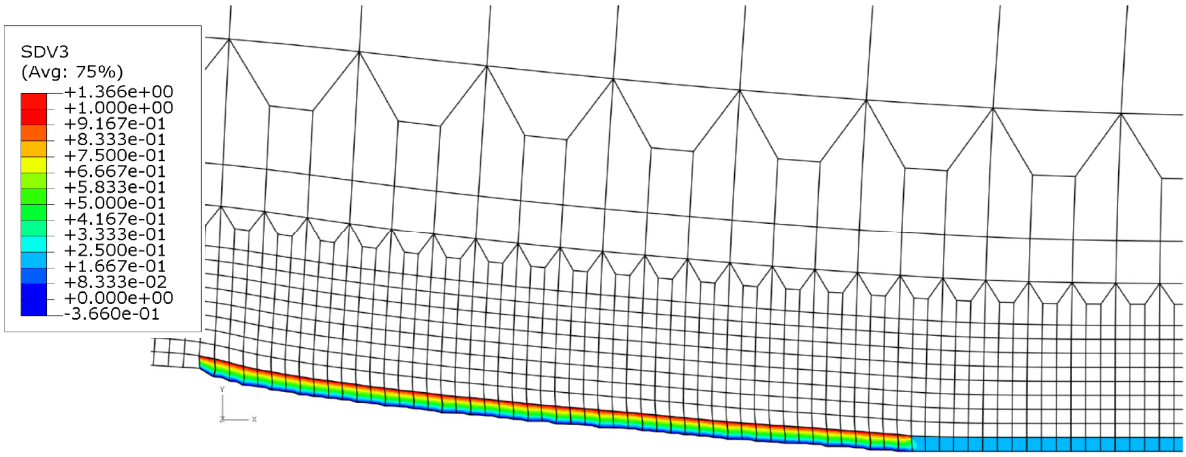

Fig. 4.21: Crack propagation for a C(T)-BM specimen at the end of the calculation (SDV3 is the user defined failure indicator of Rousselier model in ABAQUS, when f ≥ f_c, SDV3=1).

4.3 Crack propagation in an inhomogeneous region

In this section, the Rousselier model is used to study the crack propagation in inhomogeneous welded joints. The Rousselier parameters are calibrated on the notched round specimen extracted from the HAZ firstly. Then the same Rousselier parameter set is adopted to investigate the fracture behavior of C(T)-HAZ. As the experimental l_c-value for the HAZ (l_c=0.12 mm) is higher than that of the BM (l_c=0.1 mm), a higher numerical l_c-value is used in the calculation. A notched round specimen with 4 mm notch radius is used for the calibration of Rousselier parameters and the same model as shown in Fig. 4.1 is used. For the notched round specimen, the experimental F-ΔD-curve is compared with the numerical calculations when f_0 is between 0.0014-0.0016 when l_c=0.1 mm, as shown in Fig. 4.22.

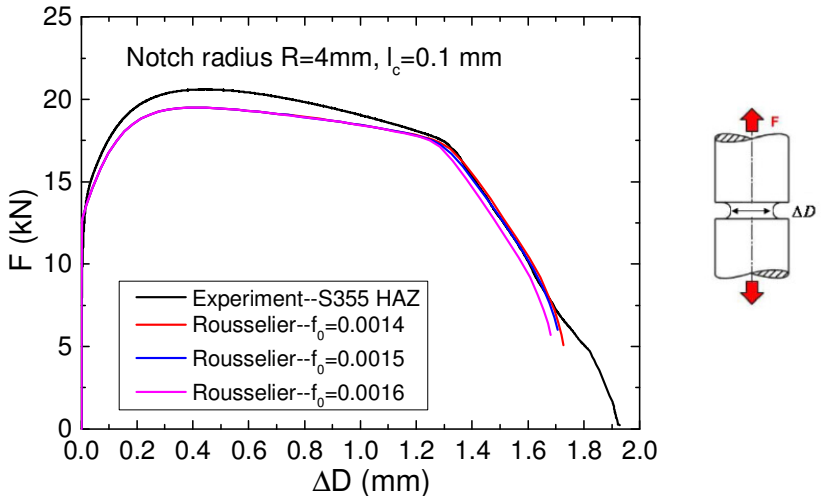

Fig. 4.22: Comparison of experimental and numerical force vs. cross section reduction (F-ΔD) curves for notched round specimens extracted from the HAZ.

Good matches can be obtained when f_0=0.0014-0.0015. The same l_c-value is adopted to investigate the crack propagation of C(T)-HAZ. For the C(T)-HAZ, the elastic plastic material behaviour of the welded joints predict good F-COD-curve in comparison to the experiments until the crack initiates. As the high degree of plane-strain constraint achieved in the side groove specimen is obvious [Larsen et al., 1993], a straight crack front was observed in the C(T)-HAZ where the crack only propagates in the HAZ. In the finite element simulations, the mechanical properties of the FZ and the BM are defined as non-damaging elastic plastic. The HAZ is divided into three tiny layer regions which can reflect different material behaviour, as shown in Fig. 4.23. The stress-strain curves for the HAZ (HAZ1, 2, 3) are obtained from flat specimens extracted from different regions of the HAZ. The true stress vs. plastic strain curves of HAZ1-HAZ3 (Specimen HAZ1 is obtained from the position of 2.5 mm from the center of the FZ, Specimen HAZ2 is 3.5 mm from the center of the FZ, HAZ3 is 4.5 mm from the center of the FZ) used in the Rousselier model are shown in Fig. 4.24. Good agreement can be found between the numerical and the experimental F-COD-curves and crack resistance J_R-curves when the l_c-value is 0.1 mm and f_0 equals to 0.0015 (close to the experimental value f_0=0.0016), as shown in Fig. 4.25. This shows that the Rousselier model can predict the crack propagation of inhomogeneous materials well. After calculation, the von Mises equivalent stress distribution of the C(T)-HAZ specimen is derived and can be found in Fig. 4.26.

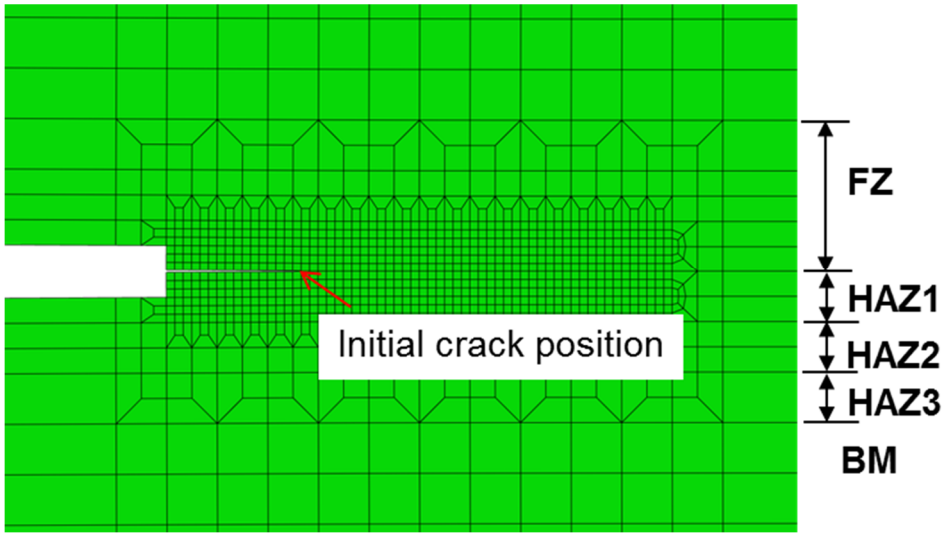

Fig. 4.23: Detailed finite element mesh used for the C(T)-specimens with the initial crack located in the HAZ which is situated at the interface between the FZ and the HAZ.

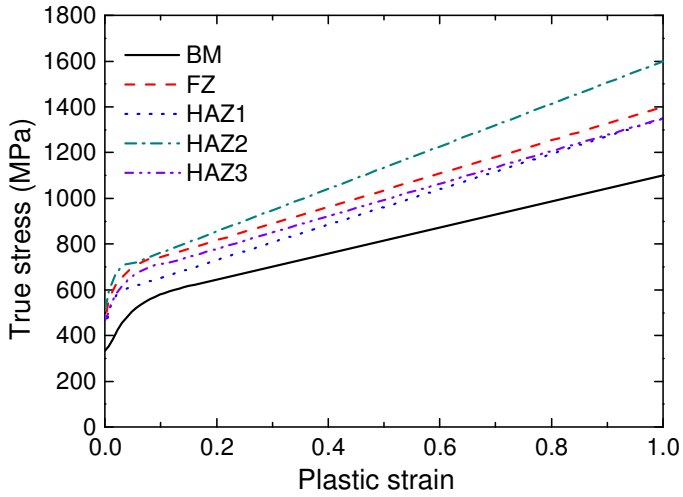

Fig. 4.24: True stress vs. plastic strain for different weld regions.

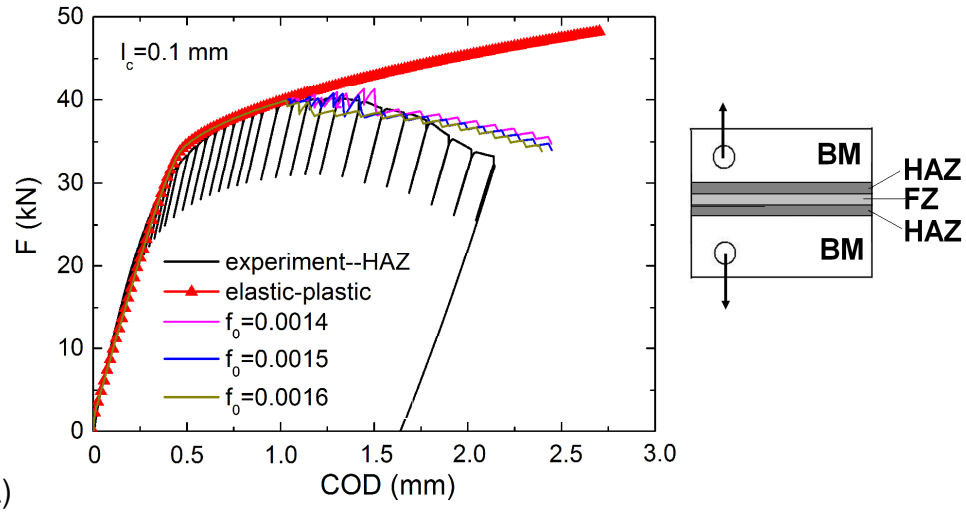

(a)

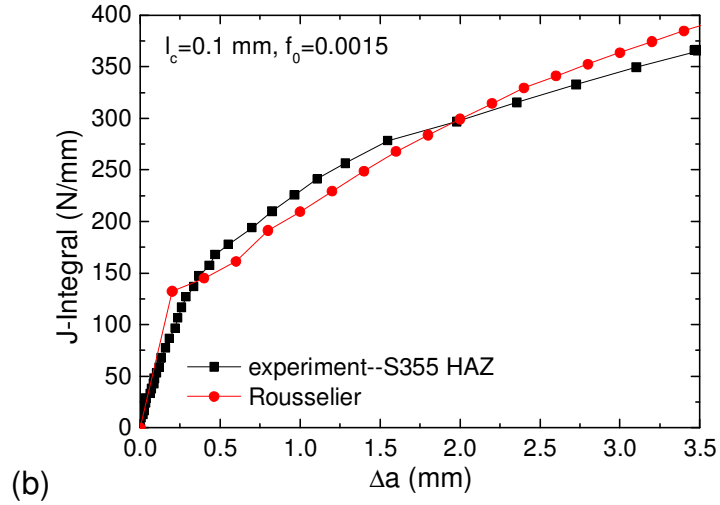

(b)

Fig. 4.25: Comparison of the experimental and numerical (a) Force vs. Crack Opening Displacement (COD) curves and (b) fracture resistance curves for C(T)-HAZ specimens (l_c=0.1 mm).

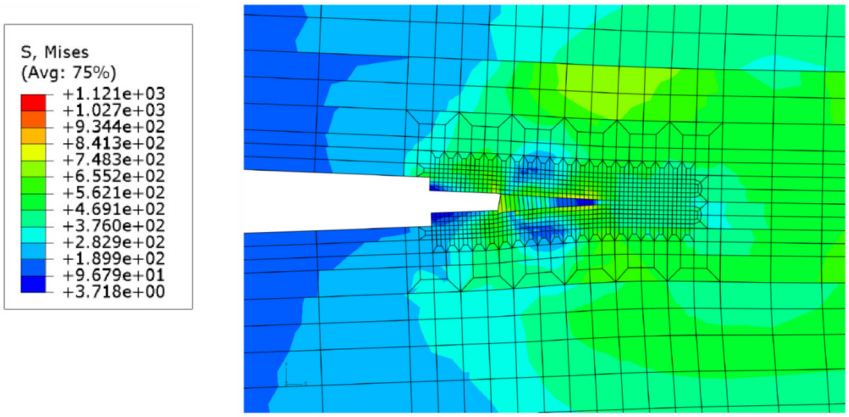

Fig. 4.26: The von Misses equivalent stress distribution in ABAQUS which was obtained from the Rousselier model calculation (COD=2.45 mm in F-COD-curve, Δa =3.6 mm in J_R-curve).

The stress carrying ability of one element decreases dramatically when it is considered as 'damaged'. The damaged elements are marked in red color and the virtual crack propagation in the C(T)-specimen can be seen in Fig. 4.27. In order to avoid convergence problem emerged during the application of the Rousselier model on C(T)-HAZ situation, linear elements with full integration points (CPE4) are adopted. When the current f-value in all four Gauss points of the element reaches the critical void volume fraction (f_c=0.05), the elements are assumed losing their stress carrying ability completely. It is assumed that the crack growth in the HAZ is slower than that of the BM because of the influence of the microstructure of the HAZ (HAZ is a transitional regions comprise of Pearlite, Ferrite and

Martensite). A longer calculation time is needed to damage all four Gauss points of the Rousselier element than to damage two Gauss points of the Rousselier element defined in the BM. All Rousselier parameters used for different structures are summarized in table 4.2. For notched round specimens extracted from the BM, three different l_c-values (l_c=0.05 mm, l_c=0.07 mm, l_c=0.1 mm with variation of f_0 between 0.0006-0.0013) are used for the calibration of the Rousselier parameters. The same Rousselier parameter set as obtained from the notched round specimens is adopted to investigate the fracture behavior of the C(T)-BM. The Rousselier parameters for the HAZ are also calibrated on the notched specimens extracted from the HAZ. Good agreement can be obtained when l_c=0.1 mm, f_0=0.0015 are adopted for the C(T)-HAZ.

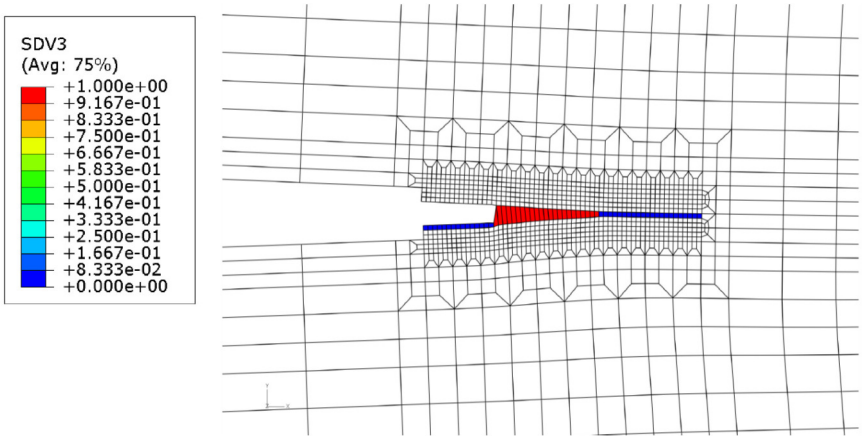

Fig. 4.27: Crack propagation in the C(T)-HAZ obtained from the Rousselier model (SDV3 is the user defined failure indicator of the Rousselier model in ABAQUS, when f ≥ f_c, SDV3=1).

Table 4.2: The Rousselier parameters of different calculations and structures.

Specimen shape	Calculation type	Average particle distance	f_c	σ_k	D	Initial void volume fraction (f_0)	Best void volume fraction
Notched round specimen (BM), R=4 mm	Axisymmetric	l_c=0.05	0.05	445	2	0.0006, 0.0008, 0.001, 0.0013	0.001
Notched round specimen (BM), R=4 mm	Axisymmetric	l_c=0.07	0.05	445	2	0.0006, 0.0008, 0.001, 0.0013	0.001
Notched round specimen (BM), R=4 mm	Axisymmetric	l_c=0.10	0.05	445	2	0.001-0.0013, 0.0015	0.001
C(T)-BM	2D/plane strain	l_c=0.05	0.05	445	2	0.0006, 0.0008, 0.001, 0.0013	0.001
C(T)-BM	2D/plane strain	l_c=0.07	0.05	445	2	0.0006, 0.0008, 0.001, 0.0013	0.001
C(T)-BM	2D/plane strain	l_c=0.10	0.05	445	2	0.0006, 0.0008, 0.001, 0.0012	/
Notched round specimen (HAZ); R=4 mm	Axisymmetric	l_c=0.10	0.05	445	2	0.0014- 0.0016	0.0015
C(T)-HAZ	2D/plane strain	l_c=0.10	0.05	445	2	0.0014-0.0016	0.0015

4.4 Discussion and Conclusions

Crack propagation was studied for S355 electron beam welded joints using the Rousselier model. C(T)-specimens with the initial crack located at different positions were investigated. In order to define the influence of the Rousselier parameters, a parameter study was performed on notched round specimens and on C(T)-specimens. As what can be found in Fig. 4.2, for a notched round specimen, a lower initial void volume fraction f_0-value leads to a later drop point of the F-ΔD-curve while the slope of the curves after the final fracture point is not affected by the f_0-value. For C(T)-specimens, a lower f_0-value results in higher forces of the F-COD-curve which can be found in Fig. 4.3. In Fig. 4.4, f_0-value results in a significant influence of the slope of the fracture resistance J_R-curves. Lower f_0-values result in a steeper J_R-curve because crack coalescence can be reached later with lower f_0-values, which means more energy is required for crack propagation. As found in Fig. 4.6, a higher Rousselier parameter σ_k lets to a later breakpoint of rapid decrease of the force. Higher σ_k-values result in higher forces of the F-COD-curve and a higher J-value, which is shown in Fig. 4.7. The l_c-value is typically chosen as the average distance between particles. A higher l_c-value results in a flatter slope after the fracture stage of the notched round specimens, which is shown in Fig. 4.8. As presented in Fig. 4.9 and Fig. 4.10, a higher l_c-value results in higher F-COD-curves and lead to a steeper J_R-curve, this is because a higher l_c-value stands for a larger element size, requiring more energy for damage. Knowing how different Rousselier parameters influencing the calculation results (F-ΔD-curve for notched round specimen and F-COD-curve for the C(T)-specimen) is beneficial to find the right parameter set in the later calculation work.

As observed in Fig. 3.1, the voids cluster in some regions. Before applying the experimental data as the Rousselier model input directly, numerical calibration was performed on notched round specimens in order to define the 'true' Rousselier parameters. As depicted in Fig. 4.13, when f_0=0.001, good agreement can be obtained when l_c=0.1 mm, l_c=0.07 mm and l_c=0.05 mm, separately. The calibrated f_0-value is very close to the experimental one (f_0=0.0009), showing the metallographic investigation on f_0 is reliable, but not for the l_c-value (l_c=0.1 mm for S355 BM). This is because of particles localizing at some regions, as shown in Fig. 3.1. The same f_0-values with different l_c-values were used to predict crack propagation for C(T)-specimens extracted from the BM, as shown in Fig. 4.17. Good agreement can be obtained in the form of the force vs. crack opening displacement and

fracture resistance J_R-curves, when l_c=0.05 mm and f_0=0.001. This confirms the Rousselier model can predict the crack propagation of the homogeneous base material well.

The Rousslier parameters for the HAZ are calibrated on notched round specimens from the HAZ. Because the optical microscopy picture obtained from the HAZ is higher than that of the BM, the value l_c=0.1 mm is applied for the calculation. Experimental F-ΔD-curves are compared with numerical ones when f_0 is between 0.0014-0.0016 for l_c=0.1 mm (Fig. 4.22). Good agreement is obtained when f_0=0.0015. The same Rousselier parameter set (l_c=0.1, f_0 =0.0015) is used to investigate the crack propagation of the C(T)-HAZ. Local mechanical properties obtained from flat specimens extracted from these regions were used as model input. The HAZ is a transition zone; there exists big scatter of the material behaviour within this region, see Fig. 3.13. For this reason, the HAZ is divided into three tiny regions which can reflect different material behaviour as shown in Fig. 4.23. Good agreement can also be achieved when l_c=0.1 mm and f_0=0.0015, which is very close to the experimental values (l_c=0.12 mm, f_0=0.0016). All in all, good simulation results for C(T)-specimens with the initial crack located in the BM and HAZ confirm that the Rousselier model can predict crack propagation of homogenous BM and inhomogeneous welded joints well.

5. The Gurson-Tvergaard-Needleman (GTN) model

In the following chapter, the GTN model is applied to study the crack propagation in S355 welded joints. As the FZ shows quasi-brittle behavior, the GTN model which is normally used describing the void initiation, growth and coalescence evolution in a ductile material is used to investigate the homogenous BM and the inhomogeneous welded joints only. In order to identify the influence of GTN parameters on the fracture behavior of test specimens, a parameter study is performed on notched round specimens and on C(T)-specimens (C(T)25 with 20% side groove). After the calibration of the GTN parameters on the notched round specimen, the same parameter set is used to predict the crack propagation in C(T)-specimens. Numerical simulation results are compared with the experimental ones in terms of F-COD- and J_R-curves.

5.1 Parameter study using the GTN model

From the explanations in chapter 2, it can be derived that there exist nine GTN parameters to be defined before the GTN damage model can be applied in the simulation. As discussed by Steglich [Steglich, 2004], the parameters (ε_n, f_n, s_n) are used to describe the void nucleation, the parameters (f_0, f_c, f_f) are used to describe the procedure of damage from void initiation to void coalescence until final failure and the parameters (q_1, q_2, q_3) are model parameters which were introduced by Tvergaard [Tvergaard, 1981; Tvergaard, 1982b] to improve the accuracy of predictions of the Gurson model. As described by Steglich, the initial void volume fraction f_0 interacts with the critical void volume fraction f_c which is the volume fraction when void coalescence happens and f_n which stands for the volume fraction of void nucleating particles. It is difficult to judge which parameter plays the major role with respect to the simulation results. Thus, the combined influence of these parameters is investigated in this chapter. Moreover, additional parameter studies have been undertaken and are described below. The q_1, q_2 and $q_3$values are chosen as 1.5, 1 and 2.25 (for most steels), respectively, which were suggested by Tvergaard [Tvergaard, 1981; Tvergaard, 1982b] and later discussed by Perrin for the case of perfect plasticity [Perrin et al., 1990]. According to the previous study on S355 laser welded steel joints [Nonn, 2008], the micromechanical modeling of weldments with the GTN model [Chhibber,

2011] and the previous investigation on S355 electron beam welded joints with the GTN model [Tu, 2012], the material parameter set shown in table 5.1 is used for the parameter study. The applied method is to change one parameter at one time while keeping the rest of the parameters constant during the simulation. In this section, the parameter study will show how the GTN parameters influence the simulation results. The influence of parameters on the fracture position and the final slope of the force vs. cross section reduction curves of notched round specimens and the F-COD and the slope of the J_R-curves of C(T)-specimens are discussed in the following.

Table 5.1: Parameters used in the parameter study with the GTN model

f_0	f_c	f_n	f_f	ε_n	s_n	q_1	q_2	q_3	l_c
0.0001	0.05	0.01	0.2	0.2	0.1	1.5	1	2.25	0.05 mm

5.1.1 Influence of f_0

The initial void volume fraction f_0 is taken as the initial volume fraction of main inclusions. As the void nucleation is considered in steel S355, void nucleation weakens the influence of void initiation, making the void initiation in the GTN model is not as important as that of the Rousselier model. Therefore, the f_0-value used in the GTN model is less than the f_0-value adopted in the Rousselier model. Smaller f_0-values than the values used in chapter 4.1.1 are used for the parameter study. As shown in Fig. 5.1, higher f_0-values result in an earlier drop point of the F-ΔD-curve of the notched round specimens while the slope of the curve after the final fracture point is not affected. This is because higher f_0 provide that the f-value reaches the f_c-values at earlier deformation stages. For the C(T)-specimen, a higher f_0 results in an earlier force decrease of the F-COD-curve which is shown in Fig. 5.2. In Fig. 5.3, the f_0-value does not influence the numerical J_i-value for the crack initiation significantly. This is because a similar energy is needed to drive the first crack under a different f_0-value (f_0 is tiny for most steels). However, a higher f_0-values results in a lower J_R-curve and a significant decrease of the slope of the fracture resistance J_R-curve. Higher f_0-values result in a more flat J_R-curve because crack coalescence can be reached earlier with higher f_0-values, which means less energy is required for crack propagation.

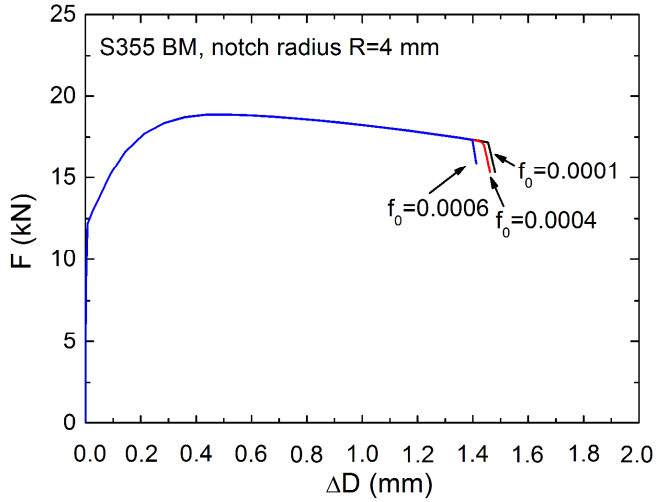

Fig. 5.1: Influence of f_0 on the F-ΔD-curve of notched round specimens extracted from S355 base material when f_c=0.05, f_n =0.01, f_f=0.2, ε_n=0.2 and l_c=0.05 mm.

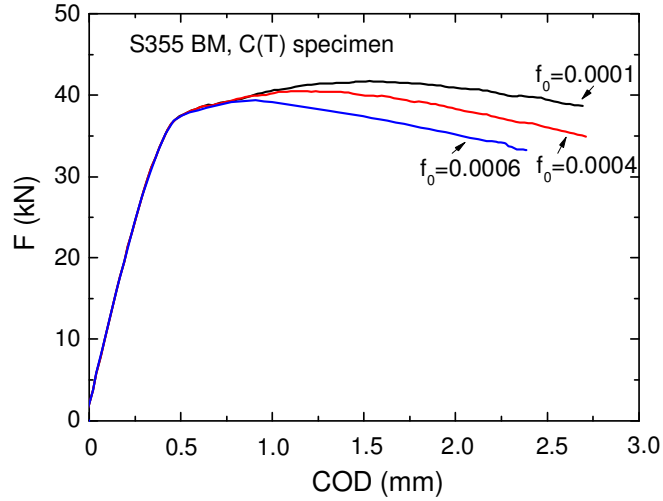

Fig. 5.2: Influence of f_0 on the F-COD-curve of a compact tension (C(T)) specimen extracted from S355 base material when f_c=0.05, f_n=0.01, f_f=0.2, ε_n=0.2 and l_c=0.05 mm.

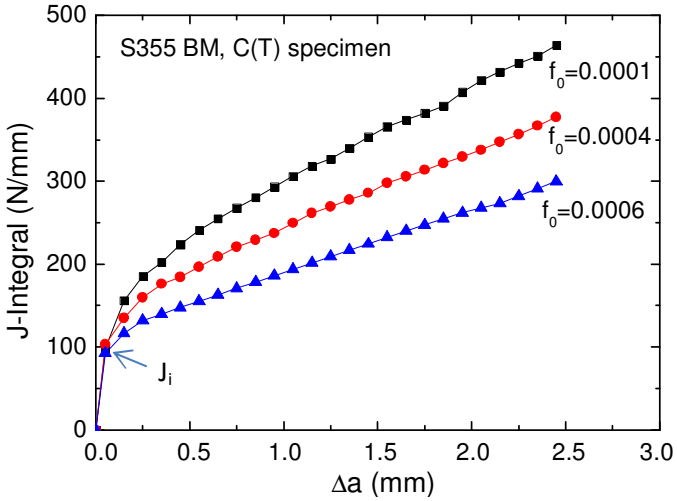

Fig. 5.3: Influence of f_0 on the J_R-curve of a compact tension (C(T)) specimen extracted from S355 base material when f_c=0.05, f_n=0.01, f_f=0.2, ε_n=0.2 and l_c=0.05 mm.

5.1.2 Influence of f_c

The f_c-value defined in the GTN model is the volume fraction when void coalescence occurs. The f_c adopted in the GTN model is different from the f_c-value defined in the Rousselier model (the f_c-value in the Rousselier model stands for the critical void volume fraction when the material loses its stress carrying ability completely). In literatures [Nègre et al., 2003, 2004; Springmann et al., 2005], f_c-values are found between 0.01-0.05. As can be seen in Fig. 5.4, the f_c-value influences the fracture position of the F-ΔD-curves of notched round specimens. Higher f_c-values let the final fracture happen later while the slopes of the curves after the final fracture point are not affected. This is because for notched round specimens, the material starts to lose its stress carrying ability later when void coalescence f_c increases. Higher f_c-values let to a higher force of the F-COD-curve and higher numerical J_i-value when first crack in the simulation happens together with steeper J_R-curves of the C(T)-specimen, as shown in Fig. 5.5 and Fig. 5.6, respectively. A higher f_c-value means the threshold for void coalescence is higher; higher force and more energy is required to drive every crack propagation, resulting in a higher force in the F-COD-curve and a higher J-value in the J_R-curves. That means the void is not as sensitive when higher f_c-value is chosen, as shown in Fig. 5.5. When the f_c-value varies between 0.02-0.04, convergence problems happen during calculation, resulting in shorter crack propagation, as shown in Fig. 5.6.

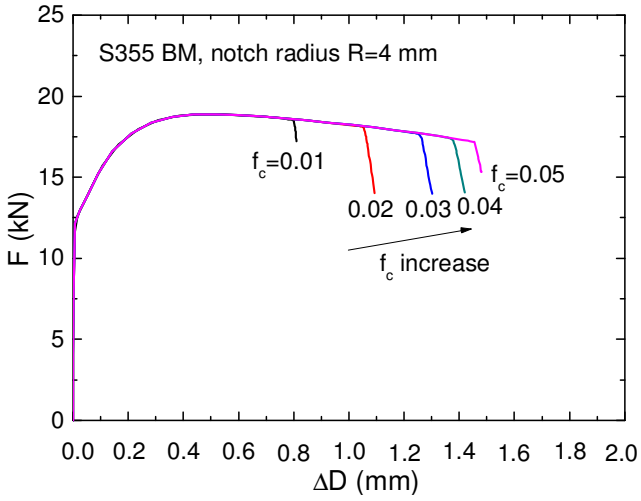

Fig. 5.4: Influence of f_c on the F-ΔD-curve of notched round specimens extracted from S355 base material when f_0=0.0001, f_n=0.01, f_f=0.2, ε_n=0.2 and l_c=0.05 mm.

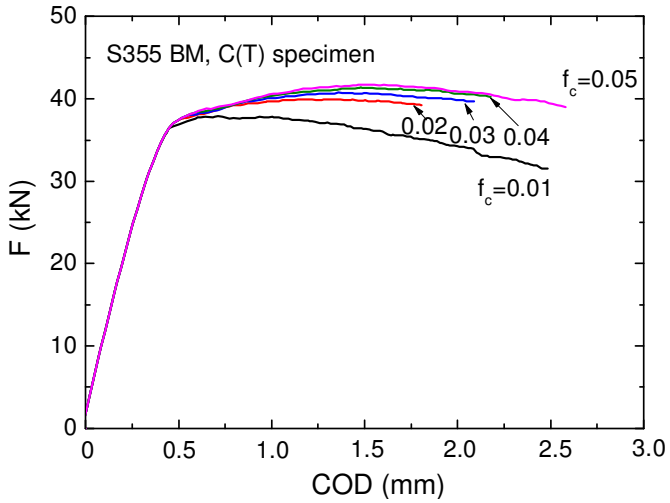

Fig. 5.5: Influence of f_c on the F-COD-curve of a compact tension (C(T)) specimen extracted from S355 base material when f_0=0.0001, f_n=0.01, f_f=0.2, ε_n=0.2 and l_c=0.05 mm.

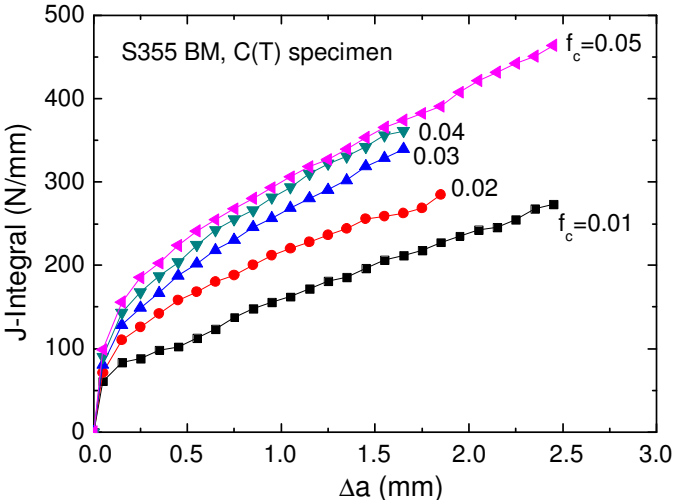

Fig. 5.6: Influence of f_c on the J_R-curve of a compact tension (C(T)) specimen extracted from S355 base material when f_0=0.0001, f_n=0.01, f_f=0.2, ε_n=0.2 and l_c=0.05 mm.

5.1.3 Influence of f_f

The final void volume fraction f_f is the volume fraction when the material loses its stress carrying ability completely. The f_f-value plays the same role as that of critical volume fraction (f_c) defined in the Rousselier model. In the GTN model, when the void coalescence value is reached, void growth will be accelerated until the void reaches the f_f-value. A lower f_f-value means the final fracture moment of the material happens earlier. As can be seen in Fig. 5.7, the f_f-value has almost no influence on the breakpoint of rapid decrease of force of the F-ΔD-curve obtained from notched round specimens. However, it influences the slope

of the curve after the drop point; a steeper slope can be obtained with a lower f_f-value. That means the time interval between the f_c and f_f is shorter when a lower f_f-value and a fixed f_c-value is adopted, resulting in a steeper slope for the F-ΔD-curve. The f_f-value does not influence the force of the F-COD-curve dramatically, which is presented in Fig. 5.8. Although a higher f_f-value leads to a higher numerical J_i-value when the first element is damaged, the J_R-curve after the first crack propagation is very similar; all J_R-curves are parallel, as shown in Fig. 5.9. This is because after crack coalescence, a higher f_f-value means more energy is needed to drive the final fracture, which results in a higher J-value.

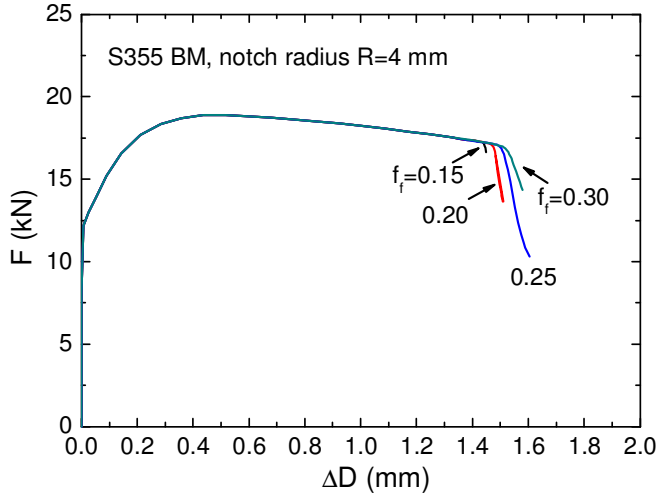

Fig. 5.7: Influence of f_f on the F-ΔD-curve of notched round specimens extracted from S355 base material when f_0=0.0001, f_c=0.05, f_n=0.01, ε_n=0.2 and l_c=0.05 mm.

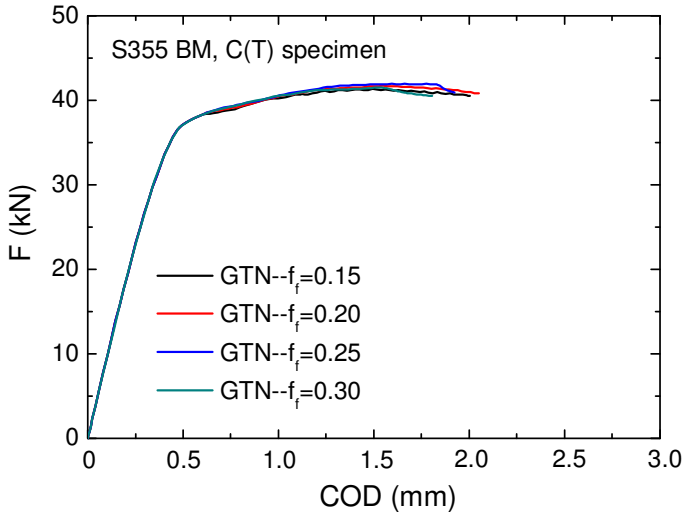

Fig. 5.8: Influence of f_f on the F-COD-curve of a compact tension (C(T)) specimen extracted from S355 base material when f_0=0.0001, f_c=0.05, f_n=0.01, ε_n=0.2 and l_c=0.05 mm.

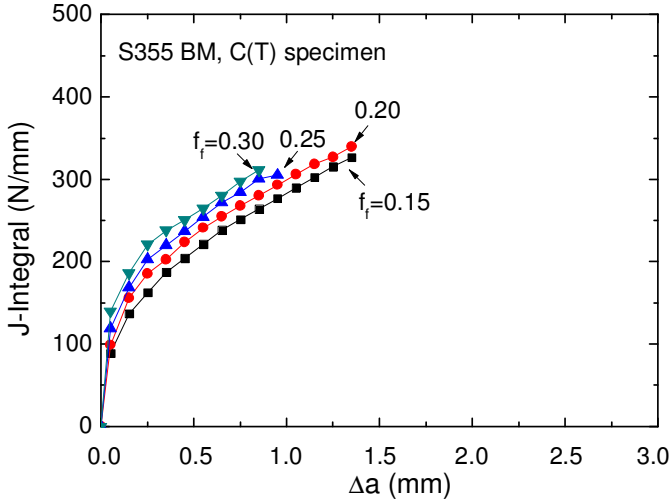

Fig. 5.9: Influence of f_f on the J_R-curve of a compact tension (C(T)) specimen extracted from S355 base material when f_0=0.0001, f_c=0.05, f_n=0.01, ε_n=0.2 and l_c=0.05 mm.

5.1.4 Influence of f_n

The f_n stands for the volume fraction when voids nucleate during the material deformation process. New voids nucleate from small particles or second phases at elevated strains ε_n. During the material deformation process, more new voids let the material fail earlier. As shown in Fig. 5.10, the f_n-value influences the sudden drop position of the F-ΔD- curve of notched round specimens. Higher f_n-values lead to earlier failure of the specimen while the slope of all the curves after the final fracture point is constant because with the appearance of new voids, the current void volume fraction can reach the f_c-value faster. The f_n-value does not influence the height of the F-COD-curve severely, as shown in Fig. 5.11. This is because the effect of f_n on the F-COD-curve is interrelated with the effect of ε_n. For the J_R-curve, the f_n-value has almost no influence on the numerical J_i-value when the first element is damaged, all the J_R-curves increase almost linearly after the first crack propagation, higher f_n-values let to slightly lower J-values, which can be seen in Fig. 5.12. Numerical calculations stop earlier when ε_n is between 0.012-0.014, less crack propagations were observed because of earlier convergence happened in the simulation in comparison to the situation of f_n=0.01.

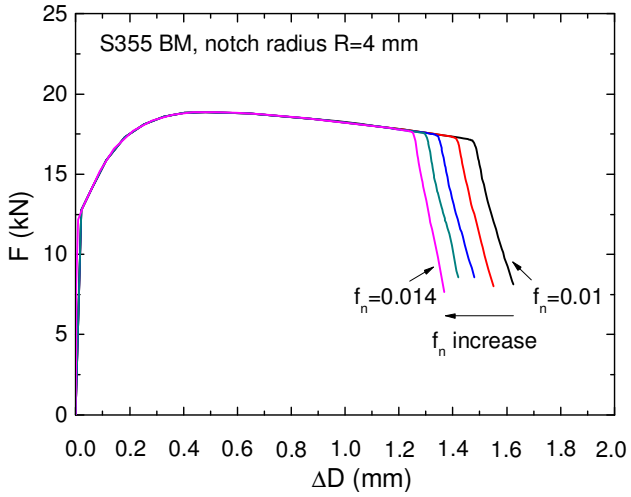

Fig. 5.10: Influence of f_n on the F-ΔD-curve of notched round specimens extracted from S355 base material when f_0=0.0001, f_c =0.05, f_f=0.2, ε_n=0.2 and l_c=0.05 mm.

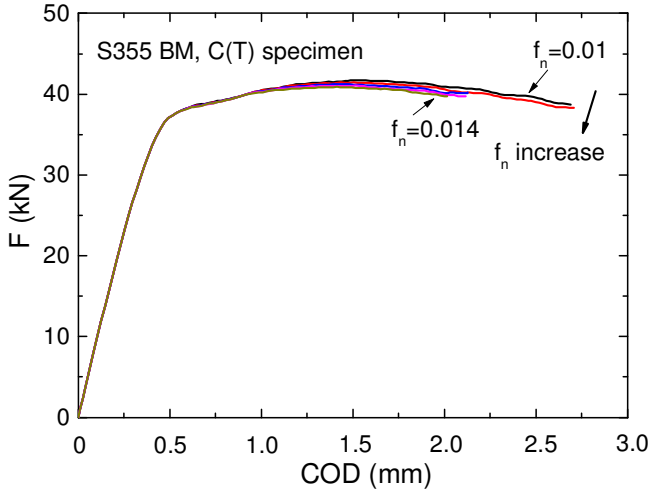

Fig. 5.11: Influence of f_n on the F-COD-curve of a compact tension (C(T)) specimen extracted from S355 base material when f_0=0.0001, f_c=0.05, f_f=0.2, ε_n=0.2 and l_c=0.05 mm.

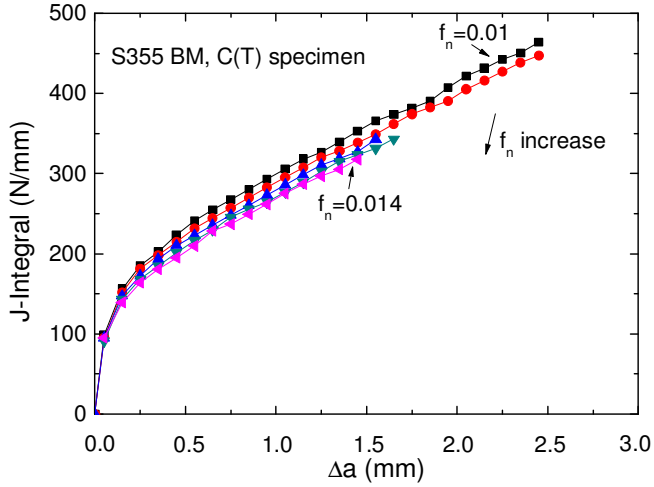

Fig. 5.12: Influence of f_n on the J_R-curve of a compact tension (C(T)) specimen extracted from S355 base material when f_0=0.0001, f_c=0.05, f_f=0.2, ε_n=0.2 and l_c=0.05 mm.

5.1.5 Influence of ε_n

The ε_n-value is the mean strain when void nucleation happens. The influence of the ε_n-value is interrelated with the influence of f_n. For the notched round specimen, as can be seen in Fig. 5.13, higher ε_n-values result in a later fracture position of the F-ΔD-curves, while the slope of the curve after fracture is the same. As depicted in Fig. 5.14, the ε_n-value has a strong influence on the F-COD-curve, a higher ε_n results in a higher F-COD-curve. The influence of ε_n on the J_R-curves can be found in Fig. 5.15. Although the ε_n-value does not provide a large influence on the numerical J_i-value when the first crack appears, higher ε_n-values result in a higher fracture resistance J_R-curve. This is because higher ε_n means void nucleation arises at higher local strains, thus more energy is needed to drive the crack, resulting in higher force and less COD of the F-COD-curve and a steeper J_R-curve and less crack propagation for the C(T)-specimen. The value of ε_n has an opposite influence on the tensile specimen compared to the influence of f_n.

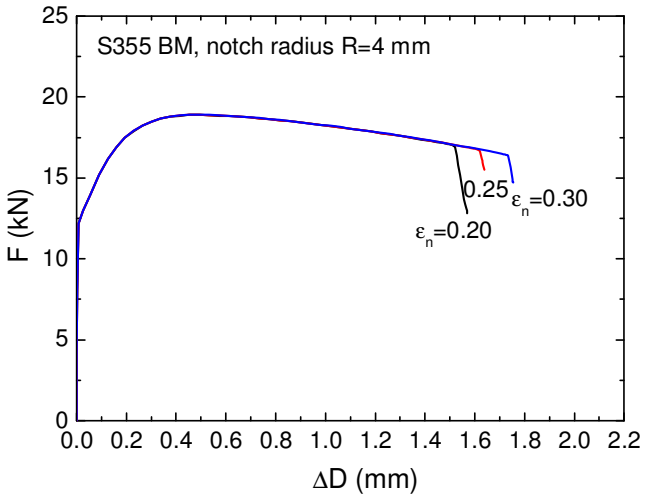

Fig. 5.13: Influence of ε_n on the F-ΔD-curve of notched round specimens extracted from S355 base material when f_0=0.0001, f_c=0.05, f_f=0.2, f_n=0.01 and l_c=0.05 mm.

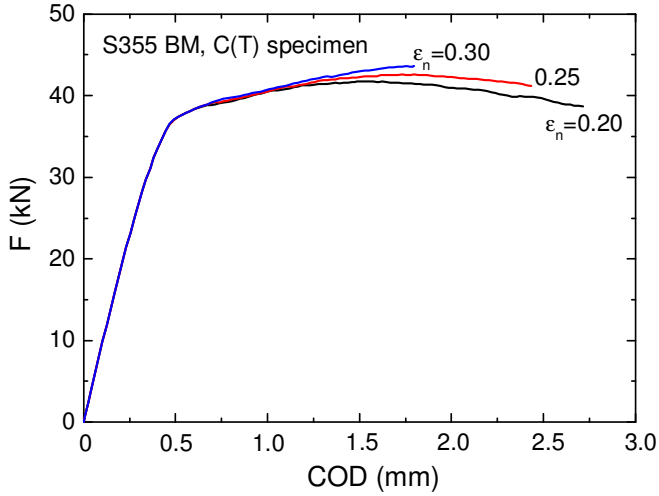

Fig. 5.14: Influence of ε_n on the F-COD-curve of a compact tension (C(T)) specimen extracted from S355 base material when f_0=0.0001, f_c=0.05, f_f=0.2, f_n=0.01 and l_c=0.05 mm.

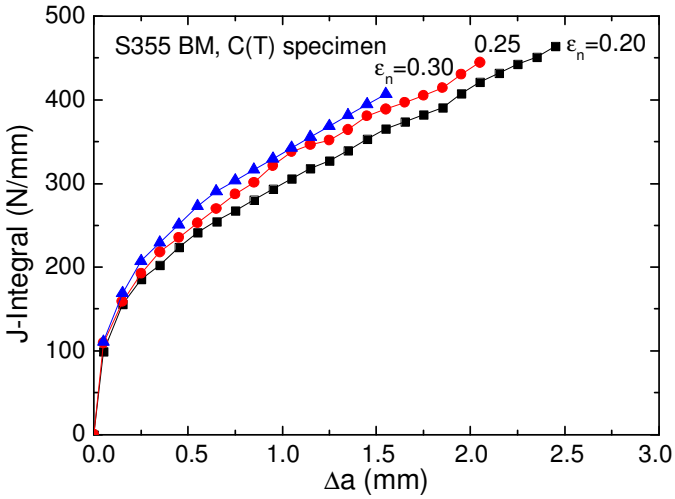

Fig. 5.15: Influence of ε_n on the J_R-curve of a compact tension (C(T)) specimen extracted from S355 base material when f_0=0.0001, f_c=0.05, f_f=0.2, f_n=0.01 and l_c=0.05 mm.

From the previous discussion, it is found that the parameters f_0, f_c, f_n, and ε_n influence the sudden drop positions of the F-ΔD-curve of notched round specimens, while the f_f-value influences the slope of the curve after fracture initiation. The influence of the GTN parameters on the Force vs. cross section reduction curve of notched round specimens can be found in Fig. 5.16(a)-(b). The influence of the GTN parameters on the C(T)-specimen are summarized in Fig. 5.17 and Fig. 5.18, separately. As can be seen in Fig. 5.17, f_0, f_c and ε_n have a strong impact on the F-COD-curve, while the f_f- and f_n-values have little influence on the F-COD-curves which is shown in Fig. 5.8 and Fig 5.11, respectively. As shown in Figs. 5.18(a)-(b), f_0 and f_c, have a strong impact on the J_R-curve, while the f_f, f_n and ε_n have a negligible influence on the J_R-curve after crack initiation, as presented in Figs.

5.18(c)-(d). The f_0-,f_n-, and ε_n-values do not influence the numerical J_i-value when the first crack initiates, as shown in Fig. 5.18(a) and Fig. 5.18(c). However, higher f_c or higher f_f lead to higher numerical J_i-values from the calculation, as shown in Fig. 5.18(b) and Fig. 5.18(d). This is because a higher f_c-value stands for a higher threshold for void coalescence and a higher f_f-value leads to an later final fracture moment of material happens, higher energy is required to drive the first crack. As discussed by Steglich [Steglich, 2004], for structure with thick thickness (e.g., standard C(T)-specimen), q_2 is set equal to 1. The commonly suggested values for q_1=1.5 and $q_3=q_1^2$ [Tvergaard, 1992] are adopted here. When the standard deviation s_n=0.1 is adopted [Tvergaard, 1981, 1982b, 1992; Steglich, 2004], so only five GTN parameters are needed in the following calculations. In the next chapter, the GTN model parameters are calibrated on the notched round specimens and the same parameters set is used to predict the crack propagation in C(T)-specimens extracted from different weld regions.

In comparison to the Rousselier model, the GTN model requires more model parameters (f_0, f_c, f_n) controlling the damage evolution of void initiation, growth and coalescence. The initial void volume fraction f_0 (volume fraction of inclusions) correlates with void nucleation (f_n) in the GTN model demonstrating the influence of the f_0 the GTN model is not as important as that of the Rousselier model. The f_0-value used in the GTN model (volume fraction of inclusions) is smaller than the f_0-value adopted in the Rousselier model (volume fraction of all inclusions). The f_c in the Rousselier model stands for the critical void volume fraction when the material loses its stress carrying ability (the same function as the f_f-value in the GTN model) where the f_c-value adopted in the GTN model is void fraction when void coalescence happens. In the numerical simulation, the crack propagates from integration point to integration point in the square element (2D) for both the GTN model and the Rousselier model. When both the Rousselier and the GTN model are adopted to investigate the fracture behavior of the same material, the numerical l_c-value is the same for both models.

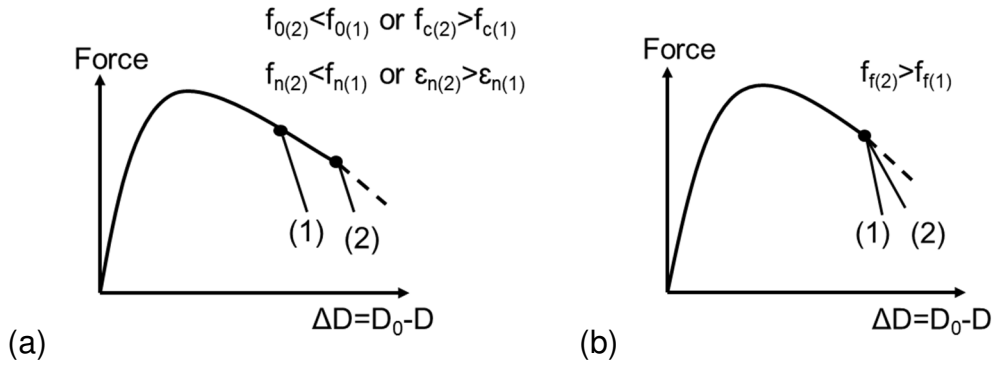

Fig. 5.16: Influence of GTN parameters f_0, f_c, f_n, f_f, ε_n on the Force vs. cross section reduction curves.

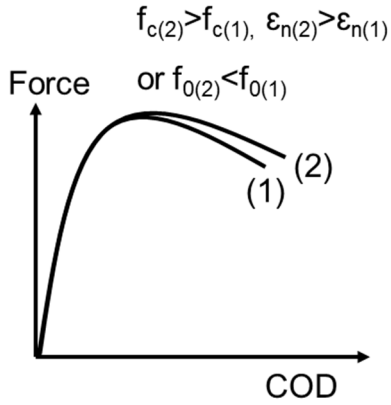

Fig. 5.17: Influence of parameters f_0, f_c, ε_n on the Force vs. Crack Opening Displacement (COD) curves.

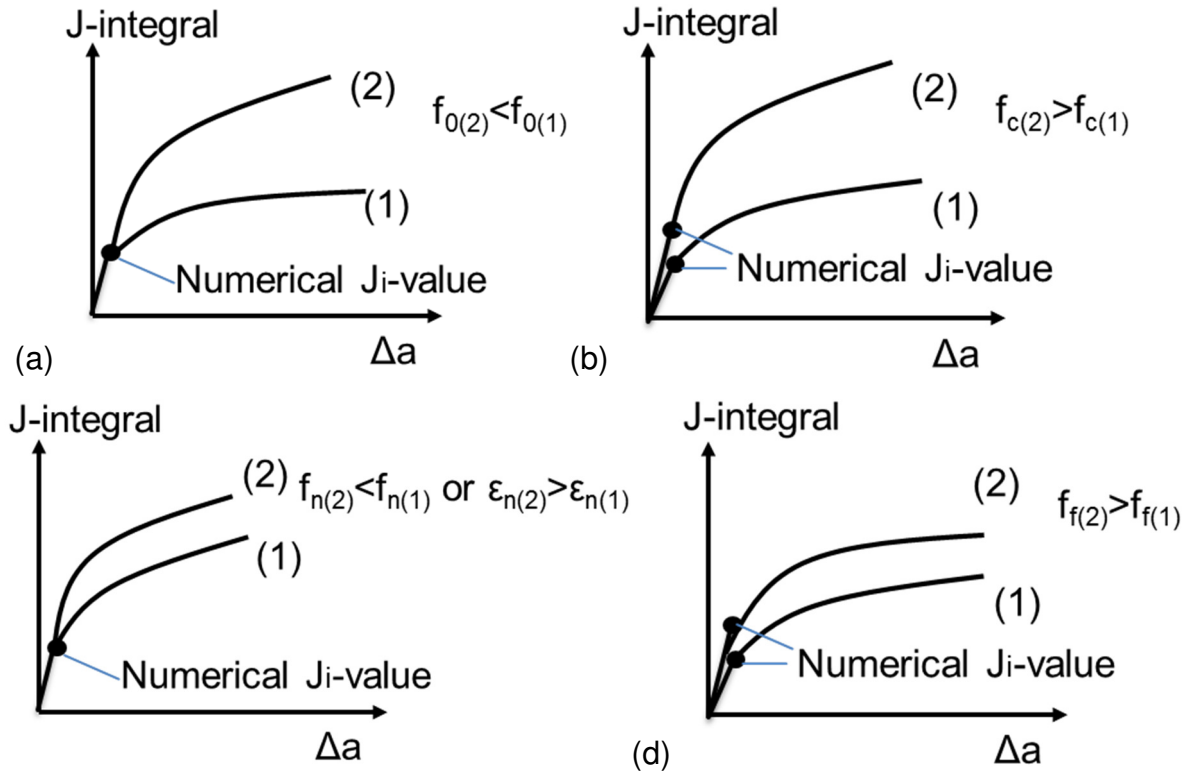

Fig. 5.18: Influence of parameters f_0, f_c, f_n, f_f, ε_n on the fracture resistance curves.

5.2 Crack propagation in the homogeneous base material

After the parameter study, the influence of the GTN parameters on the tensile test results of notched round specimens and compact tension specimens are investigated. According to the previous numerical study of the Rousselier model, l_c-values of l_c=0.05 mm for the BM and l_c=0.1 mm for the HAZ are adopted for the calculation. The GTN parameters are calibrated on notched round specimens. As the consequence of the parameter study discussed in subchapter 5.1 and according to the information in the literature [Nonn et al., 2008], the parameter set given in table 5.1 is adopted for the first numerical calibration. The parameter set given in table. 5.1 with varying f_c-values are used for the further calibration. As shown in Fig. 5.19, the simulated F-ΔD-curves are compared with the experimental ones when f_c=0.05, f_c=0.04 and f_c=0.03, respectively. For the homogeneous BM, when f_c=0.05 is chosen, good agreement can be achieved between the numerical and the experimental F-COD-curves, which is shown in Fig. 5.20(a). However, the GTN model predicts much higher numerical J_i-value and J-values at the early stage of the J_R-curve, as shown in Fig. 5.20(b). This shows that more energy is needed to damage a Rousselier element and the f_c-value used is too high for the simulation according to influence of f_c on the J_R-curve shown in Fig. 5.18(b). In order to obtain a reasonable J_R-curve in comparison to the experimental data, lower f_c values (f_c=0.04, f_c=0.03) with the other parameters kept the same (as shown in table 5.1) are used for the adjustment. When f_c =0.04 is chosen, good agreement is achieved between the numerical and the experimental F-COD-curves when COD<1.3 mm, a lower force is obtained when COD>1.3 mm, as shown in Fig. 5.21(a). The GTN model predicts still higher J_i-values and J-values at the early stage of the J_R-curve (Δa <1.0 mm), as shown in Fig. 5.21(b), depicting the current f_c-value being still high for the simulation. As shown in Fig. 5.22(a), the numerical simulation provides good agreement in comparison with the experiments until the crack initiates when elastic plastic material behavior is adopted. When considering the influence of damage, the GTN model can fit Force vs. Crack Opening Displacement curves as well as fracture resistance curves well when f_c is reduced to 0.03, which is shown in Fig. 5.22(b).

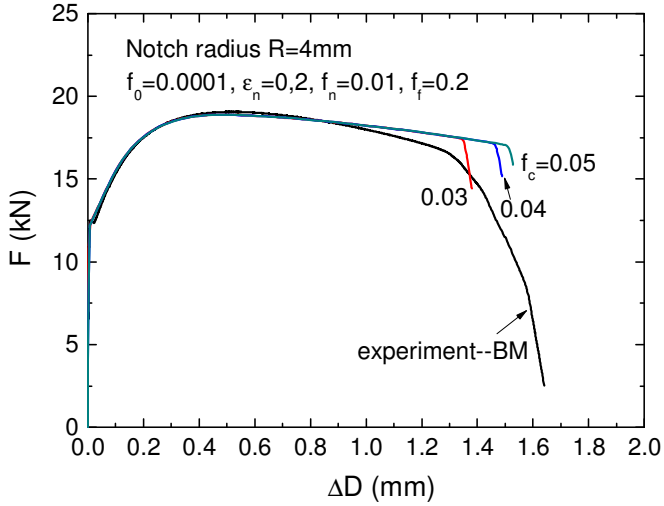

Fig. 5.19: Comparison of experimental and numerical Force vs. cross section reduction curves for notched round specimens extracted from the BM when f_c=0.03, f_c=0.04 and f_c=0.05 is used.

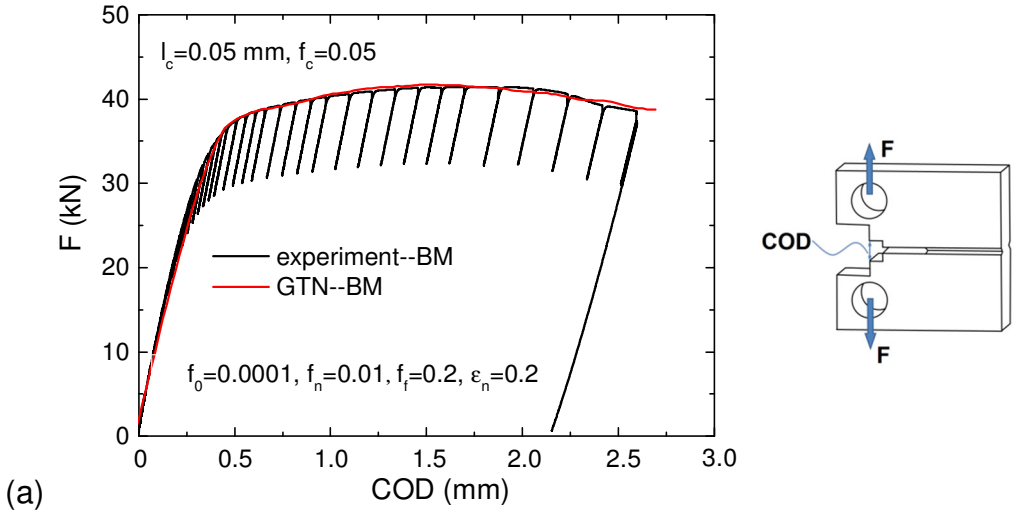

(a)

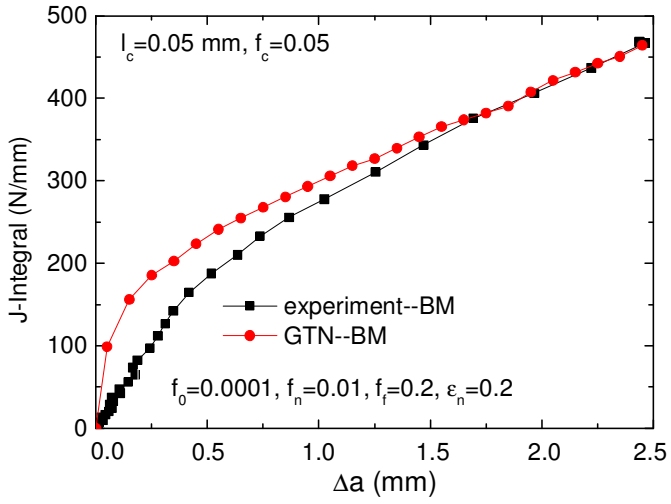

(b)

Fig. 5.20: Comparison of experimental and numerical (a) Force vs. Crack Opening Displacement (F-COD) curves, and (b) fracture resistance curves for C(T)-BM specimens (l_c=0.05 mm, f_c=0.05).

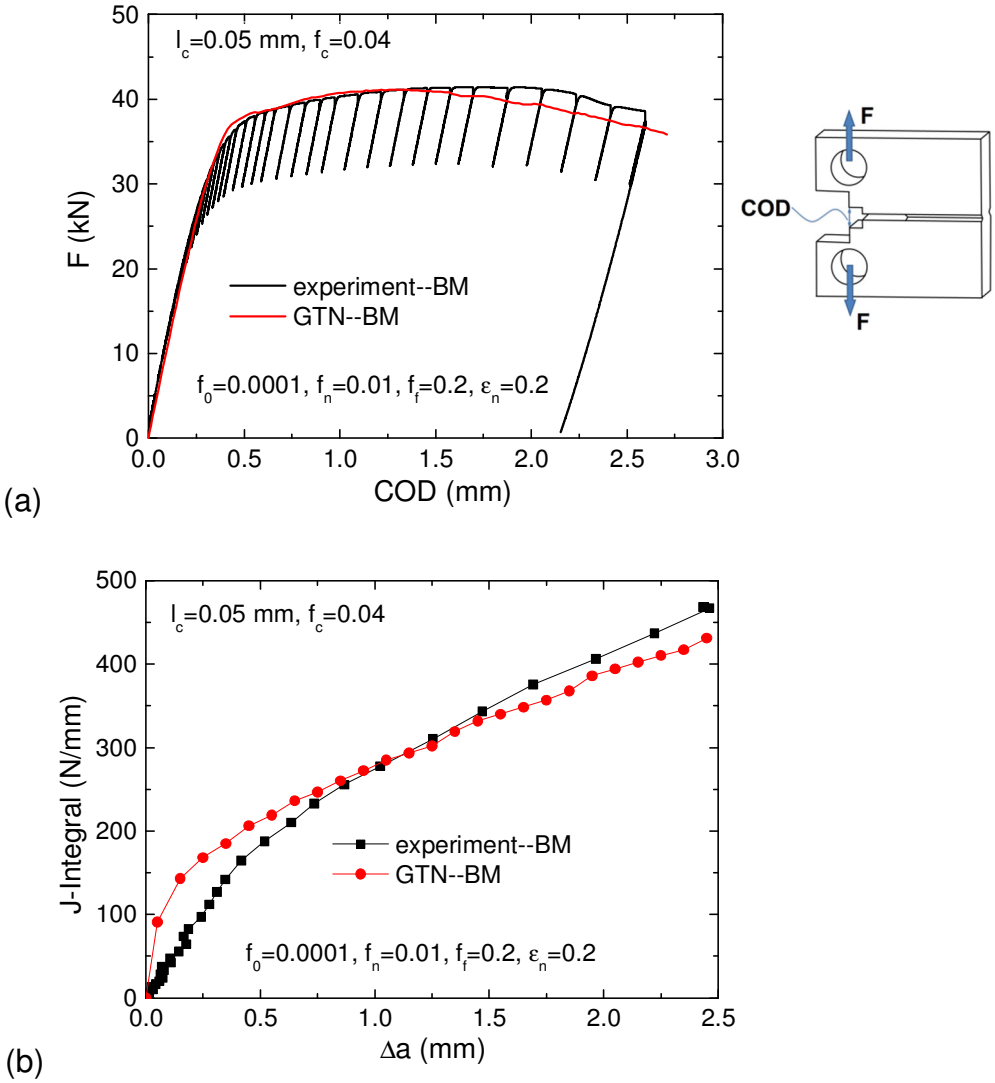

Fig. 5.21: Comparison of experimental and numerical (a) Force vs. Crack Opening Displacement (F-COD) curves, and (b) fracture resistance curves for C(T)-BM specimens (l_c=0.05 mm, f_c=0.04).

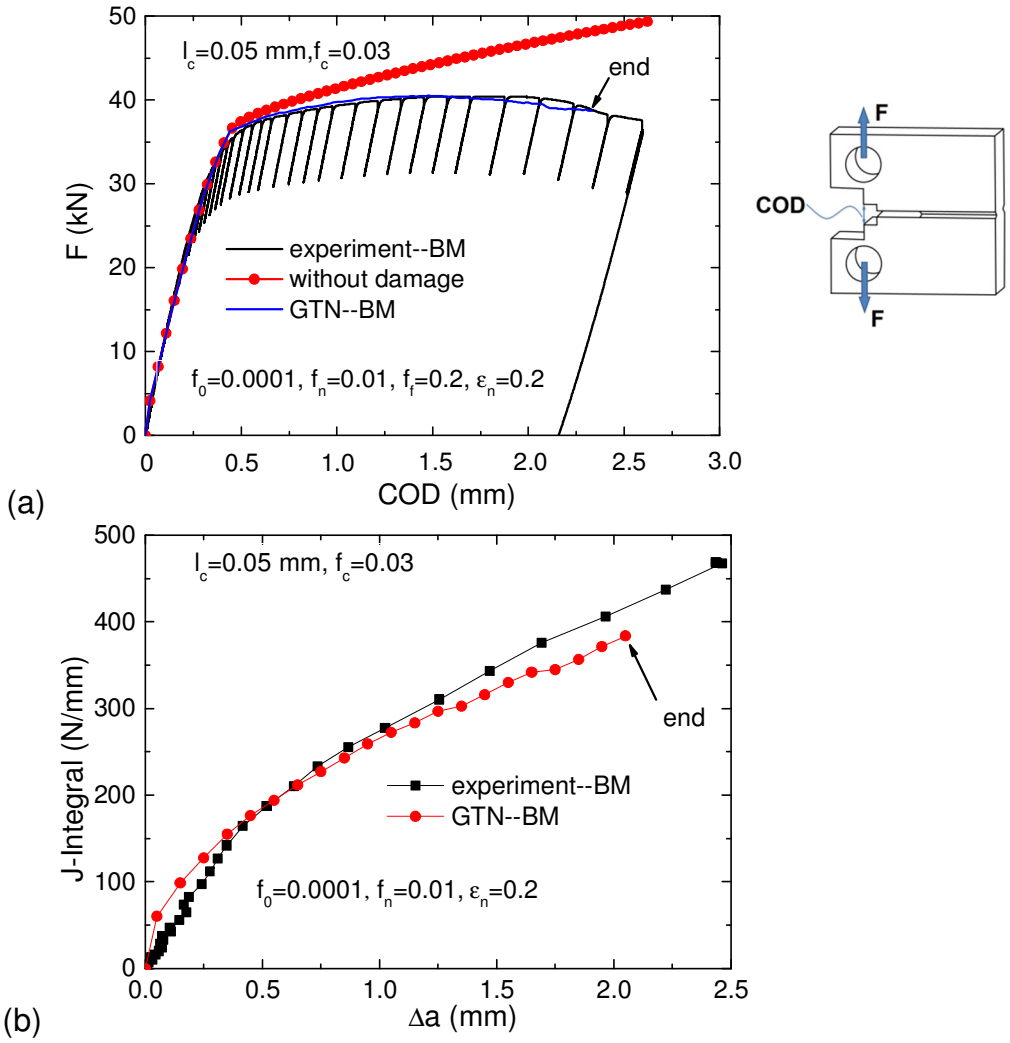

Fig. 5.22: Comparison of experimental and numerical (a) Force vs. Crack Opening Displacement (F-COD) curves, and (b) fracture resistance curves for C(T)-BM specimens (l_c=0.05 mm, f_c=0.03).

The von Mises equivalent stress distributions of the C(T)-BM specimens obtained from the GTN calculation (when f_c=0.03, the other GTN parameters is the same as table 5.1) at the end of the calculation (The moment of COD=2.33 mm in FCOD curve, Δa =2.05 mm in J_R-curve) is shown in Fig. 5.23. When the element is considered as damaged, the stress carrying ability of the element decreases quickly. The damage elements near the boundary are marked in dark blue color, as shown in Fig. 5.23. The virtual crack propagation is shown in Fig. 5.24. In Fig. 5.24, the user defined failure indicator of GTN model in ABAQUS (SDV6) indicates the damage of the element for the GTN model. When the current volume fraction $f^* \geq f_U^*$, the GTN elements are assumed totally damaged where the failure indicator reads the value SDV6=1.

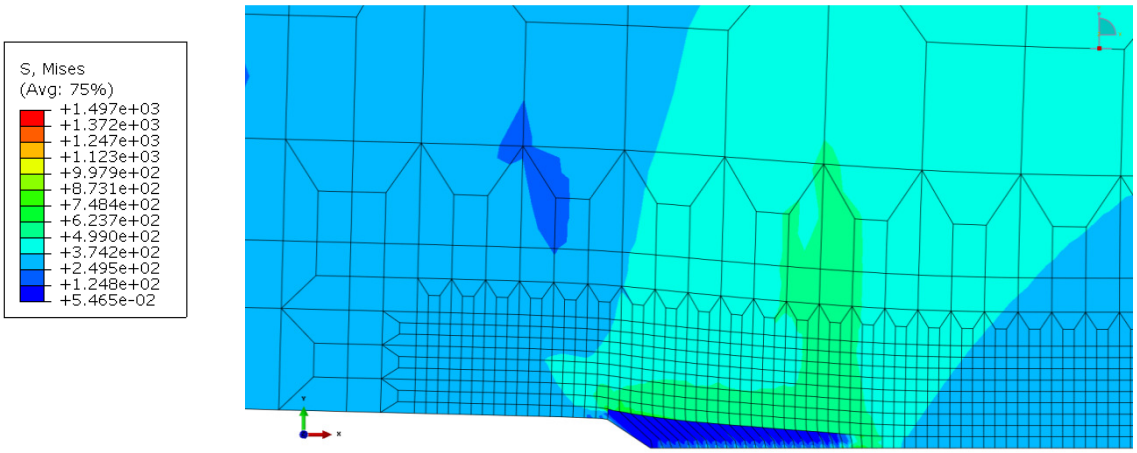

Fig. 5.23: The von Mises equivalent stress distribution of C(T)-specimen extracted from BM at the end of the calculation (COD=2.33 mm in the F-COD-curve and Δa =2.05 mm in J_R-curve).

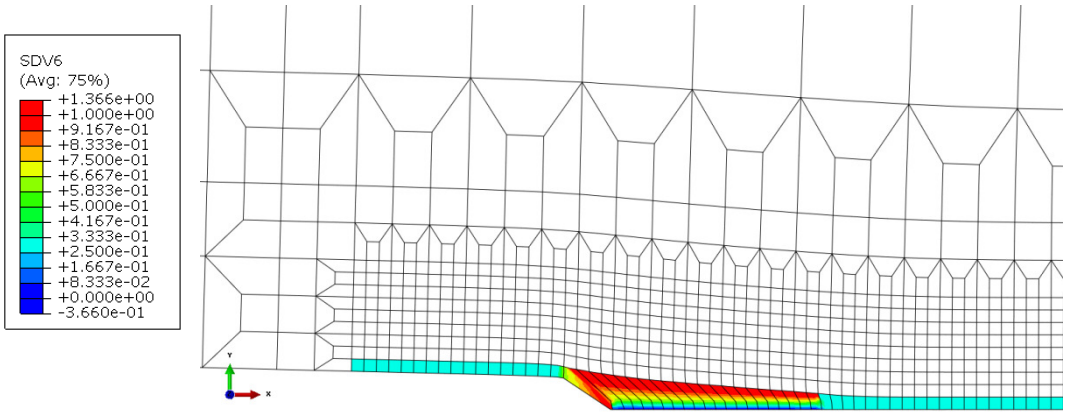

Fig. 5.24: Crack propagation in C(T)-specimens extracted from the BM (SDV6 is the user defined failure indicator of GTN model in ABAQUS, elements are considered as damaged when SDV6=1).

5.3 Crack propagation in an inhomogeneous material

In this section, the GTN model is used to study the crack propagation in C(T) where the initial crack located in the HAZ region which is at the interface between the FZ and the HAZ (C(T)-HAZ). The value l_c=0.1 mm is adopted in the calculations for the HAZ and is derived from the previous investigations of the Rousselier model. The GTN parameters are calibrated on the notched round specimen extracted from the HAZ, as shown in Fig. 5.25. Reasonably simulated F-ΔD-curves are obtained when f_0=0.013, f_c=0.03, f_n=0.01, f_f=0.2 and ε_n=0.2. The same GTN parameter set is used to predict crack propagation of C(T)-HAZ.

In the finite element simulations, the mechanical properties of the FZ and the BM are now defined as non-damaging elastic-plastic because of the experimental observation where cracks propagate in the HAZ only. The HAZ is divided into three thin layer regions which can reflect different material behaviour, as already shown in Fig. 4.23. For the C(T)-HAZ, the elastic plastic material behaviour is also in good agreement with the experimental one until the crack initiates. However, as no damage is considered during the deformation, the elastic plastic behaviour overestimates the force after the crack appears. As shown in Fig. 5.26(a), the GTN model simulates good F-COD-curves compared to the experimental data before COD=1.5 mm. After that, the predicted force is slightly higher that the experimental one, the maximum error is acceptable (around 8%). This can explain why the predicted J_R-curve is found to be slightly higher than the experimental curve, as displayed in Fig. 5.26(b). The GTN parameters for the HAZ are summarized in table 5.2. The von Mises equivalent stress distribution from the GTN calculation for the C(T)-HAZ specimen is shown in Fig. 5.27. The von Mises stresses of the GTN elements (blue color) along the middle section of the whole C(T)-specimen are very small as they are considered damaged, as shown in Fig. 5.27. The virtual crack propagation from a GTN calculation can be found in Fig. 5.28. As shown in Fig. 5.28, the crack propagates straightly in the HAZ, which coincides with the experimental observation.

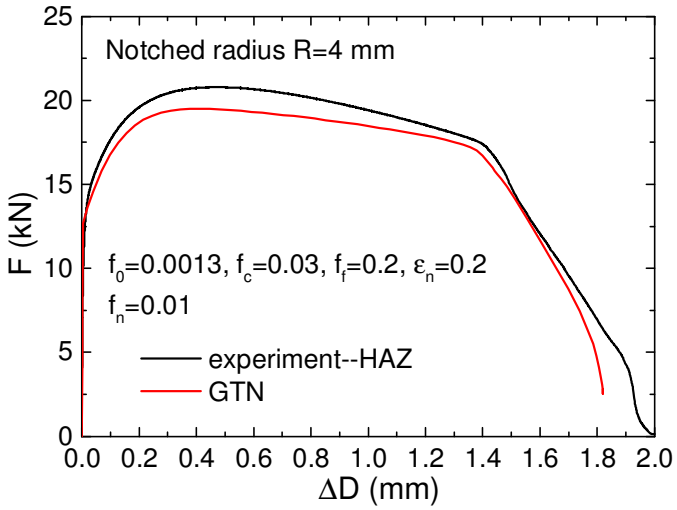

Fig. 5.25: Comparison of experimental and numerical force vs. cross section reduction curves for notched round specimens extracted from the HAZ.

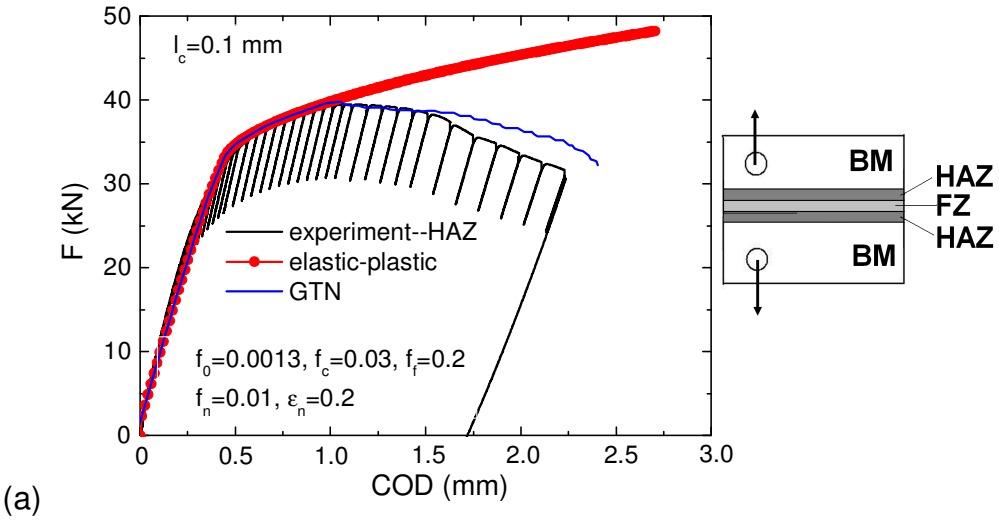

(a)

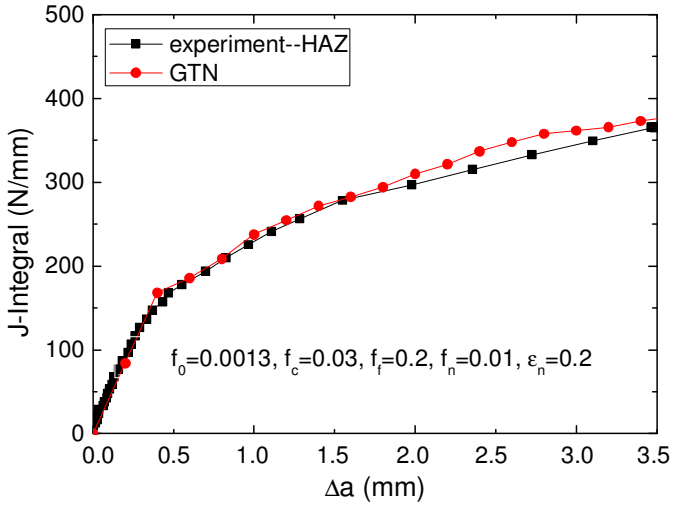

(b)

Fig. 5.26: Comparison of experimental and numerical (a) Force vs. Crack Opening Displacement (F-COD) curves, and (b) fracture resistance curves for C(T)-HAZ.

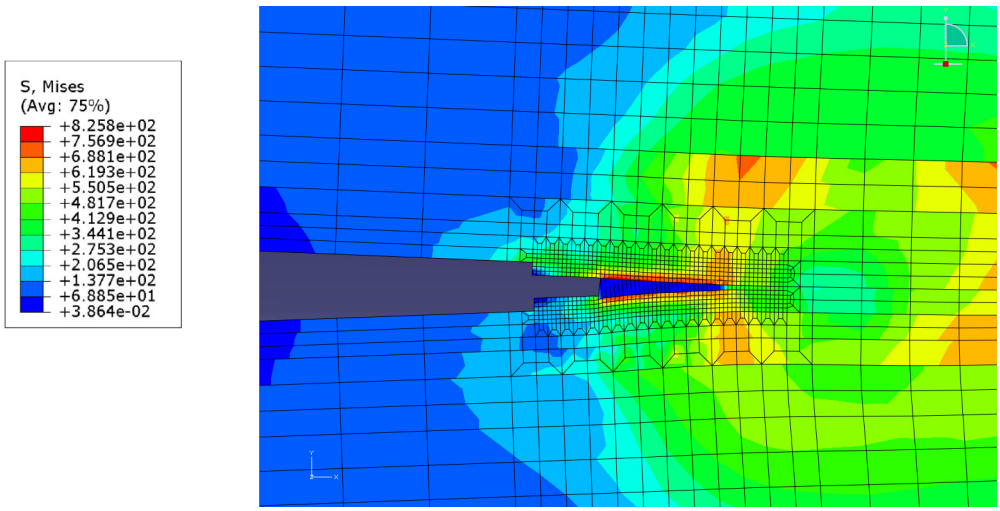

Fig. 5.27: The von Mises equivalent stress distribution of C(T)-HAZ at the end of calculation (COD=2.33 mm in the F-COD-curve and Δa =2.05 mm in the J_R-curve).

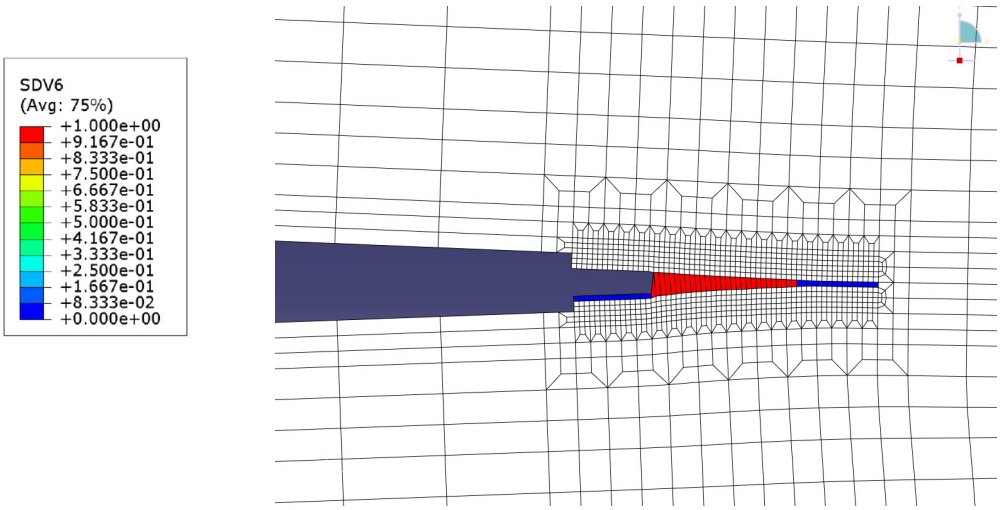

Fig. 5.28: Crack propagation in C(T)-HAZ (SDV6 is the user defined failure indicator of GTN model in ABAQUS, when $f^* \geq f_U^*$, SDV6=1).

Table 5.2: The GTN parameters of different calculations and structures.

Specimen shape	Calculation type	f_0	f_c	f_n	f_f	ε_n	s_n	q_1	q_0	l_c
Notched round specimen (BM), R=4 mm	Axisymmetric	**0.0001**	**0.03**	**0.01**	**0.2**	**0.2**	**0.1**	**1.5**	**1**	**0.05 mm**
C(T)-BM	2D/plane strain	**0.0001**	**0.03**	**0.01**	**0.2**	**0.2**	**0.1**	**1.5**	**1**	**0.05 mm**
Notched round specimen (HAZ), R=4 mm	Axisymmetric	**0.0013**	**0.03**	**0.01**	**0.2**	**0.2**	**0.1**	**1.5**	**1**	**0.1 mm**
C(T)-HAZ	2D/plane strain	**0.0013**	**0.03**	**0.01**	**0.2**	**0.2**	**0.1**	**1.5**	**1**	**0.1 mm**

5.4 Discussion and Conclusions

Crack propagation was studied for the steel S355 EBW using the Gurson-Tvergaard-Needleman (GTN) model. Two different C(T)-specimens with the initial crack located in the base material (BM) and in the HAZ situated at the interface between the fusion zone (FZ) and the heat affect zone (HAZ) were investigated. In order to define the influence of the GTN parameters, a parameter study was performed for notched round specimens and for C(T)-specimens. For notched round specimens, the f_0, f_c, f_n, ε_n influence the final fracture positions of the F-ΔD-curves in the calculations. Higher f_0, f_n result in earlier fracture, however lower f_c and ε_n produce earlier fracture positions for notched round specimens.

During the deformation of all materials, higher f_0-, f_n-values result in that the current void volume fraction reaches the f_c threshold earlier, leading to an earlier fracture position on the F-ΔD-curves. Lower f_c-values mean that void coalescence arises earlier. Lower ε_n-values mean that void nucleation occurs earlier, and results in that the current void volume fraction reaches the f_c limit earlier. The f_f-value does not influence the position of the fracture point on notched round specimens but influences the slope of the F-ΔD-curve after the fracture point. Lower f_f -values produce a smaller slope after the fracture point. After void coalescence, the material stress carrying ability becomes weaker. When the current void volume fraction f reaches the final void volume fraction at failure f_f, the material looses its stiffness totally. A lower f_f means its stress carrying ability will decrease faster after void coalescence, leading to a smaller slope of the F-ΔD-curve after facture initiation of notched round specimens. For the C(T)-specimens, the numerical J_i-value for the crack initiation is influenced severely by f_c- and f_f-values whereas f_0-, f_n- and ε_n-values have almost no influence on the J_i-value. Higher f_c and f_f lead to higher J_i-value. The fracture resistance J_R-curve is strongly influenced by the f_0- and f_c-values. Lower f_0-values or higher f_c-values can produce steeper J_R-curves and higher J-values. The f_f, f_n and ε_n do not influence the J_R-curve dramatically but shift the J_R-curve in a parallel manner. Higher f_f- and ε_n-values or lower f_n-values produce higher J_R-curves. The summary how the GTN parameters influence the numerical F-ΔD-, F-COD- and J_R-curves will help the author finding out the right parameter set during the calibration of the GTN parameters later.

The numerical calibration of the GTN parameters was performed on the notched round specimens with the parameter set as shown in table 5.1 firstly. Then the same parameter set is adopted to predict the crack propagation of the C(T)-specimen. For C(T)-specimens with the initial crack in the BM, according to the previous investigation of the Rousselier model, the value l_c=0.05 mm is adopted for the numerical calculation. The GTN model simulates reasonable F-COD-curves in comparison with the experimental data when the parameter set shown in table 5.1 is used. However, the J-value obtained from the GTN model at the crack initiation stage is much higher than the experimental one, which is shown in Fig. 5.20(b). Since the f_c-value has a huge influence on the numerical J_i-value and J_R-curve as shown in Fig. 5.18(b), lower f_c-values should be used in order to obtain better calculated J_R-curve. After reduction of the f_c-value (f_c=0.03), the GTN model can produce good simulation results compared to experiments in the form of F-COD as well as J_R-curves with the parameter set which are summarized in table 5.2. For the specimen extracted from

the HAZ, the GTN parameters are calibrated on the notched round specimen obtained from the HAZ, also. For C(T)-HAZ, the value l_c=0.1 mm value is adopted for the calculation. The HAZ is divided into three tiny regions which can reflect different material behaviour as shown in Fig. 4.23. Local mechanical properties obtained from flat specimens extracted from these regions were used as model input. Good agreement can also be achieved in terms of F-COD- and J_R-curves when the parameter set shown in table 5.2 is used. In summary, good simulation results for C(T)-specimens with the initial crack located in the BM and at the HAZ confirm that the GTN model can predict the crack propagation of homogenous BM and welded joints well. In comparison to the Rousselier model, the GTN model possesses more parameters (nine parameters) which is more complex to the user. Good match between the simulated and experimental F-COD- and J_R-curves are obtained for the C(T)-BM and C(T)-HAZ when using a good model parameter set. The F-COD- and J_R-curves obtained from the Rousselier model match the experiments a bit better than that of the GTN model. This shows that using simple assumption in the Rousselier model is successful (without considering the influence of void nucleation and the acceleration of damage after void coalescence). As the damage is accelerated after void coalescence in steels, it is necessary to adopt the GTN model considering the damage acceleration in the calculation. These explanations show both the Rousselier model and the GTN model can be used to describe the damage evolution of the ductile behavior very well. However, the Rousselier model and the GTN model have their disadvantages, i.e., both models cannot be used to investigate brittle fracture behavior of materials. In the following chapter, one superior model - the cohesive model will be introduced to investigate the ductile and brittle fracture behavior of C(T)-specimens extracted from the different positions of the electron beam welded joints.

6. The Cohesive zone model

According to what has been summarized in the previous chapters, simulations are performed with the Rousselier and the Gurson-Tvergaard-Needleman (GTN) models predicting the crack propagation of the C(T)-specimens with different initial crack positions, i.e., the initial crack located in the BM, in the centre of the FZ and at the interface between the FZ and the HAZ. As explained in the previous chapters, the phenomenological model - the cohesive model - is able to describe ductile and brittle fracture behaviour of materials when the proper traction-separation law is adopted. In this chapter, the dimensions and the mechanical properties of different weld regions are derived from the previous chapters. Compact tension specimens (C(T)25 with 20% side groove) are investigated with the cohesive model. The numerical simulation results are compared with the experimental one in terms of the F-COD- and J_R-curves.

6.1 Parameter study using the cohesive model

As what has been illustrated in chapter 2.5, there are two independent cohesive parameters: the cohesive strength T_0 and the cohesive energy Γ_0. The cohesive strength is the maximal stress obtained at the moment of crack initiation and the cohesive energy is the energy for the separation of a unit material. The parameter δ represents the separation of the cohesive element which can be calculated with the equation as follows:

$$\Gamma_0 = \int_{\delta}^{\delta_0} T(\delta)\, d\delta \tag{6.1}$$

In ABAQUS standard/explicit, there are three typical traction-separation laws (TSL) which are shown in Figs. 6.1 - 6.3. The TSL with triangular softening is described in Fig. 6.1. The stress on the cohesive element increases with the slope of cohesive stiffness K_{nn} until the stress reaches the critical stress (cohesive strength T_0), then damage evolution happens until the cohesive element loses its stress carrying ability completely where the separation is equal to δ_0. The cohesive stiffness K_{nn} can be found from the equation:

$$K_{nn} = T_0/\delta_{init} \tag{6.2}$$

In ABAQUS, for a pure mode I loading situation, the damage evolution is described by the damage variable D and the strength reduction can be calculated with the equation:

$$\mathrm{T} = \begin{cases} (1-\mathrm{D})\mathrm{T_n}, & \mathrm{T_n} \geq 0 \\ \mathrm{T_n}, & \text{otherwise (no damage to compressive stiffness)} \end{cases} \tag{6.3}$$

For the cohesive law with triangular softening behaviour, the damage variable D was proposed by Camanho and Davila [Camanho et al., 2002]:

$$\mathrm{D} = \frac{\delta_0(\delta_{\max}-\delta_{\mathrm{init}})}{\delta_{\max}(\delta_0-\delta_{\mathrm{init}})} \tag{6.4}$$

where δ_{max} is the maximum value of effective displacement of the cohesive element attained during the loading history.

For the cohesive law with exponential softening, see Fig. 6.2, the damage variable D is given as follows:

$$\mathrm{D} = 1 - \left\{\frac{\delta_{\mathrm{init}}}{\delta_{\max}}\right\}\left\{1 - \frac{1-\exp\left(-\propto\left(\frac{\delta_{\max}-\delta_{\mathrm{init}}}{\delta_0-\delta_{\mathrm{init}}}\right)\right)}{1-\exp(-\propto)}\right\} \tag{6.5}$$

where, δ_0 is again the critical displacement at failure, δ_{init} is the displacement when void initiation happens, δ_{max} is the maximum displacement during the loading history, and α is a non-dimensional material parameter that defines the rate of damage evolution.

For the cohesive law with user defined softening behavior, see Fig. 6.3, the damage variable D can be defined directly in the tabular way which D is specified as function of the effective displacement relative to the effective displacement at crack initiation [ABAQUS, 2008].

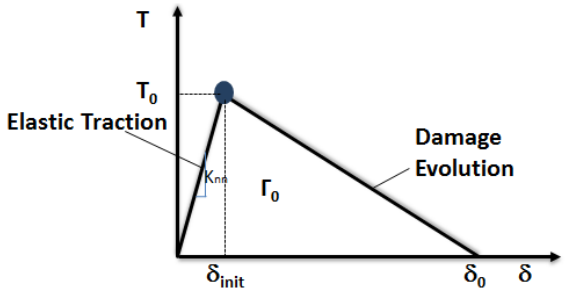

Fig. 6.1: Traction separation law (TSL) with linear softening behavior.

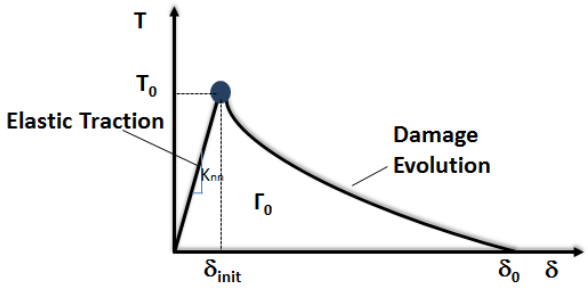

Fig. 6.2: Traction separation law (TSL) with exponential softening behavior.

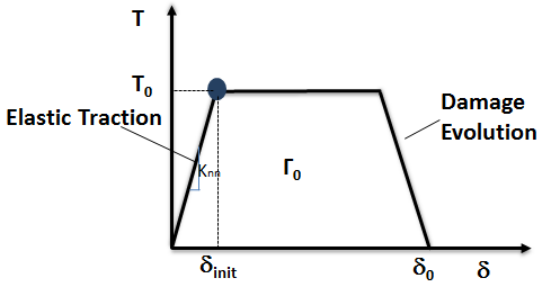

Fig. 6.3: Traction separation law (TSL) with user defined softening behavior (Trapezoidal shaped TSL).

In this section, parameter studies are performed on the C(T)-BM under the exponential shape of the TSL which is available in ABAQUS (as shown in Fig. 6.2). 2D plane strain continuum elements in combination with 2D cohesive elements are used to predict the crack propagation of C(T)-specimens. Due to symmetry reasons, only half of the structure is used for the calculation. The cohesive element width is the same as that of the neighboring continuum element. The detailed finite element mesh around the symmetry plane is shown in Fig. 6.4. The material properties adopted in the calculations of parameter studies are shown in Fig. 3.13. T_0 values which are around $3.1\sigma_0^{BM}$ (1100 MPa) according to the suggestion of Schwalbe [Schwalbe et al., 2009] and the cohesive energy which is around 20 N/mm are used for the parameter study, as shown in table 6.1.

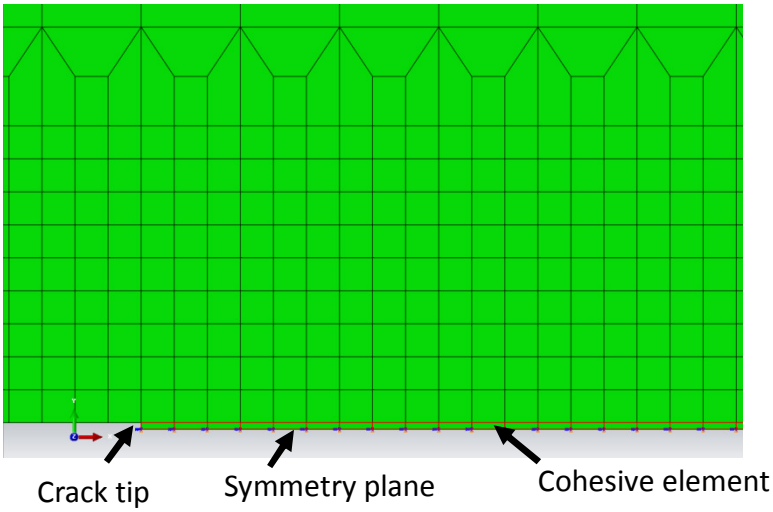

Fig. 6.4: Finite element mesh around the initial crack position.

Table 6.1: Parameters used in the parameter study with the cohesive model

T_0	Γ_0	Cohesive element width (w)	Cohesive element height (h)
1100 MPa	20 N/mm	0.1 mm	0.02 mm

6.1.1 Influence of cohesive strength T_0 and cohesive energy Γ_0

As shown in Fig. 6.5 and Fig. 6.6, a higher cohesive strength T_0 leads to a higher F-COD-curve and a higher J_R-curve but the influence is small here. Compared to the influence of T_0, the cohesive energy Γ_0 possesses a more severe influence on the F-COD- and J_R-curves. A higher cohesive energy Γ_0 leads to higher F-COD- and steeper J_R-curves, as shown in Fig. 6.7 and Fig. 6.8, separately. Each minor decrease moment of the force in the F-COD-curve stands for the damage of one cohesive element. The reason for the serious influence of the cohesive energy Γ_0 on the F-COD- and J_R-curves is because the cohesive energy is a more direct impact factor on the damage of the cohesive element which is shown in equation 6.1. The influence of T_0 is affected by other cohesive parameter as well, i.e., the separation δ_0.

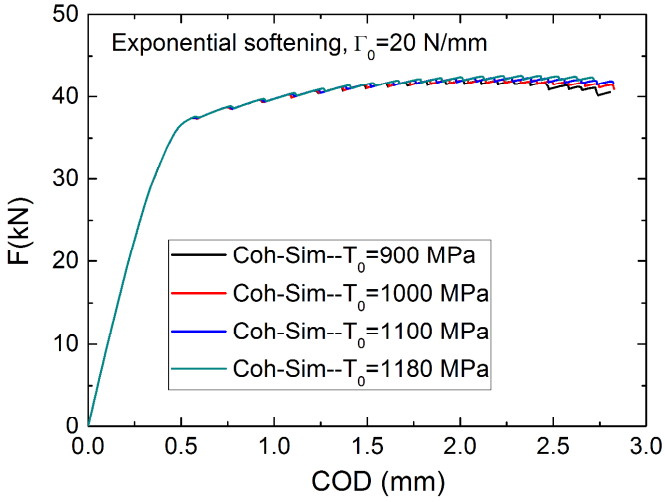

Fig. 6.5: Force vs. (COD) curves with different cohesive strength.

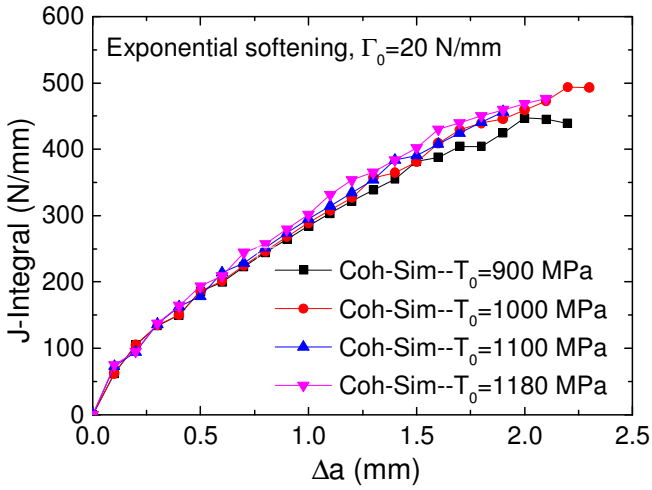

Fig. 6.6: Influence of cohesive strength T_0 on fracture resistance J_R-curves.

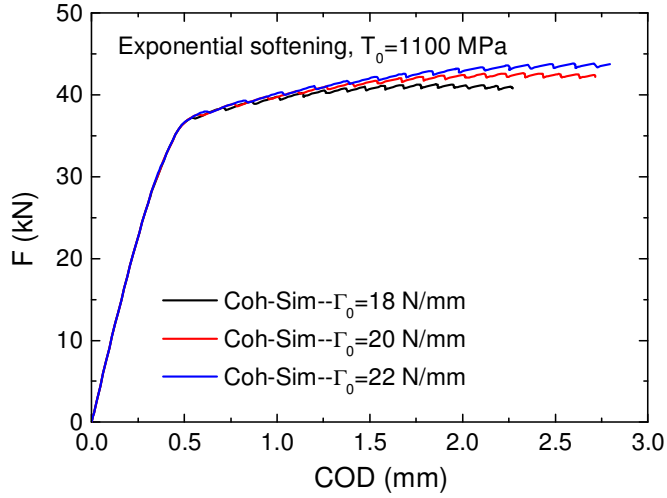

Fig. 6.7: Force vs. (COD) curves with different cohesive energy Γ_0.

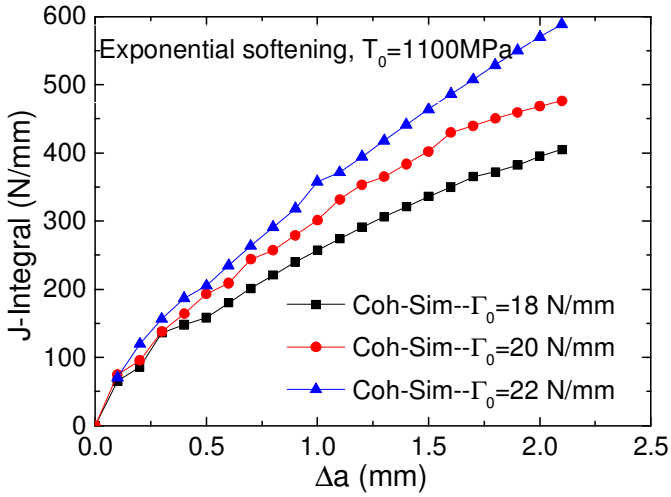

Fig. 6.8: Influence of cohesive energy Γ_0 on fracture resistance J_R-curves.

6.1.2 Influence of the cohesive element

Crack propagations for the C(T)-specimen from the BM are studied with different sizes of the cohesive elements. Two cohesive element widths (w) are analyzed: w=0.02 mm and w=0.1 mm (same element size as that of the Rousselier model). A smaller width of cohesive elements means the distance between neighboring voids is smaller in reality, with the consequence that less energy is needed to drive one crack prapagation. Higher widths of the cohesive elements result in a higher F-COD-curve and a higher J-value as well as strong crack extension in the fracture resistance curve, as can be seen in Fig. 6.9 and Fig. 6.10, separately. This can explain the lower F-COD- and lower J_R-curves, as depicted in Fig. 6.9 and Fig. 6.10. In this chapter, a 0.1 mm cohesive element width is adopted, which is derived from experimental investigations shown in Fig. 3.1. The 0.1 mm cohesive element width is the same as that of the element adopted in the Rousselier and GTN model calculations. As shown in Fig. 6.11, the thickness of the cohesive element (h) has a negligible influence on the F-COD-curve of the C(T)-specimen, a smaller element height (h) leads to a higher F-COD-curve. However, for the fracture resistance curve, the influence of the thickness of cohesive elements is obvious; a smaller element thickness leads to a higher J-value which is displayed in Fig. 6.12. As shown in Fig. 6.12, numerical calculations stop earlier because of convergence problems when 0.002 mm and 0.01 mm of the thickness of cohesive element (h) is adopted, respectively. Best convergence and stable calculation is obtained when 0.02 mm thickness of cohesive element is used. In the following simulations, the 0.02*0.1 mm^2 cohesive element dimension is chosen for the calculation of the BM. As symmetry condition is adopted to simulate C(T)-BM, the true

thickness of the cohesive element is twice of the current value (0.04 mm) when the whole C(T) structure is used for the simulation. The fracture process zone described by one cohesive element should be similar to the damaged region a continuous damage element defines (Rousselier & GTN model). Normally, the fracture process zone defined with one continuous element is determined by the damage variation of two upper Gauss points in one element, thus the damage zone defined by half of the continuous element is equal to the damaged region described by one of the cohesive elements. Therefore, the thickness of the cohesive element is assumed as around half of the size of a continuous element, where the height of the cohesive element for the BM, the FZ and the HAZ is 0.04 mm. This can explain why the thickness of the cohesive element (h) adopted in this chapter is around half of the height of the Rousselier (GTN) element used in chapter 4 and chapter 5.

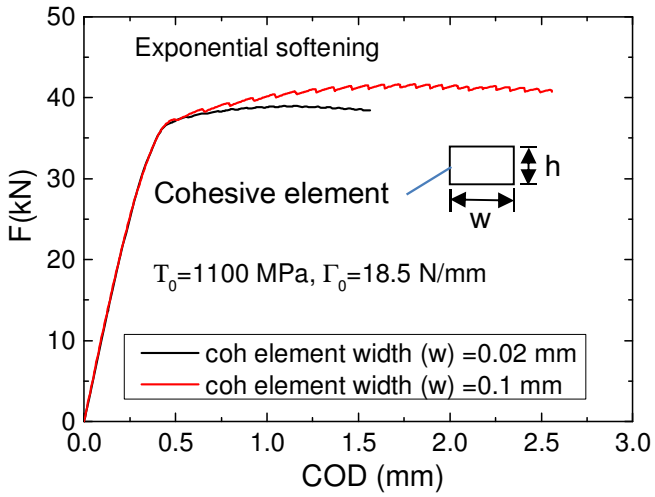

Fig. 6.9: Influence of the width of cohesive element on force vs. (COD) curves.

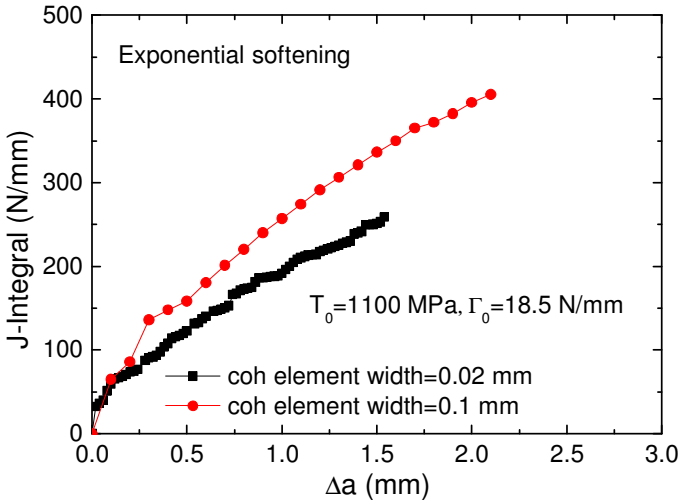

Fig. 6.10: Influence of the width of the cohesive element on fracture resistance J_R-curves.

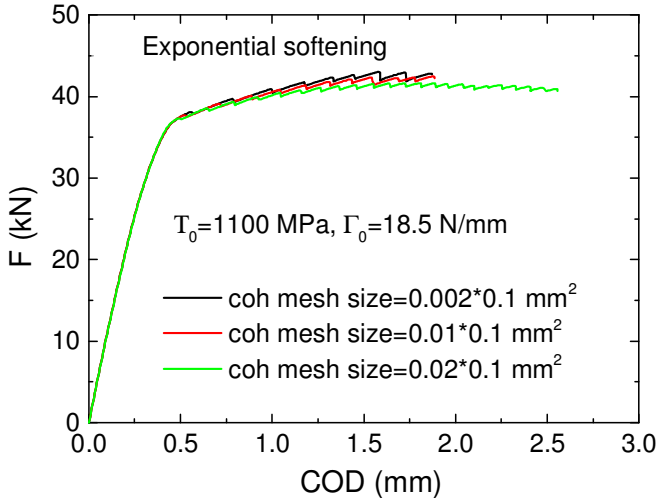

Fig. 6.11: Influence of the height of the cohesive element on force vs. (COD) curves.

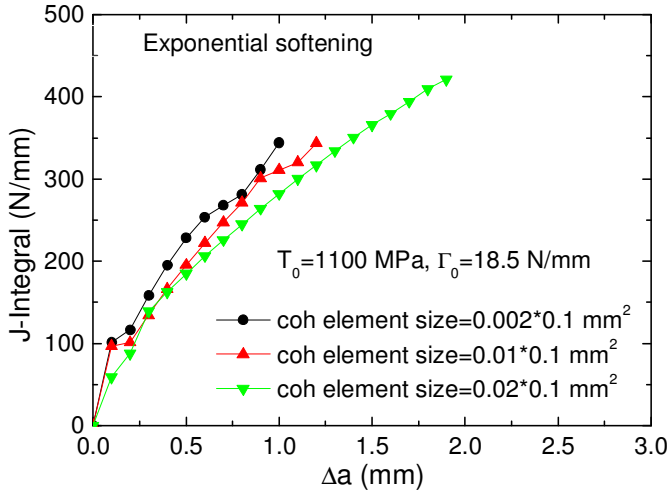

Fig. 6.12: Influence of the height of the cohesive element on fracture resistance J_R-curves.

6.1.3 Influence of the shape of the TSL

As discussed in chapter 2.5, there are different TSLs which can be used to study the ductile behavior of a material. As depicted in Fig. 6.13, the exponential softening TSL leads to slightly lower forces at the early stage (COD<1.5 mm) of the F-COD-curve and higher forces of the F-COD-curve later. Each minor wave moment in the F-COD-curve stands for the damage of a cohesive element. The numerical crack initiation moment obtained from the cohesive calculation with the exponential softening TSL is earlier than that of the trapezoidal TSL. The time interval between two damaged elements in the F-COD-curve obtained from the exponential softening TSL is shorter than that of the trapezoidal softening. This can explain why the numerical J_i-value calculated with exponential softening is lower than that obtained from trapozodial TSL and lower J-values are obtained from the

exponential softening TSL when the crack propagation is less than 0.9 mm, as shown in Fig. 6.14.

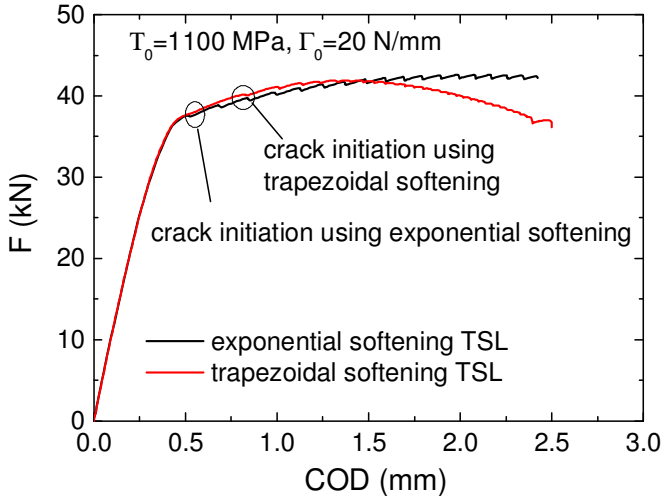

Fig. 6.13: Influence of the shape of the TSL on Force vs. (COD) curves.

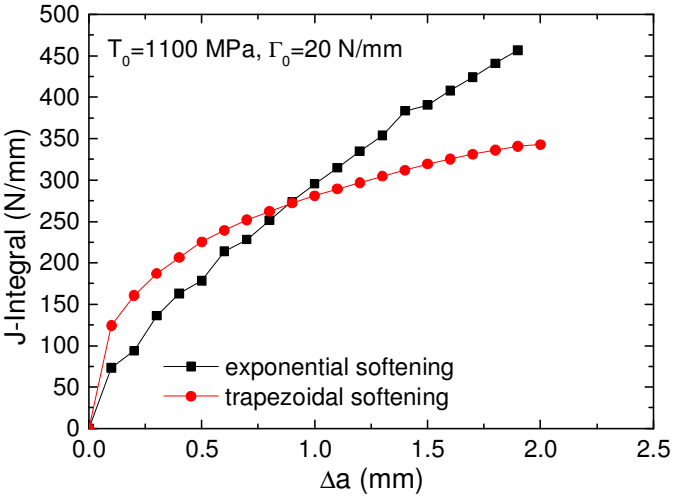

Fig. 6.14: Influence of the shape of the TSL on fracture resistance J_R-curves.

6.2 Crack propagation in S355 base material

6.2.1 Identification of the cohesive parameters

As illustrated in chapter 2.5, there exist two independent cohesive parameters, i.e., the cohesive strength T_0 and the cohesive energy Γ_0. Before using the cohesive model, these cohesive element parameters have to be fixed. According to the discussion of Cornec and Scheider [Cornec et. al., 2003], for the mode I loading situation, the cohesive strength T_0 is

equal to the maximal stress over the cross section (of a notched round specimen) when the experimental force-cross section reduction curve drops. For the BM, a notched round specimen with a 4 mm notch radius is adopted for the determination of T_0, with the geometry as shown in Fig. 6.15. From the tensile test, the external force vs. cross section reduction curve is measured. As the geometry and loading are axisymmetric and symmetric to the cross section, only one quarter of the structure is modeled for the calculation. The finite element mesh of the notched round specimen and the detailed mesh are shown in Fig. 6.16 where the element size along the symmetry plane is the same as that for the Rousselier model. A comparison of the axial stress versus the cross section reduction curve from the FE simulation and the experiment as well as the maximum true axial stress in the center of the specimen is depicted in Fig. 6.17. The simulated axial stress versus the cross section reduction curve coincides with the experimental one until crack initiation happens where the experimental curve drops suddenly. At this point, the maximum stress over the cross section of the notched round specimen is determined from the simulation and is set equal to the cohesive stress T_0. After comparison of simulation and experimental results for the BM, the value T_0=1180 MPa is derived (Fig. 6.17).

In order to determine the cohesive energy, compact tension specimens are used. For the C(T)-specimens extracted from the BM, (as the structure shows symmetry with respect to the crack plane, only one half of the C(T)-specimen is modeled), the finite element mesh and boundary conditions are shown in Fig. 6.18. Fig. 6.19 shows the detailed mesh around the initial crack tip. The cohesive element size around the initial crack tip is 0.02*0.1 mm^2 which is in accordance to the discussion in 6.1.2.

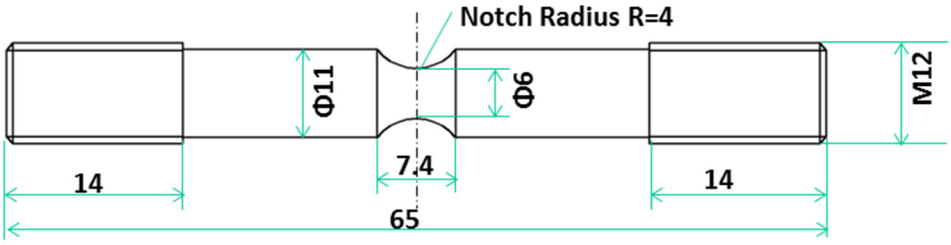

Fig. 6.15: Sketch of 4mm notched round bar.

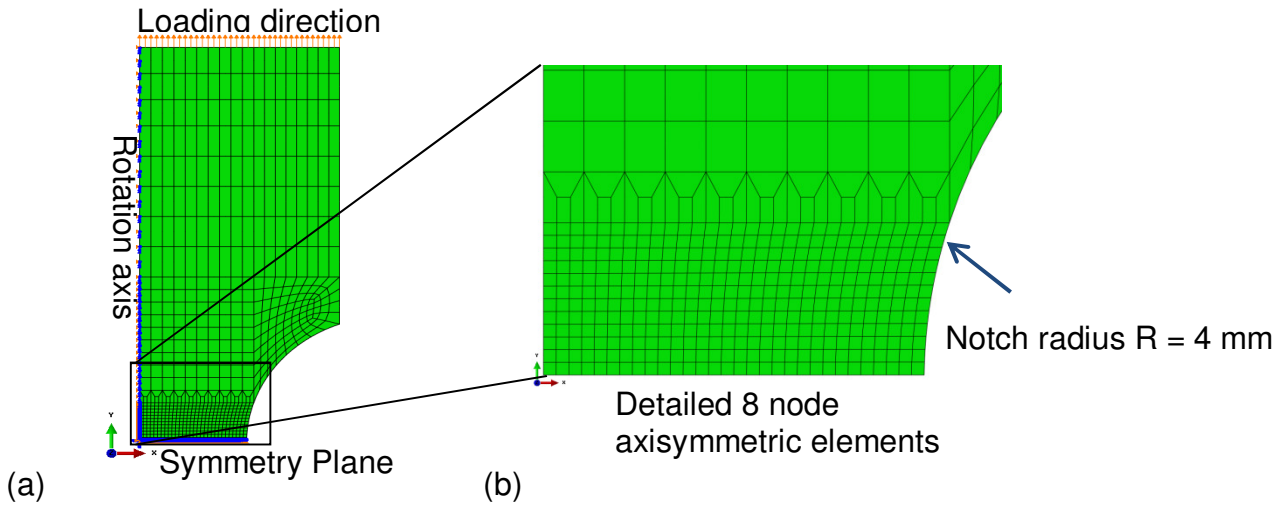

Fig. 6.16: (a) Finite element mesh and boundary conditions of the notched round specimen and (b) detailed mesh.

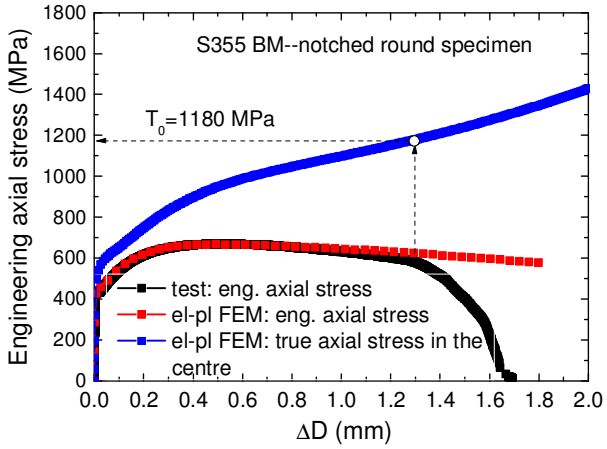

Fig. 6.17: Determination of the cohesive stress T_0: comparison of axial stress versus the cross section reduction curve from FE simulation and the experiments as well as the maximum true axial stress in the center of the notched specimen.

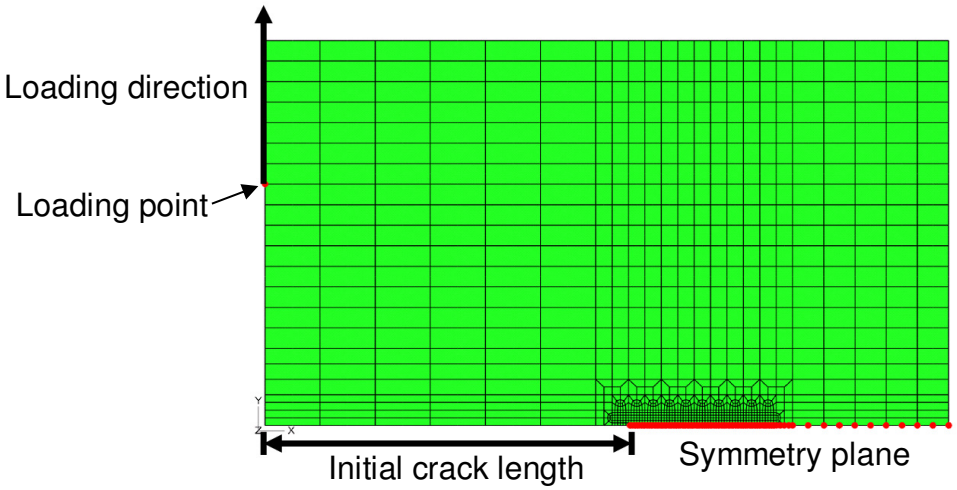

Fig. 6.18: Finite element mesh and boundary conditions of the C(T)-specimen.

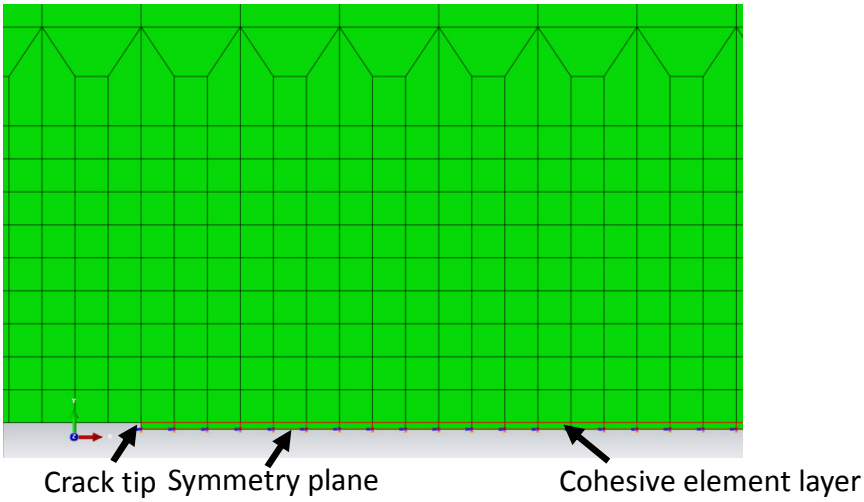

Fig. 6.19: Detailed finite element mesh around the initial crack position.

Firstly, the exponential TSL shown in Fig. 6.2 is used to study the fracture behavior of the C(T)-BM specimen. For the cohesive strength T_0=1180 MPa, numerical simulations are performed with different cohesive energy values. The comparison between the numerical and experimental F-COD- and J_R-curves can be found in Fig. 6.20 and Fig. 6.21. Good agreement between the numerical and experimental results can be obtained in terms of F-COD- and J_R-curves when T_0=1180 MPa and Γ_0=18.5 N/mm are applied, see Fig. 6.22 (a-b). As shown in Fig. 6.22(a), partial unloading is simulated with the cohesive zone model when crack initiation happens (damage of the first cohesive element). Numerical crack initiation happens when COD=0.52 mm and the corresponding numerical J_i-value (J_i=59 N/mm) is calculated with the domain integral method in ABAQUS [Brocks et al., 2001].

Alternatively, the trapezoidal shaped TSL depicted in Fig. 6.3 is adopted to study the fracture behavior of the C(T)-BM specimen. After calculation, good agreement between the numerical and experimental results can be obtained in terms of F-COD- and J_R-curves when T_0=1180 MPa and Γ_0=23.8 N/mm is used, as shown in Figs. 6.23(a)-(b). As shown in Fig. 6.23(a), partial unloading is also simulated with the cohesive zone model adopting the trapezoidal shaped TSL. Numerical crack initiation happens when the COD=0.68 mm which is larger than that from exponential softening (COD=0.52 mm). This can explain why a higher numerical J_i-value (J_i=90 N/mm) is obtained from the trapezoidal shaped TSL (Fig. 6.23(b)) than that obtained from exponential softening (J_i=59 N/mm) (Fig. 6.22(b)). As summarized in the MPA report [Eisele et al., 2006], the width of the stretched zone for most steels varies within 0.03-0.1 mm. The experimental J_i-value calculated based on the width of the stretched zone [Roos et al., 1988] is usually smaller than the experimental $J_{0.1}$-value

(when Δa=0.1 mm, $J_{0.1}$=67.9 N/mm) obtained according to ASTM. The numerical J_i-value (J-value when Δa=0.1 mm in current cohesive element width) obtained from the exponential TSL shape is similar to the experimental $J_{0.1}$-value (when Δa=0.1 mm), showing the numerical J_i-value obtained from the exponential TSL is reasonable and the relative cohesive energy Γ_0 is a more precise one than the one obtained from the trapezoidal shaped TSL. Both an exponential and a trapezoidal shaped traction separation law can fit the crack propagation of C(T)-specimens obtained from the BM well although different cohesive energies have to be chosen.

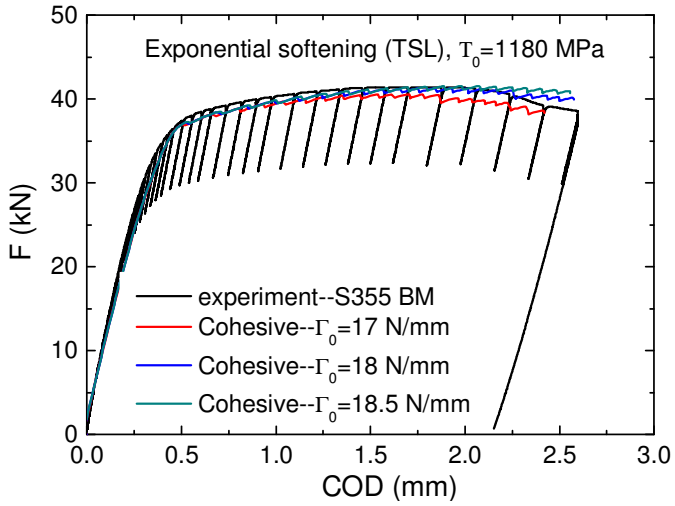

Fig. 6.20: Comparison of the simulated and experimental F-COD-curves with different cohesive energies with the exponential TSL.

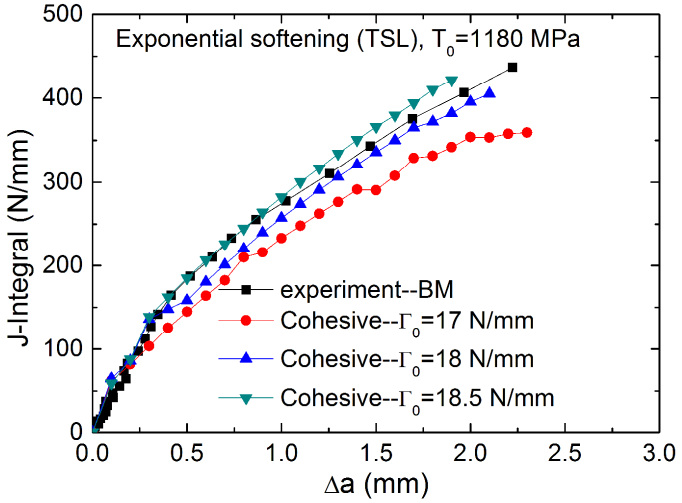

Fig. 6.21: Comparison of the simulated and experimental J_R-curves with different cohesive energies with the exponential TSL.

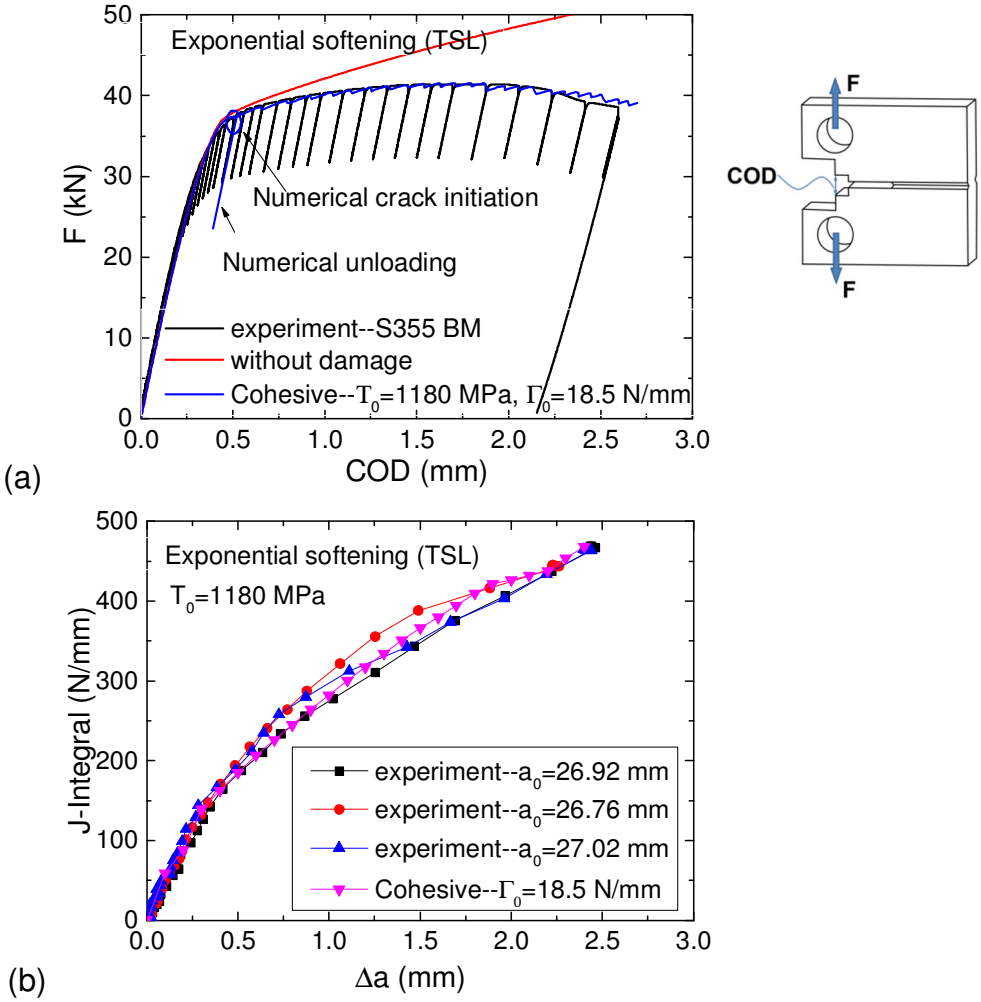

Fig. 6.22: Comparison of experimental and numerical (a) Force vs. Crack Opening Displacement (COD) curves, and (b) fracture resistance curves for C(T)-BM specimens when an exponential shape of the traction-separation law is adopted.

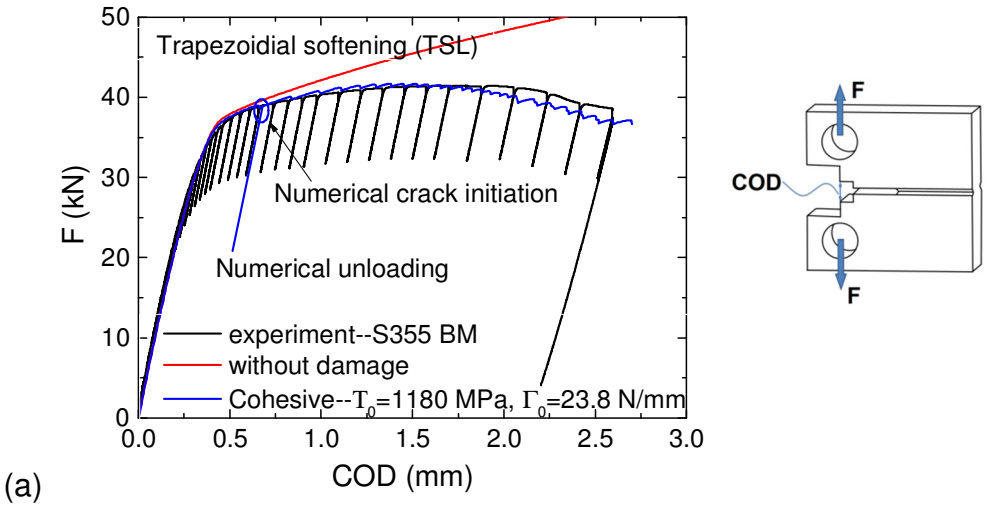

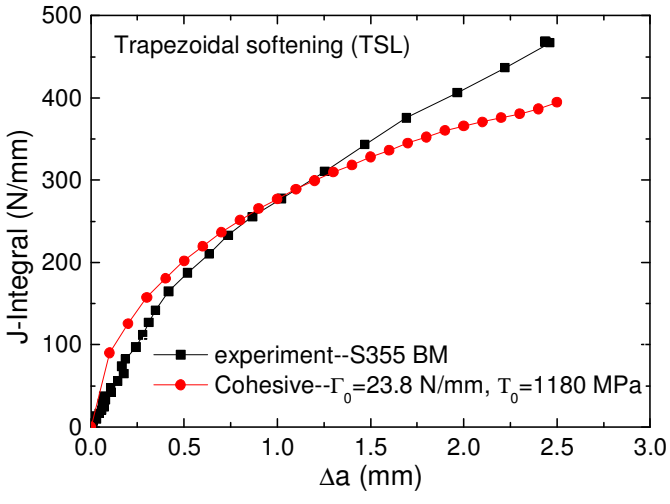

(b)

Fig. 6.23: Comparison of experimental and numerical (a) Force vs. Crack Opening Displacement (COD) curves, and (b) fracture resistance curves for C(T)-BM specimens when a trapezoidal shaped traction separation law (TSL) is adopted.

6.2.2 Identification of the shape of the TSL

Since good fitted F-COD- and J_R-curves in comparison with the experiments can be obtained with the exponential softening TSL and trapezoidal shaped TSL under different cohesive parameters, the question arises: which shape of the TSL and the corresponding parameters is more realistic? As discussed by Schwalbe [Schwalbe et al., 2009], for ductile fracture, the cohesive model can describe the process of void nucleation, growth and coalescence. The shape of the TSL can be derived from micro-mechanical modeling of a one element Gurson model. For the S355 BM, the Gurson parameters adopted for the micro-mechanical modeling with such a one element Gurson model are summarized in table 5.2. As discussed in chapter 5, the best fitted results are obtained with the GTN model with theses parameters. For the C(T)-BM situation, the shape of the TSL obtained from one element Gurson model is shown in Fig. 6.24 where the horizontal axis of the diagram is the relative separation of the element (separation δ vs. height of the element h), the vertical axis of the curve is the relative stress (current axial stress σ vs. the yield stress σ_0). This curve can be adjusted to the common used shape in the finite element code, i.e., in ABAQUS. The shape obtained in Fig. 6.24 with the one element Gurson model is similar to the exponential softening TSL, which can be defined by the user directly in ABAQUS. This means for the S355 BM, the exponential softening TSL is the most appropriate traction-separation law, the T_0=1180 MPa and Γ_0=18.5 N/mm is the suitable cohesive element parameter set.

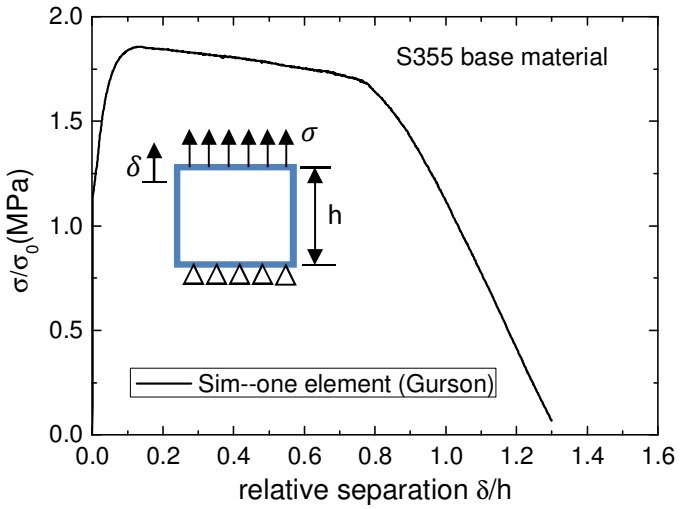

Fig. 6.24: Relative stress vs. relative separation curve from a one element Gurson simulation for the determination of the shape of the traction-separation law of the cohesive zone model.

6.3 Crack propagation in S355 fusion zone (FZ)

For the C(T)-FZ, the initial crack is created in the center of the FZ as observed in Fig. 3.25. The material properties of the FZ and the HAZ can be found in Fig. 4.24. Due to the symmetric geometry with respect to the center line of the C(T), only half of the C(T) structure is modeled. The size of the continuous element and the cohesive element is the same as what is used in the C(T)-BM structure, which can be found in Fig. 6.18 and Fig. 6.19, respectively. The fracture toughness test was performed according to ASTM1820 standard [ASTM, 2003], the F-COD-curve for the C(T)-FZ was observed to be broken suddenly, showing the brittle behavior of the C(T)-FZ, as described in Fig. 3.27. Therefore, a linear decreasing softening TSL which describes the brittle material behavior (as shown in Fig. 6.1) is used for the simulation. Because the tensile test of the notched round specimen from the FZ is not available in experiment, according to the discussion of Brocks [Brocks et al., 2002], the cohesive strength T_0 can be roughly estimated as three times of the yield stress σ_0 which is a rough estimation for steel, values are also reported between 2.5 σ_0 and 5 σ_0 [Schwalbe et al., 2009]. In the calculations, as the yield stress of the FZ is 513 MPa, T_0=1693 MPa (3.3σ_0) [Brocks et al., 2014] is adopted. The numerical F-COD-curve matches the experimental one well when T_0=1693 MPa and Γ_0=70 N/mm is chosen, showing that the cohesive model can predict the brittle fracture behavior of the C(T)-FZ specimen, as depicted in Fig. 6.25. Higher cohesive energy is obtained for the C(T)-FZ than that of the

C(T)-BM showing more energy is needed to drive the crack propagation in C(T)-FZ. This is because the material behavior obtained from the FZ is stronger than that of the BM, as shown in Fig. 3.13.

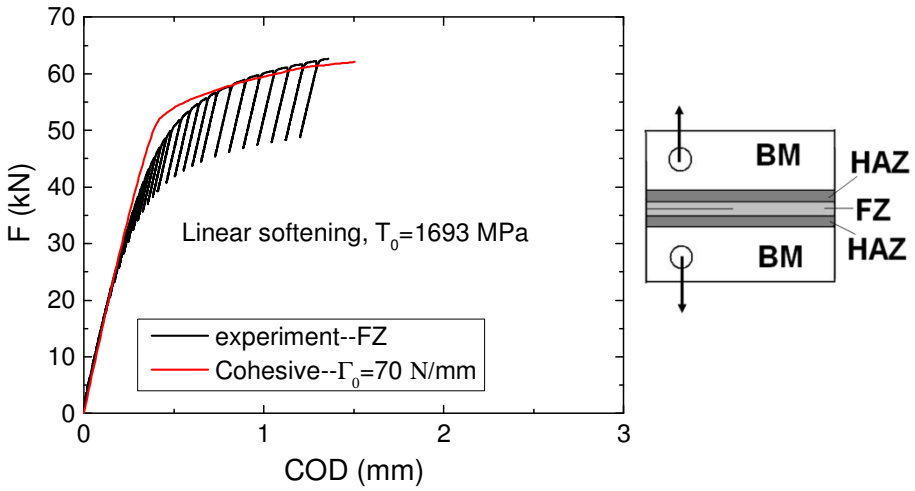

Fig. 6.25: Comparison of experimental and numerical Force vs. Crack Opening Displacement (COD) curves for C(T)-specimen with the initial crack located in the center of the FZ.

6.4 Crack propagation at the interface between the FZ and the HAZ

In the present section, the cohesive model is used to study the crack propagation in inhomogeneous welded joints. Simulations are performed for C(T)-specimens with the initial cracks located at the interface between the FZ and the HAZ. Due to the inhomogeneous material behavior with respect to the crack plane of the C(T)-specimen, the whole C(T) structure is used for the simulation (cohesive element length is 0.1 mm, cohesive element thickness=0.04 mm). A detailed finite element mesh around the initial crack tip is shown in Fig. 6.26. The height of the cohesive element is twice that in the BM situation because the whole C(T) structure is adopted for the simulation. As depicted in Fig. 6.26, one cohesive element layer is designed between the FZ and the HAZ, which is used to describe the damage of the material. This is arisen from the experimental investigation that the crack propagation tunnel is straight because of the plane-strain constraint achieved in the side grooved specimen. The material properties of the BM, the FZ and the HAZ is elastic-plastic during deformation.

For the C(T)-HAZ specimen, firstly, an exponential traction-separation law is chosen for the cohesive model which is easy to use. As discussed before, the notched round specimen with the HAZ located in the center of the notched region is used for the determination of the cohesive strength T_0. The comparison of axial stress versus the cross section reduction curve from FE simulation and the experiments and the maximum true axial stress in the center of the specimen is presented in Fig. 6.27. In Fig. 6.27, the maximal axial stress in the center of the notched specimen can be fixed as T_0=1350 MPa (2.9 σ_0). After the numerical calculation with the cohesive model (when COD≤1.5 mm, Δa≤0.7 mm), good agreement between the numerical and experimental results can be obtained in terms of F-COD- and J_R-curves when T_0=1350 MPa and Γ_0=16.5 N/mm is used, as shown in Fig. 6.28.

Alternatively, the trapezoidal shaped TSL depicted in Fig. 6.3 is adopted to study the fracture behavior of the C(T)-HAZ. Good agreement between the numerical and experimental results can be obtained in terms of F-COD- and J_R-curves when T_0=1350 MPa and Γ_0=22.5 N/mm is used, which are shown in Figs. 6.29(a)-(b). The TSL for the heat affected zone is again obtained from a one element Gurson model as depicted in Fig. 6.30. This shape is very close to the trapezoidal shaped TSL used in ABAQUS. Therefore, the trapezoidal shaped TSL is chosen as the more appropriated traction-separation law for the HAZ situation with T_0=1350 MPa and Γ_0=22.5 N/mm being a suitable correct cohesive element parameter set for the HAZ.

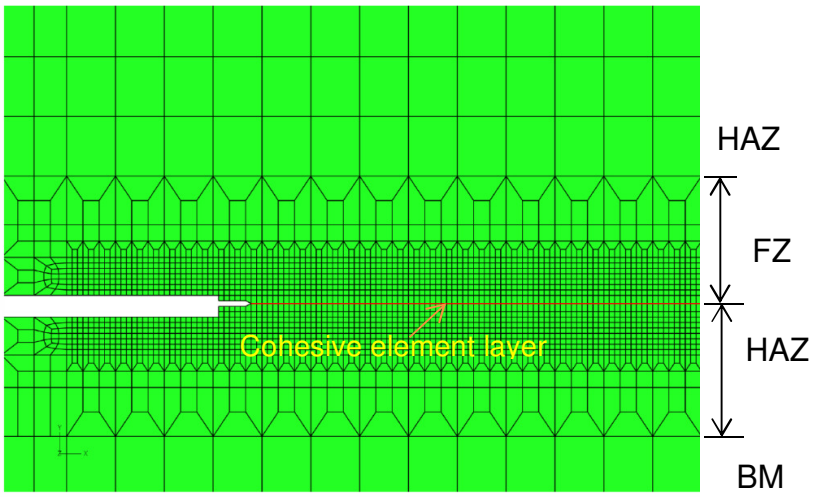

Fig. 6.26: Detailed finite element mesh used for the C(T)-specimens with the initial crack located in the HAZ which is situated at the interface between the FZ and the HAZ.

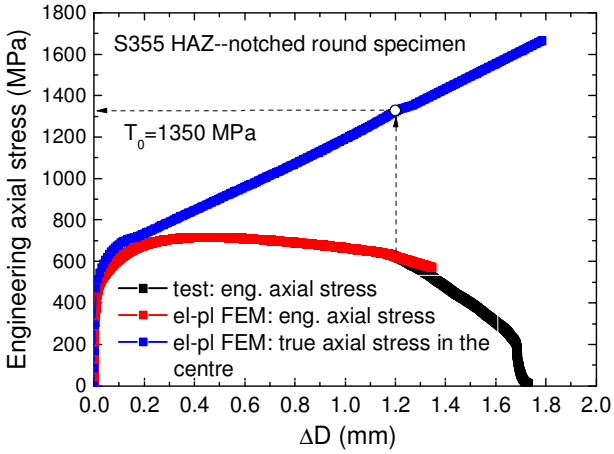

Fig. 6.27: Determination of the cohesive stress T_0: comparison of axial stress versus the cross section reduction curve from FE simulation and the experiments as well as the maximum true axial stress in the center of the specimen.

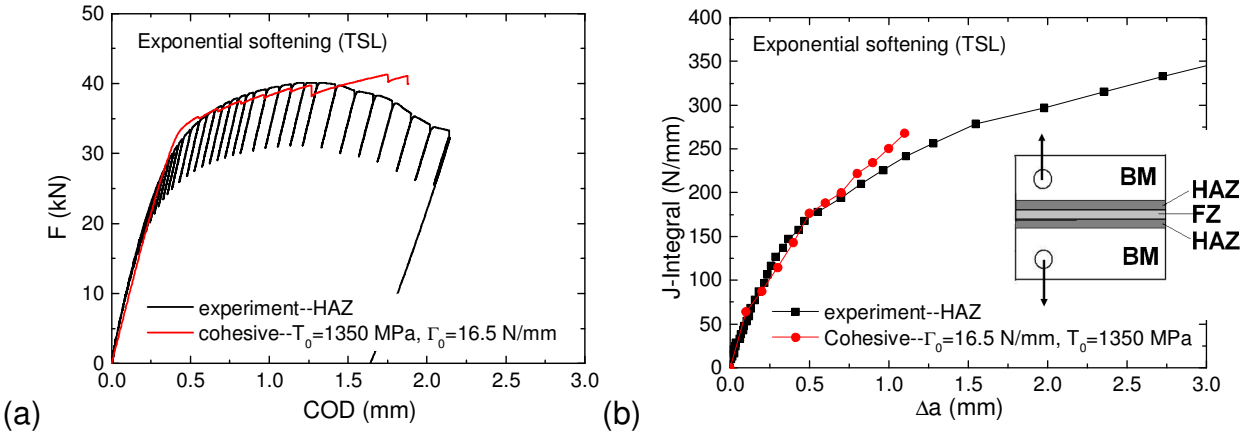

Fig. 6.28: Comparison of experimental and numerical (a) force vs. Crack Opening Displacement (COD) curves, and (b) fracture resistance curves for C(T)-specimens with the initial crack located at the interface between the FZ and the HAZ when an exponential traction separation law (TSL) is adopted.

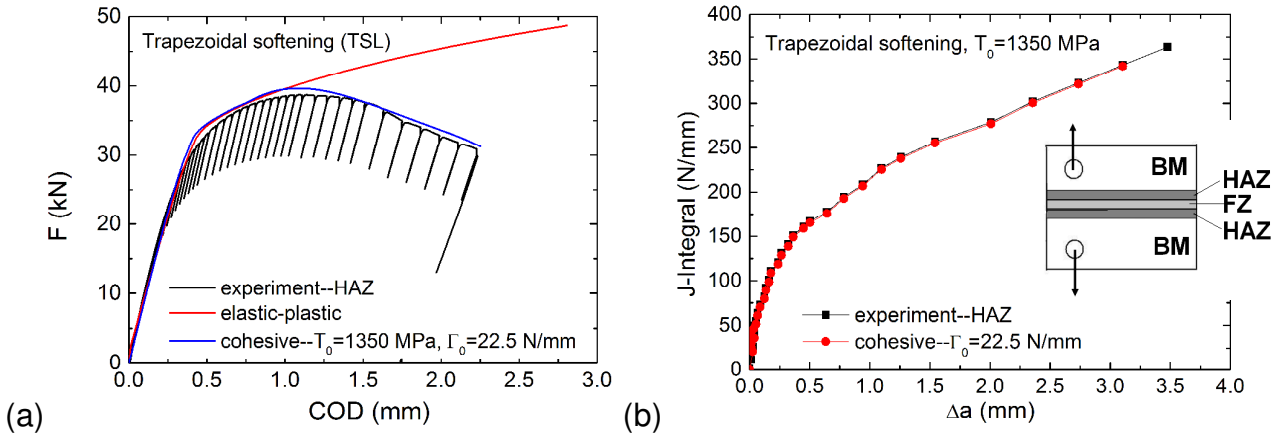

Fig. 6.29: Comparison of experimental and numerical (a) force vs. Crack Opening Displacement (COD) curves, and (b) fracture resistance curves for C(T)-HAZ when the trapezoidal softening traction separation law (TSL) is adopted.

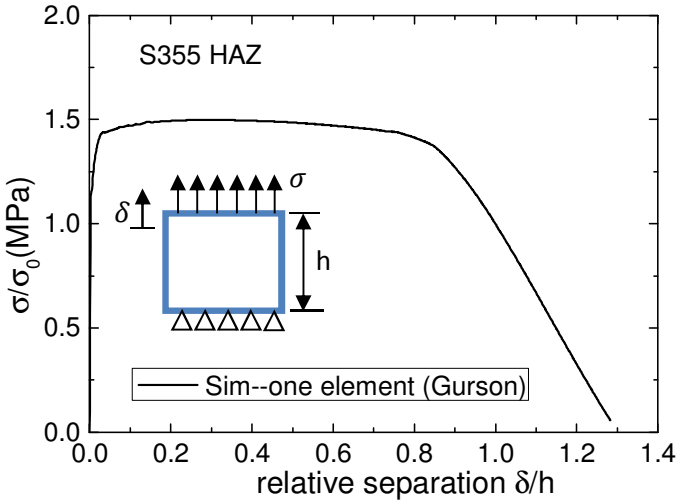

Fig. 6.30: Relative stress vs. relative separation curve from a one element Gurson model for the determination of the shape of the traction-separation law of the cohesive model.

6.5 Discussion and Conclusions

In this chapter, the cohesive model is used to study the fracture behavior of the S355 EBW joints. Crack propagation was investigated in three different C(T)-specimens with the initial crack located in the base material, in the center of the fusion zone and at the interface between the fusion zone and the heat affected zone. As discussed above, there exist only two independent cohesive parameters, i.e., the cohesive strength T_0 and the cohesive energy Γ_0. The shape of the TSL has a minor influence on the F-COD-curve at the early crack propagation (see Fig. 6.13) and a strong influence on the numerical J_i-value at the crack initiation stage, as shown in Fig. 6.14. In order to define the influence of these cohesive parameters, a parameter study was performed for C(T)-specimens. Compared to the influence of the T_0-value, the cohesive energy Γ_0 possesses a strong influence on the numerical F-COD- and J_R-curves obtained from the cohesive zone model because the energy is a direct factor influencing the fracture process. The width of the cohesive element is the same as that of the neighboring continuum elements which is obtained from experimental investigations in chapter 3. The fracture process zone described by one cohesive element is similar to half of one continuous element defines (Rousselier & GTN model), thus the thickness of cohesive element is assume as around half of size of continuous element, where the thickness of the cohesive element for the BM, the FZ and the HAZ is 0.04 mm.

According to the discussion of Scheider [Scheider, 2003a] for ductile fracture behavior, the cohesive strength T_0 can be determined from notched round specimen tests. At the moment of fracture, the maximal axial stress over the cross section of a notched round specimen is set equal to the cohesive strength T_0. The T_0-value for the BM and the HAZ is found to be 1180 MPa and 1350 MPa respectively, as shown in Fig. 6.17 and Fig. 6.27. For the ductile fracture behavior of C(T)-BM and C(T)-HAZ, TSLs with exponential softening or user defined softening (trapezoidal shape) were used for the simulations. Compared to experiments, for the C(T)-BM situation, well fitted F-COD- and J_R-curves are obtained when T_0=1180 MPa and Γ_0=18.5 N/mm were used for exponential softening and when T_0=1180 MPa and Γ_0=23.8 N/mm were applied for the trapezoidal shaped TSL. Partial unloading is simulated with the cohesive zone model adopting different TSLs and the numerical J_i-values are calculated with the domain integral method in ABAQUS [Brocks et al., 2001]. The experimental J_i-value calculated based on the width of the stretched zone [Roos et al., 1988] is usually smaller than the experimental $J_{0.1}$-value. The numerical J_i-value (Δa=0.1 mm) obtained from the cohesive model with an exponential softening TSL is close to the experimental $J_{0.1}$-value (Δa=0.1 mm), showing the exponential softening TSL is a suitable shape and the corresponding cohesive energy obtained from the simulation is a more precise value for steel S355 than the value obtained from the trapezoidal shaped TSL. For the C(T)-FZ, a TSL with linear softening is used for the numerical simulations because of the brittle behavior of the FZ. As the tensile test result of notched round specimen extracted from the FZ is not available, the cohesive strength is roughly assumed around three times of the yield stress for FZ (T_0=1693 MPa) as suggested by Brocks [Brocks et al., 2002]. The predicted F-COD- and J_R-curves agree well with the experiment when T_0=1693 MPa and Γ_0=70 N/mm are used. For the C(T)-HAZ structure, compared to experiments, well fitted F-COD- and J_R-curves are obtained when T_0=1350 MPa, Γ_0=16.5 N/mm for exponential softening and when T_0=1350 MPa and Γ_0=22.5 N/mm for the trapezoidal shape TSL are used. These numerical simulations confirm that the cohesive zone model is able to predict the crack propagation of welded joints when the appropriate TSLs with corresponding parameters are adopted.

In order to select the more suitable TSL shape, one single element Gurson model was adopted, which was discussed by Schwalbe [Schwalbe et al., 2009]. The Gurson material parameters for the simulation are derived from table 5.2. The shapes of the TSLs for the S355 BM and for the S355 HAZ are obtained from the calculation of one single element

Gurson model, are shown in Fig. 6.24 and Fig. 6.30, separately. For S355 C(T)-BM, the relative stress vs. relative separation curve obtained from a one element Gurson model simulation is similar to the shape of exponential softening TSL and the numerical J_i-value (Δa=0.1 mm) obtained from the cohesive model with an exponential softening TSL is close to the experimental $J_{0.1}$-value (Δa=0.1 mm), the exponential softening TSL is assumed as a suitable shape and T_0=1180 MPa, Γ_0=18.5 N/mm is believed as the good cohesive parameters. For S355 C(T)-HAZ, the TSL obtained from a one element Gurson model is very close to the trapezoidal shaped TSL, T_0=1350 MPa, Γ_0=22.5 N/mm is thus believed to describe well the fracture behavior of the S355 HAZ situation. All in all, good simulation results on C(T)-specimens for the initial crack located in the BM, in the center of the FZ and at the interface between the FZ and the HAZ confirm that the cohesive zone model can predict the crack propagation of electron beam welded joints very well. Compared to the previously applied Rousselier and GTN model, the cohesive zone model for fracture simulations shows its superiority because of simplicity and reduced model parameters. Additionally, the cohesive zone model is considered as a phenomenological model and can be used to study arbitrary fracture (ductile and brittle fracture). It is concluded that the cohesive zone model is the best suited for the investigation of the fracture behavior of S355 electron beam welded joints as it can simulate both ductile and brittle fracture. As discussed in this chapter, good simulation results can be obtained under different TSLs with different cohesive parameters. From the simulation result of a one element Gurson model, the cohesion-decohesion curve [Broberg, 1997] which relates the separation of the element to the average stress in the loading direction is produced. This curve is considered as the TSL of the cohesive zone model. From these explanations, the connection between the cohesive model and one damage model (i.e., the GTN model) is found. Before adopt the advanced model (the cohesive zone model) investigating the fracture behavior of S355 welded joints, many simulation works finished with the damage model (e.g., the GTN model) is important and worthy.

7. Optical measurement of crack propagation with the ARAMIS system

As explained in chapter 2, the ARAMIS system is able to capture the surface deformation of the material and monitor the crack propagation on the surface of e.g., the C(T)-specimen. In this chapter, fracture toughness tests of S355 base material are performed on C(T)-specimens with an RMC 100 universal test machine. During the tensile test process of the C(T)-specimen, the ARAMIS system captures the live crack propagation on the surface of the C(T)-specimen. The sketch of a C(T)-specimen tested with the universal test machine in combination with the ARAMIS system is shown in Fig. 7.1. During the test of C(T)-specimens, pictures of the notch area on the surface of C(T)-specimens are obtained from both cameras and saved in the computer. The ARAMIS system will be used to analyze and calculate the crack propagation of C(T)-specimen.

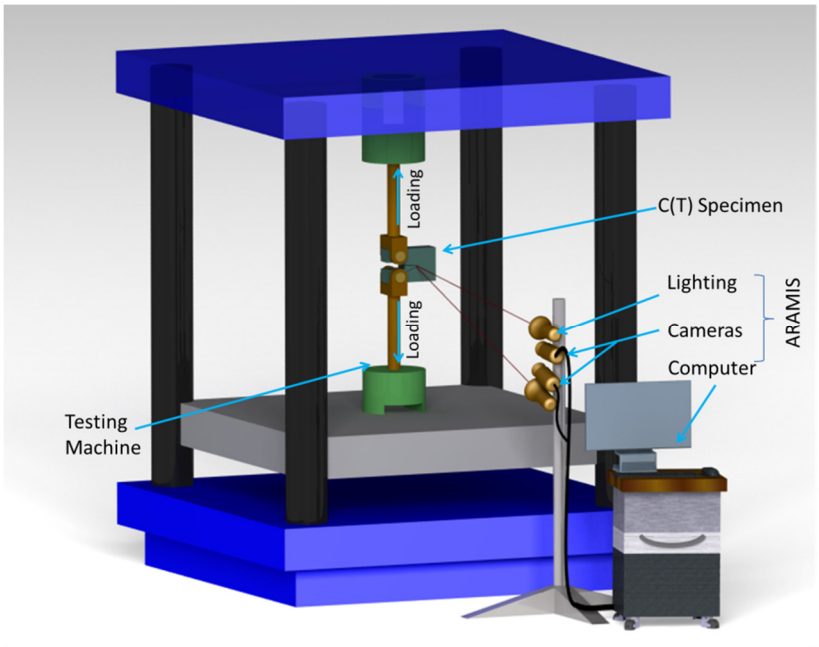

Fig. 7.1: Sketch of the test of a C(T)-specimen in combination with the ARAMIS system.

7.1 Specimen preparation

In order to use the ARAMIS system capturing the material deformation and crack propagation in the notched region on the surface of a sample, a pattern on the surface of

the C(T) is needed. After surface cleaning of the specimen, a white paint (TiO_2) was sprayed on the surface, firstly. Then a black dot pattern was applied using spray paint in order to create a high contrast random pattern, as shown in Fig. 7.2. This will provide a surface pattern from which the deformation measurement can be made using the ARAMIS system.

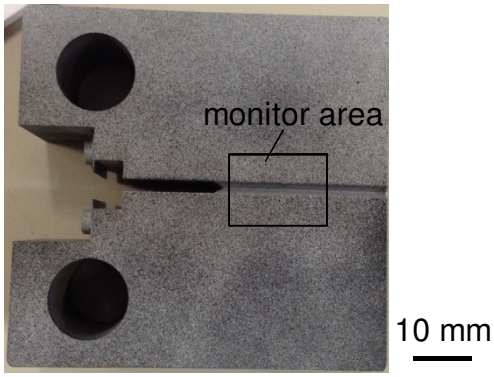

Fig. 7.2: Side grooved C(T)-specimen extracted from S355 BM with a surface pattern.

7.2 Experimental results obtained with ARAMIS

Three side grooved standard C(T)-specimens which are the same as the C(T)-BM specimens tested in chapter 3 are used for the present ARAMIS testing. The C(T)-specimens are produced from S355 base material. The initial crack length a_0 values are obtained with cyclic fatigue loading. In order to monitor the crack propagations on the surface of the notched area in C(T)-specimens, the C(T)-specimens are monotonically loaded (instead of the unloading compliance test process) using a RMC 100 universal test machine. The idea is to adopt a new test procedure instead of the ASTM standard obtaining the fracture toughness of the C(T)-specimen and to capture the crack propagation in the C(T)-specimen with the ARAMIS system. In the unloading compliance test process, loading was controlled by quasi-static displacements perpendicular to the initial crack and the force vs. Crack Opening Displacement (COD) curve was recorded. The crack length is computed at regular intervals during the test by partially unloading the specimen and measuring the compliance (C). This is an indirect measurement of the crack length. In combination with the ARAMIS system, the actual crack length of the C(T)-specimen is directly monitored during the tensile test process. The deformation of the notched area of the C(T)-specimen is monitored with the ARAMIS system during the test process. As the limitation of the storage ability of the current ARAMIS system (max. 500 pictures), one picture per 0.4 second is used during the test process of the C(T)-specimens. After the test of C(T)-

specimens, the experimental results are shown in terms of force vs. Crack Opening Displacement (COD) which is presented in Fig. 7.3. The peak value of the F-COD-curve might be influenced by the initial crack length, where smaller a_0 values lead to higher forces of the F-COD-curve. When the COD value is larger than 2.3 mm (Meeting point of the three tested curves), a sudden drop of the F-COD-curves is obtained, especially for specimens C(T)25-2 and C(T)25-3. This is due to the fact that the crack might meet localized particles. In order to show the crack propagation for one C(T)-specimen (C(T)25-1, a_0=27.45 mm) during deformation, the output results from the ARAMIS system are shown in Fig. 7.4-7.9.

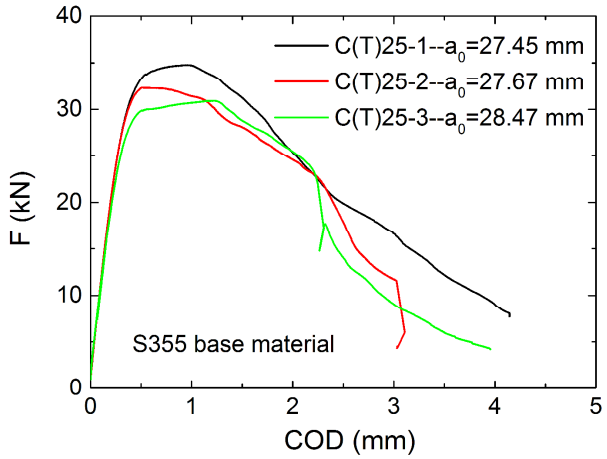

Fig. 7.3: Experimental force vs. Crack Opening Displacement (COD) curves obtained from the test of C(T)-specimens.

Fig. 7.4(a) shows the image of the notched region of the C(T)-specimen which is captured from the left camera of the ARAMIS system and the equivalent strain distribution around the notched area at the initial status is displayed in Fig. 7.4(b). Since there is no material deformation before loading, the equivalent strain at the observed region is zero, which is marked in blue color. Fig. 7.5 shows the optical presentation obtained from the left camera of the ARAMIS system at the early stage of the test process when COD=0.1262 mm, no crack propagation is observed except the initial fatigue notch. The initial fatigue crack notch length measured from Fig. 7.5(a) is Δa=3.92 mm where the initial fatigue length calculated from ARAMIS system is 3.55 mm, as shown in Fig. 7.5(b). Fig. 7.6(a) shows the crack propagation in the C(T)-specimen before reaching the maximal force where obvious crack propagation is observed and the corresponding equivalent strain distribution is shown in Fig. 7.6(b). The current crack length including the initial notch is Δa=9.19 mm which is measured from Fig. 7.6(a) where the crack length obtained from ARAMIS system is Δa=8.62 mm, as shown in Fig. 7.6(b). The regions with the equivalent strain higher than 20%

are shown in red color and some broken regions are wrongly assumed as non-damaged areas in ARAMIS system, as displayed in Fig. 7.6(b).

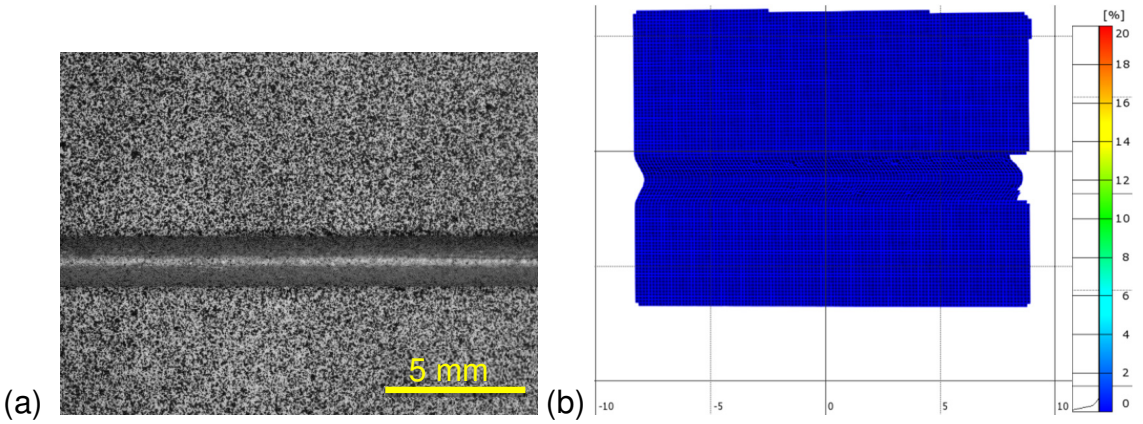

Fig. 7.4: (a) The image from the left camera and (b) the equivalent strain distribution calculated from the ARAMIS system at the initial status.

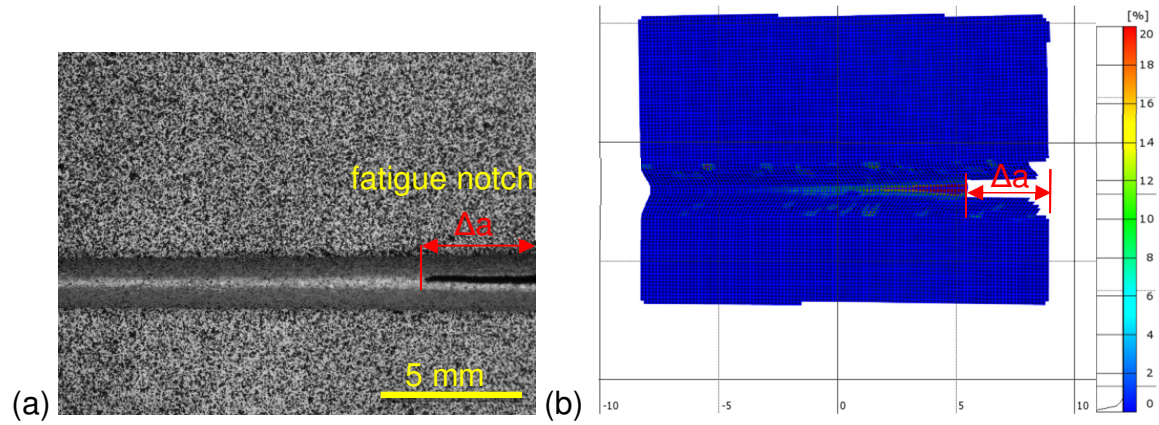

Fig. 7.5: (a) The image from the left camera and (b) the equivalent strain distribution calculated from the ARAMIS system for COD=0.1262 mm, F=13.600 kN.

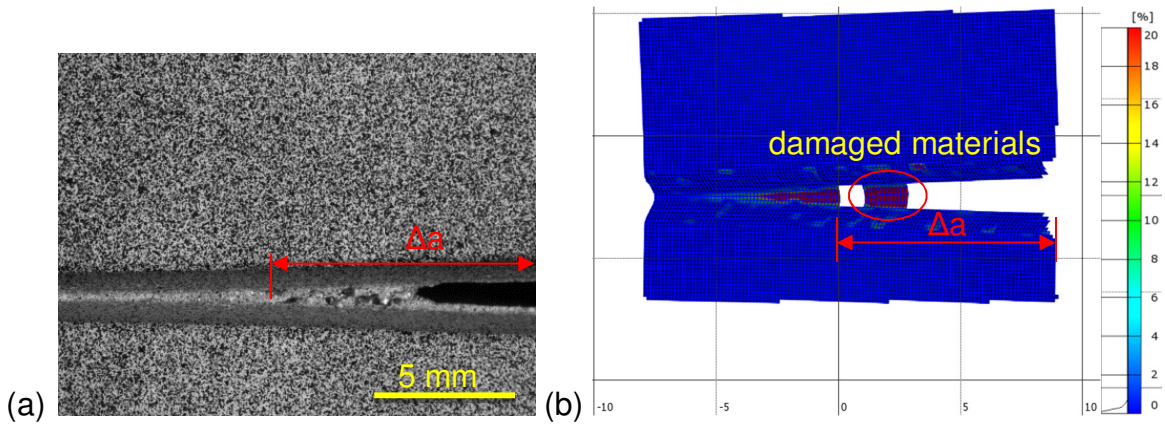

Fig. 7.6: (a) The image from the left camera of and (b) the equivalent strain distribution calculated from the ARAMIS system for COD=0.770 mm and F=34.597 kN.

Fig. 7.7(a) shows the crack propagation of the C(T)-specimen after the peak load during the test where the corresponding equivalent strain distribution are shown in Fig. 7.7(b). The

current crack length obtained from Fig. 7.7(a) is Δa=10 mm and the crack length obtained from Fig. 7.7(b) is Δa=9.83 mm. The crack propagation obtained from Fig. 7.8(a) is Δa=11.08 mm and the calculated crack propagation from ARAMIS system is Δa=11.9 mm, as shown in Fig. 7.8(b). Fig. 7.9 shows the image of final crack occurs and the equivalent strain distribution of the C(T)-specimen calculated from the ARAMIS system at the end of the test. The current crack length obtained from Fig. 7.9(a) is Δa=12.85 mm and the calculated value from ARAMIS output is Δa=13.79 mm, as shown in Fig. 7.9(b). It seems that the current ARAMIS system cannot calculate the accurate crack propagation lengths on the surface of the side grooved C(T)-specimen at each loading moment during the test progress. The reason for the longer crack length obtained from ARAMIS system in comparison to the image obtained from the camera is that some non-destroyed regions are assumed as damaged (The losses of spray points in the notched region of the C(T) due to serious deformation) in ARAMIS system. The reason for the less crack length obtained from ARAMIS software is that some damaged materials are assumed as non-damaged ones where in reality they are damaged.

(a) 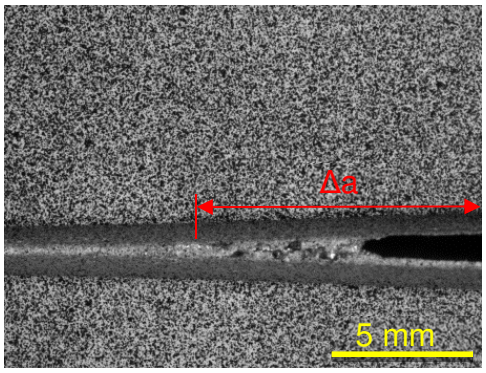

(b) 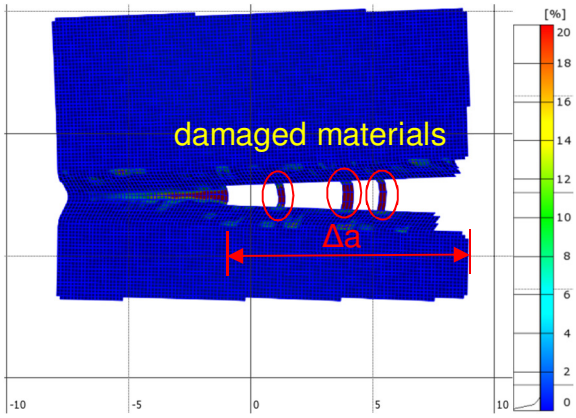

Fig. 7.7: (a) The image from the left camera and (b) the equivalent strain distribution calculated from the ARAMIS system for COD=1.092 mm and F=34.296 kN.

(a) 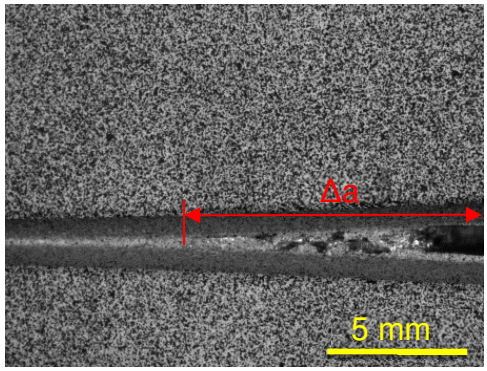

(b) 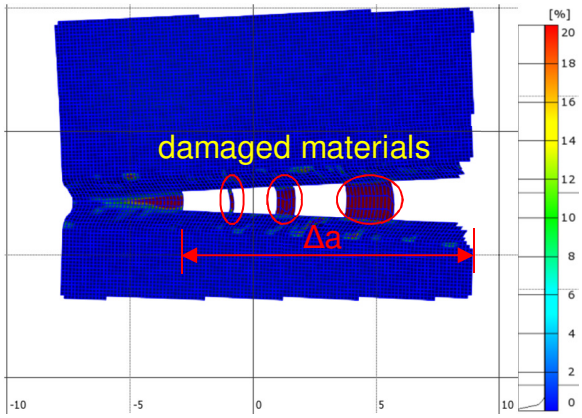

Fig. 7.8: The image from the left camera and (b) the equivalent strain distribution calculated from the ARAMIS system for COD=2.7053 mm and F=18.671 kN.

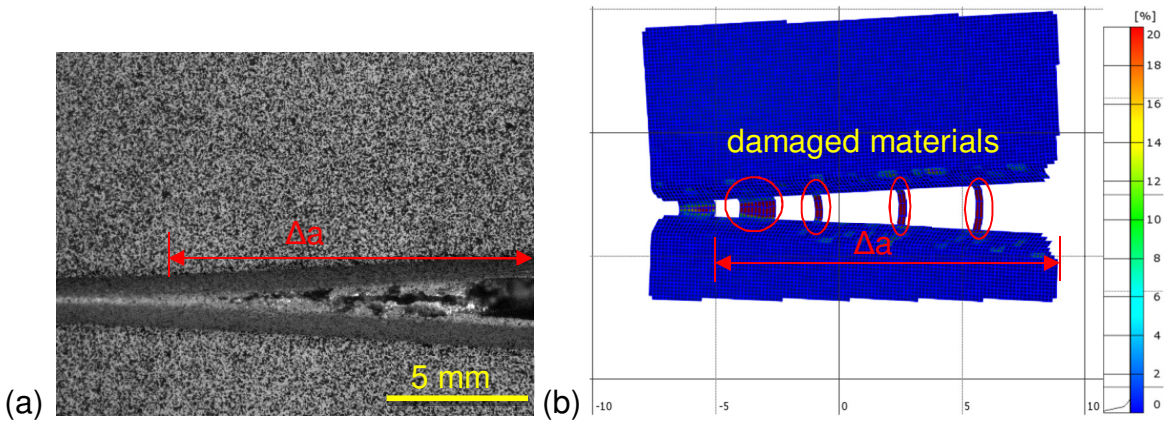

Fig. 7.9 (a) The image from the left camera and (b) the equivalent strain distribution calculated from the ARAMIS system for COD= 4.144 mm and F=7.591 kN.

In comparison to the unloading compliance method, the ARAMIS test method has its advantages. During the test process of the C(T)-specimen, the F-COD-curve is obtained from the output of the universal test machine and the corresponding crack propagation is obtained from the CCD camera of the ARAMIS system. For the unloading compliance method, the crack length is computed at regular intervals during the test by partially unloading the specimen and measuring the compliance (C). Many calculations are required for obtaining the crack length, showing the inconvenience of the ASTM method. The crack propagation is obtained directly from the ARAMIS system during the test and the F-Δa-curve is shown in Fig. 7.10. This shows the ARAMIS technique is a direct method of the crack propagation during the test. Meanwhile, the strain variations around the notch region during the test of the C(T)-specimen can also be obtained from the ARAMIS software, which is not available in the unloading compliance method. These advantages confirm it is worth to adopt the ARAMIS system monitoring the test process of the C(T)-specimen.

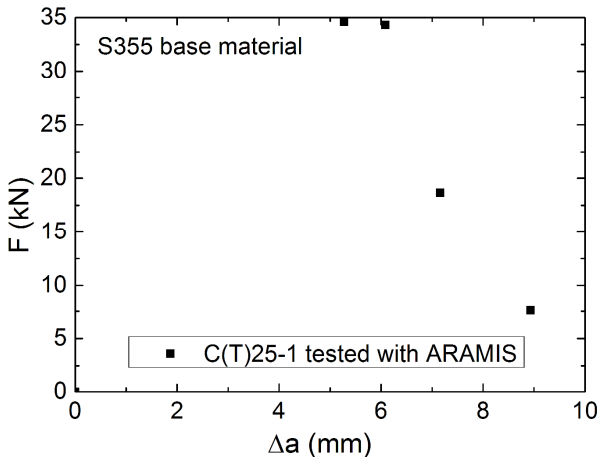

Fig. 7.10: F vs. Δa curve for a C(T)-BM specimen tested together with the ARAMIS system.

7.3 Comparison of experiment with simulation results obtained with the GTN model

In order to describe the damage behavior of the C(T)-specimen extracted from the BM, the GTN model is adopted. As the geometry of the C(T)-specimen shows symmetry with respect to the crack plane, only half of the C(T)-specimen is considered for the case of two-dimensional modeling. Loading is defined on the loading point by displacements, the finite element mesh and boundary conditions are shown in Fig. 4.15. The comparison between the F-COD-curves obtained from the C(T)-specimens tested in combination with the ARAMIS system and with the unloading compliance technique is shown in Fig. 7.11(a). A weaker F-COD-curve is obtained from the C(T)-BM specimen tested in combination with ARAMIS system. The results showed anisotropic fracture behaviour due to the influence of the elongated microstructure where lower fracture toughness along the rolling direction is obtained. Good simulated F-COD-curve is obtained with the GTN model for the C(T)-specimen tested according to ASTM when the parameter set summarized in table 5.2 is used, as shown in Fig. 7.11(b). Since a weaker F-COD-curve is obtained for the C(T)-specimen tested in combination with ARAMIS system (Fig. 7.11(a)) and the extraction position is different from the C(T)-specimen tested with the unloading compliance technique (see Fig. 7.12, L is the rolling direction, T is the loading direction for the C(T) specimen tested in combination with the ARAMIS system and S is the thickness direction), the volume fractions of particles in these C(T)-specimens are assumed being different. A higher void volume fraction (than the f_0-value for the C(T)-specimen tested according to ASTM) is assumed for the C(T)-specimen tested in combination with ARAMIS system. A higher f_0-value (f_0=0.002) is adopted in the GTN model, making the predicted F-COD-curve more reasonable, as shown in Fig. 7.11(c). As we have found in chapter 3, elongated particles are found in the S355 base material. The schematic geometry of one non-metallic particles is shown in Fig. 7.13, where the longest dimension of the particle is named as dx (the direction of the major axis of the particle coincides with the crack propagation direction), the shortest dimension of the particle is dz (the direction of the minor axis is parallel to the loading direction T). According to literature [Weber, 2006], if the maximal measurement in the major axis direction and minimal measurement of the minor axis of the particle is defined as dx, and dz, respectively, the revised factor F* for the volume fraction of one particle $F^* = (dx/dz)^2$. The revised volume fraction of particles is assumed as $f_0^* = f_0 \times F^*$. Since the dx/dz is 4.5 which is obtained for the S355 base material, the revised factor F* is

defined as 20.25. This can explain why the current f_0=0.002 value is 20 times of f_0=0.0001 value which was used in the GTN calculation in chapter 5.2. Detailed information about the revised factor of the volume fraction of particles can be found in the literature [Weber, 2006]. For this C(T)-specimen, higher volume fraction of particles are assumed in front of the initial crack than for the C(T)-specimen used in chapter 3 (Fig. 3.27), showing a lower fracture toughness. In comparison to the C(T)-specimen tested according to the ASTM standard (Fig. 7.14(a)), a wider and longer stable crack growth region is found on the fracture surface of the C(T)-specimen monotonically loaded in combination with the ARAMIS system as shown in Fig. 7.14(b).

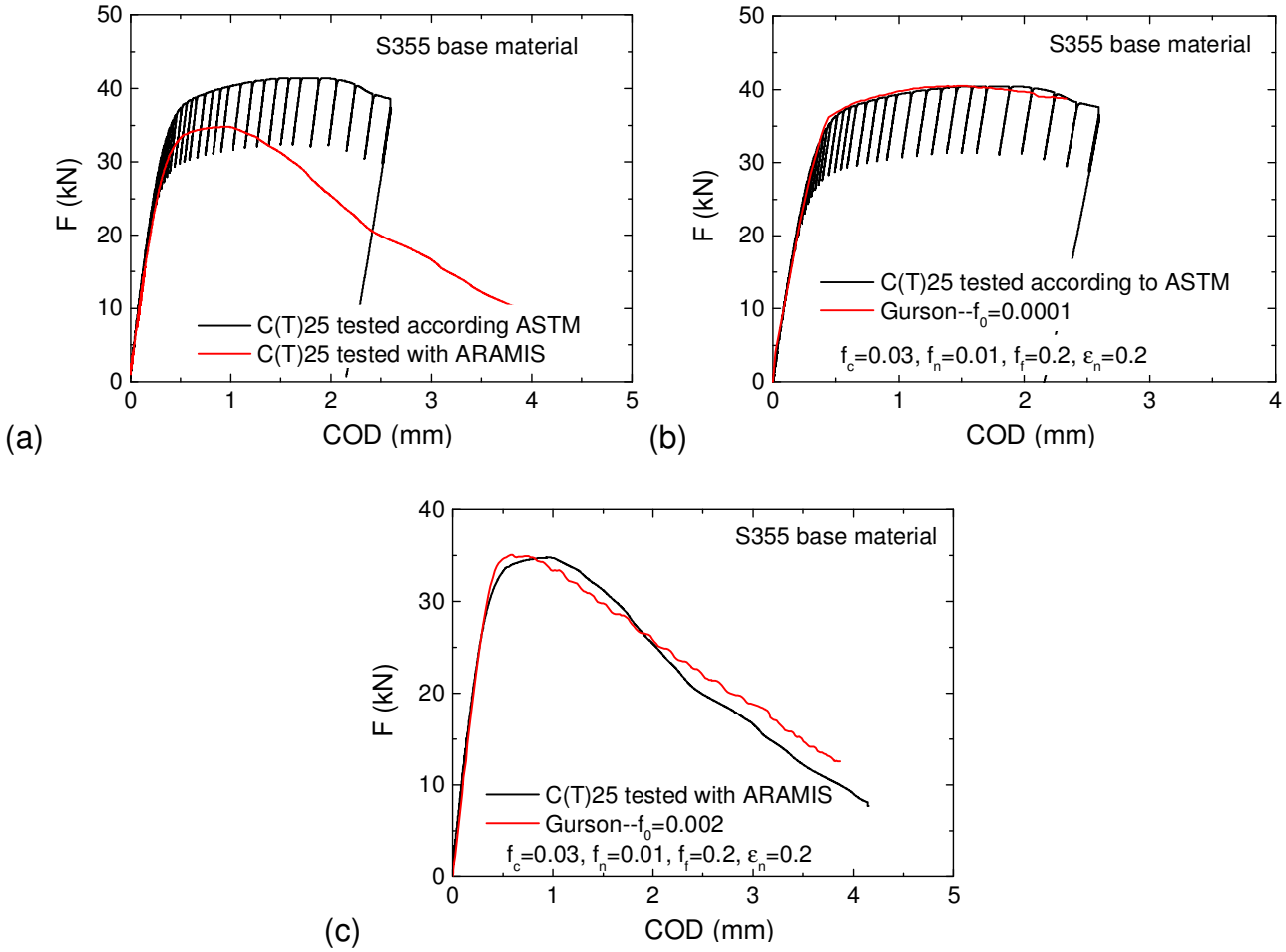

Fig. 7.11: Comparison of Force vs. Crack Opening Displacement (F-COD) curves (a) for C(T)-BM specimens tested according to ASTM and with the ARAMIS system (b) for the C(T)- specimen tested according to ASTM together with the GTN simulation and (c) for the C(T)-specimen tested together with the ARAMIS system and the GTN simulation.

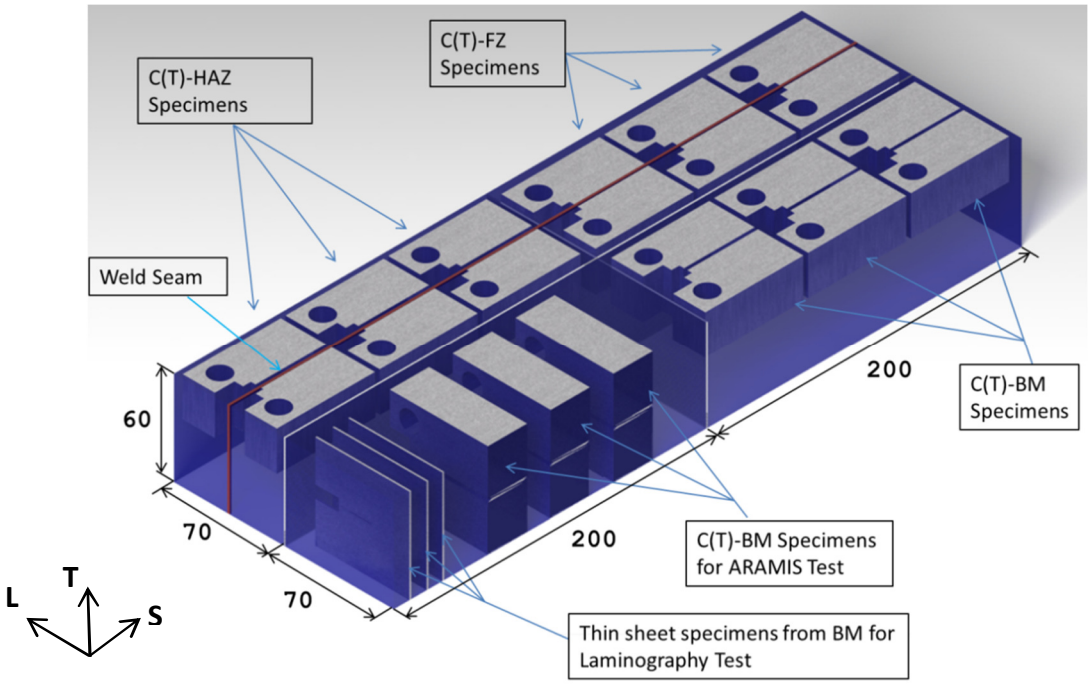

Fig. 7.12: Sketch of extraction positions for compact tension (C(T)) specimens and thin sheet specimens from the S355 welded joints.

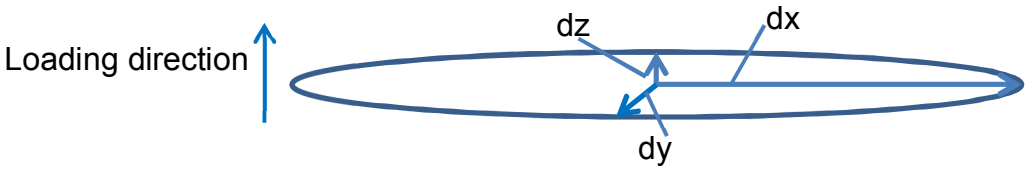

Fig. 7.13: Schematic geometry of the non-metallic inclusions and the loading direction.

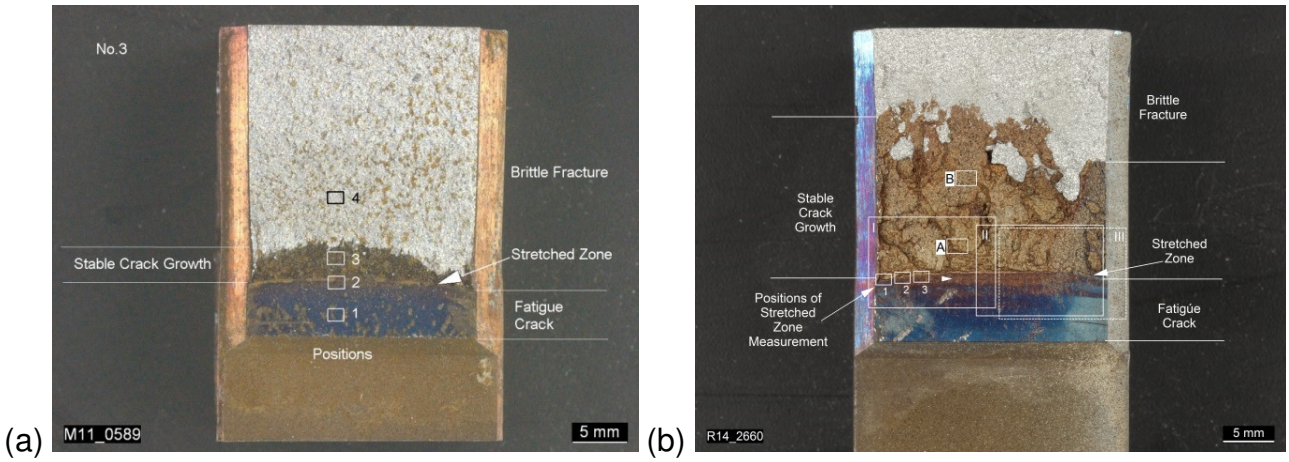

Fig. 7.14: Comparison of fracture surfaces from C(T)-BM specimens tested (a) with ASTM standard and (b) under monotonic loading condition.

In order to simulate the crack shape on the fracture surface of a C(T)-specimen, one quarter of the C(T)-specimen is used for the 3D GTN model because of symmetry. The load is defined on the loading line by external displacements, the finite element mesh and boundary conditions are shown in Fig. 7.15. The GTN parameter set summarized in table 5.2 and the GTN parameter set but with f_0=0.002 (instead of f_0=0.0001) are used for the calculations. As can be found in Fig. 7.16(a), when the GTN parameter set summarized in table 5.2 is adopted (f_0=0.0001), the 3D GTN model can predict a similar shape of the fracture surface where the crack propagation is longer in the center but shorter on the surface of the specimen and possesses a similar crack length (maximal crack length in the center of the specimen is 2 mm due to 2 elements is damaged (red)). However, the maximal predicted crack length from the 3D GTN calculation (f_0=0.002) is 6 mm which is less than the experimental observation of the C(T)-BM tested with monotonic tensile loading (Fig. 7.14). This is because in a monotonic loading process of the C(T)-specimen, beside the flat crack, other fracture mechanisms (slant fracture) (judged from the rugged shape of the stable crack growth region as shown in Fig. 7.14(b)) also contribute to the final fracture, making the maximal crack length on the fracture surface of the C(T) being longer than the simulation result.

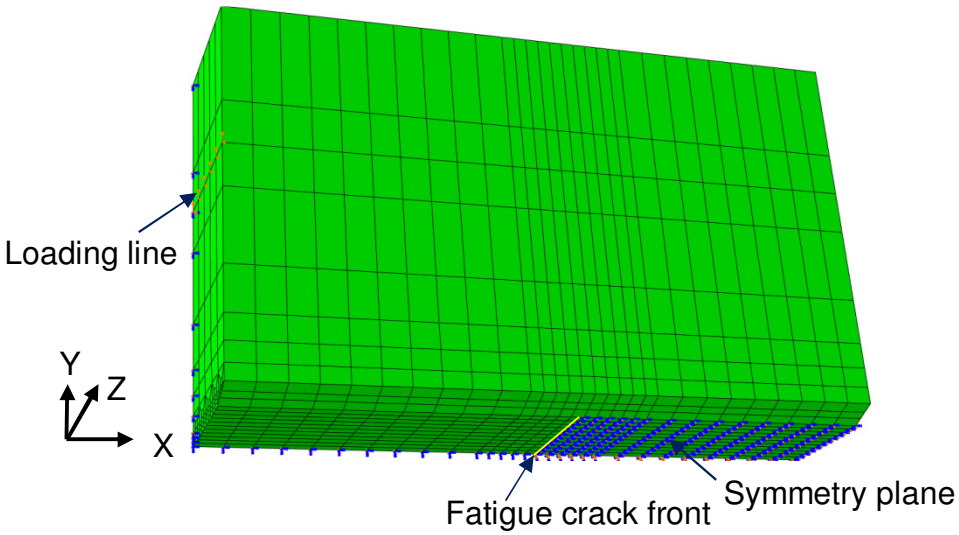

Fig. 7.15: Finite element mesh and boundary conditions of one side grooved C(T)-specimen.

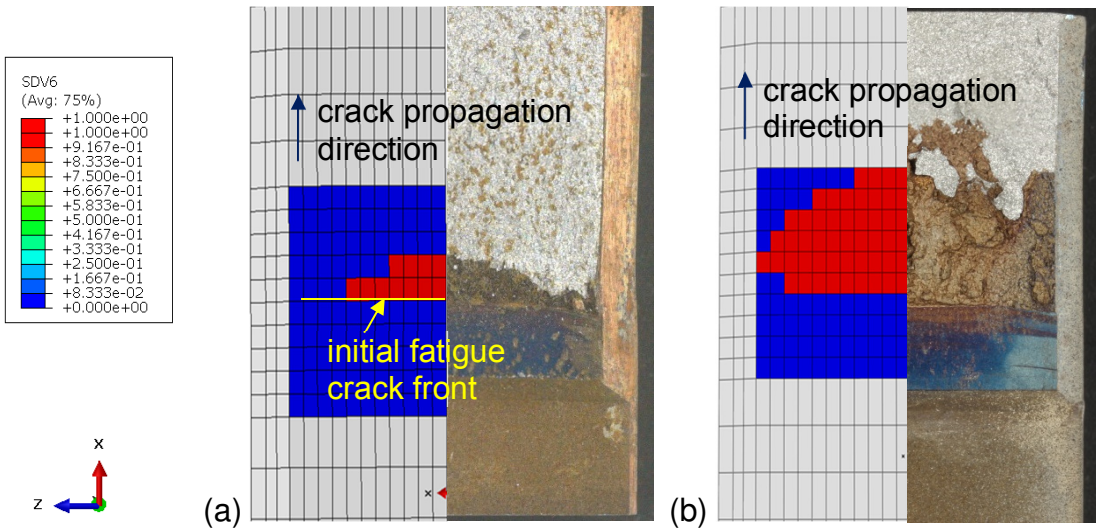

Fig. 7.16: 3D Simulation of fracture surfaces from GTN model when (a) f_0=0.0001 and (b) f_0=0.002.

7.4 Discussion and Conclusions

The ARAMIS system is used to monitor the crack propagation at the side groove of a C(T)-specimen. During the monotonic loading process of C(T) specimens in combination with the ARAMIS system, some technical problems should be noticed or be solved. Firstly, in order to have high quality pictures captured by the ARAMIS camera, a pattern with a sharp contrast should be prepared on the surface of the C(T)-specimen, especially in the notched area where the crack propagation will occur. Low contrast patterns or poor patterns cannot be recognized by the ARAMIS system which will affect the monitoring of the crack propagation. Secondly, the camera should be adjusted to the right place in front of the specimen, where the proper notched region of the C(T) can be viewed from left and right cameras. The notched region should be small enough to capture the tiny variation of crack propagation. However, a too small observation area may miss some crack propagation since the observation areas may jump outside the view. Thirdly, in order to quantitatively analyze the crack propagation of the C(T), small frame rate of the ARAMIS system as possible should be adopted. However, one picture per 0.4 seconds is used for the current test as the limitation of the storage ability of the existing ARAMIS system (max. storage amount to around 500 pictures in one test). A low frame rate results in missing important crack propagation information during the monotonic loading process of the C(T) specimen. An advanced ARAMIS system with higher picture storage ability during one test is required. This suggest to increase the monitoring frame rate to store more pictures during the

experiment and to provide more exact information of crack propagation, making a quantitative analysis possible. Although the current ARAMIS machine cannot quantitatively analyze the crack propagation of the side grooved C(T)-specimen, the ARAMIS system shows the ability monitoring the crack propagation at the notched region of the C(T)-specimen during the test process. Some damaged materials are assumed as non-damaged ones because of the existing spray points on the broken surfaces where in reality they are damaged. Some un-destructive regions are assumed as damaged ones because of the losses of the spray points on the material surface due to serious deformation. The unexpected loss of the adherences of spray paints on the monitored region results in the wrong calculation of the ARAMIS software and can explain why the current ARAMIS system cannot calculate the correct crack lengths on the surface of the C(T) at each loading moments. When these technical problems during the tensile test of the C(T) are solved, the test procedure in combination with ARAMIS system may supplement the ASTM standard for testing the fracture toughness of the C(T)-specimens and provides optical images of the crack propagation on the surface of the C(T)-specimens which is required in order to evaluation the damage evolution of specimens.

Since the C(T)-25 specimen tested under monotonic loading condition shows a lower fracture toughness and larger stable crack regions at the fracture surface of the C(T)-specimens than that of the C(T)-specimens tested in the chapter 3 according to ASTM standard [ASTM E1820, 2003], more particles were assumed to be located in front of the initial crack. This assumption is confirmed by the extraction positions of the C(T)-specimens from the welded joints where elongated particles localize in front of the initial fatigue notch of the C(T)-specimens due to the influence of rolling, as shown in Fig. 7.12.

In order to predict the F-COD-curve of the C(T)-specimen, a 2D GTN model was adopted firstly. For the C(T)-specimen tested according to ASTM standard, good agreement between the experimental and numerical F-COD-curves is obtained when the Gurson parameter set shown in table 5.2 is used. For the C(T)-specimen tested in combination with the ARAMIS system, good agreement between the experimental and numerical F-COD-curves is also obtained when the Gurson parameter set shown in table 5.2 except higher f_0 (f_0=0.002) were used for the calculation, showing the GTN model can fit well the fracture behavior of the C(T)-BM. The particles are found as of elongated shape due to the rolling influence, a revised factor F*=20.25 is introduced which the revised void volume fraction

$f_0^*=f_0 \times F^*$. This can explain why the current f_0=0.002 value is 20 times of f_0=0.0001 value which was used in previous GTN calculation.

The 3D GTN model is used in order to predict the fracture surface of one side grooved C(T)-specimen. Similar shapes and crack length (about 2 mm) on the fracture surface of the side grooved C(T)-specimen is obtained when the GTN parameter set summarized in table 5.2 is adopted (f_0=0.0001). However, the 3D GTN model predicts a smaller crack length than the experimental observation when the GTN parameter set summarized in table 5.2 with higher f_0-value is adopted. This is because in monotonic loading process of the C(T)-specimen, both the flat crack and the slant fracture mechanism lead to the final shape of the fracture surface. The slant fracture is not considered in the GTN model calculation, making the calculated crack length on the stable crack region being smaller than the experimental observation.

8. In situ laminography investigation of damage evolution in S355 base material

The ARAMIS system introduced in the previous chapter has been used monitoring the crack propagation for the C(T)-specimen extracted from the S355 base material. The ARAMIS system allows only observing crack propagation at the surface of the object, the evolution of void initiation, growth and coalescence inside the material remains unknown. In order to understand the 3D damage evolution and to show the nature of crack propagation during the material deformation process, it is necessary to adopt a technique to display the imaging of the damage. Without touching the integrity of the entire material, synchrotron radiation-computed laminography (SRCL) allows for capturing a small region of interest out of a relatively large body, which is not accessible by other techniques [Helfen et al., 2005, Cheng, 2013a]. In this chapter, the SRCL technique is adopted to reveal the damage evolution of the S355 BM for the first time. After the reconstruction of the scanning data, 3D visualized laminographic images of the bulk material are shown. The damage evolution and crack propagation in an S355 sheet specimen will be shown and analyzed.

8.1 Laminography

Laminographic imaging was performed on the laminography instrument from the Karlsruhe Institute of Technology (KIT) installed at the high-energy beamline ID15A [Helfen et al., 2005] of the European Synchrotron Radiation Facility (ESRF) in Grenoble, France [Morgeneyer et al., 2014]. The X-ray transmission over the entire scanning region is performed during the scanning process where reliable projection data are acquired. Using a filtered back-projection algorithm [Helfen et al., 2011], a 3D image of the scanned specimen is reconstructed from 2D projections. Figure 8.1(a) depicts the laminography instrument installed at beamline ID15A of ESRF. In order to prevent the sample from severe buckling and out of plane movement during the test process, an anti-buckling device is adopted, as shown in Fig. 8.1(b). The thin sheet specimen together with the loading device is shown in Fig. 8.1(c) where the CMOD is obtained from the opening of two wedging rigs [Morgeneyer et al., 2011; 2013].

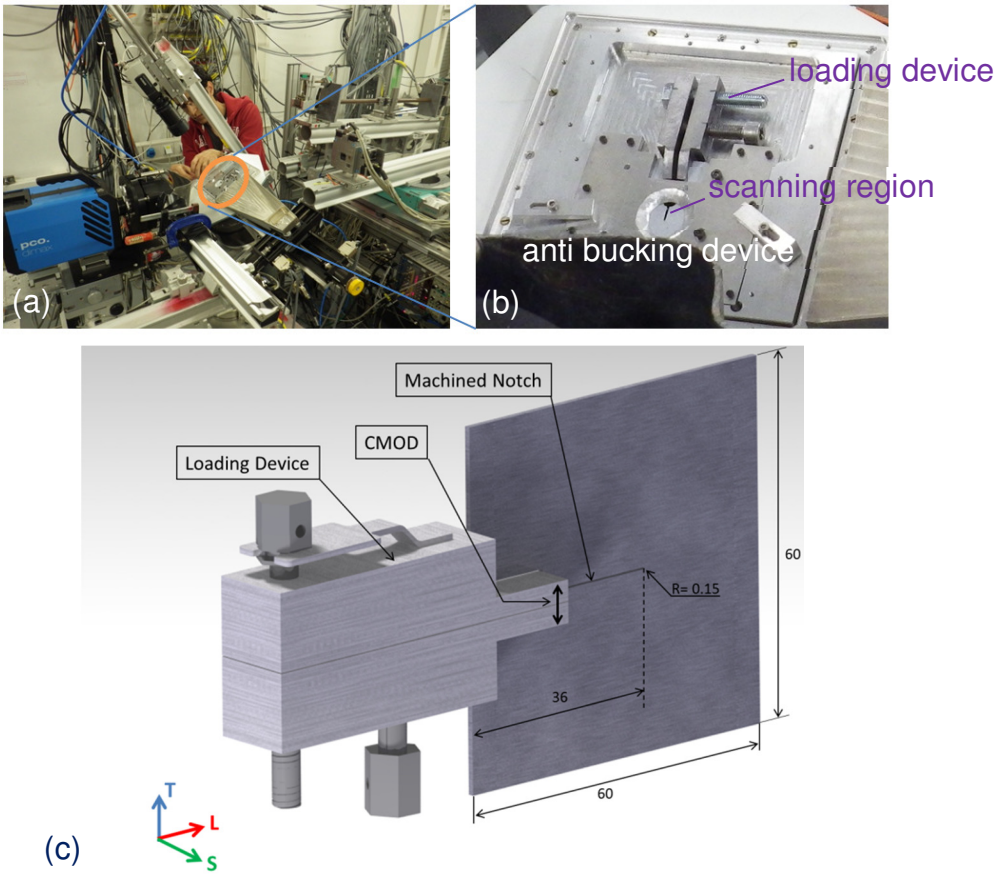

Fig. 8.1: The laminography instrument installed at beamline ID15A of ESRF (a-b) and (c) the thin sheet (1 mm) specimen together with the loading device [Morgeneyer et al., 2011].

In order to reveal the damage evolution of S355 base material, in situ laminography imaging was performed on a 1 mm thick sheet specimen, of which the geometry is shown in Fig. 8.2. The sheet specimen was prepared by Electrical Discharge Machining (EDM) with a width of 60 mm and a height of 60 mm. The notch was manufactured via EDM cutting, where the notch radius is around 0.15 mm which is close to the wire radius. The initial notch length is 36 mm. The loading was performed via a two-screw displacement-controlled wedging rig that controls the specimen crack mouth opening displacement (CMOD) [Morgeneyer et al., 2014]. Stepwise monotonic loading was applied between different laminography scans. A scan was performed before every loading step and the total number of scans is 5. Further details of the mechanical testing are summarized by Morgeneyer [Morgeneyer et al., 2011; 2013].

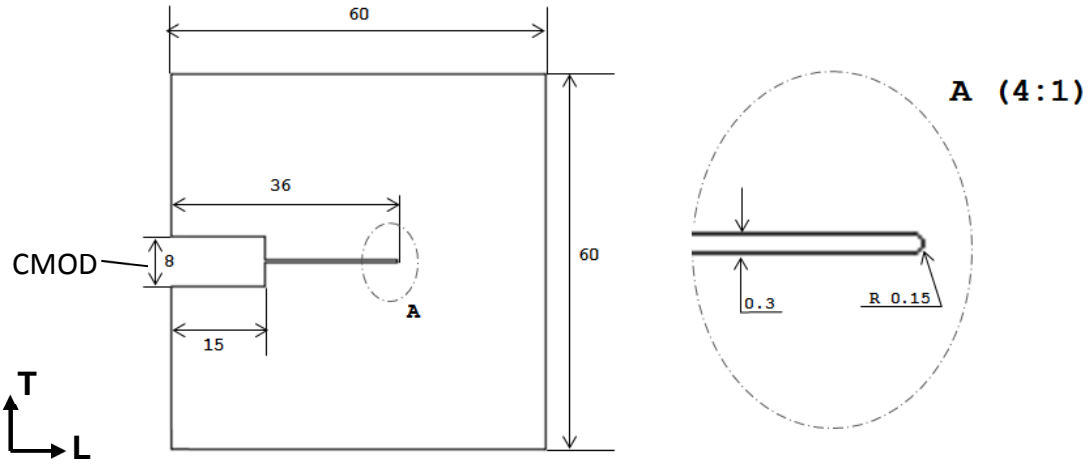

Fig. 8.2: Sketch of the thin sheet (1 mm) specimen used for in situ laminography study with the dimensions of 60 x 60 x 1 mm^3.

8.2 In situ observation of damage evolution by laminography reconstruction

The laminographic reconstruction is performed together with the KIT in house developed reconstruction program [Helfen et al., 2011]. After the reconstruction, the scanning data is saved as '.raw' files which can be processed by the image process and analysis software Image J [Image J, 2012]. The 2D section of 3D laminography data in the middle section of the sheet specimen is shown in Fig. 8.3(a)-(f).

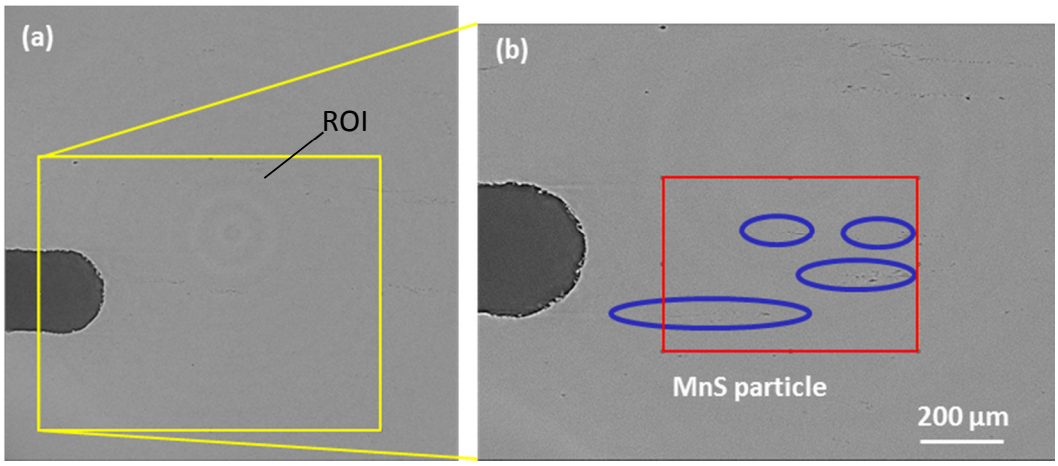

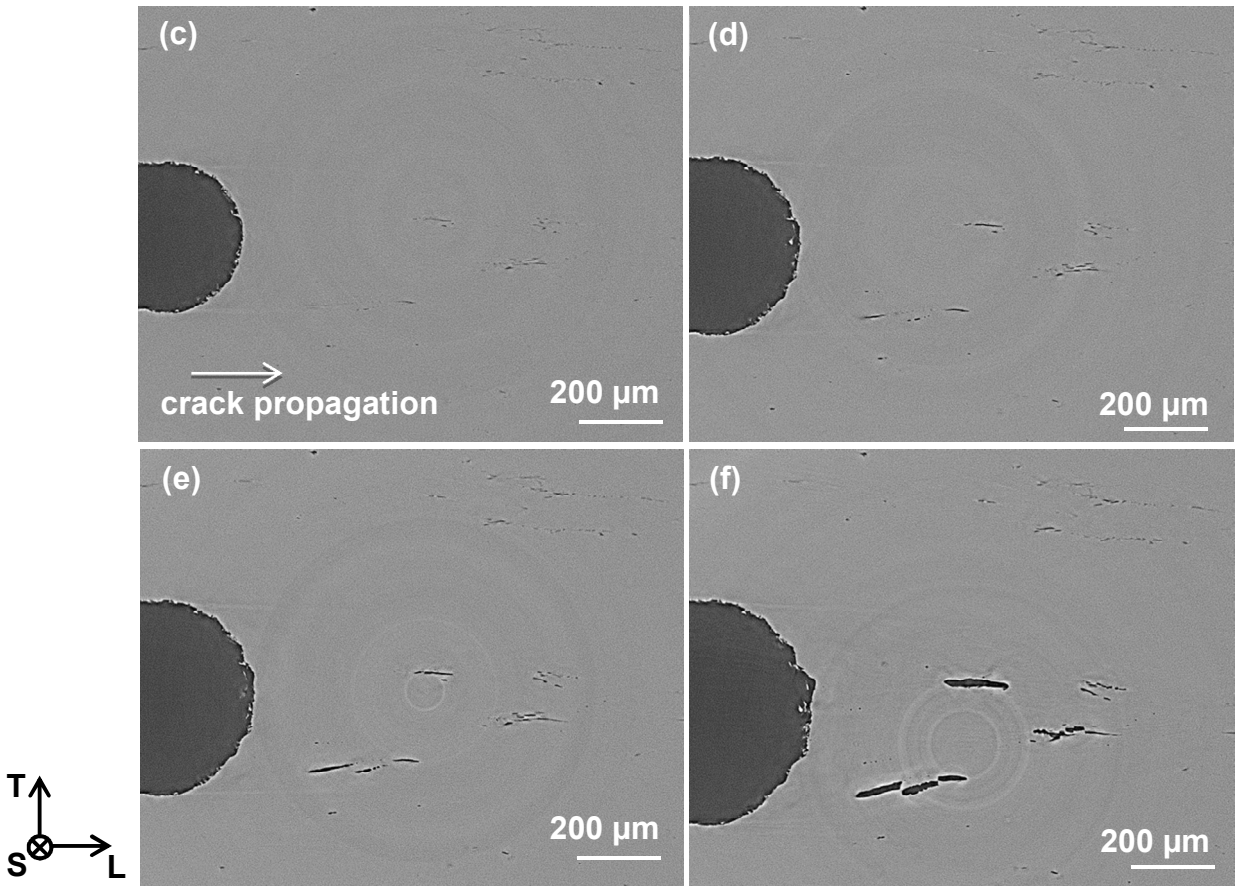

Fig. 8.3: The reconstructed 2D cross-sections (T-L) imaging of the middle section of a sheet specimen at (a) initial status and imaging of region of interest (ROI) at: (b) initial status (c) CMOD=0.625 mm (start of void nucleation) (d) CMOD=1.25 mm (e) CMOD=1.56 mm (f) CMOD=1.875 mm.

The 2D reconstructed imaging of the scanning region before the tensile test is shown in Fig. 8.3(a), which contains the resolution of 1600 x 1600 pixels. Since the effective pixel size is about 1.095 µm, the corresponding size of the scanned region of interest is 1.752 x 1.752 mm^2. The region of interest (ROI) in the marked region contains 960 x 1200 pixels which correspond to an area of 1.051 x 1.314 mm^2, as shown in Fig. 8.3(b). As can be observed in Fig. 8.3(b), MnS particles (based on EDX analysis) which nucleate voids during the material deformation process can be found to be localized in front of the initial notch. The loading test was performed in the T-L configuration, where T is the loading direction, L is the rolling direction which coincides with the crack propagation direction (S is the thickness direction).

After the first stepwise loading (CMOD=0.625 mm), voids originate around the particles, as shown in Fig. 8.3(c). During the material deformation process, microcracks are found

forming around particles due to the evolution of void initiation, growth and coalescence, as shown in Fig. 8.3(d). These microcracks are of elongated flat shape due to the influence of the elongated localized particles. The evidence of the emergence of the microcracks is that black flat regions are surrounded by white edges, showing obvious phase contrast (details are presented later in Fig. 8.4). As shown in Fig. 8.3(e), microcracks grow and combine with each other thus, leading to the appearance of obvious cracks. At the final loading step, existing cracks open widely and neighboring cracks are trying to form the large crack with slant crack propagation, as displayed in Fig. 8.3(f). No cracks are observed in front of the initial notch tip where the stress is maximal. This shows that less energy is required to nucleate a void around one particle than for the pure matrix material, showing the particles give the main contribution to the void nucleation.

Fig. 8.4 shows a zoom out of the rectangular region (marked red in Fig. 8.3(b)) at a distance of 200 µm ahead of the initial notch. As can be found in Fig. 8.4(a), elongated MnS particles with particle sizes of 8-14 µm localize at some regions of the material. MnS particles start to nucleate voids firstly for CMOD=0.625 mm that the particles become darker and are surrounded by a white edge, as shown in Fig. 8.4(b).The sudden emergence of black areas surrounded by the white edges is the hint of the debonding of particles from the matrix. The evidence of voids nucleation from particles is also mentioned by other scientist: when a void nucleates around a particle, the interface between the void and the particle or the void and the matrix leads to strong phase contrast in the used imaging mode [Shen et al., 2013]. Normally the existing initial void is spherical and is surrounded by the white edges before loading. This is different from the void nucleate from elongated particles where the voids are also elongated. After the second loading steps (CMOD=1.25 mm), obvious cracks are found which due to the void coalescence around particles and the combination process of neighboring microcracks, as shown in Fig. 8.4(c). The process of void nucleation, growth and coalescence happens at almost every particle. Existing cracks forming from previous loading steps open widely and neighboring cracks connect each other, forming the obvious big cracks, which are shown in Fig. 8.4(d). After the last loading step (CMOD=1.875 mm), several large cracks are found in front of the initial notch, as shown in Fig. 8.4(e). Although the material deformation between these large cracks are high, no microcracks are found between these main cracks, showing the voids are mainly originating from particles and give the main contribution to cracks during the damage evolution.

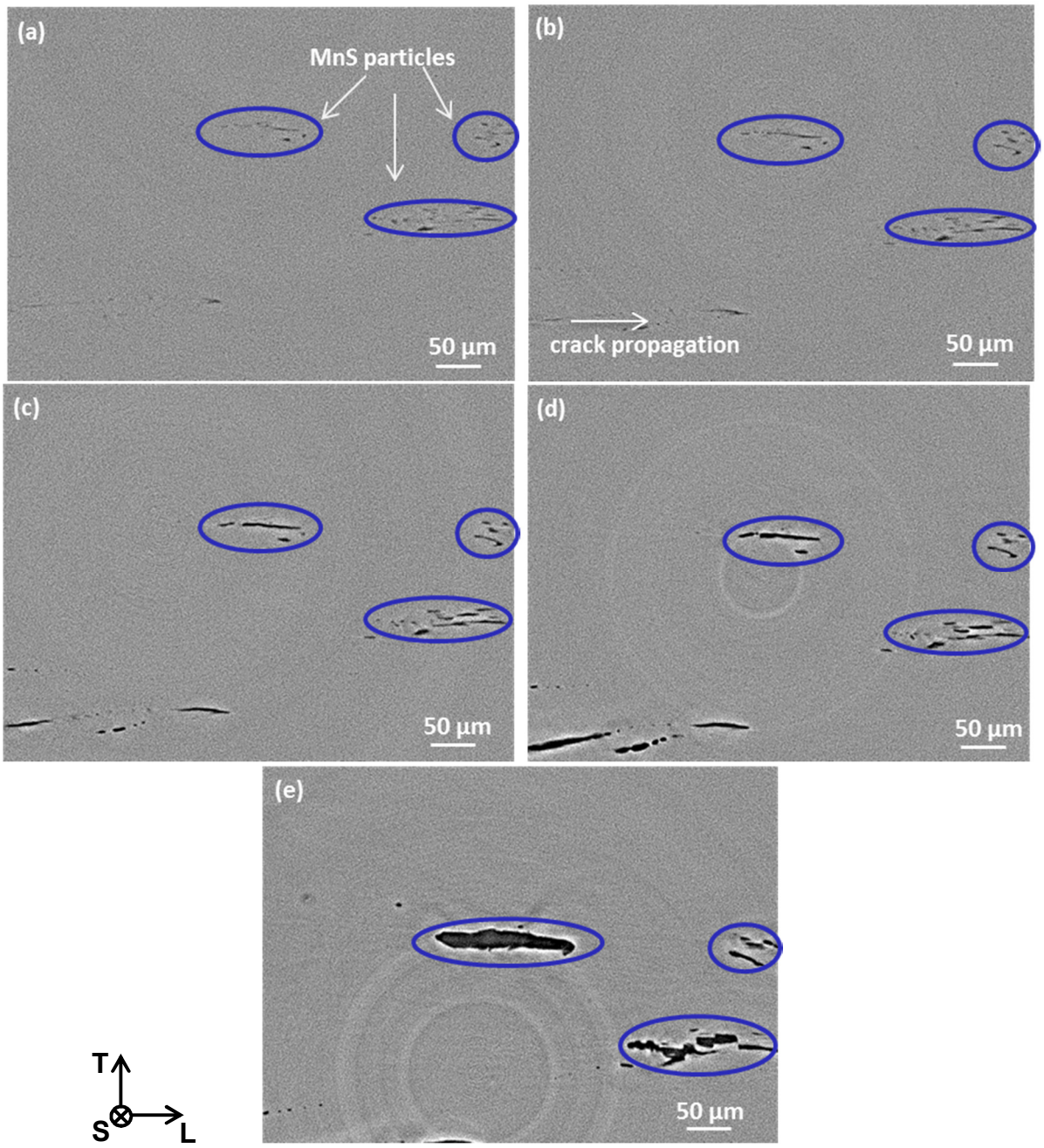

Fig. 8.4: Zoom of the rectangular region of middle section (in red color) in Fig. 8.3(b) at (a) initial status (b) CMOD=0.625 mm (c) CMOD=1.25 mm (d) CMOD=1.56 mm (e) CMOD=1.875 mm.

Reconstructed 2D laminography imaging of the scanning layer around 200 µm away from the middle section of the 1 mm thin sheet specimen is shown in Fig. 8.5(a)-(f) where the longest 2D crack is observed. The 2D imaging of the scanning region and the corresponding ROI before the stepwise loading is shown in Fig. 8.5(a)-(b). The particles are observed localize in front of the initial notch which is marked in Fig. 8.5(b). After the first loading step (CMOD=0.625 mm), microcracks are found ahead of the notch where the local

stresses are assumed maximum, see Fig. 8.5(c). After the second loading step (CMOD=1.25 mm), the microcracks ahead of the notch connect with the neighboring elongated crack, forming the first main crack, which is shown in Fig. 8.5(d). The second large crack is observed in front of the first big crack. Between these two major cracks, there exist some small cracks originated from particles during material deformation. The two major cracks open wider and small cracks between the two major cracks grow at CMOD=1.56 mm, as shown in Fig. 8.5(e). After the last loading step (CMOD=1.875 mm), the main crack propagates towards the second crack in order to form the final main crack of the thin sheet specimen, see Fig. 8.5(f). Void sheet mechanisms [Garrison et al., 1987] are expected to happen between these two cracks in the later material deformation stage due to the formation of shear band between these two cracks.

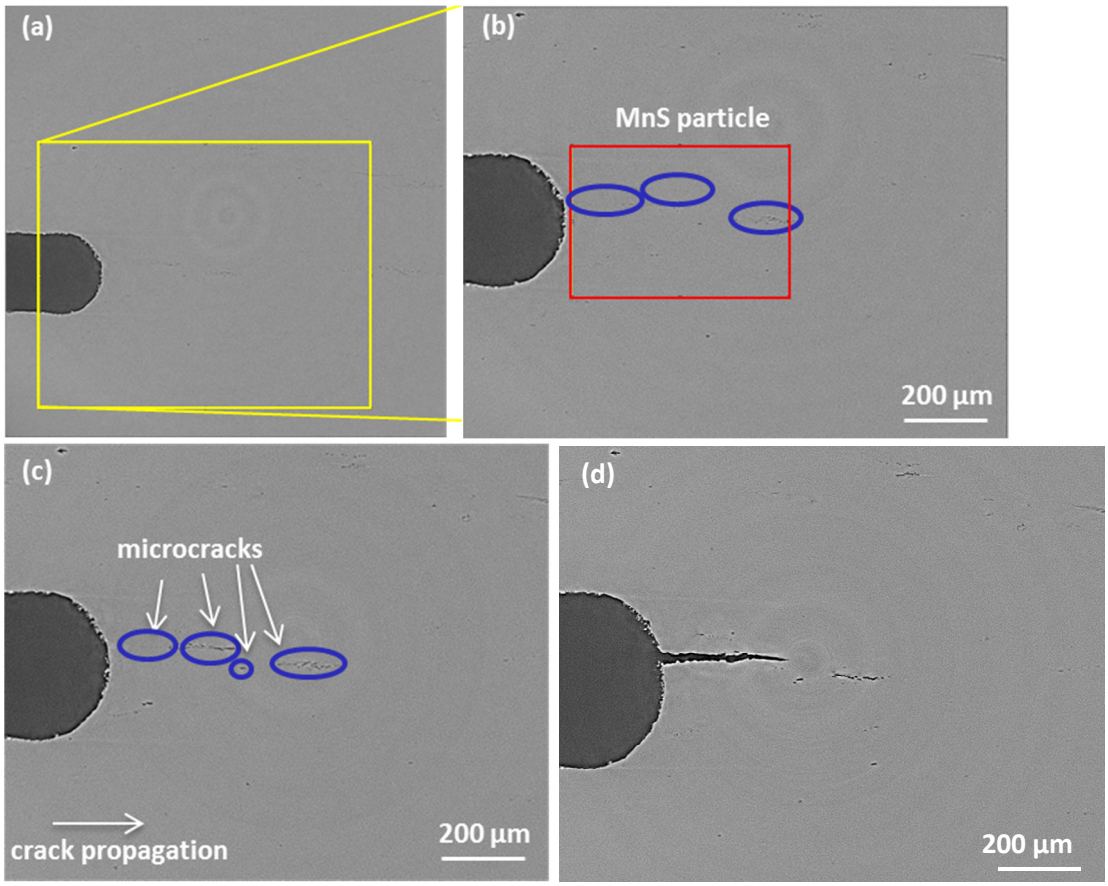

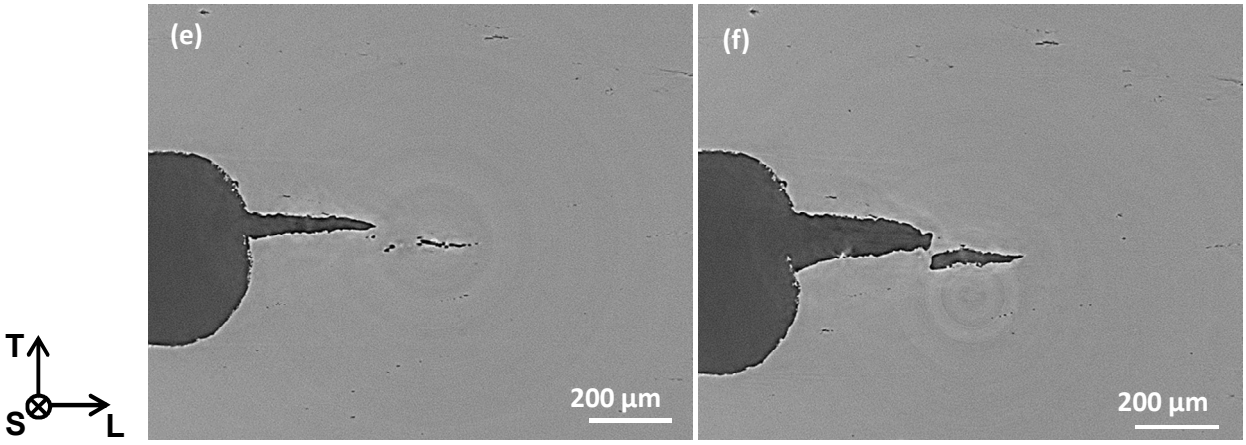

Fig. 8.5: Imaging of 2D cross-sections (T-L) at the scan layer which is about 200 µm from the middle section of the sheet specimen at (a) the initial status and the image of region of interest (ROI) at: (b) the initial status, (c) CMOD=0.625 mm,(d) CMOD=1.25 mm, (e) CMOD=1.56 mm, and (f) CMOD=1.875 mm.

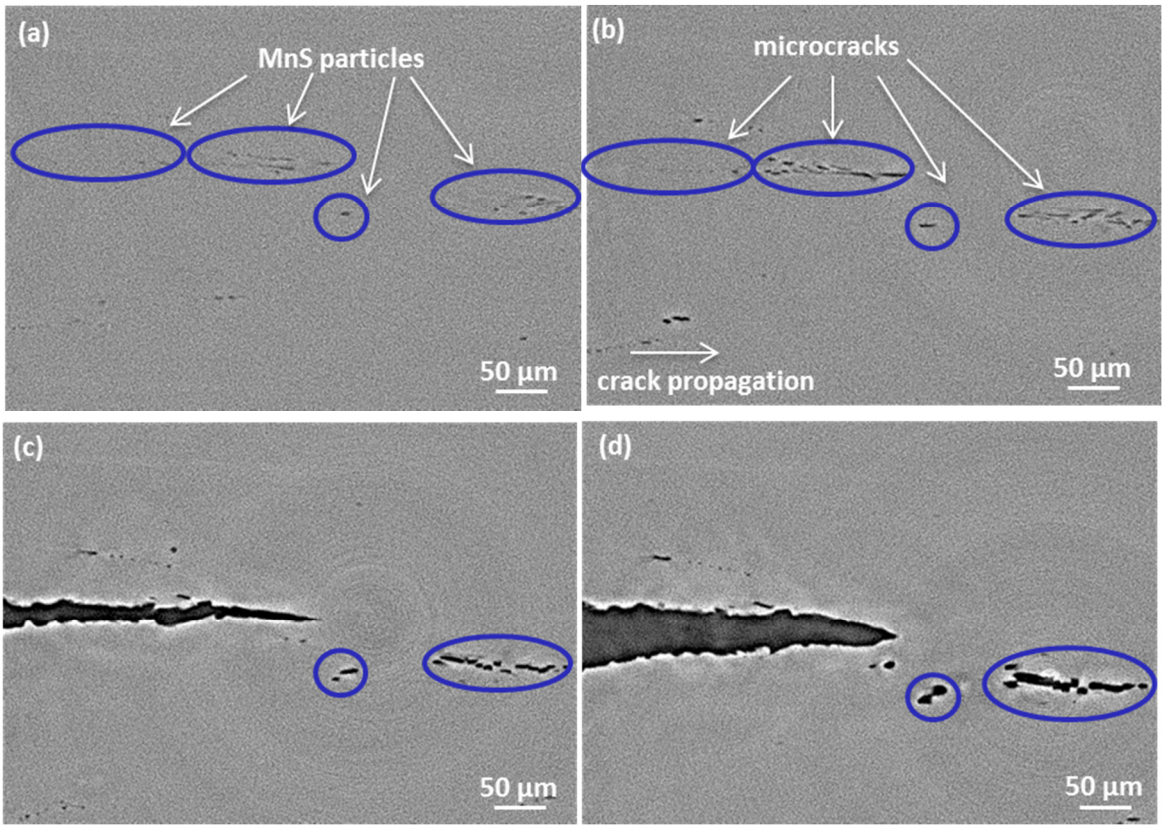

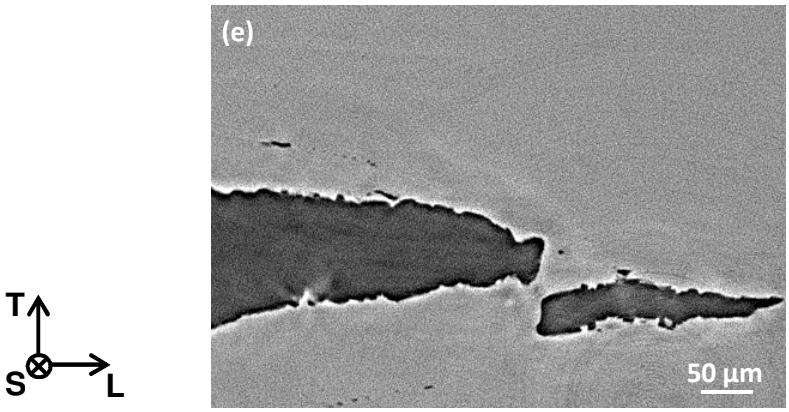

Fig. 8.6: Zoom of the rectangular region (in red color) in Fig. 8.5(b) (200 µm from the middle section) during the damage evolution of the thin sheet specimen at: (a) initial state, (b) CMOD=0.625 mm, (c) CMOD=1.25 mm, (d) CMOD=1.56 mm, and (e) CMOD=1.875 mm.

Fig. 8.6(a)-(e) show the zoom out of the rectangular region (marked red in Fig. 8.5(b)) with a distance of 15 µm ahead of the initial notch root. As can be seen from Fig. 8.6(a), elongated MnS particles localize at some regions. MnS particles start to nucleate voids firstly after the first loading step (CMOD=0.625 mm), as shown in Fig. 8.6(b). This can be seen by the particles becoming darker and being surrounded by a white edge. As these particles mainly localize in front of the initial notch, void coalescence and the combination of neighboring microcracks happens quickly. Therefore, obvious cracks connect with initial notch, forming the main big crack, as displayed in Fig. 8.6(c). Another large crack is formed which is about 100 µm ahead of the first big crack. Between these two large obvious cracks, some small cracks are found due to the void initiation, growth and coalescence. After the third loading step (CMOD=1.56 mm), the existing long cracks open widely, trying to connect with each other as shown in Fig. 8.6(d). The second main cracks are formed ahead of the first main crack due to the combination of cracks and their neighboring minor cracks after the previous loading step. These two main cracks expand and propagate along the loading (T) direction, and are expect to connect with each other in the subsequent loading, as shown in Fig. 8.6(e)

The comparison between laminographic results from T-L cross sections of the sheet specimen, i.e., the middle section (Fig. 8.3) and the section where the longest 2D cracks are located (Fig. 8.5) is addressed here. At the material initial status, particles localize at some regions in front of the initial notch for both cross sections. For the center section of the specimen, particles cluster in some regions which are far away from the initial notch, as

shown in Fig. 8.3(b). No cracks are found connected with the initial notch when CMOD=1.25 mm, obvious cracks localize at some regions far from the initial notch, as displayed in Fig. 8.3(d). For the cross section which is 200 μm from the middle section, as the particles cluster in regions near the initial notch, an obvious large crack connects with the initial notch, forming the main crack after the second loading step (CMOD=1.25 mm), as shown in Fig. 8.5(d). The main cracks are observed at the cross section (Fig. 8.5) which is 200 μm from the middle section (Fig. 8.3) showing the particles are prominent in creating voids during the material deformation process and this is a more important factor than local stresses.

It is interesting to see in details the damage evolution through the thickness direction (T-S). The first cutting through thickness is 100 μm ahead of the initial notch, which is shown in Fig. 8.7(a). As shown in Fig. 8.7(b), both left and right material boundaries are observable and parallel to the T direction before loading. After the first loading step (CMOD=0.625 mm), mirocracks together with small cracks are found along the S direction and some cracks locate on the right boundary, as shown in Fig. 8.7(c). The material boundaries begin to shrink after the first loading step. After the second loading step (CMOD=1.25 mm), due to the combination of neighboring microcracks, two large cracks are found located at different positions along the T direction and both cracks are around 1/3 position from the left boundary of material. A shear band where the orientation of the band is about 45˚ from the thickness direction (S direction) is visible between the two neighboring cracks and the cracks located at the right surface boundary become larger, as shown in Fig. 8.7(d). When the material deformation continues, the material boundary continues shrinking, more shear bands are found between neighboring cracks (Fig. 8.7(e)), leading to the variation of the crack tunnel along the thickness (S) direction and emergence of a slant crack propagating after the last loading step (CMOD=1.875 mm), as depicted in Fig. 8.7(f). Two different types of crack mechanisms are found during the damage evolution process. The first one is flat cracking due to void initiation, growth and coalescence. In the second mechanism, shear bands are forming around cavities or between two neighboring cracks, forming shear cracks during the material deformation process. Shear crack propagation changes the crack tunnels formed during the flat crack propagation. Before the appearance of shear cracks, several discontinuous cracks along the S direction are found. This shows that the cracks propagate not only mainly along the L direction but also along the thickness direction during the damage evolution. Moreover, shear cracks appearing at the 2D T-S cross

section are also observed, showing the complexity of the real damage evolution of the thin sheet specimen. The nature of the damage evolution of the sheet specimen shows the current 2D model cannot accurately describe the damage evolution of the 3D material as well as the crack propagation both along the L direction and also along the thickness direction. It is, thus, necessary to establish a 3D damage mode prediction the 3D crack propagation.

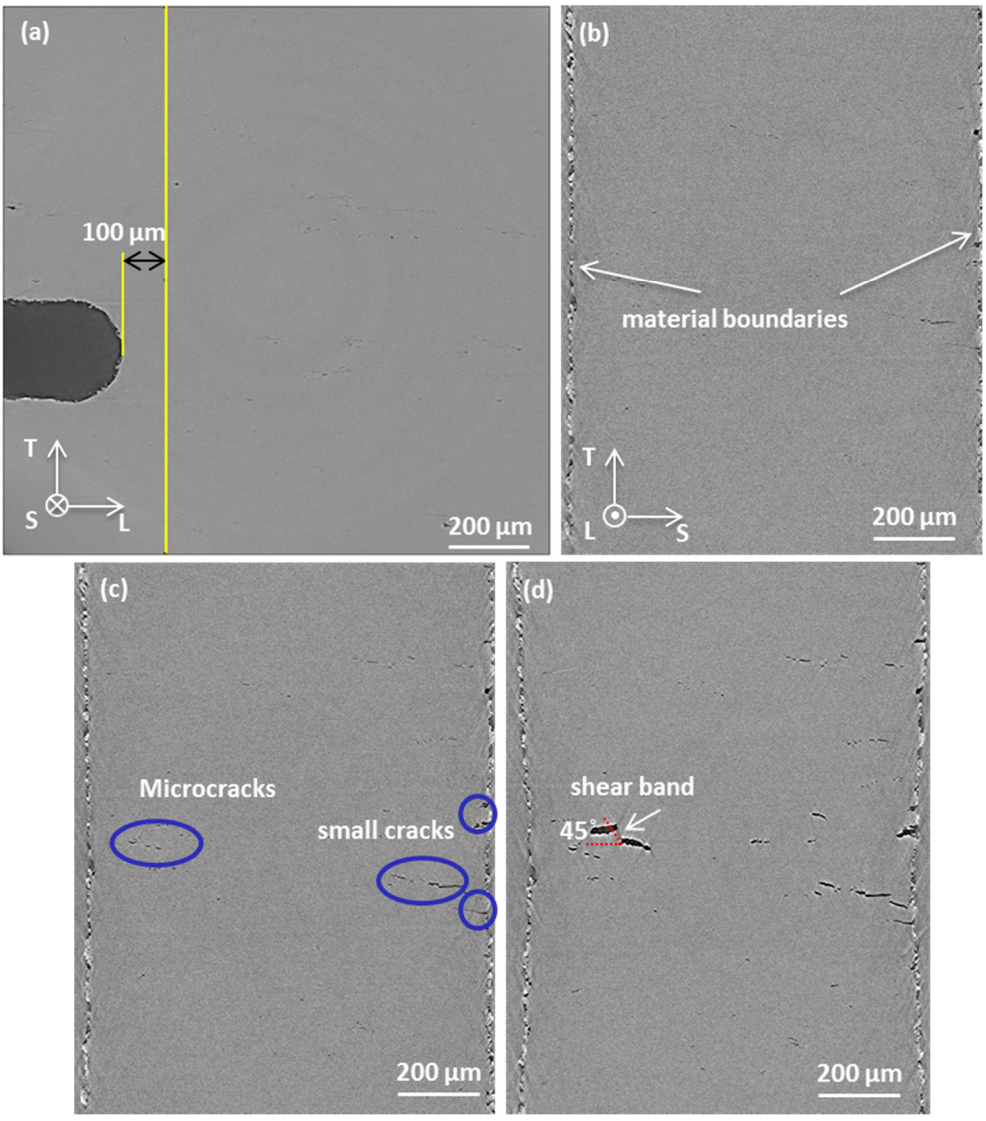

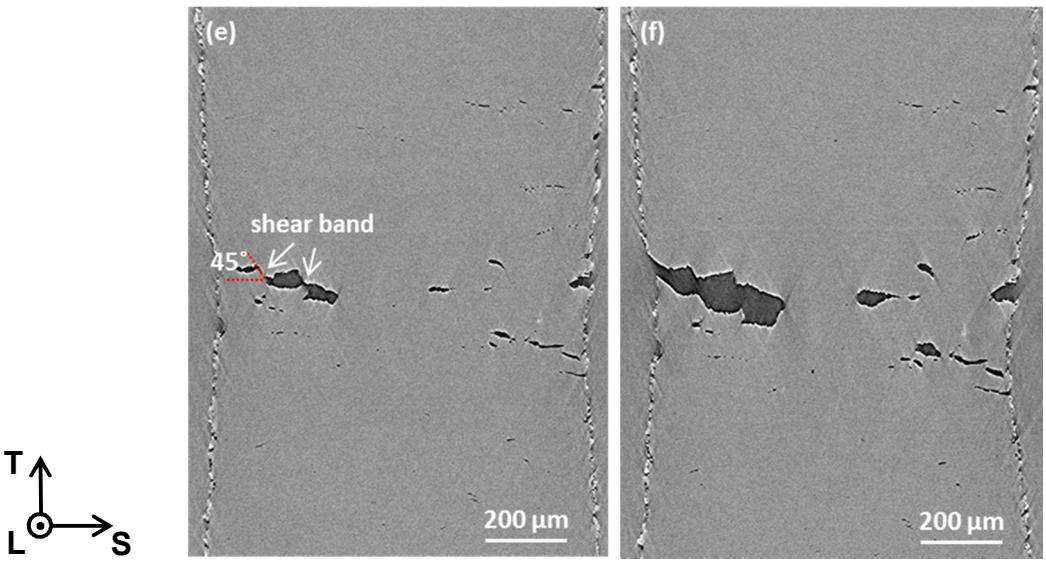

Fig. 8.7: 2D cross-sections at the through thickness (T-S) plane which is 100 µm from the initial notch shown with increasing crack mouth opening displacement (CMOD): (a) The through thickness position and damage evolution at: (b) initial status, (c) CMOD=0.625 mm, (d) CMOD=1.25 mm, (e) CMOD=1.56 mm and (f) CMOD=1.875 mm.

The second through thickness scanning is performed 400 µm ahead of the initial notch tip, which is shown in Fig. 8.8(a). As shown in Fig. 8.8(b), no obvious void or microcrack is observed before loading. One obvious particle is found at the material surface, as shown in Fig. 8.8(b). After the first loading step, some microcracks and cracks are observed, as shown in Fig. 8.8(c). In comparison to cutting position one (100 µm ahead of the notch tip), less elongated cracks are found along the thickness direction. Some cracks (less than what is observed in position one) arise at the material surface, as shown in Fig. 8.8(d). This is because the material in the position two (400 µm ahead of the notch tip) is far from the initial notch root. The material deformations in position two (400 µm) is smaller than that of position one (100 µm) and the corresponding local stresses are smaller, leading to less void initiation, growth and coalescence. Some obvious cracks are found in Fig. 8.6(d) due to the combination of existing small cracks shown in Fig. 8.6(c). The length of the cracks and the number of cracks observed in Fig. 8.6 in position two is shorter and smaller than in position one. The material boundaries begin to shrink after the last loading step, cracks can be found at the surface and a shear band is observed between two cracks, as displayed in Fig. 8.8(f). The delayed appearance of shear bands when CMOD=1.875 mm (the shear band appears in position one at CMOD=1.25 mm) in position two is mostly influenced by lower material deformation and lower stresses than in position one (100 µm).

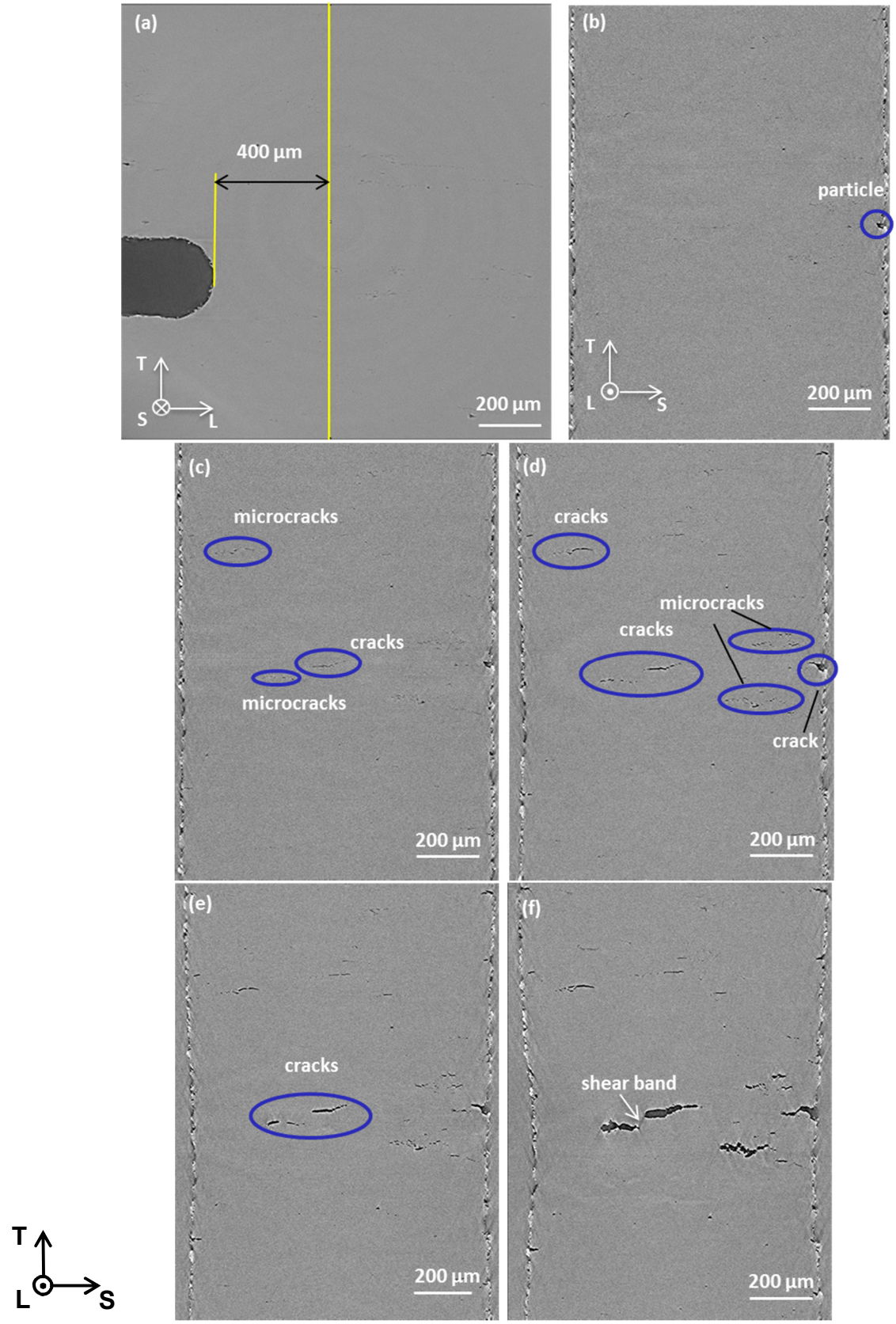

Fig. 8.8: 2D cross-sections at the through thickness (T-S) plane which is 400 µm from the initial notch shown with increasing crack mouth opening displacement (CMOD): (a) The through thickness position and damage evolution at: (b) initial status, (c) CMOD=0.625 mm, (d) CMOD=1.25 mm, (e) CMOD=1.56 mm, and (f) CMOD=1.875 mm.

Laminographic images are processed to binary pictures with the Image J software [Image J, 2012]. The optical separation of the particles and matrix are made where the initial voids and particles are marked as one color and the matrix are another. In order to build 3D laminographic imaging, all binary images are combined using the commercial 3D visualization software Amira which is a powerful 3D visualization viewing and analysis tool [Amira, 2009].

The initial status of the S355 base material is shown in Fig. 8.9. The initial notch is shown in green color and the boundary of the notch is dark green. Elongated MnS particles and spherical voids are also shown in green color while the matrix is in white. The initial voids are smaller than the particles and randomly distributed in the bulk material. MnS particles localize at some regions, especially in marked layers inside the 3D cubic bulk, see Fig. 8.9. The reason for the occurrence of flat laminated particles is due to the rolling influence during the production of the material. After the first loading step (CMOD=0.625 mm), as the stress ahead of the initial notch is high in comparison to other regions and due to the existence of particles, many new green laminated layers are found which represent the formation of voids or mirocracks, as shown in Fig. 8.10. After the second loading step (CMOD=1.25 mm), due to the combination of neighboring microcracks ahead of the initial notch, two main cracks are formed in front of the initial notch and some voids are trying to connect with the initial notch (green color in front of notch), as shown in Fig. 8.11. It is expected that the main crack will emerge in front of the initial notch during the further deformation process. Some initial voids are found at other regions which are far from the initial notch and the volume fraction is small. During the material deformation process, almost no void coalescence happens in material regions far from the notch because the stresses are not sufficient to drive the damage evolution of void initiation, growth and coalescence. After the third loading step (CMOD=1.56 mm), neighboring microcracks connect with each other in front of the initial notch, forming obvious cracks (dark green color), as shown in Fig. 8.12. The main two cracks are close, a shear band is found between these cracks and shear cracks connecting the neighboring cracks are expected in the next loading step. The cracks propagate and deviate quickly in front of the initial notch where the local stress is the highest and the final big crack is depicted in Fig. 8.13. Meanwhile, more microcracks are found at other positions in front of the initial notch. In order to visualize the 3D flat cracks in the laminographic imaging, the scanning data contained in the laminographic image at CMOD=1.25 mm is subtracted from the information

contained in the laminographic image at the initial status, then the flat crack propagation is displayed in Fig. 8.14 (dark purple). The cracks are observed localizing in front of the initial notch. The crack shape due to the emergence of shear cracks can also be visualized in the laminographic imaging. The scanning data contained in the laminographic image at CMOD=1.875 mm is subtracted from the information contained in the laminographic image at CMOD=1.25 mm, the crack propagation between CMOD=1.25 mm and CMOD=1.875 mm is presented in Fig. 8.15 (dark purple). The cracks propagate not only along the rolling direction (L) but also along the loading direction (T) and through the thickness direction (S).

The 3D laminographic images show that the elongated particles localize at some regions in the bulk material before loading. This information of clustered particles coincides with the metallographic investigations of S355 base material as shown in chapter 3.2. The volume fraction of all inclusions (initial voids plus MnS particles) for the thin sheet specimen is 0.0015 which is calculated from the Image J software. Due to huge expense and time consuming of the laminographic scanning, it is suggested to get the volume fraction of inclusions (f_0) from metallographic investigations if the laminographic analysis is not available. This value obtained from metallographic investigation is reliable for the calculation with the 2D Rousselier model as discussed in chapter 4 but not exactly for the 3D calculation. What is more, slant cracks which originate from the shear coalescence between the neighboring microcracks are found after some loading steps of the sheet specimen tested in the laminographic experiment. This fracture mechanism is different from the situation of a standard C(T)25 specimen with side grooves tensile tested as described in chapter 3 where crack propagation is straight. This shear fracture mechanism has not been explained and simulated in the current GTN model and the Rousselier model where the damage evolution is primarily influenced by the hydrostatic stresses due to the basic equations of the GTN model and the Rousselier model [Bleck et al., 2009].

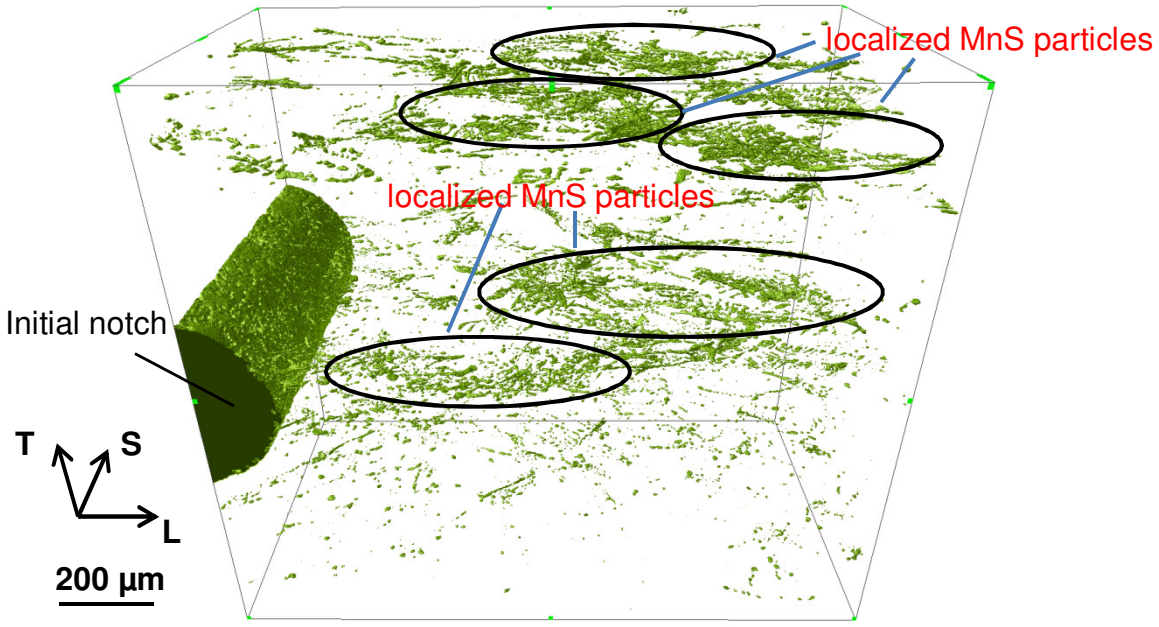

Fig. 8.9: 3D laminographic imaging (L x T x S=1200 x 960 x 600 µm^3) at the initial status. The green color shows the presence of MnS precipitates and initial voids.

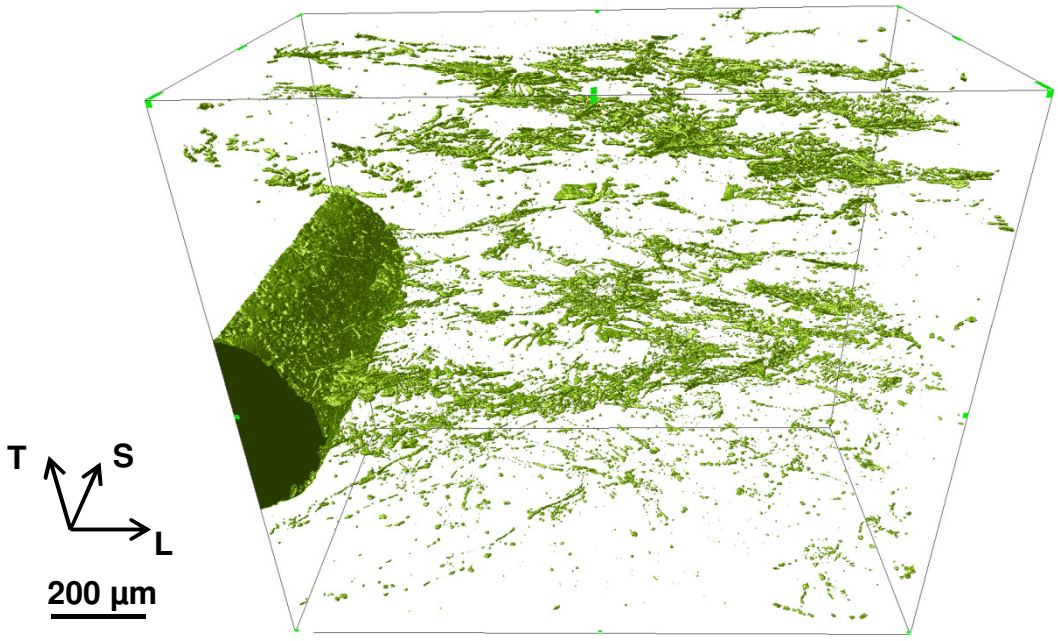

Fig. 8.10: 3D laminographic imaging (L x T x S=1200 x 960 x 600 µm^3) when CMOD=0.625 mm.

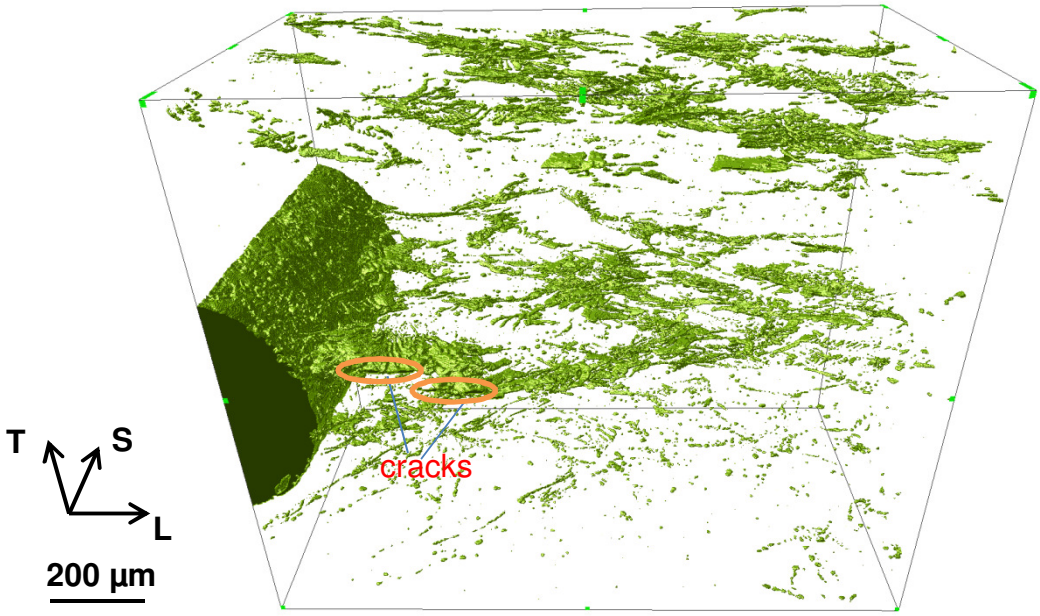

Fig. 8.11: 3D laminographic imaging (L x T x S=1200 x 960 x 600 µm^3) when CMOD=1.25 mm.

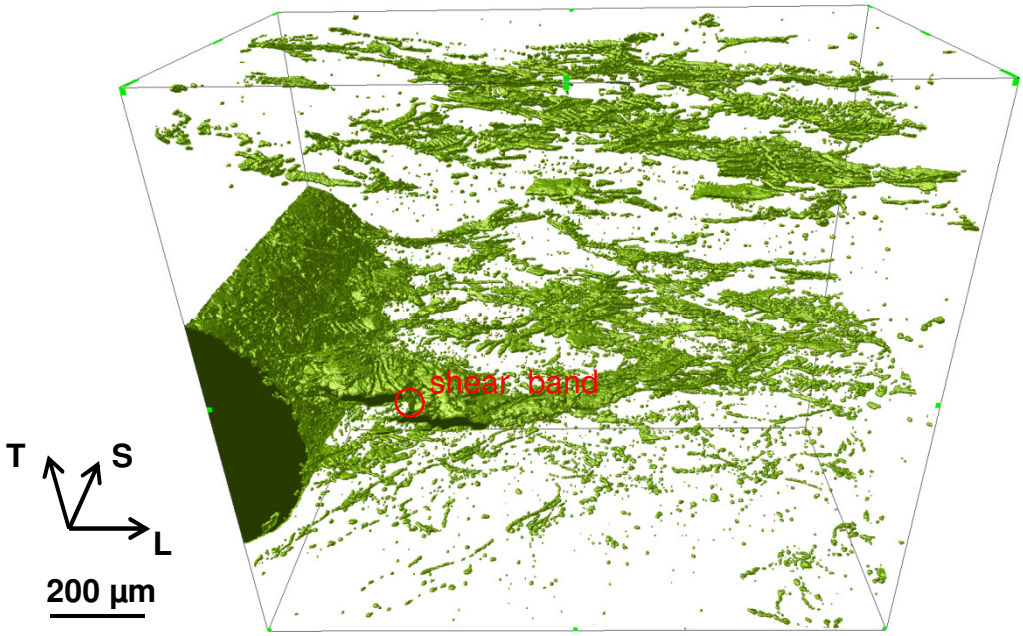

Fig. 8.12: 3D laminographic imaging (L x T x S=1200 x 960 x 600 µm^3) when CMOD=1.56 mm.

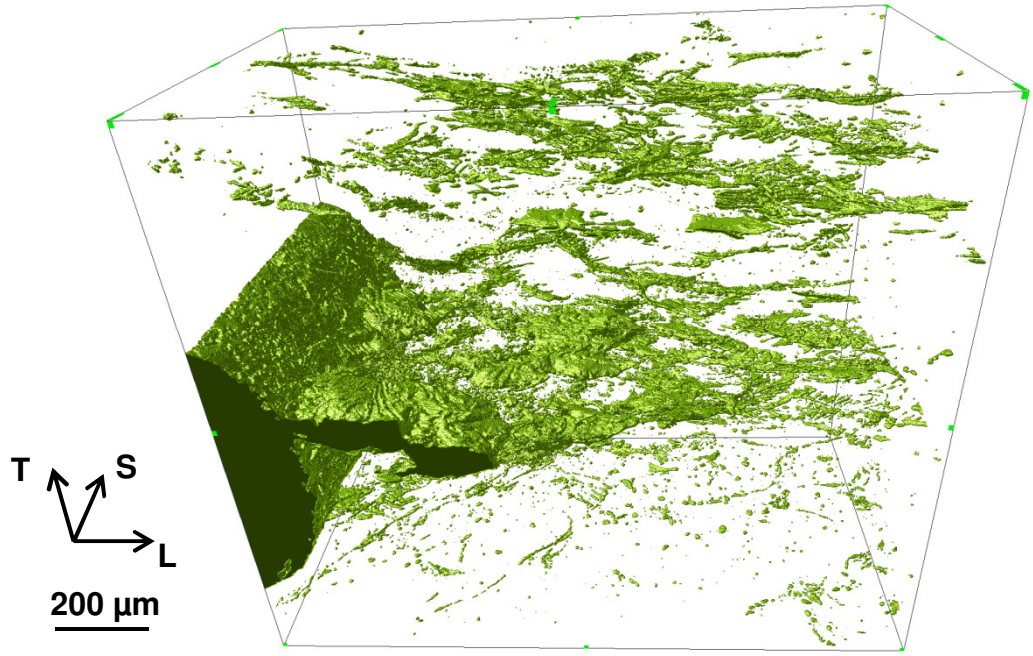

Fig. 8.13: 3D laminographic imaging (L x T x S=1200 x 960x 600 µm^3) when CMOD=1.875 mm.

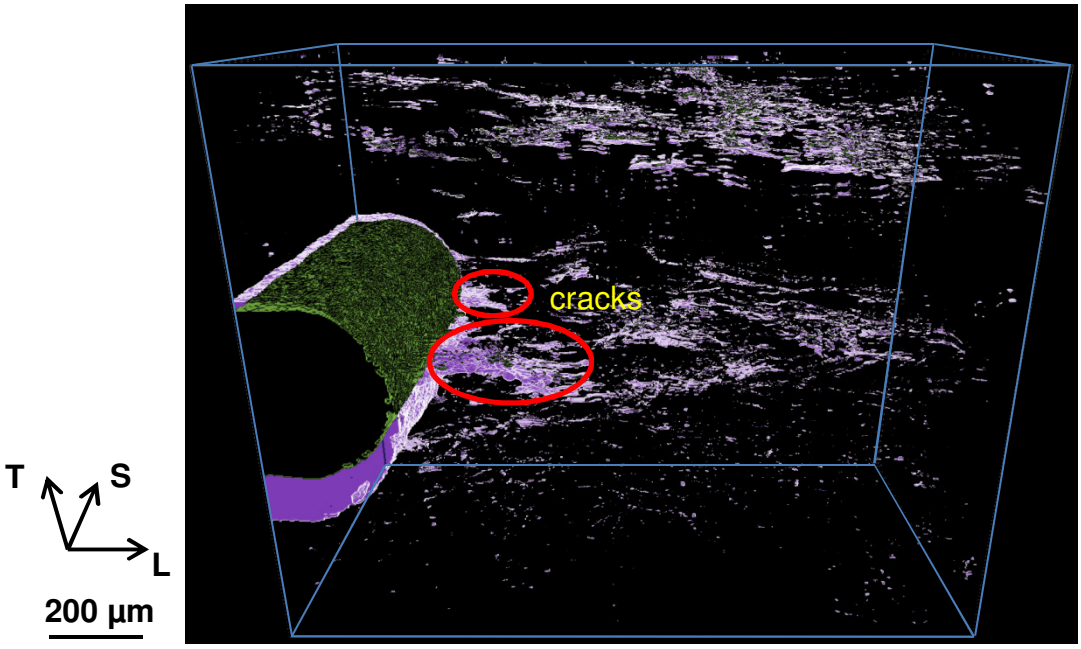

Fig. 8.14: 3D laminographic imaging (L x T x S=1200 x 960x 600 µm^3) showing the crack propagation (dark purple) when CMOD=1.25 mm.

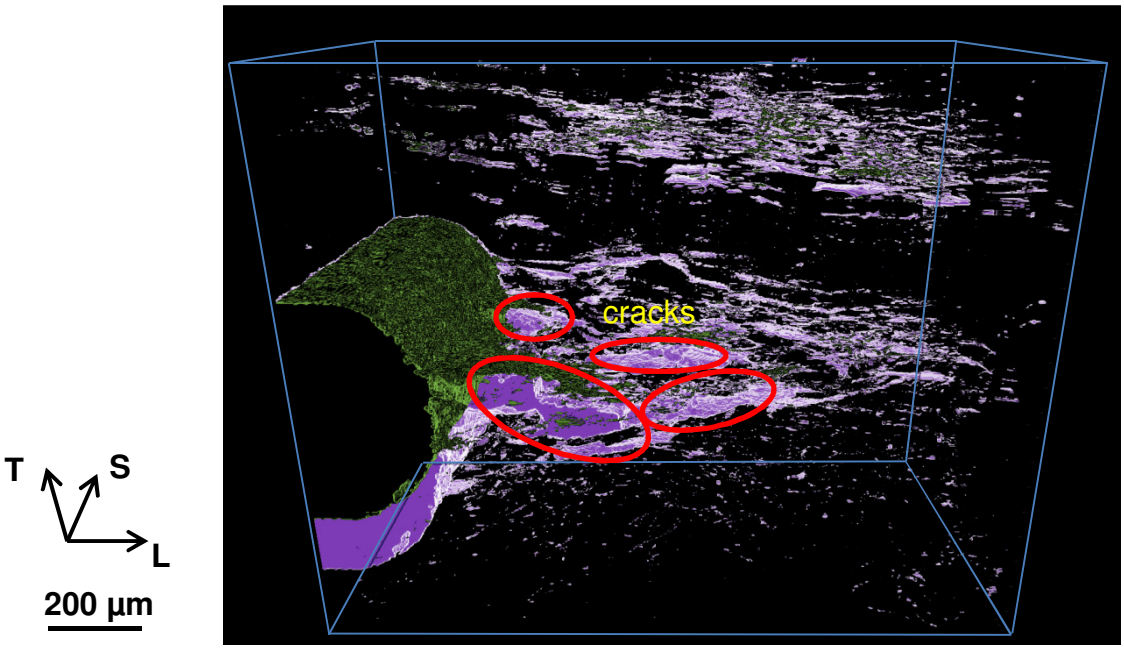

Fig. 8.15: 3D laminographic imaging (L x T x S=1200 x 960x 600 μm^3) showing the crack propagation (dark purple) between CMOD=1.25 mm and CMOD=1.875 mm.

In order to simulate the flat crack propagation in 1 mm thick sheet specimens, a 3D finite element model is built in ABAQUS. To simplify the geometry of the finite element model, the real shape of the notch is approximate by a sharp crack tip in the meshed structure. As the distribution of the particles do not have obvious influence on the damage behavior of the sheet specimen (e.g., F-CMOD curve, details is shown later), only half of the sheet specimen is modeled, loading is defined on the loading line by external displacements, the finite element mesh and boundary conditions are shown in Fig. 8.16. The detailed finite element mesh around the initial notch is shown in Fig. 8.17. The size of the cubic elements along the symmetry line is 50 x 50 x 50 x μm^3 which is according to literature [Shen et al., 2012, Ueda et al., 2014]. The crack mouth opening displacement (CMOD) is obtained from the CMOD line which is marked in Fig. 8.16. The volume fraction of all particles (initial voids plus non-metallic inclusions) obtained from the thin sheet specimen is 0.0015 which is calculated from the Image J software. The Rousselier parameter set (f_0=0.0015, σ_k=445 MPa) is used for the calculation and the critical region around the initial notch where crack propagation may appear are defined as Rousselier elements where a user defined material behavior is adopted for the calculation, which is shown in Fig. 8.18. As the stress triaxiality is high in the center of the specimen, the maximal numerical crack is expected locating at the middle section of the specimen in front of the initial notch. After the calculation, when CMOD is 1.25 mm, 17 elements are damaged (red elements in Fig. 8.19) at the middle

section of the specimen and the corresponding maximal crack length is 850 µm. This value is larger than that of the crack length (454.5 µm) observed in Fig. 8.5(d) (sum of lengths of several flat cracks). This is because the damage is overestimated in the Rousselier model where the first few elements being damaged when numerically CMOD=0.55 mm which is earlier than the appearance of microcracks in experimental observation (CMOD=0.625 mm). The laminographic imaging shows the longest 2D crack located at the cross section which is 200 µm from the middle section of the specimen, showing the non-metallic inclusions play a dominant role in creating voids. Defining the Rousselier parameter (f_0) at all elements in front of the initial notch the same is not proper.

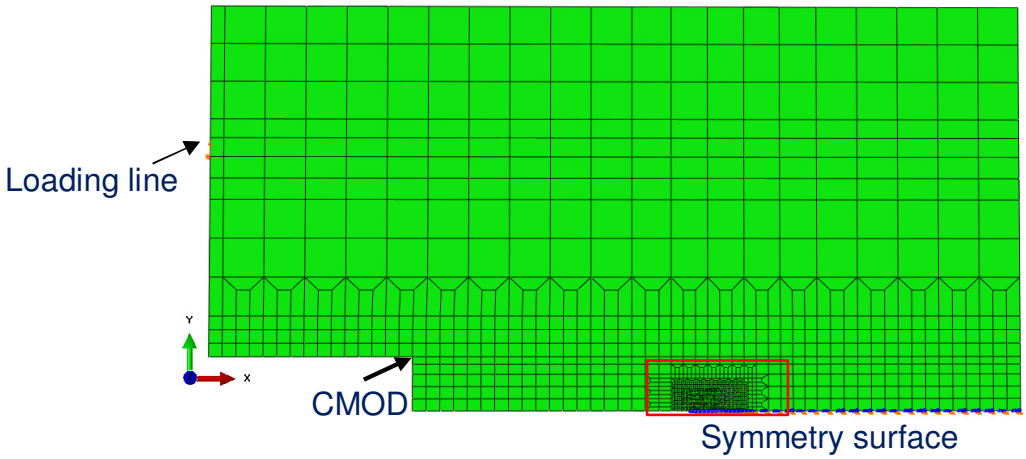

Fig. 8.16: Finite element mesh and boundary conditions of one sheet specimen used for the laminographic test.

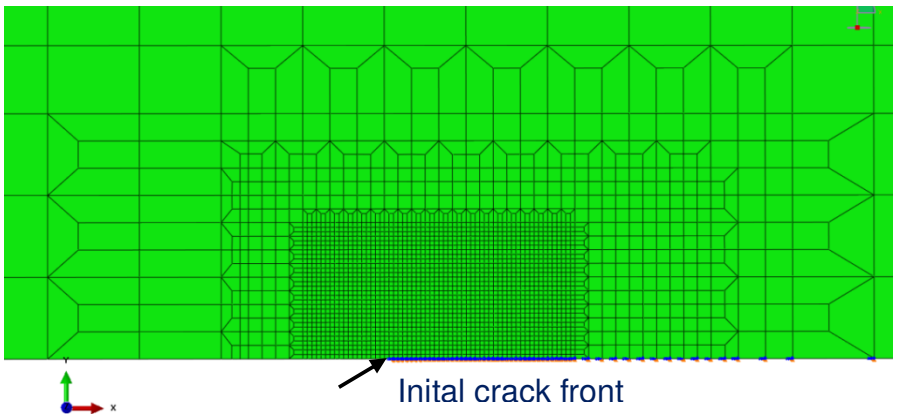

Fig. 8.17: Detailed finite element mesh around initial notch for the one sheet specimen.

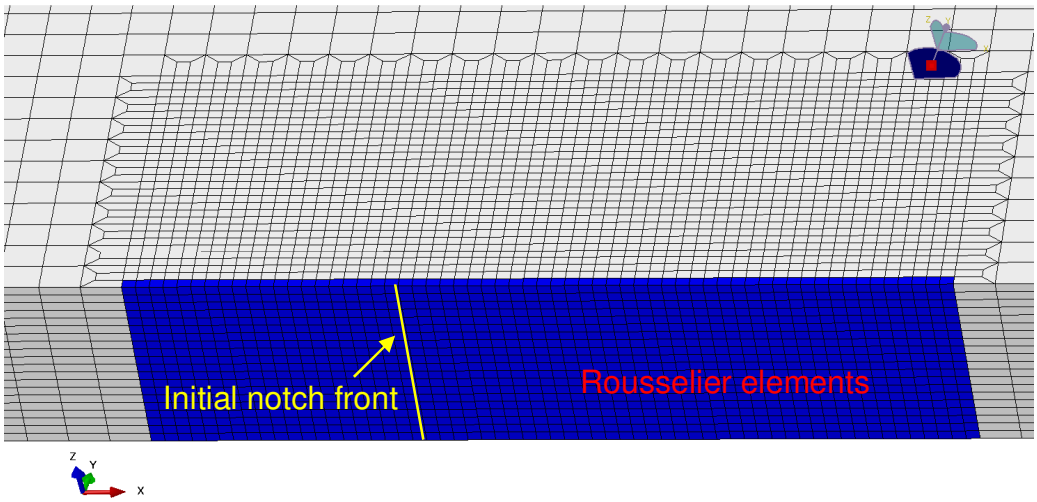

Fig. 8.18: Rousselier elements (blue color) around the initial notch front are defined in the center of the specimen.

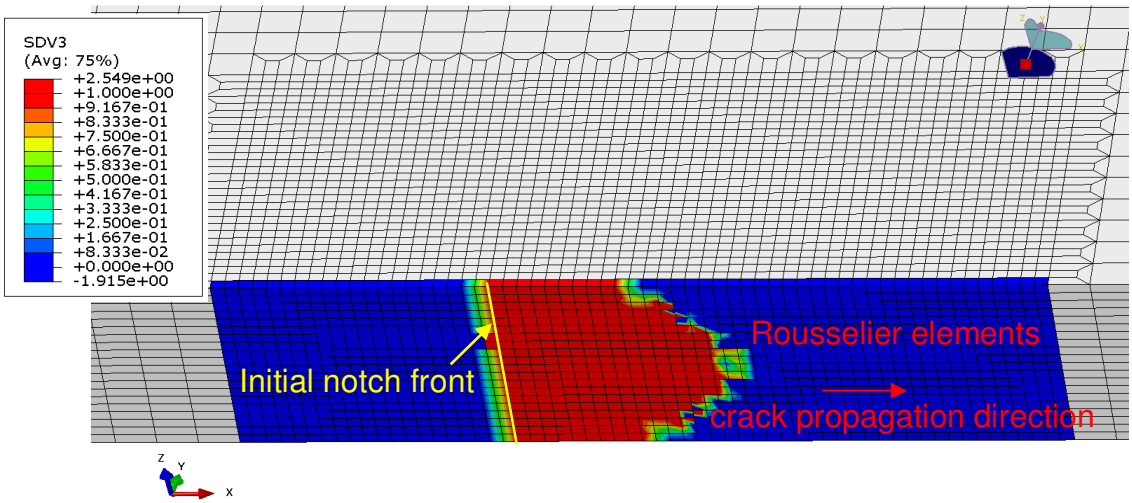

Fig. 8.19: Simulated damaged elements (red color) on the fracture surface of the sheet specimen (SDV3 is the user defined failure indicator of Rousselier model in ABAQUS, when current f ≥ f_c=0.05, SDV3=1).

In order to predict the crack propagation on the fracture surface of the thin sheet specimen, especially the crack propagation on the cross section where the longest crack appears, the elements around the initial notch are divided into three different regions which stand for three different volume fractions of inclusions in the material. As shown in Fig. 8.20, the high f_0-value (f_0=0.00714) region (highlighted in red color) stands for the f_0-value in this region is higher than the average f_0-value (f_0=0.0015). The low f_0-value region (f_0=0.00046) covers all the six rows of elements in the center of the specimen (yellow) and the f_0-value in this region is lower than the average f_0-value. The f_0-value defined in the average f_0-value region (blue elements regions) is equal to the experimental one. When CMOD=1.25 mm, the simulated crack shape obtained on the fracture surface of the specimen is shown in Fig.

8.21 where the maximal crack length is observed at the cross section which is 150 µm apart from the middle section of the specimen. The simulation result shows that the Rousselier model is able to predict the position of the main crack when defining the f_0-values at the different regions in front of the initial notch being different. However, when CMOD=1.25 mm, the simulated crack propagation length is 600 µm which is longer than the experimental observation (454.5 µm). This is because the damage is overestimated in the Rousselier model and the first crack appears when numerically CMOD=0.4 mm is reached which is earlier than the appearance of microcracks in laminographic imaging (CMOD=0.625 mm). Voids originate from MnS particles easily under small material deformation (Fig. 8.3(c)), no cracks are found in the matrixes locating in front of the notch even after the last loading step (Fig. 8.3(f)), showing the non-metallic inclusions play a critical role in creating voids. From the laminographic imaging, flat crack propagation is observed at different crack planes in front of the initial notch (Fig. 8.11).

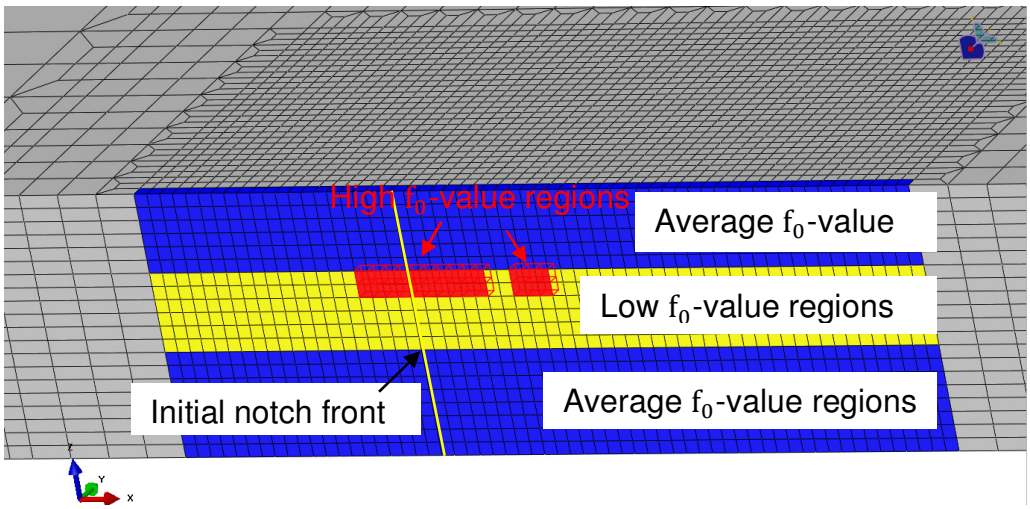

Fig. 8.20: Rousselier elements around the initial notch front are defined with different f_0-value (high f_0=0.00714, low f_0=0.00046, average f_0=0.0015).

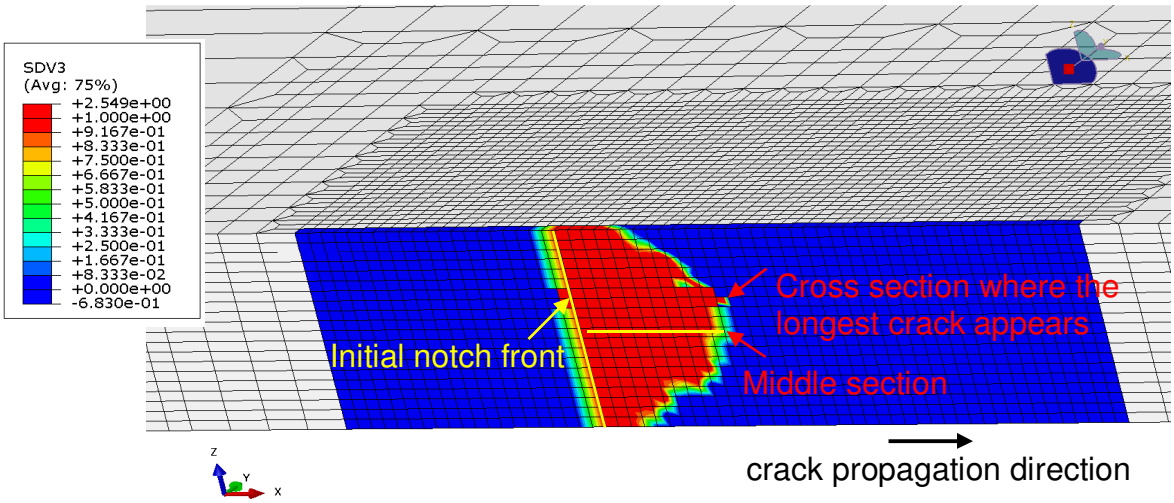

Fig. 8.21: Simulated damaged elements (red color) on the fracture surface of the sheet specimen where the longest crack appears at the cross section which is 200 µm from the middle section of the specimen.

In order to simulate the flat crack propagation on the different crack planes in front of the initial notch, it is necessary to adopt the real f_0-values for the 3D Rousselier model. As shown in Fig. 8.22, the regions in front of the initial notch are divided into 18 areas (each 150 x 150 µm^2). For each area (named 1-1, 1-2, 1-3, etc. as shown in Fig. 8.22), the 3D region is divided into 4 partitions through the thickness (S) direction (named 1-1-1, 1-1-2, 1-1-3, 1-1-4). Partition 1-1-1 stands for the laminographic data in area 1-1 within 1-150 µm (S direction). Partition 1-1-2 stands for the laminographic data within area 1-1 within 151-300 µm (S direction). Partition 1-1-3 stands for the laminographic data within area 1-1 within 301-450 µm (S direction). Partition 1-1-4 stands for the laminographic data within area 1-1 within 451-600 µm (S direction). The dimension of each partition is 150 µm^3. By this way, the sheet regions in front of the initial notch are partitioned into 72 partitions where the f_0-value of each partition region is calculated with the Image J software. The f_0-values of partitions ahead of the initial notch are summarized in table. 8.1. The partitions with higher f_0-values (f_0>0.0015) are marked in red and the partition with average f_0-value (f_0=0.0015) is marked in green. Fig 8.23 shows how the f_0-values vary according to the positions of partitions. The f_0-values of the 72 partitions are shown with colored balls where the colors vary with f_0-values. The rough f_0-value order for one partition can be estimated according to the color of the ball. A solid ball with a larger diameter stands for the f_0-value in this partition is higher than in the region with a smaller ball. The elements ahead of the initial notch are partitioned into 72 Rousselier element sets (each set contains 3 x 3 x 3 elements), the f_0-values from each partition as summarized in table 8.1 are used for the Rousselier elements

set (150 x 150 x 150 μm^3) located at the respective location, as shown in Fig. 8.24. After calculation, when numerical CMOD=1.25 mm, the predicted crack propagation is shown in Fig. 8.25 where cracks propagate not only along the x-direction (crack propagation direction) but also along the z-direction (thickness direction) and the maximal crack length is observed at the sections which are 50-200 µm from the middle section of the specimen. The damaged elements extracted from Fig. 8.25 where the longest flat cracks are located at other cross sections which are 50-200 µm apart from the middle section of the specimen are shown in Fig. 8.26. However, when CMOD=1.25 mm, the simulated crack propagation length is 600 µm which is longer than the experimental observation (454.5 µm). This might be due to the fact that the f_0-value in the region near the initial notch is higher than the exact experimental value, leading to the first crack appearing numerically at CMOD=0.43 mm which is earlier than the appearance of microcracks during laminographic imaging (CMOD=0.625 mm). When numerical CMOD=1.875 mm, the predicted crack propagation on the fracture surface is shown in Fig. 8.27. The longest crack propagation is found at the section which is 50-100 µm apart from the middle section of the specimen. Some undamaged elements are surrounded by damaged elements. This is the evidence showing the void volume fraction possesses a strong influence on the damage.

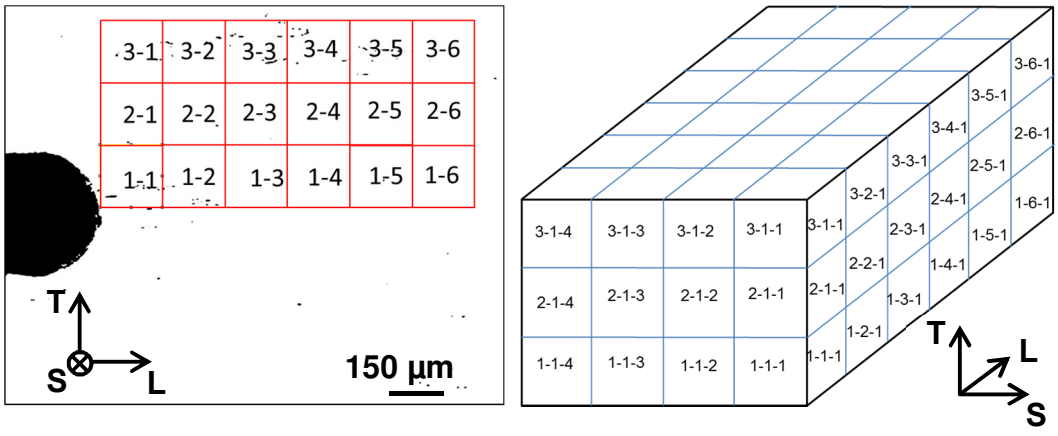

Fig. 8.22: The region in front of the initial notch is divided into 18 areas and 72 partitions where the real f_0-value is calculated.

Table 8.1: Statistic analysis of void volume fraction (f_0) contained in partitions.

Partition position	f_0	Partition position	f_0	Partition position	f_0
1-1-1	0.002571	2-1-1	0.000350	3-1-1	0.000799
1-1-2	0.000622	2-1-2	0.000005	3-1-2	0.001830
1-1-3	0.000888	2-1-3	0.000043	3-1-3	0.000353
1-1-4	0.001050	2-1-4	0.000257	3-1-4	0.001418
1-2-1	0.002953	2-2-1	0.000204	3-2-1	0.001596
1-2-2	0.000332	2-2-2	0.000185	3-2-2	0.002972
1-2-3	0.000144	2-2-3	0.000059	3-2-3	0.001661
1-2-4	0.002518	2-2-4	0.000306	3-2-4	0.002054
1-3-1	0.000316	2-3-1	0.000060	3-3-1	0.000873
1-3-2	0.001521	2-3-2	0.000084	3-3-2	0.004362
1-3-3	0.001501	2-3-3	0.000131	3-3-3	0.005592
1-3-4	0.001673	2-3-4	0.000466	3-3-4	0.001518
1-4-1	0.000034	2-4-1	0.000018	3-4-1	0.004158
1-4-2	0.000132	2-4-2	0.000036	3-4-2	0.005463
1-4-3	0.002978	2-4-3	0.000023	3-4-3	0.002250
1-4-4	0.002135	2-4-4	0.000539	3-4-4	0.002556
1-5-1	0.000938	2-5-1	0.000110	3-5-1	0.006090
1-5-2	0.000576	2-5-2	0.000034	3-5-2	0.004404
1-5-3	0.000829	2-5-3	0.000661	3-5-3	0.003313
1-5-4	0.002127	2-5-4	0.000183	3-5-4	0.006381
1-6-1	0.000215	2-6-1	0.000065	3-6-1	0.001326
1-6-2	0.001032	2-6-2	0.000375	3-6-2	0.007234
1-6-3	0.000055	2-6-3	0.000449	3-6-3	0.002977
1-6-4	0.000304	2-6-4	0.000261	3-6-4	0.004602

Mark red: partitions with higher f_0-value, Mark black: partitions with lower f_0-value, Mark green: partition with average f_0-value.

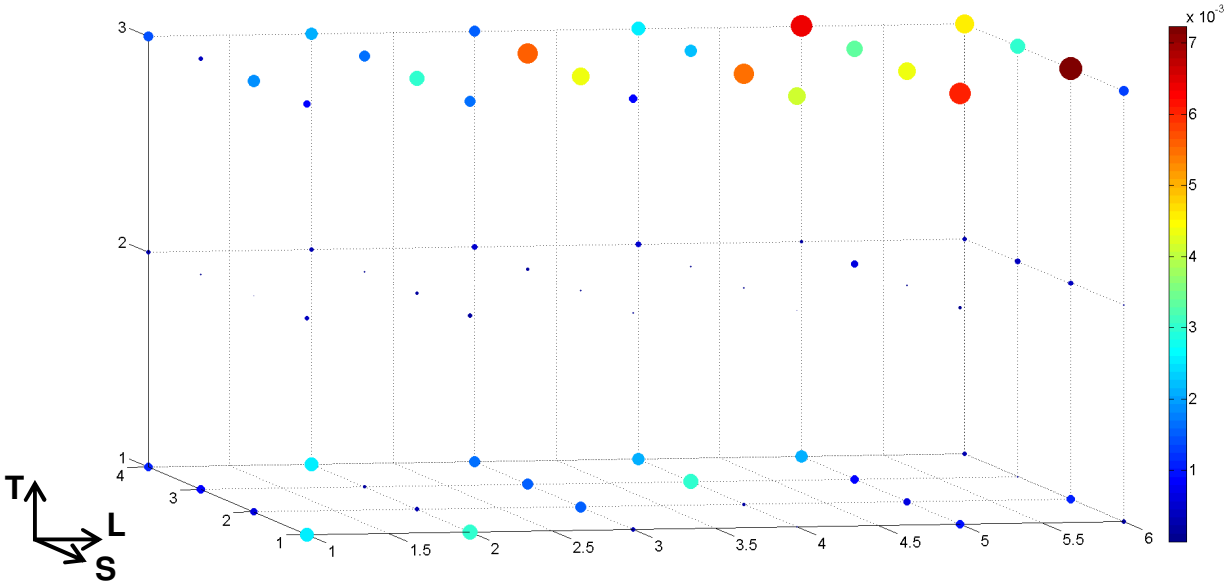

Fig. 8.23: The f_0-values for different partitions where a larger diameter of the ball stands for the f_0-value in this partition is higher than in the region with a smaller ball.

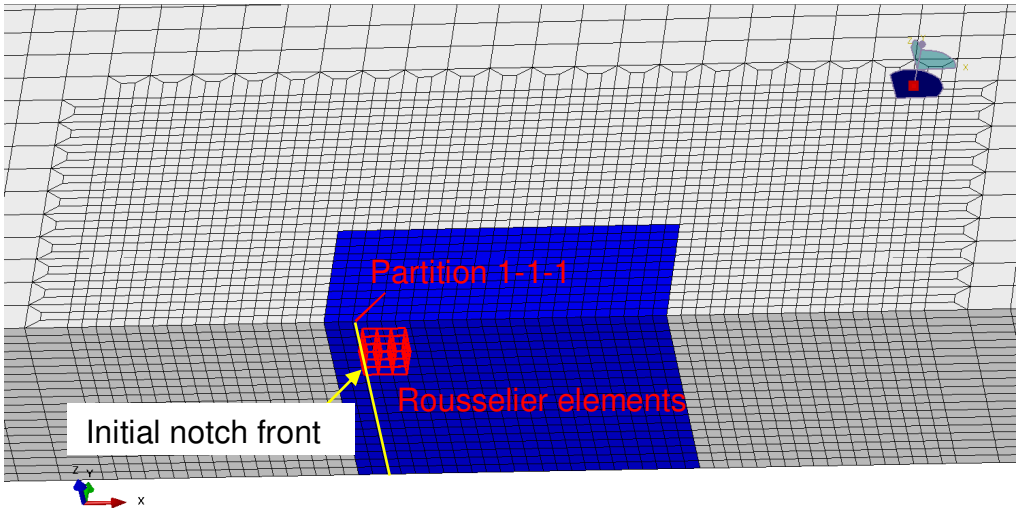

Fig. 8.24: Rousselier elements around the initial notch front are defined with the real f_0-values.

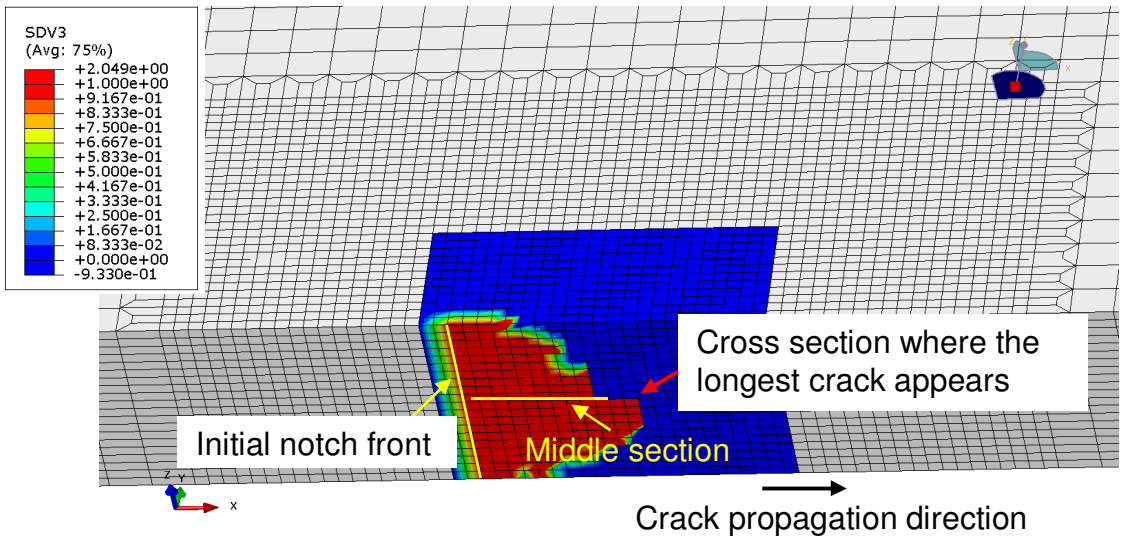

Fig. 8.25: Simulated damaged elements (red color) at CMOD=1.25 mm with definition of real f_0-values for 150 µm^3 partitions.

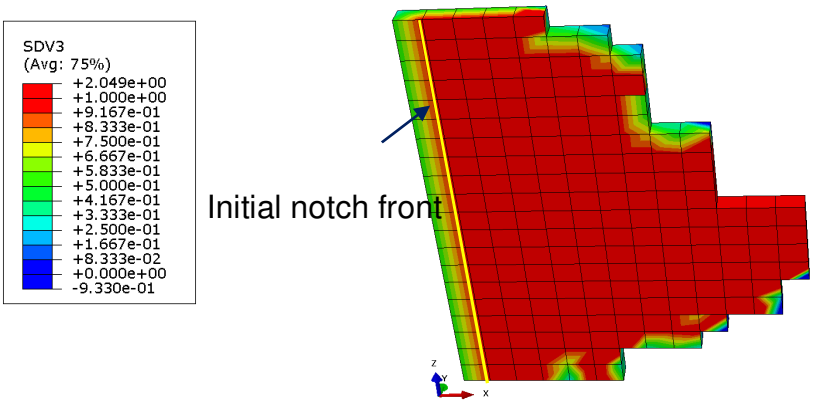

Fig. 8.26: Simulated damaged elements (red color) as in Fig. 8.24 on the fracture surface of the sheet specimen.

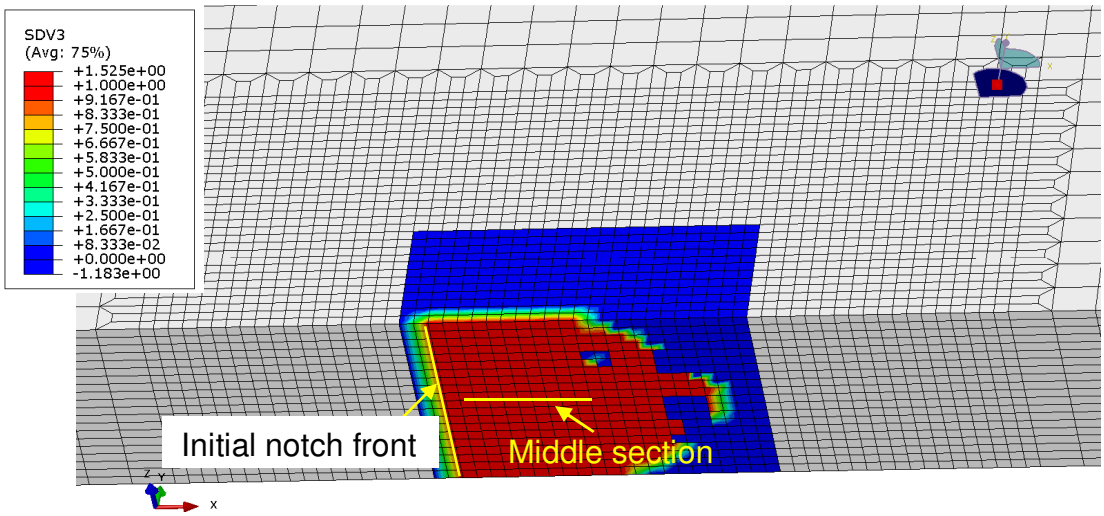

Fig. 8.27: Simulated damaged elements (red color) at CMOD=1.875 mm with definition of true f_0-values for 150 µm^3 partitions.

Simulations are also performed when using a doubled partition area (300 x 300 x 300 µm^3) and the corresponding Rousselier element set in the simulation containing 6 x 6 x 6 elements. After calculation, when numerical CMOD=1.25 mm, the predicted crack propagation is shown in Fig. 8.28 where the maximal crack length is observed at sections which are 50-200 µm apart from the middle section of the specimen. When numerical CMOD=1.875 mm, the predicted crack propagation is shown in Fig. 8.29 where the maximal crack length is observed at the sections which are 100-200 µm apart from the middle section of the specimen.

In order to reduce the numbers of partitions, the elements around the initial notch are divided into three regions which stand for different volume fractions of inclusions in the material, the elements highlighted in red color stand for the material regions with higher Rousselier parameter (f_0=0.00714), the f_0-values (f_0=0.00046) in the blue elements are smaller than the experimental f_0-value (f_0=0.0015) obtained from Image J, as shown in Fig. 8.30. After the calculation, when numerical CMOD=1.25 mm, the predicted crack propagation are shown in Fig. 8.31 and Fig. 8.32 where cracks propagate not only along the x-direction (crack propagation direction) but also along the y-direction (loading direction) together with the thickness direction (z-direction) and the maximal crack length is observed at the cross section which is 200 µm apart from the middle section of the specimen. The damaged elements extracted from Fig. 8.31 are shown in Fig. 8.33 where the longest flat cracks located at the cross section which is 200 µm from the middle section of the specimen is shown. This simulation result is the same to the laminographic imaging where

the cracks propagate also in the same two directions in reality (Fig. 8.14). The simulated crack propagation length is 450 µm (9 damaged elements) which is very close to the experimental observation (454.5 µm). The comparison between the simulated crack shape and the 2D laminographic imaging where the longest crack is observed are shown in Fig. 8.33. The simulation result compares very well with the laminographic observations (T-L) where the flat cracks comprise two main cracks. This shows, by adopting different f_0-values for different material regions in front of the initial notch, the Rousselier model can fit the position of the longest flat crack well.

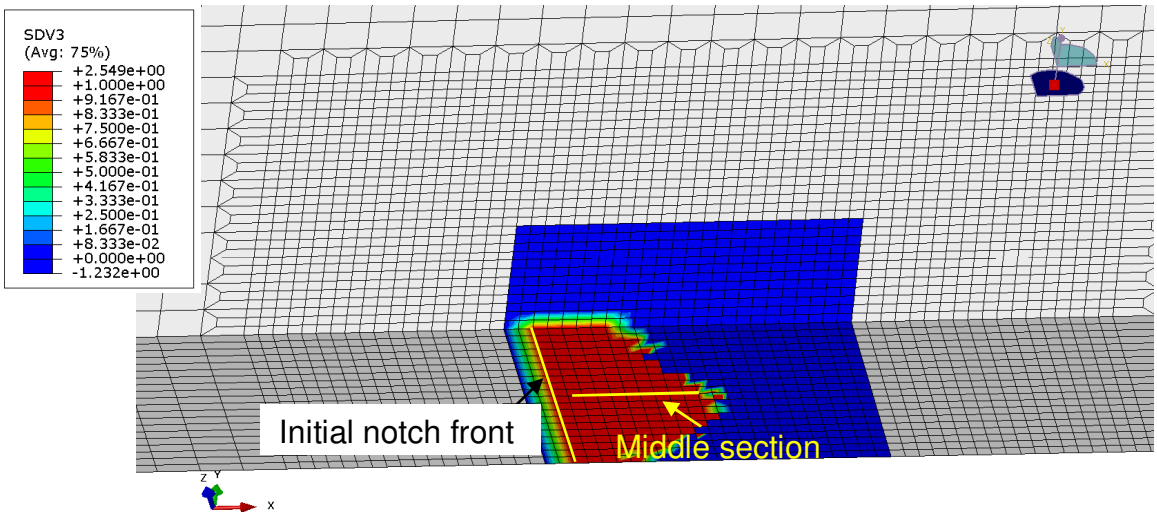

Fig. 8.28: Simulated damaged elements (red color) at CMOD=1.25 mm with definition of true f_0-values for 300 µm^3 partitions.

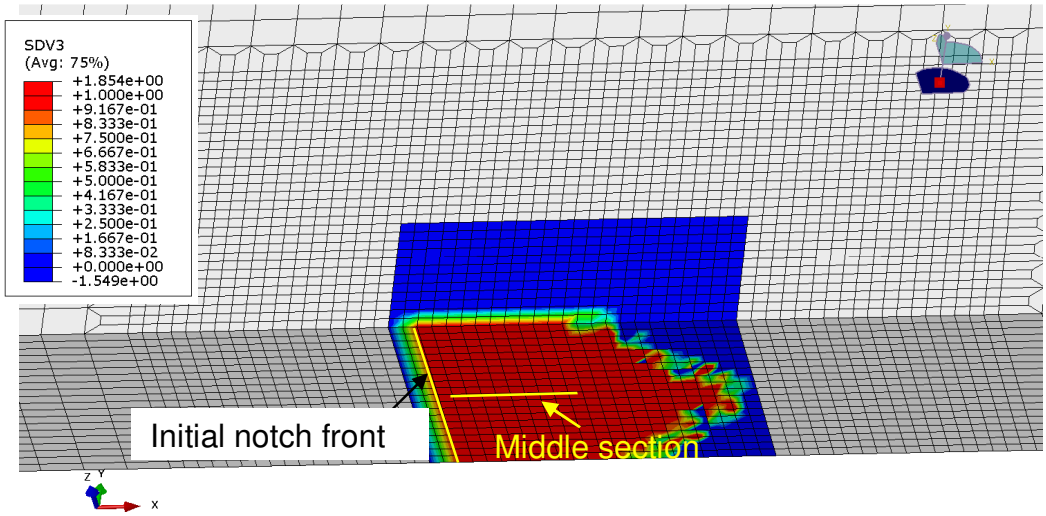

Fig. 8.29: Simulated damaged elements (red color) at CMOD=1.875 mm with definition of true f_0-values for 300 µm^3 partitions.

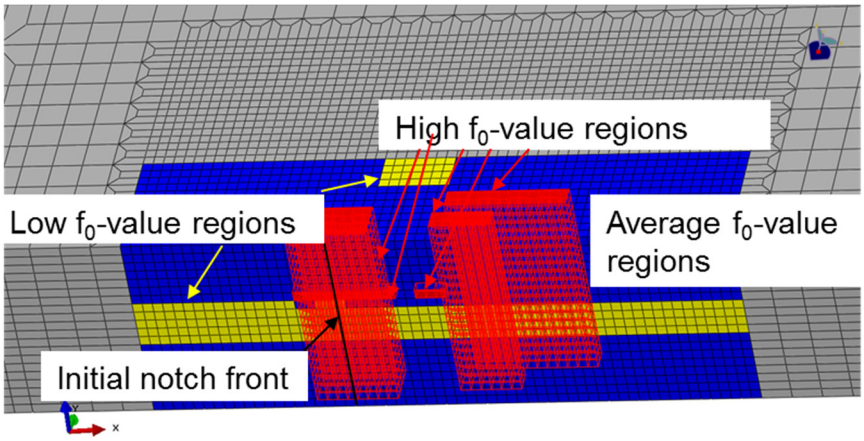

Fig. 8.30: Rousselier elements around the initial notch front are defined with different f_0-value (high f_0=0.00714, low f_0=0.00046, average f_0=0.0015).

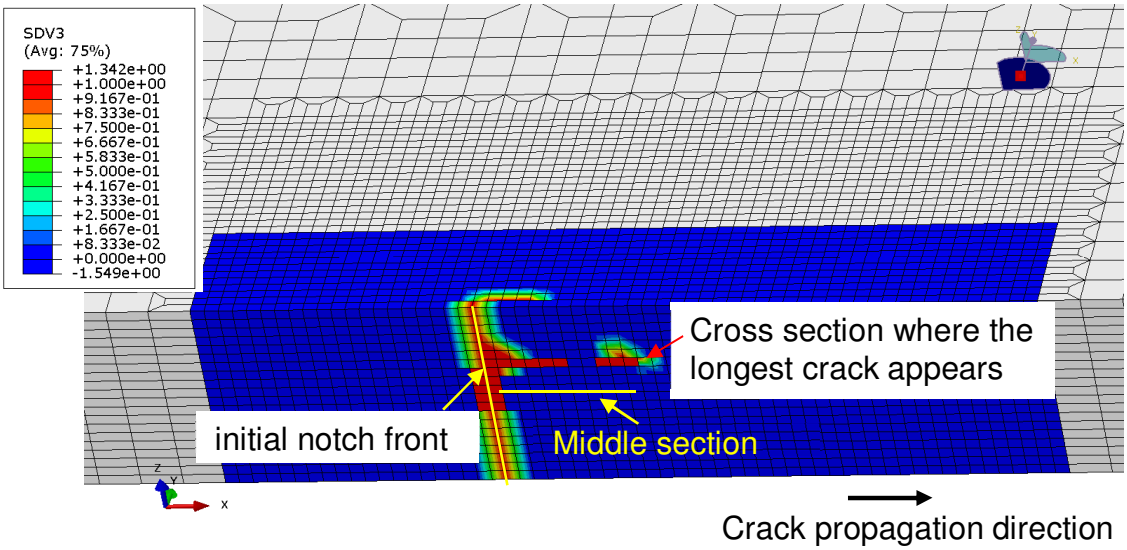

Fig. 8.31: Simulated damaged elements (red color) on the fracture surface of the sheet specimen where the longest crack appears at the cross section which is 200 µm from the middle section of the specimen.

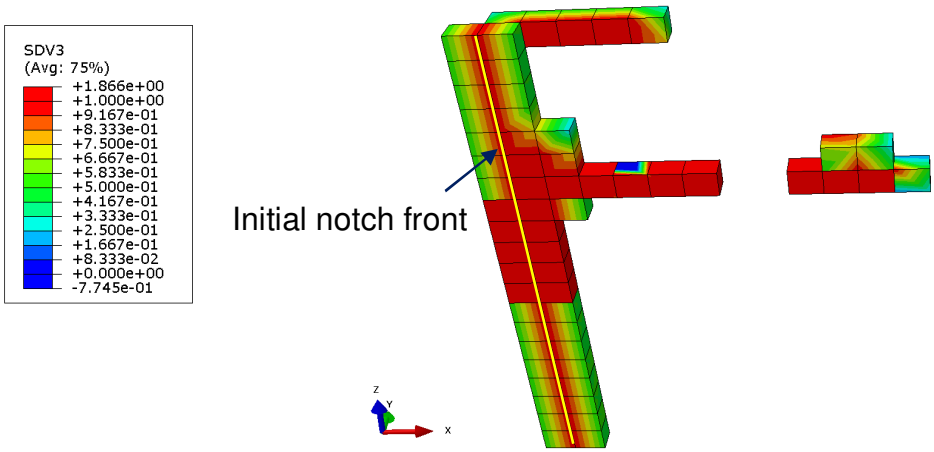

Fig. 8.32: Simulated damaged elements (red color) as in Fig. 8.31 on the fracture surface of the sheet specimen are shown.

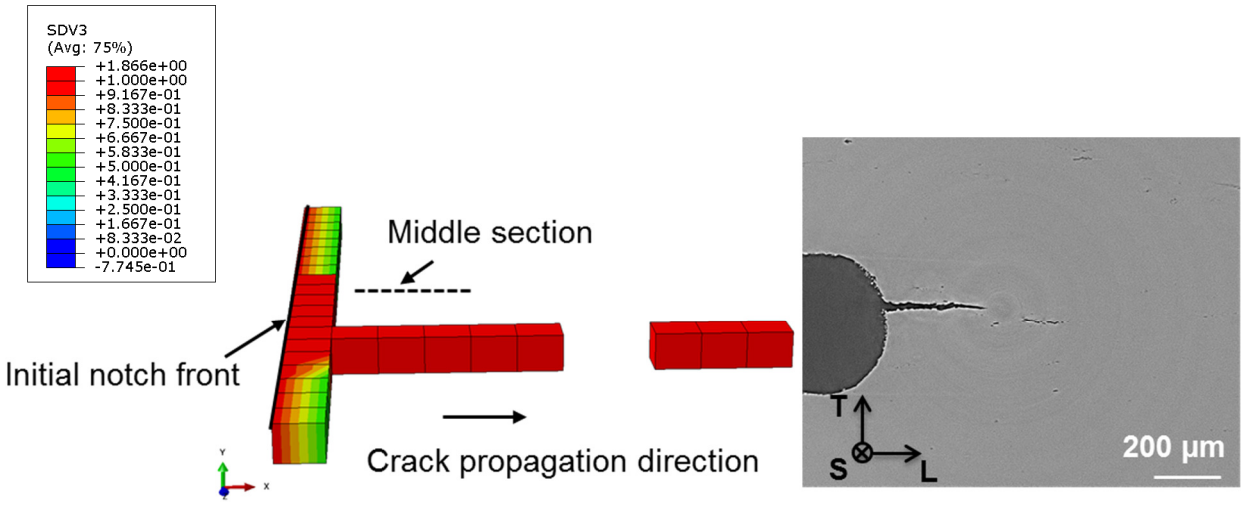

Fig. 8.33: Comparison between the simulation and the laminographic imaging of 2D cross-section (T-L) where the longest cracks are observed.

Simulated F-CMOD-curves obtained with the Rousselier model with different f_0-values is shown in Fig. 8.34. The simulated F-CMOD-curve when defining for all the Rousselier elements the same f_0-value (f_0=0.0015) leads to the highest F-CMOD-curve compared to the case when using the real f_0-values in the Rousselier model. This is because when defining different partitions the real f_0-values, crack initiation appears easier and earlier at particle localized regions (f_0>0.0015) in the present case at the middle section of the specimen during the simulation, resulting in a lower F-CMOD-curve as shown in Fig. 8.34. The simulated F-CMOD-curves obtained from the Rousselier models using real f_0-valus for 150 x 150 x 150 µm^3 partitions, 300 x 300 x 300 µm^3 partitions and three main regions are very close. This can explain although some differences (Fig. 8.21 vs. Fig. 8.25 vs. Fig. 8.28 vs. Fig. 8.31) exist on the fracture surfaces with different definition of f_0-values in the Rousselier model, if the real f_0-values are used for the partitions, the size of the partitions do not have obvious influences on the F-CMOD-curves. The simulated F-Δa-curves at the middle section of the sheet specimen with different definition of f_0-values is shown in Fig. 8.35. When Δa ≥ 0.55 mm, the simulated force obtained with the average f_0 -values definition in the Rousselier model has higher force in comparison to other definition of f_0-values. This coincides with the F-CMOD curve when CMOD>1.1 mm as shown in Fig. 8.34.

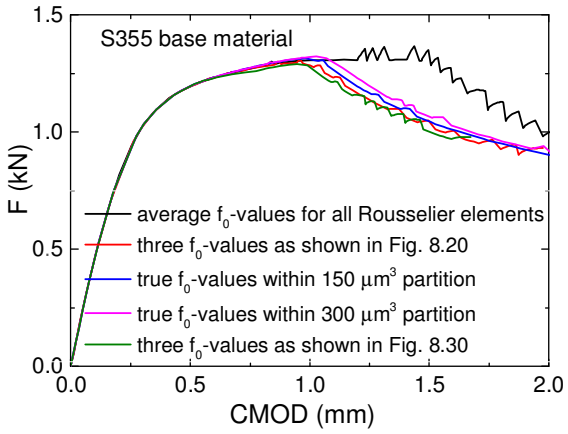

Fig. 8.34: Simulated F-CMOD-curves obtained from the Rousselier models with different definition of f_0-values in the model.

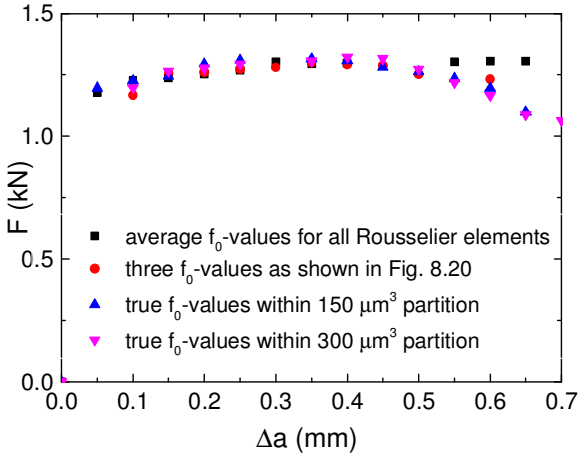

Fig. 8.35: Simulated F-Δa-curves obtained from the Rousselier models with different definition of f_0-values in the model.

8.3 Discussion and Conclusions

The 3D initial status and the crack progress of a 1 mm thickness sheet specimen loaded under different loading steps from S355 base material are successfully obtained with synchrotron radiation-computed laminography technique for the first time. Reconstructed 2D (T-L) laminography images of the middle section and the section where the longest crack located are shown in Fig. 8.3 and Fig. 8.5 separately. MnS particles are found localized at some regions which coincide with the metallographic investigations (Fig. 3.1) and cracks originate from these particles during material deformation. The volume fraction of the inclusions (initial voids plus MnS particles) is 0.0015 which is obtained from the Image J software. This value is used for the calculation of the 3D Rousselier model.

Although the stress triaxility from the calculation is high in the center of the sheet specimen, the main crack is found located at another scan section, showing the MnS particles are the dominant factor for damage. The laminography images at two different cutting positions through the thickness (T-S) are shown where a shear band is found between two neighboring cracks at the loading step when CMOD=1.25 mm. The laminographic images of the T-S section shows that cracks propagate not only along the crack propagation direction (L) but also through the thickness (S). The laminographic imaging of 2D cross sections (T-L) and the imaging through the thickness (T-S) show the complexity of the real damage evolution of the thin sheet specimen.

3D laminographic imagines were built with the Amira software. The spherical initial voids are randomly distributed in the bulk material. In comparison to the voids, MnS particles are flat shaped and localize at some regions, e.g., in front of the initial notch. The elongated MnS particles are due to the influence of rolling during material production. This observation information from laminographic imaging (Fig. 8.9) coincides with the experimental data of optical microscope pictures which is shown in Fig. 3.1. During the material deformation process, void nucleation, growth and coalescence happen from these particles at early strain stages. Microcracks originate mostly from localized particles (Fig. 8.10) in front of the initial notch where the local stress is very high. Neighboring microcracks propagate and connect each other not only along the crack propagation L direction but also along the thickness (S direction) direction, forming obvious cracks in front of the notch, as shown in Fig. 8.11. A shear band is observed between the two main cracks (Fig. 8.12) and the final main crack is formed when the shear crack connecting these two main cracks. The damage evolution comprising the flat and the slant fracture mechanisms is observed for the first time with the assistance of SRCL. In order to describe the real damage evolution before shear cracks arise, 3D model is required to predict the crack propagation not only along the L direction but also along the loading (T) direction and through the thickness (S) direction.

The Rousselier model which describes the damage evolution of void initiation, growth and coalescence is adopted to predict the crack propagation of a sheet specimen before the shear cracks happen. The first calculation is made where the Rousselier parameter (f_0) is defined the same for the all materials around the initial notch. After the calculation, the longest simulated crack is found in the center of the specimen where the stress triaxility is high. However, the simulated crack front on the fracture surface of the C(T) shows the

longest crack situated in the center of the specimen which is different from laminographic imaging where the longest crack is found at the cross section which is 200 µm from the middle section of the specimen. In order to simulate the flat crack propagation on the different crack planes in front of the initial notch, the regions in front of the initial notch are divided into 72 partitions (150 x 150 x 150 μm^3). The true f_0-values obtained from the Image J software are used for the respective Rousselier element set (3 x 3 x 3 elements) in front of the initial notch. After the calculation (CMOD=1.25 mm), cracks propagate not only along the x-direction (crack propagation direction) but also along the z-direction (thickness direction) in the model and the maximal crack length is found located at other cross sections which are 50-200 µm from the middle section of the specimen, as shown in Fig. 8.25. The simulated maximal crack length on the fracture surface of the sheet specimen (600 µm) is larger than the laminographic imaging (454.5 µm) at a 2D cross section (T-L) when CMOD is 1.25 mm. Simulations are also performed when using a doubled partition area (300 x 300 x 300 μm^3) and the corresponding Rousselier element set in the simulation containing 6 x 6 x 6 elements. After calculation, when numerical CMOD=1.25 mm, the predicted crack propagation is shown in Fig. 8.28 where the maximal crack length is observed at sections which are 50-200 µm apart from the middle section of the specimen. The simulated crack length on the fracture surface of the sheet specimen (600 µm) is also larger than the laminographic imaging (454.5 µm) at a 2D cross section (T-L) when CMOD is 1.25 mm. In order to reduce the number of partitions, the elements around the initial notch are divided into three regions which stand for different volume fraction of inclusions in the material. After calculation, the longest flat crack is located at the cross section which is 200 µm from the middle section of the specimen when CMOD=1.25 mm. This simulation result is the same as the laminographic imaging as shown in Fig. 8.33. The simulated crack propagation length is 450 µm which is very close to the experimental observation (454.5 µm). This shows the 3D Rousselier model can predict the fracture surface of the sheet specimen well before the shear cracks happen.

The final crack propagation is not predicted with the Rousslier model as the shear coalescence fracture mechanism has not been considered in the current model, indicating the requirement for a better coalescence model. A modified GTN model which considers the shear fracture mechanism is given in the literature [Nahshon and Hutchinson, 2008], the modified Rousselier model which consider the damage progress of shear cracks during the damage evolution is needed in the future work.

9. Summary and Outlook

9.1 Summary

This work is motivated by the demands of the safety assessment of structural weldments and the demand to predict crack propagation in the weldment. The main focus concentrates on fracture mechanisms and crack propagation of an S355 electron beam welded joint. The thesis consists of two main parts, the experimental investigations and the numerical works performed on the welded joints.

The chemical composition of S355 base material was measured by spectrometric analysis. MnS particles are non-metallic inclusions which are assumed as to nucleate voids during material deformation. In order to define the different weld regions, hardness measurements were performed across the welded joint at three different locations, namely at the weld root, the middle-section and the top part of the joints. The dimensions of the weld regions are obtained from Vickers hardness values across the S355 welded joints. In order to know the volume fraction of MnS particles and the average distances between particles, optical microscopy analyses are performed on the BM, the FZ and the HAZ, separately. It can be observed from the microscope pictures that the particles are not equally distributed in the material but localized in some regions. The volume fraction of all inclusions for the BM, the FZ and the HAZ are 0.0009, 0.0018 and 0.0016, respectively. The mean distance between neighboring inclusions for the BM, the FZ and the HAZ is found to be 0.10 mm, 0.08 mm and 0.12 mm, respectively. After surface etching, microstructures of different weld regions are obtained and presented. The BM shows a typical microstructure of steel, which is comprised of Ferrite and Perlite. Acicular martensite structures can be found in the FZ. The microstructure of the HAZ consisting of Ferrite, Pearlite and Martensite is a transitional region between the BM and the FZ. Smooth round specimens extracted from the BM and flat specimens obtained from the BM, the FZ and the HAZ are tensile tested. The comparison of engineering stress-strain curves obtained from a smooth round specimen and from a flat specimen extracted from the BM is made. Good match between these two curves shows that the flat specimen produces the same stress-strain curves as the smooth round specimen. Stress-strain curves of different weld regions are shown which are used as the finite element model input. Notched cylindrical specimens with 4 mm notch radius were extracted from the BM and from the HAZ, of which the length direction is

perpendicular to the weld line. The experimental results are shown in the form of F-ΔL- and F-ΔD-curves. Transverse flat tensile specimens where the weld seam is located in the middle of the specimen were tensile tested. Final fracture is found being located in the BM, showing the FZ is stronger than the BM and the electron beam welded steel joint is strong enough for the application in structural components in industry. Fracture toughness tests are performed on the C(T)-specimens extracted from different positions of weldment, i.e., the initial crack was located in the BM, in the middle of the FZ as well as at the interface between the FZ and the HAZ. The unloading compliance method was adopted in order to capture the crack growth. The experimental data are shown in the form of F-COD-curves together with the fracture resistance J_R-curves. After the investigation of the fracture surfaces of C(T)-specimens (obtained from SEM), both C(T)-BM and C(T)-HAZ show typical ductile fracture behavior where large dimples are connected by small voids. The C(T)-FZ shows quasi-brittle behavior.

As the BM and the HAZ show ductile fracture behavior, the Rousselier model and the GTN model which describe the evolution of void nucleation, growth and coalescence are adopted to investigate the fracture behavior of C(T)-BM and C(T)-HAZ specimens. A parameter study of the Rousselier model and the GTN model is performed on a notched round specimen and a C(T)-specimen extracted from the BM. The influence of the Rousselier and GTN parameters on the F-ΔD-, F-COD- and J_R-curves are shown. Based on metallographic investigations on the BM and the HAZ, the Rousselier and GTN parameters are calibrated on notched round specimens, both for the BM and for the HAZ. The same Rousselier and GTN parameter set is used to predict the crack propagation of C(T)-BM and C(T)-HAZ. Good match between the experimental data and numerical simulations results are obtained in forms of F-COD-curves and fracture resistance J_R-curves, showing the Rousselier and GTN models can predict crack propagation in the homogeneous base material and in inhomogeneous welded joints well.

In comparison to the damage models (Rousselier model and GTN model), a phenomenological model – the cohesive zone model is adopted to investigate crack propagation in an electron beam welded joint. A parameter study was performed on the C(T)-BM under the TSL with exponential softening. The influences of the cohesive strength (T_0), the cohesive energy (Γ_0), the size of the cohesive element and the shape of the TSL on the F-COD- and J_R-curves were derived. An exponential and a trapezoidal shaped

traction separation law (TSL) are adopted to investigate the damage behaviour of C(T)-BM and C(T)-HAZ. Good predicted F-COD- and J_R-curves are obtained when different appropriate cohesive parameter sets with different TSLs are chosen. With exponential and trapezoidal shaped TSL, the partial unloading process of the F-COD-curve from a C(T)-BM specimen is simulated with the cohesive zone model. The numerical J_i-values are calculated with the domain integral method. The shapes of the cohesive models for C(T)-BM and C(T)-HAZ are derived from a one element Gurson model simulation. For the C(T)-BM, the relative stress vs. relative separation curve obtained from a one element Gurson model simulation is similar to the shape of exponential softening TSL and the numerical J_i-value (Δa=0.1 mm) obtained from the cohesive model with an exponential softening TSL is close to the experimental $J_{0.1}$-value (Δa=0.1 mm), the exponential softening TSL is assumed as a suitable shape and the corresponding cohesive energy obtained from the simulation is a more precise value. For the C(T)-FZ, a well simulated F-COD-curve is obtained when a TSL with linear softening is used. For the C(T)-HAZ, since the relative stress vs. relative separation curve from a one element Gurson model is very close to the trapezoidal shape, the trapezoidal shaped TSL is assumed as reasonable. The corresponding cohesive parameter set obtained with the trapezoidal shaped TSL is assumed to be realistic. No matter whether the fracture behavior of the material behavior is ductile or brittle, the cohesive zone model is able to simulate the crack propagation of the C(T) extracted from S355 welded joint, showing its superiority.

C(T)-specimens obtained from the S355 base material are monotonic tensile tested in combination with the ARAMIS system. The ARAMIS system monitored the crack propagation on the surface of the C(T)-specimen. Damage evolution on the surface of the C(T)-specimens are captured by the cameras and the photos are shown at different loading time during the experiment. The equivalent strain distributions calculated from the ARAMIS system at different load moments were obtained. In comparison to the values obtained from the images of the ARAMIS camera, the crack length obtained from the output of the ARAMIS software is not accurate. Some damaged materials are assumed as non-damaged ones or some non-damaged regions are assumed as damaged ones because of the losses of the spray points on the surface of the undamaged material. The unexpected loss of the adherences of spray paints on the monitored region is the reason why the current ARAMIS system cannot give the correct crack lengths on the surface of the C(T) at each loading instant. However, the crack propagation on the surface of the C(T)-specimen is monitored

during the test of C(T) and the force vs. crack propagation curve is made which cannot be obtained directly from the unloading compliance method and the ASTM standard. This test procedure in combination with ARAMIS may supplement the ASTM standard for testing the fracture toughness of the C(T)-specimens after solving these technical problems during the tensile test of the C(T). The 2D and 3D GTN models are adopted to predict the crack propagations of one side grooved C(T)-specimen tensile tested under monotonic loading condition. Simulated F-COD-curves from the 2D GTN model fit the experimental ones well. The 3D GTN model can simulate a similar fracture surface of side grooved C(T)-specimens when the GTN parameter set summarized in table 5.2 is used. However, less crack extension areas and shorter crack lengths are obtained when the GTN parameter set summarized in table 5.2 but with f_0=0.002 is used. This is because in the monotonic tensile test of the C(T)-specimen, both flat fracture and slant fracture (confirmed by the rugged region in the stable crack growth region in Fig. 7.14(b)) give contributions to the final fracture. Whereas, only the flat crack due to the void initiation, growth and coalescence is considered in the GTN calculation, leading to the maximal crack length on the fracture surface of the C(T) being smaller than the experimental observation.

The damage evolution of S355 base material under load is obtained with a synchrotron radiation-computed laminography (SRCL) technique for the first time. Reconstructed 2D (T-L) laminography images of the middle section and the section where the main crack were observed are derived. Although the stress triaxility is high in the middle section of the sheet specimen, the main crack is found located at another scan section (200 µm from the middle section of the sheet specimen), showing the MnS particles are the dominant factor for the damage evolution. The laminographic images of the T-S section show that cracks propagate not only along the L direction but also through the thickness (S). The laminographic imaging of 2D cross sections (T-L) and through the thickness (T-S) show the complexity in the real damage evolution in thin sheet specimens. **After the reconstruction of the scanning data, void initiation, growth and coalescence from elongated and localized particles are visualized in 3D pictures.**

Microcracks are found localized at some regions, e.g., in front of the initial notch where cracks can easily be formed at the early strain stage. A shear band is observed between the two main cracks and the final main crack is formed when the shear crack connects these two main cracks. This complex damage evolution of the S355 base material

comprising the flat and slant crack is observed with the assistance of SRCL. As the crack propagates both along the L direction and thickness (S) direction during the monotonic loading, the **3D Rousselier model is adopted to predict the fracture shape of the C(T)-specimen before shear cracks arise.** The material in front of the initial notch is divided into many partitions of which the true f_0-values are obtained. According to the positions of the partitions, the Rousselier elements in front of the initial notch are divided into many sets where the corresponding true f_0-values are used in the simulations. The maximal simulated crack length (CMOD=1.25 mm) is found located at the T-L cross section which is the similar as the experimental one (200 µm from the center section of the specimen). However, when 150 x 150 x 150 μm^3 and 300 x 300 x 300 μm^3 Rousselier element sets are used separately, simulated crack lengths (600 µm) on the fracture surface of the sheet specimen are longer than laminographic image (454.5 µm) at a 2D cross section (T-L) when CMOD is 1.25 mm. The damage is overestimated in the Rousselier model where the first crack occurs at a numerical CMOD=0.43 mm which is earlier than the appearance of microcracks in the experimental observation (CMOD=0.625 mm). When the Rousselier elements around the initial notch are divided into three regions as shown in Fig. 8.30, the Rousselier model can simulate the fracture surface well where the longest flat cracks are located at the cross section which is 200 µm from the middle section of the specimen at CMOD=1.25 mm. This simulation result is the same as the laminographic imaging as shown in Fig. 8.33 and the simulated crack propagation length is 450 µm which is very close to the experimental observation (454.5 µm) showing the Rousselier model can simulate the crack propagation of the sheet specimen well before the shear cracks appearance.

9.2 Outlook

Improvements are still possible about the experimental investigation and simulation work on S355 electron beam welded joints. Some possible improvements are listed as follows:

As what has been discussed in chapter 7, the current ARAMIS machine at MPA cannot quantitatively analyze the crack propagation of the C(T)-specimen. Future tests in combination with an advanced ARAMIS system which can store more images should be made. It is expected that the F-COD- and F-Δa-curves will be obtained in these future tests when advanced ARAMIS systems are adopted.

Due to the limitation of the current beamline, energy absorption of the voids and particles during laminography scanning is very similar. After the reconstruction of the scanning data, it is not possible to separate initial voids and non-metallic particles with the current experimental data. A new technique should be adopted in future laminography experiments on the S355 sheet specimens where the particles and initial voids can be distinguished.

Current damage models have not considered the shear crack coalescence mechanism which is observed in the laminographic scanning. In order to describe such fracture mechanism, an improved damage model (e.g., the modified Rousselier model) considering the shear crack coalescence mechanism is needed in the future work.

Appendix

Sketches of different tested specimens used in the thesis are shown.

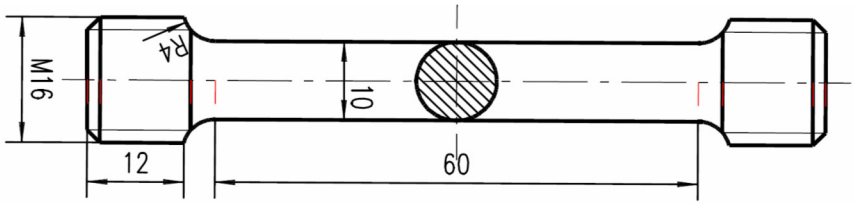

A. 1: Sketch of standard tensile round bar (M16).

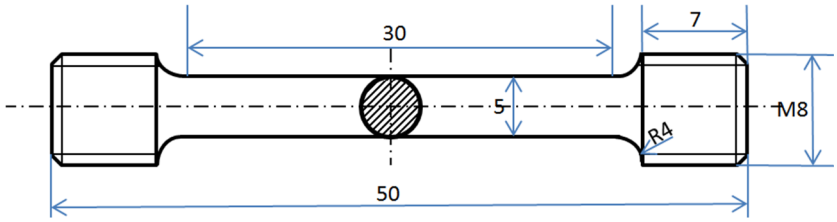

A. 2: Sketch of standard tensile round bar (M8).

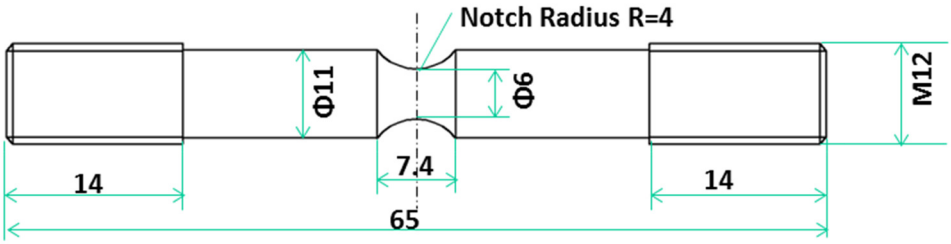

A. 3: Sketch of 4 mm notched round bar.

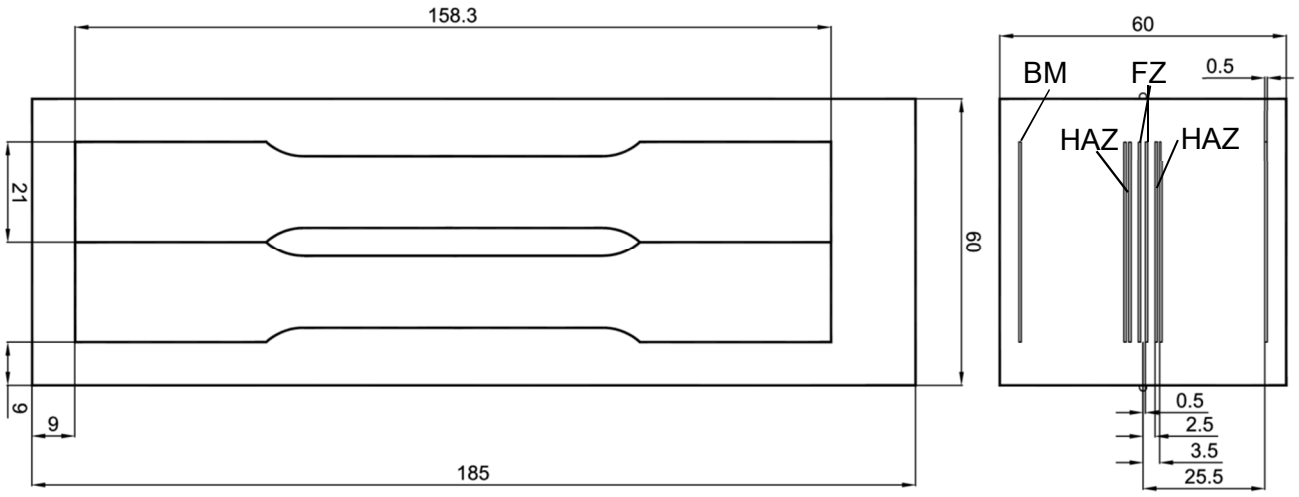

A. 4: Sketch of extraction positions of manufacture blocks and the dimension of the flat specimens.

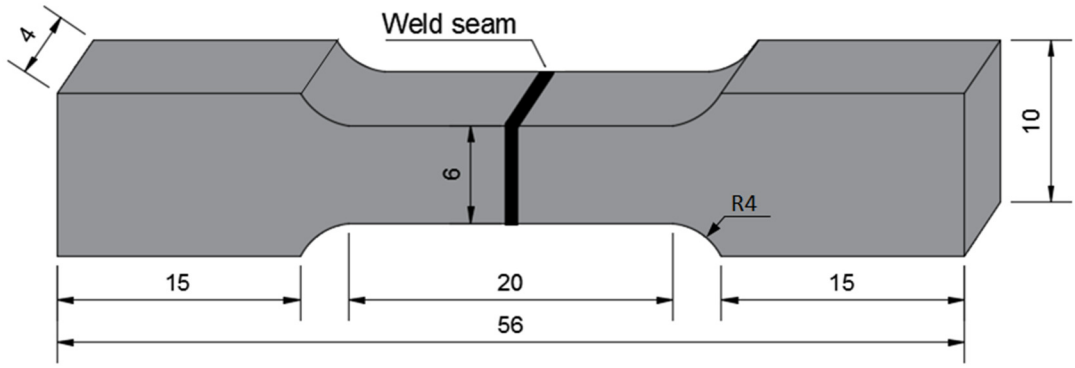

A. 5: Sketch of transverse flat specimen where the weld seam is located in the center of the specimen.

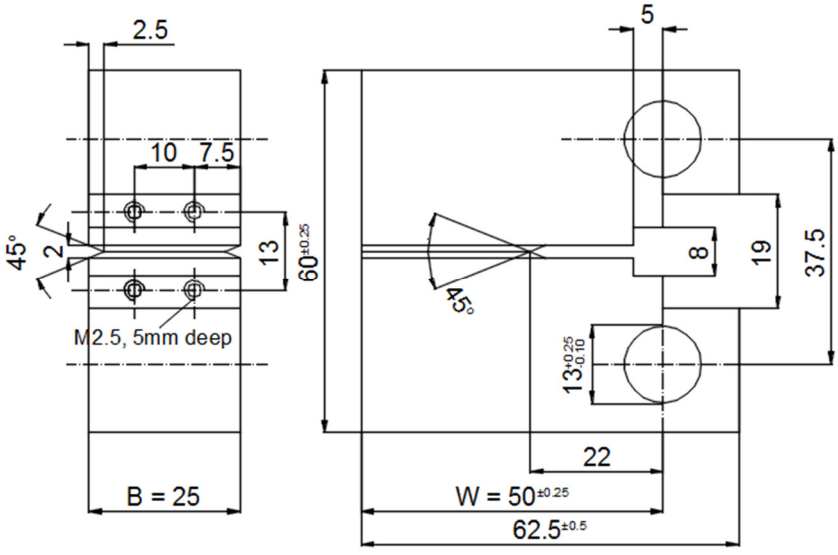

A. 6: Sketch of the compact tension specimen ((C(T)25) with 20% side groove.

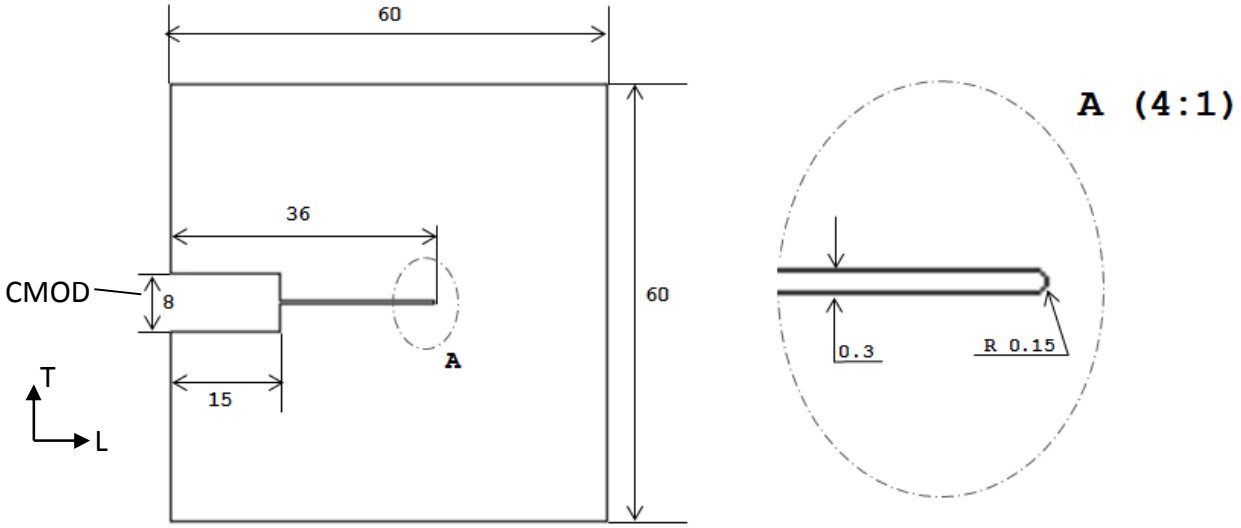

A. 7: Sketch of the thin sheet (1 mm) specimen used for in situ laminography study with the dimensions of 60 x 60 x 1 mm^3.

10. List of Publications

1. H. Y. Tu, S. Schmauder, U. Weber, Numerical simulation and experimental investigation of damage behaviour on Al6061 laser welded joints, Key Engineering Materials Vol. 627 (2015), pp. 105-108.

2. H. Y. Tu, S. Schmauder, U. Weber, Numerical simulation of crack propagation in Al6061 laser welded joints. Procedia Materials Science 3 (2014), pp. 414-420.

3. H. Tu, S. Schmauder, U. Weber, Numerical study of the fracture behavior of an electron beam welded steel joint by cohesive zone modeling. Proceedings of the 13th International Conference on Fracture, 16th -21st June, 2013, volume 7, pp. 5863-5871.

4. H. Y. Tu, S. Schmauder, U. Weber, Y. Rudnik, V. Ploshikhin. Simulation of the damage behavior of electron beam welded joints with the Rousselier model. Engng Fract. Mech 103 (2013), pp. 153-161.

5. H. Tu, S. Schmauder, U. Weber. Numerical study of electron beam welded butt joints with the GTN model. Comput Mech 50 (2012), pp. 245-255.

6. H. Y. Tu, S. Schmauder, U. Weber, Y. Rudnik, V. Ploshikhin. Numerical simulation and experimental investigation of the damage behavior on electron beam welded joints. Proceedings of the 11th International Conference on the Mechanical Behavior of Materials, Procedia Engineering, Volume 10, pp. 875-880, 2011.

7. H. Y. Tu, Y. Rudnik, S. Schmauder, U. Weber, V. Ploshikhin. Numerical simulation of crack propagation in electron beam welded joints. Proceedings of the 18th European Conference on Fracture, 30. August-03. September, 2010, CD-ROM.

11. Bibliography

[ABAQUS, 2008] ABAQUS Theory manual 6.7. Hibbitt, Karlsson & Sorensen, 2008.

[Amira, 2009]. AmiraR@5, Amira User's Guide. VSG - Visualization Sciences Group, 2009.

[Anderson, 2005] T. L. Anderson. Fracture Mechanics: Fundamentals and Applications. Third Edition, CRC Press, 2005.

[Anvari, 2006] M. Anvari, I. Scheider, C. Thaulow. Simulation of dynamic ductile crack growth using strain-rate and triaxiality-dependent cohesive elements. Engng Fract Mech 73 (2006), 2210-2228.

[ARAMIS, 2008] ARAMIS user manual- software, ARAMIS V6.1, GOM mbH, 2008.

[ASTM, 2003] ASTM E 1820-96. Standard test method for measurement of fracture toughness. In: Annual Book of ASTM Standards, Vol. 03.01. American Society for Testing and Materials, Philadelphia, PA, USA.

[Barenblatt, 1962] G. I. Barenblatt. The mathematical theory of equilibrium cracks in brittle fracture. Adv Appl Mech 7 (1962), 55-129.

[Begley, 1972] J. A. Begley, J. D. Landes. The J-integral as a fracture criterion, Fracture Mechanics, ASTM STP 514 (1972), 1-23.

[Bernauer, 2002] G. Bernauer, W. Brocks. Micro-mechanical modelling of ductile damage and tearing - results of a european numerical round robin. Fatigue Fract Engng Mater Struct 25 (2002), 384-463.

[Beremin, 1983] F.M. Beremin. A local criterion for cleavage fracture of a nuclear pressure vessel steel. Metall Trans A 14A (1983), 2277-2287.

[Bishop, 1951] J. Bishop, R. Hill. A theoretical derivation of the plastic properties of a polycrystalline face-centred matal. Phil Mag 42 (1951), 1298-1307.

[Bleck, 2009] W. Bleck, W. Dahl, A. Nonn, L. Amlung, M. Feldmann, D. Schäfer, B. Eichler. Numerical and experimental analyses of damage behaviour of steel moment connection. Engng Fract Mech 76 (2009), 1531-1547.

[Broberg, 1997] K. B. Broberg. The cell model of materials. Comput Mech 19 (1997), 447-452.

[Brocks, 2001] W. Brocks, I. Scheider. Numerical Aspects of the Path-Dependence of the J-Integral in Incremental Plasticity. Technical Note GKSS/WMS/01/08, GKSS-Forschungszentrum Geesthacht, 2001.

[Brocks, 2002] W. Brocks, A. Cornec, I. Scheider. Computational aspects of nonlinear fracture mechanics. Technical note GKSS/WMS/02/05, GKSS-Forschungszentrum Geesthacht, 2002.

[Brocks, 2004] W. Brocks. Computational Fracture Mechanics, in Continuum Scale Simulation of Engineering Materials: Fundamentals - Microstructures - Process Applications. In: Roters F, Barlat F, Chen LQ (eds) Wiley-VCH Verlag GmbH & Co. KGaA, Weinheim, 2004.

[Brocks, 2014] W. Brocks, D. Arafah. Computational Fracture Mechanics, Students Project, Final report. Politecnico di Milano, 2014.

[Camanho, 2002] P. P. Camanho, C. G. Dávila. Mixed-mode decohesion finite elements for the simulation of delamination in composite materials. NASA-Technical paper 211737 (1), 33.

[Cambrésy, 2006] P. Cambrésy. Damage and fracture mechanisms investigations of an aluminium laser beam weld. Dissertation, GKSS-Forschungszentrum Geesthacht, 2006.

[Çam, 1999] G. Çam, M. Koçak, J. F. Dos Santos. Developments in laser welding of metallic materials and characterization of the joints. Weld World 43 (1999), 13-26.

[Chabanet, 2003] O. Chabanet, D. Steglich, J. Besson, V. Heitmann, D. Hellmann, W. Brocks. Predicting crack growth resistance of aluminium sheets. Comp Mater Sci 26 (2003), 1-12.

[Chen, 2003] C. R. Chen, O. Kolednik, I. Scheider, T. Siegmund, A. Tatschl, F. D. Fischer. On the determination of the cohesive zone parameters for the modelling of microductile crack growth in thick specimens, Int J Fract 120 (2003), 417-536.

[Cheng, 2013a] Y. Cheng. In situ Synchrotron radiation computed laminographz for materials failure analysis. Dissertation, Albert-Ludwigs-Universität Freiburg, 2013.

[Cheng, 2013b] Y. Cheng, V. Altapova, L. Helfen, F. Xu, T. dos Santos Rolo, P. Vagovič, M. Fiederle, T. Baumbach. Multi-contrast computed laminography at ANKA light source. J Phys: Conf Ser 463 (2013), 012038.

[Chu, 1980] C. C. Chu, A. Needleman. Void nucleation effects in biaxially stretched sheets. J Engng Mater Technol 102 (1980), 249-256.

[Cloetens, 1999] P. Cloetens, R. Barrett, J. Baruchel, J. P. Guigay, M. Schlenker. Phase objects in synchrotron radiation hard x-ray imaging. J Phys D 29 (1996), 133-146.

[Cornec, 2003] A. Cornec, I. Scheider, K.-H. Schwalbe. On the practical application of the cohesive model. Engng Fract Mech 70 (2003), 1963-1987.

[Chhibber, 2011] R. Chhibber, P. Biswas, N. Arora, S. R. Gupta, B. K. Dutta. Micromechanical modelling of weldments using GTN model. Int J Fract 167 (2011), 71-82.

[Dugdale, 1960] D. S. Dugdale, Yielding of steel sheets containing slits. J Mech Phys Solids 8 (1960), 100-104.

[Eisele, 2006] U. Eisele, R. Lammert, D. Restemeyer, X. Schuler, H. P. Seebich, M. Seidenfuß, H. Silcher, L. Stumpfrock. Reactor safety research - Project No. 1501240: Critical examination of the master curve approach regarding application in German nuclear power plants. Report-No: 8886000000, MPA Stuttgart, 2006.

[Franklin, 1969] A. G. Franklin. Comparison between a quantitative microscope and chemical methods for assessment of non-metallic inclusions. J Iron Steel Inst 207 (1969), 181-186.

[Garrison, 1987] W. M. Garrison, N. R. Moody. Ductile fracture. J Phys Chem Solids 48 (1987), 1035-1074.

[GOM, 2014] http://www.gom.com/, 2014.

[Grazinai, 2014] L. Graziani, M. Knećb, T. Sadowski, M. D. Orazio, S. Lenci. Measurement of R-curve in clay brick blocks using optical measuring technique. Engng Fract Mech 121-122 (2014), 1-10.

[Griffith, 1920] A. A. Griffith, The phenomena of rupture and flow in solids. Phil. Trans. Roy. Soc. London, 1920, A211, 163-198.

[Griffiths, 1971] J. R. Griffiths, An elastic-plastic stress analysis for a notched bar in plane strain bending. J Mech Phys Solids 19 (1971), 419-431.

[Gurson, 1977] A. L. Gurson, Continuum theory of ductile rupture by void nucleation and growth, Part I - yield criteria and flow rules for pourous ductile media. J Engng Mater Techol 99 (1977), 2-15.

[Helfen, 2005] L. Helfen, T. Baumbach, P. Pernot, P. Cloetens, H. Stanzick, K. Schladitz, J. Banhart. Investigation of pore initiation in metal foams by synchrotron-radiation tomography, Appl Phys Lett 86 (2005), 231907-1-231907-3.

[Helfen, 2011] L. Helfen, A. Myagotin, P. Mikulik, P. Pernot, A. Voropaev, M. Elyyan, M. DiMichiel, J. Baruchel, T. Baumbach. On the implementation of computed laminography using synchrotron radiation. Rev Sci Instrum 82 (2011), 063702-1-063702-8.

[Hillerborg, 1976] A. Hillerborg, M. Modéer, P.-E. Petersson. Analysis of crack formation and crack growth in concrete by means of fracture mechanics and finite elements. Cem Conc Res 6 (1976), 773-782.

[Huang, 1991] Y. Huang. Accurate dilatation rates for spherical voids in triaxial stress fields. J Appl Mech Trans ASME 58 (1991), 1084-1086.

[Huang, 2011] J. Huang, S. Schmauder, U. Weber, S. Geier. Micromechanical modelling of the elastoplastic behaviour of nanodispersed elastomer particle-modified PA 6. Comp Mater Sci 52 (2011), 107-111.

[Image J, 2011] Image J User Guide, I J 1.46r, 2012.

[Irwin, 1957] G. R. Irwin. Analysis of stresses and strains near the end of a crack traversing a plate. J Appl Mech 24 (1957), 361-364.

[Kou, 2002] S. Kou, Welding metallurgy. (2nd Ed.) John Wiley & Sons. Inc., Hoboken, New Jersey, 2003.

[Kussmaul, 1995] K. Kussmaul, U. Eisele, M. Seidenfuss. On the applicability of local approach models for the determination of the failure behaviour of steels with different toughness. Mehta (Ed.), et al., Fatigue & Fract Mech in Press Vess & Piping 304 (1995), 17-25.

[Laiarinandrasana, 2012] L. Laiarinandrasana, T. F. Morgeneyer, H. Proudhon, F. N'guyen, E. Maire. Effect of Multiaxial Stress State on Morphology and Spatial Distribution of Voids in Deformed Semicrystalline Polymer Assessed by X-ray Tomography. Macromolecules 45 (2012), 4658-4668.

[Landes, 1972] J. D. Landes, J. A. Begley. The J-Integral as a fracture criterion. ASTM STP 514, American Society for testing and Materials, Philadelphia (1972), 1-20.

[Larsen, 1993] J. M. Larsen, T. Nicholas. Load sequence crack growth transient in a superalloy at elevated temperature. Fracture mechanics, fourteenth symposium, Vol II, testing and application, STP 791 (1983), 536-552.

[Li, 2002] W. Li, T. Siegmund. An analysis of crack growth in thin-sheet metal via a cohesive zone model. Engng Frac Mech 69 (2002), 2073-2093.

[Lin, 1998a] G. Lin, A. Cornec, K.-H. Schwalbe. Three-dimensional finite element simulation of crack extension in aluminum alloy 2024-FC. Fatigue Fract Engng Mater Struct, 21 (1998), 1159-1173.

[Lin, 1998b] G. Lin. Numerical investigation of crack growth behaviour using a cohesive zone model. PhD thesis, TU Hamburg-Harburg, Geesthacht, 1998.

[Lin, 1999] G. Lin, X.-G. Meng, A. Cornec, K.-H. Schwalbe. The effect of strength mis-match on mechanical performance of weld joints. Int J Fract 96 (1999), 37-54.

[Mohanta, 2003] A. Mohanta. Numerical determination of failure curves. Master thesis, University of Stuttgart, 2003.

[Morgeneyer, 2009] T. F. Morgeneyer, J. Besson, H. Proudhon, M. J. Starink, I. Sinclair. Experimental and numerical analysis of toughness anisotropy in AA2139 Al-alloy sheet. Acta Mater 57 (2009), 3902-3915.

[Morgeneyer, 2011] T. F. Morgeneyer, L. Helfen, I. Sinclair, H. Proudhon, F. Xu ,T. Baumbach. Ductile crack initiation and propagation assessed via in situ synchrotron radiation-computed laminography. Scripta Mater 65 (2011), 1010-1013.

[Morgeneyer, 2013] T. F. Morgeneyer, L. Helfen, H. Mubarak, F. Hild. 3D Digital Volume Correlation of Synchrotron Radiation Laminography images of ductile crack initiation: An initial feasibility study. Experimental Mech 53 (2013), 543-556.

[Morgeneyer, 2014] T. F. Morgeneyer, T. T. Thomas, L. Helfen, T. Baumbach, I. Sinclair, S. Roux, F. Hild. In situ 3-D observation of early strain localization during failure of thin Al alloy (2198) sheet. Acta Mater 69 (2009), 78-91.

[Nahshon, 2008] K. Nahshon, J. W. Hutchinson. Modification of the Gurson Model for shear failure. European Journal of Mechanics A/Solids 27 (2008), 1-17.

[Needleman, 1978] A. Needleman, J. R. Rice. Limits to ductility by plastic flow localization. Mechanics of Metal Sheet Forming 1978, 237-267.

[Needleman, 1987] A. Needleman. A continuum model for void nucleation by inclusion debonding. J Appl Mech ASME 54 (1987), 525-531.

[Needleman, 1990] A. Needleman. An analysis of decohesion along an imperfect interface. I J Fract 42 (1990), 21-40.

[Needleman, 1999] A. Needleman, V. Tvergaard. A micromechanical analysis of ductile-brittle transition at a weld. Engng Frac Mech 62 (1999), 317-338.

[Nègre, 2003] P. Nègre, D. Steglich, W. Brocks. Numerical simulation of crack extension in aluminium welds. Compu Mater Sci 28 (2003), 723-731.

[Nègre, 2004] P. Nègre, D. Steglich, W. Brocks. Crack extension in aluminium welds: a numerical approach using the Gurson-Tvergaard-Needleman model. Engng Frac Mech 71 (2004), 2365-2383.

[Nielson, 2008] K. L. Nielsen. Ductile damage development in friction stir welded aluminum (AA2024) joints. Engng Frac Mech 71 (2008), 2795-2811.

[Nonn, 2008] A. Nonn, W. Dahl, W. Bleck. Numerical modelling of damage behaviour of laser-hybrid welds. Engng Frac Mech 75 (2008), 3251-3263.

[Nugent, 1996] K. A. Nugent, T. E. Gureyev, D. F. Cookson, D. Paganin, Z.Barnea. Phys Rev Lett 77 (1996), 2961-2964.

[Østby, 2007a] E. Østby, C. Thaulow, Z. L. Zhang. Numerical simulations of specimen size and mismatch effects in ductile crack growth - Part I: Tearing resistance and crack growth paths. Engng Frac Mech 74 (2007), 1770-1792.

[Østby, 2007b] E. Østby, C. Thaulow, Z. L. Zhang. Numerical simulations of specimen size and mismatch effects in ductile crack growth - Part II: Near-tip stress fields. Engng Frac Mech 74 (2007), 1793-1809.

[Paganin, 2002] D. Paganin, S. C. Mayo, T. E. Gureyev, P. R. Miller, S. W. Wilkins. Simultaneous phase and amplitude extraction from a single defocused image of a homogeneous object. J Microsc 206 (2002), 33-40.

[Perrina, 1990] G. Perrina, J. B. Leblond. Analytical study of a hollow sphere made of plastic porous material and subjected to hydrostatic tension-application to some problems in ductile fracture of metals. I J Plasticity 6 (1990), 677-699.

[Rice, 1968] J. R. Rice. A path independent integral and the approximate analysis of strain concentrations by notches and cracks. J Appl Mech 35 (1968), 379-386.

[Rice, 1969] J. R. Rice, D. M. Tracey. On the ductile enlargement of voids in triaxial stress fields. J Mech Phys Solids 17 (1969), 201-217.

[Rivalin, 2001a] F. Rivalin, A. Pineau, M. Di Fant, J. Besson. Ductile tearing of pipeline-steel wide plates: I. Dynamic and quasi-static experiments. Engng Frac Mech 68 (2001), 329-345.

[Rivalin, 2001b] F. Rivalin, J. Besson, A. Pineau, M. Di Fant. Ductile tearing of pipeline-steel wide plates: II. Modeling of in-plane crack propagation. Engng Frac Mech 68 (2001), 347-364.

[Roos, 1988] E. Roos, U. Eisele. Determination of material characteristic values in elastic-plastic fracture mechanics by means of J-Integral crack resistance curves. Journ. of Testing and Evaluation 16 (1988), 1-11.

[Rousselier, 1987] G. Rousselier. Ductile fracture models and their potential in local approach of fracture. Nucl Eng Design 105 (1987), 97-111.

[Rousselier, 2001] G. Rousselier. The Rousselier model for porous metal plasticity and ductile fracture. Handbook of materials behaviour models (2001), 436-445.

[Sadowski, 2010] T. Sadowski, M. Knec, P. Golewski. Experimental investigations and numerical modelling of steel adhesive joints reinforced by rivets. Int J Adhe & Adhes 30 (2010), 338-346.

[Samal, 2008] M. K. Samal, M. Seidenfuss, E. Roos, B. K. Dutta, H. S. Kushwaha. Finite element formulation of a new nonlocal damage model. Fin Elem Anal Des 44 (2008), 358-371.

[Samal, 2009] M. K. Samal, M. Seidenfuss, E. Roos. A new mesh-independent Rousselier's damage model: Finite element implementation and experimental verification. Int J Mech Sci 51 (2009), 619-630.

[Santos, 2000] J. F. Dos Santos, G. Çam, F. Torster, A. Insfran, S. Riekehr, V. Ventzke. Properties of power beam welded steel, Al-and Ti alloys: Significance of strength mismatch. Weld World 44 (2000), 42-64.

[Schmauder, 2002] S. Schmauder, D. Uhlmann, G. Zies. Experimental and numerical investigations of two material states of the material 15NiCuMoNb5 (WB 36). Comp Mater Sci 25 (2002), 174-192.

[Schmauder, 2009] S. Schmauder, L. J. Mishnaevsky. Micromechanics and Nanosimultion of Metals and Composites, Eds.: S. Schmauder, L. J. Mishnaevsky, Springer-Verlag, Berlin, Heidelberg (2009), 420 p.

[Schwalbe, 2009] K.-H. Schwalbe, I. Scheider, A. Cornec. SIAM CM09 - The SIAM method for application cohesive models of the damage behaviour of engineering materials and structures. GKSS report, 2009/1, GKSS-Forschungszentrum Geesthacht, 2009.

[Scheider, 2001] I. Scheider. Bruchmechanische Bewertung von Laserschweißverbindungen durch numerische Rissfortschrittsimulation mit dem Kohäsivzonenmodell. Dissertation, TU Hamburg-Harburg, Geesthacht, 2001.

[Scheider, 2003a] I. Scheider, W. Brocks Simulation of cup-cone fracture using the cohesive model. Engng Fract Mech 70 (2003), 1943-1961.

[Scheider, 2003b] I. Scheider, W. Brocks. The effect of the traction separation law on the results of cohesive zone crack propagation analyses. Key Engng Mater 251-252 (2003), 313-318

[Seib, 2006] Residual strength analysis of laser beam and friction stir welded aluminum panels for aerospace applications. Dissertation, TU Hamburg-Harburg, Geesthacht, 2006.

[Seebich, 2007] H. P. Seebich. Mikromechanisch basierte Schädigungsmodelle zur Beschreibung des Versagensablaufs ferritischer Bauteile. Dissertation, Universität Stuttgart, 2007.

[Seidenfuss, 1992] M. Seidenfuss. Untersuchungen zur Beschreibung des Versagensverhaltens mit Hilfe von Schädigungsmodellen am Beispiel des Werkstoffs 20MnMoNi55. Dissertation, Universität Stuttgart, 1992.

[Shen, 2013] Y. Shen, T. F. Morgeneyer, J. Garnier, L. Allais, L. Helfen, J. Crépin. Three-dimensional quantitative in situ study of crack initiation and propagation in AA6061 aluminum alloy sheets via synchrotron laminography and finite-element simulations. Acta Mater 61 (2013), 2571-2582.

[Siegmund, 2000] T. Siegmund, A. Needleman. A numerical study of dynamic crack growth in elastic-viscoplastic solids. Int J Solids Struct 34 (1997), 769-787.

[Springmann, 2005] M. Springmann, M. Kuna. Identification of material parameters of the Gurson-Tvergaard -Needleman model by combined experimental and numerical techniques. Comp Mater Sci 32 (2005), 544-552.

[Steglich, 2004] D. Steglich. Structure Damage Simulation, in Continuum Scale Simulation of Engineering Materials: Fundamentals - Microstructures - Process Applications. In: Roters F, Barlat F, Chen LQ (eds) Wiley-VCH Verlag GmbH & Co. KGaA, Weinheim.

[Tanguy, 2008] B. Tanguy, T. T. Luu, G. Perrin, A. Pineau, J. Besson. Plastic and damage behaviour of a high strength X100 pipeline steel: Experiments and modeling. Int J Press Vess & Piping 85 (2008), 322-335.

[Tu, 2011] H. Y. Tu, S. Schmauder, U. Weber, Y. Rudnik, V. Ploshikhin. Numerical simulation and experimental investigation of the damage behavior on electron beam welded joints. Proc Engng 10 (2011), 875-880.

[Tu, 2013] H. Y. Tu, S. Schmauder, U. Weber, Y. Rudnik, V. Ploshikhin. Simulation of the damage behavior of electron beam welded joints with the Rousselier model. Engng Fract Mech 103 (2013), 153-161.

[Tu, 2013] H. Y. Tu, S. Schmauder, U. Weber, Numerical study of the fracture behavior of an electron beam welded steel joint by cohesive zone modeling. Proc. Int. Conf. Fracture, ICF13 (2013), 5863-5871.

[Tu, 2012] H. Tu, S. Schmauder, U. Weber. Numerical study of electron beam welded butt joints with the GTN model. Comput Mech 50 (2012), 245-255.

[Tvergaard, 1981] V. Tvergaard .Influence of voids on shear band instabilities under plane strain conditions. Int J Fract 17 (1981), 389-407.

[Tvergaard, 1982a] V. Tvergaard. On localization in ductile materials containing spherical voids. Int J Fract 18 (1982), 237-252.

[Tvergaard, 1982b] V. Tvergaard. Influence of void nucleation on ductile shear fracture at a free surface. J Mech Phys Solids 30 (1982), 399-425.

[Tvergaard, 1984] V. Tvergaard, A. Needleman. Analysis of the cup-cone fracture in a round tensile bar. Acta Metall 38 (1984), 157-169.

[Tvergaard, 1989] V. Tvergaard. On the analysis of ductile fracture mechanisms. Proc. Int. Conf. Fracture, ICF7 (1989), 159-179.

[Tvergaard, 1992] V. Tvergaard, J. W. Hutchinson. The relation between crack growth resistance and fracture process parameters in elastic-plastic solids. J Mech Phys Solids 40 (1992), 1377-1397.

[Tvergaard, 2001] V. Tvergaard, A. Needleman. Handbook of Materials Behavior Models. Academic Press, Incorporated, 2001, 430-435.

[Tvergaard, 2000] V. Tvergaard, A. Needleman. Analysis of the Charpy V-notch test for welds. Engng Frac Mech 65 (2000), 627-643.

[Tvergaard, 2004] V. Tvergaard, A. Needleman. 3D analyses of the effect of weld orientation in Charpy specimens. Engng Frac Mech 71 (2004), 2179-2195.

[Ueda, 2014] T. Ueda, L. Helfen, T. F. Morgeneyer. In situ laminography study of three-dimensional individual void shape evolution at crack initiation and comparison with Gurson-Tvergaard Needleman-type simulations. Acta Mater 78 (2014), 254-270.

[Uhlmann, 1999] D. Uhlmann. Reactor Safety Research - Project No. 1501029: Material characterization of the material 15 NiCuMoNb 5 including the determination of the local approach parameter for the Rousselier model for two material states. Report-No: 878701004, MPA Stuttgart , 1999.

[Weber, 2006] U. Weber. Modellierung von Verformung und Schädigung in Werkstoffgefügen mit unterschiedlich großen Teilchen und unter Wasserstoffeinfluss. Dissertation, Universität Stuttgart, 2006.

[Weber, 2007] U. Weber, A. Mohanta, S. Schmauder. Numerical determination of parameterised failure curves for ductile structural materials. Int J Mat Research 98 (2007), 1071-1080.

[Xia, 1996] L. Xia, and C. F Shih. Ductile crack growth - III. Transition to cleavage fracture incorporating statistics. J Mech Phys Solids 44 (1996), 603-639.

[Xu, 2010] F. Xu, L.Helfen, A. J. Moffat, G. Johnson, I. Sinclair, T. Baumbach. J Synch Radiat 17 (2010), 222-226.

[Yuan, 1991] H. Yuan, G. Lin, A. Cornec. Verification of a cohesive zone model for ductile fracture. J Engng Mater Techno 118 (1996), 192-200.

[Zhang, 2000] Z. L. Zhang, C. Thaulow, J. Odegard. A complete Gurson model approach for ductile fracture. Engng Frac Mech 67 (2000), 155-168.

Acknowledgements

Firstly, I would like to express my deep thanks to Prof. Dr. rer. nat. Siegfried Schmauder for supervising me at the Institute for Materials Testing, Materials Science and Strength of Materials (IMWF), University of Stuttgart. I thank him for providing me the free working environment and continuous encouragement for trying new ideas in my work. After several years' work with him, I realize that scientist should not be satisfied with what has been achieved and shoulder the duty for innovation. Our deep discussions always provide me the direction of research. I also thank him for reading the thesis and provide me many useful suggestions.

Secondly, I would like to thank Associate Prof. Thilo Frank Morgeneyer, Chargé de recherches, HDR, PhD, from Mines ParisTech for agreeing to be the second supervisor of my thesis and his interest of my work.

Special thanks are given to Dr.-Ing. Ulrich Weber who helped me a lot during my work and kind discussion about the thesis.

I also would like to thank Prof. Dr.-Ing. Vasily Ploshikhin from University of Bremen who provided me S355 electron beam welded samples and coordinate some tensile tests at Bayreuth GmbH. Special thanks is due to Dr.-Ing. Yegor Rudnik from Bayreuth GmbH for discussion the tensile results about the weldment.

The work of laminography chapter could not have been performed without the help of Associate Prof. Thilo Frank Morgeneyer, Chargé de recherches, HDR, PhD, from Mines ParisTech and the working of staff at ID15A beamline, ESRF, Grenoble. Special thanks are given to Dr.-Ing. Lukas Helfer from ANKA, KIT and ESRF who helps me performing the laminography experiment. Many thanks are given to Dr. rer. nat. Yin Cheng from Mines ParisTech and KIT, who helped me for reconstruction the scanning data of laminography experiment.

I also would like to thank Prof. Dr.-Ing. Wolfgang Brocks, Dr.-Ing. Ingo Scheider, Dr.-Ing. Dirk Steglich from Helmholtz-Zentrum Geesthacht, Centre for Materials and Coastal

Research for warm discussions about the damage models and the cohesive model. The deep discussions between us widened my knowledge about fracture mechanics.

The colleagues from Materials Testing Institute (MPA) and IMWF, University of Stuttgart are also acknowledged. I thank Dr.-Ing. Yanling Schneider, Dr. rer. nat. Ewa Soppa, Dr. rer. nat. Herbert Ruoff, Dr.-Ing. Harald Diem, Dr.-Ing. Annett Udoh, Dr.-Ing. Horst Silcher, Dipl.-Ing. Jing Wiedmaier, Dr. rer. nat. Galina Lasko, PD Dr.-Ing. Michael Seidenfuß, Dr. rer. nat. Alejandro Mora, Dipl.-Ing. Peter Weidmann, Dr.-Ing. Peter Binkele, Dr.-Ing. Alen-Pilip Prskalo, Dr.-Ing. David Molnar, mag. ing. mech. Marijo Mlikota, Dipl.-Phys. Martin Hummel, Dr. rer. nat. Stefan Hocker, Dr.-Ing. Axel B. Krebs, Prof. Dr. Vera Petrova, Dipl.-Biol. Immanuel Schäfer, Dipl.-Math. techn. Stefan Küster, Dipl.-Ing. Wolfgang Verestek, Dipl.-Ing. Vinzenz Guski and M. Sc. Dennis Rapp. I also would like to express my thanks to Ms. Kerstin Hilscher, Ms. Erika Laukenmann, Ms. Iris Weber and Ms. Stefanie Bisinger for their assistances during the running of the project.

I would like to thank my family who always support me during my academic career for many years. Special thanks are given to my wife **Rong** who always encourages me when I am puzzled during research work.

Last but not least, I thank the China Scholarship Council (CSC) and German Science Foundation (DFG) for the financial supports which make this work possible.

April, 2016, Stuttgart